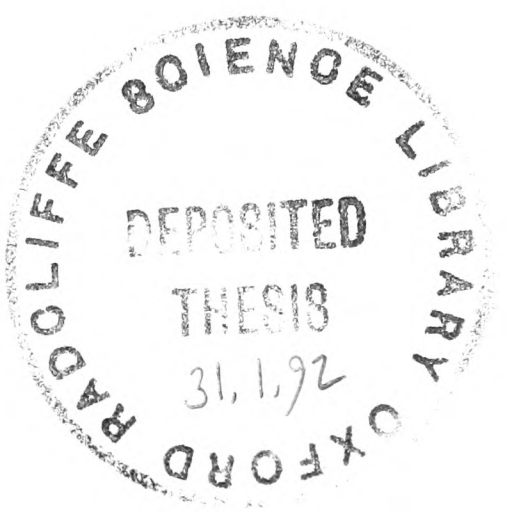
STRUCTURAL STUDIES ON NONLINEAR OPTICAL MATERIALS

A thesis submitted to the Board of the Faculty of Physical Sciences of the University of Oxford in partial fulfilment of the requirements for the degree of Doctor of Philosophy.

Susan J. Crennell,

Christ Church,

Trinity Term 1991.



ABSTRACT

Structural Studies on Nonlinear Optical Materials

A thesis submitted for the degree of Doctor of Philosophy in the University of Oxford by S. J. Crennell, Christ Church, Trinity Term 1991.

This thesis reports the synthesis and structural characteristics of solid solutions derived from KTP, $KTiOPO_4$ (space group $Pn2_1a$, Z=8, a =12.814(6)Å, b =10.616(5)Å, c = 6.404(2)Å) with substitution of K by Na and Rb; Ti by Sn, Ge and Cr; and P by As. The $KTiOPO_4$ structure contains two formula units per asymmetric unit and hence two crystallographically distinct K, Ti and P sites. This makes substituent ordering possible with selective modification of the nonlinear optical properties.

$K_{0.5}Na_{0.5}TiOPO_4$, (occupancy K(1):96(7)%Na, K(2):105(8)%K) was characterised by Rietveld analysis of combined time-of-flight (TOF) neutron and X-ray powder diffraction, the X-ray diffraction data being required to distinguish between K and Na . Constant wavelength neutron powder diffraction data were used to refine the $Na_{0.5}Rb_{0.5}TiOPO_4$ structure (K(1):97(3)%Na, K(2):96(3)%Rb). The cations in both these materials were fully ordered over the two possible K sites, while in $K_{0.5}Rb_{0.5}TiOPO_4$,(K(1):71(2)%K, K(2):71(2)%Rb) the cation distribution, determined from a TOF neutron powder diffraction study, was only partially ordered. A single crystal X-ray diffraction study of an ion-exchanged $K_{1-x}Na_xTiOPO_4$ sample (x=0.58), confirmed that the cation distribution observed in the powder diffraction analysis was also present after ion-exchange at lower temperatures (350°C), (K(1):93.3(1)%Na, K(2):77.3(7)%K). An ion-exchanged crystal that had been annealed at a temperature closer to the $KTiOPO_4$ synthesis temperature gave almost identical results (K(1):94.4(6)%Na, K(2):81.0(4)%K).

Substitution for Ti by Sn or Ge gave rise to only partial ordering. The structures of $KTi_{0.5}Sn_{0.5}OPO_4$ (Ti(1):63.9%Ti, Ti(2):64.6(5)%Sn) and $KTi_{0.5}Ge_{0.5}OPO_4$ (Ti(1):76.7(4)%Ti, Ti(2):66.1(5)%Ge) were determined through combined analysis of X-ray and TOF neutron powder diffraction data. The X-ray data were required to define the Ti(1) site as the average weighted neutron scattering length was approximately zero. An apparently random distribution of As over the two P sites was demonstrated by time-of-flight powder neutron diffraction from $KTiOP_{0.5}As_{0.5}O_4$ (P(1):56(1)%P, P(2):56(1)%As). Measurements on $KTiOP_{1-x}As_xO_4$ powders indicated that the Nd:YAG second harmonic intensity increased with As. The structures of $RbTi_{0.5}Sn_{0.5}OPO_4$ and $RbTiOP_{0.5}As_{0.5}O_4$ were investigated by powder X-ray diffraction and showed similar ordering to the K isomorphs.

Simultaneous substitution for both K and Ti was investigated by Rietveld analysis of combined X-ray and TOF neutron powder diffraction data on $K_{0.5}Na_{0.5}Ti_{0.5}Sn_{0.5}OPO_4$ (K(1):73(4)%Na, Ti(1):66.9(3)%Ti), $Na_{0.5}Rb_{0.5}Ti_{0.5}Sn_{0.5}OPO_4$ (K(1):54(2)%Rb, Ti(1):67.0(5)%Ti), $K_{0.5}Rb_{0.5}Ti_{0.5}Sn_{0.5}OPO_4$ (K(1):77(1)%K, Ti(1):66.1(3)%Ti) and $K_{0.5}Rb_{0.5}SnOPO_4$ (K(1):64(2)%K).

Cr-doped materials were studied by single crystal X-ray and TOF neutron powder diffraction. Doping a small quantity of Cr into KTP produced the $KTi_{.95}Cr_{.05}OPO_4$ isomorph, (3.2(6)%Cr on both Ti sites). Substitution of a larger amount of Cr produced $K_{1.8}Ti_{1.2}Cr_{.8}(PO_4)_3$, (space group $P2_13$, a=9.7902(1)Å, Ti(1):69.4(6)%Ti, Ti(2):54.9(6)%Ti) isomorphous with Langbeinite. Magnetic measurements using a SQUID susceptometer found a value for the moment consistent with Cr(III).

Acknowledgements

I wish to thank my supervisor, Prof. A.K. Cheetham, for his unending enthusiasm.

I am indebted to Amoco Technology Company for the provision of a studentship and for the opportunity to visit the Amoco Research Center near Chicago for two summers. Thanks are due to a large number of people who made my eight months there a very rewarding experience: Richard Jarman for supervising my synthetic work and organising the visits, Patti Mayo-Katsion for helping me with the synthesis; Bob Thrash and Roger Raddatz for their tolerance of a "grad student" in their laser lab., for giving me an understanding of the basics of nonlinear optics and for many amusing hours of discussion on English history and semantics; to Jim Kaduk for teaching me all that I know about Rietveld refinement and to Maria Kaminsky and Ying-Mei Chen for running all my analytical X-ray diffraction patterns and introducing me to the pattern analysis software. Finally I would like to thank Jim, Cathy, Anne and Benjamin Kaduk for looking after me on recent visits to Naperville.

The instrument scientists of GPPD and POLARIS, Dick Hitterman and Steve Hull were very helpful during my neutron diffraction data collection, and Fred Wondre kindly collected X-ray powder diffraction data on the Clarendon Stoe diffractometer. Back in the Chemical Crystallography Lab., I would like to thank Jerry Skarnulis, Ann Stoker and Nicola Stedman for help with the analytical electron microscope; David Watkin for many valuable crystallographic discussions; Jon, Lucy and Clare for running and interpreting the m.a.s.n.m.r spectra; Joanne for measuring magnetic moments; Angus and Joanne for many helpful discussions on GSAS, and everyone in Room 27 for helping me survive the last three years: Alex, Angus, Ann, Clare, Joanne, Joe, Jon, Julian,

Acknowledgements

Lucy, Neil, Nicola and Paul.

Finally I would like to thank Benomy and my parents for the loan of the printer and computer, for their proof-reading endeavours and their support during my time in Oxford.

Contents

Abstract

Acknowledgements

CHAPTER ONE: Introduction 1

1.1 Introduction 1

1.2 Introducion to nonlinear optics 2

1.2.1 Second harmonic generation 2

1.2.2 Microscopic physical origin of nonlinear optical behaviour 5

1.2.3 Phase-matching 6

1.2.4 Walkoff 11

1.2.5 Non-critical phase-matching 12

1.3 Nonlinear Optical materials 15

1.3.1 Organic nonlinear optical materials 15

1.3.2 Inorganic nonlinear optical materials 21

1.4 The Structure of $KTiOPO_4$ 28

1.5 Structure-property relationships in nonlinear optical materials 32

1.5.1 The bond-charge model 33

1.5.2 The anionic group theory 35

1.6 The structural chemistry of $KTiOPO_4$ 37

CHAPTER TWO: Experimental 40

2.1 Synthetic techniques 40

2.1.1 Solid State synthesis 40

2.1.2 Flux crystal growth 40

2.1.3 Ion exchange 41

2.2 Analytical techniques 42

2.2.1 Powder X-ray diffraction 42

2.2.2 Analytical electron microscopy 43

2.3 Single Crystal X-ray diffraction 46

2.3.1 Data collection 46

Contents

2.3.2 Data reduction 51

2.3.3 Structure refinement 53

2.4 Powder diffraction 55

2.4.1 Neutron vs. X-ray diffraction 56

2.4.2 Neutron diffraction techniques 58

2.4.3 D2B, a constant wavelength neutron diffractometer 60

2.4.4 GPPD, a time-of-flight neutron diffractometer 62

2.4.5 POLARIS, a time-of-flight neutron diffractometer 64

2.4.6 the Stoe STADI-P diffractometer 66

2.5 The Rietveld method 68

2.5.1 the Generalised Structure Analysis System 69

2.6 Bond Valence calculations 74

2.7 Measurement of nonlinear optical properties 75

2.7.1 Methods of measuring nonlinear optical coefficients using crystals 75

2.7.2 Measuring second harmonic generated from powders 76

2.7.3 Preparation of $KTiOPO_4$ derivatives for second harmonic measurements 80

2.7.4 Second Harmonic Generation testing 81

CHAPTER THREE: Cation substitution into $KTiOPO_4$ 85

3.1 Introduction 85

3.2 Synthesis and Characterisation of cation-substituted $KTiOPO_4$ isomorphs 89

3.2.1 Synthesis 89

3.2.2 Characterisation 90

3.3 Determination of the crystal structure of $K_{0.5}Na_{0.5}TiOPO_4$ (KNTP) 92

3.4 Determination of the crystal structure of $Na_{0.5}Rb_{0.5}TiOPO_4$ (NRTP) 104

3.5 Determination of the crystal structure of $K_{0.5}Rb_{0.5}TiOPO_4$ (KRTP) 112

3.6 Discussion of alkali-metal cation exchange into KTP 123

CHAPTER FOUR: Single crystal X-ray diffraction study of $K_{0.5}Na_{0.5}TiOPO_4$ 132

4.1 Waveguide formation 132

Contents

4.2 Synthesis and Characterisation of ion-exchange products 135

4.2.1 $K_{1-x}Rb_xTiOPO_4$ 136

4.2.2 $K_{1-x}Na_xTiOPO_4$ 137

4.3 Single crystal diffraction study of an annealed $K_{0.5}Na_{0.5}TiOPO_4$ crystal 141

4.3.1 Structure refinement 141

4.4 Single crystal diffraction study of ion-exchanged $K_{0.5}Na_{0.5}TiOPO_4$ crystal 146

4.4.1 Structure refinement 146

4.5 Results and Discussion 147

4.5.1 Bond valence calculations 157

4.5.2 Correlation with SHG properties 158

4.6 Ramifications for powder refinements 160

CHAPTER FIVE: Framework substitution in $KTiOPO_4$ 163

5.1 Introduction 163

5.2 Sn substitution into $KTiOPO_4$ isomorphs 164

5.2.1 Synthesis of $MTi_{1-x}Sn_xOPO_4$ solid solutions 164

5.2.2 Powder diffraction study of $KSn_{0.5}Ti_{0.5}OPO_4$ 164

5.2.3 X-ray powder diffraction study of $RbSn_{0.5}Ti_{0.5}OPO_4$ 173

5.3 A combined X-ray and time-of-flight neutron powder diffraction study of $KTi_{0.5}Ge_{0.5}OPO_4$ 179

5.4 As Substitution into $KTiOPO_4$ isomorphs 191

5.4.1 Synthesis of $MTiOP_{0.5}As_{0.5}O_4$ compounds 191

5.4.2 Time-of-flight neutron powder diffraction study of $KTiOP_{0.5}As_{0.5}O_4$ 192

5.4.3 SHG measurements in the $KTiO(P_{1-x}As_x)O_4$ solid solution field 201

5.4.4 X-ray powder diffraction study of $RbTiOP_{0.5}As_{0.5}O_4$ 206

CHAPTER SIX: Simultaneous cation and framework substitution in $KTiOPO_4$ 212

6.1 Synthesis and characterisation of cation and framework substituted KTP isomorphs 212

6.2 Combined X-ray and time-of-flight neutron powder diffraction study of $K_{0.5}Rb_{0.5}SnOPO_4$ 213

6.3 Combined X-ray and time-of-flight neutron powder diffraction study of $K_{0.5}Na_{0.5}Ti_{0.5}Sn_{0.5}OPO_4$ 221

Contents

6.4 Combined X-ray and time-of-flight neutron powder diffraction study of $Na_{0.5}Rb_{0.5}Ti_{0.5}Sn_{0.5}OPO_4$ 234

6.5 Combined X-ray and time-of-flight neutron powder diffraction study of $K_{0.5}Rb_{0.5}Ti_{0.5}Sn_{0.5}OPO_4$ 246

6.6 Mechanisms of substituent ordering over the framework and cation cavities of $KTiOPO_4$ 257

CHAPTER SEVEN: Cr exchange into K_2O-TiO_2-P_2O_5 261

7.1 Introduction 261

7.2 Inclusion of Cr in $KTiOPO_4$ isomorphs 262

7.2.1 Synthesis 262

7.2.2 Rietveld analysis of X-ray diffraction data from Cr-doped KTP isomorphs 263

7.3 Structure determination of $KTi_{0.95}Cr_{0.05}OPO_4$ 268

7.3.1 Single crystal structure determination of flux-grown $KTi_{0.95}Cr_{0.05}OPO_4$ 268

7.3.2 X-ray and time-of-flight neutron powder diffraction study of $KTi_{0.95}Cr_{0.05}OPO_4$ 272

7.4 Structure determination of $K_2Ti_{1.2}Cr_{0.8}(PO_4)_3$ 282

7.4.1 Single crystal structure determination of flux-grown $K_2Ti_{1.2}Cr_{0.8}(PO_4)_3$ 282

7.4.2 X-ray and time-of-flight neutron powder diffraction study of $K_2Ti_{1.2}Cr_{0.8}(PO_4)_3$ 288

7.5 Summary 296

CHAPTER EIGHT: Summary and Conclusions 298

8.1 Cation substitution into $KTiOPO_4$ 298

8.2 Substitution into the $KTiOPO_4$ framework 300

8.3 Cation and framework substitution 301

8.4 Cr inclusion in the K_2O-TiO_2-P_2O_5 system 303

References 305

Appendix 1 Observed and calculated structure factors for the annealed and ion-exchanged $K_{0.5}Na_{0.5}TiOPO_4$ crystal.

Appendix 2 Observed and calculated structure factors for the ion-exchanged $K_{0.5}Na_{0.5}TiOPO_4$ crystal.

Appendix 3 Observed and calculated structure factors for the $KTi_{0.95}Cr_{0.05}OPO_4$ crystal.

Appendix 4 Observed and calculated structure factors for the $K_2Ti_{1.2}Cr_{0.8}(PO_4)_3$ crystal.

CHAPTER ONE

1.1 Introduction

Lasers are used in a wide variety of modern technological fields: from the powerful lasers used in machining, manufacturing and surgery; through the lasers used in spectroscopic applications taking advantage of the well defined wavelength; to those used in CD players and supermarket bar code readers.

However only a finite number of laser wavelengths (or tunable laser wavelength regions) are currently available. In order to expand the range of available wavelengths, research interest has centred on the design and use of nonlinear optical (NLO) materials[1] which can convert one frequency of radiation to another through harmonic generation, sum and difference frequency mixing, parametric oscillation and other phenomena.[2,3] In general, nonlinear optical materials are used to provide laser light at shorter wavelengths, creating ultra-violet (uv) and visible radiation from infra-red (ir) fundamental radiation.

Low power green laser light from frequency doubled ir radiation is used in optical scanning, medical instruments and laser printing. Optical discs, used to store large quantities of data, are written and read by laser radiation. The shorter the wavelength used, the greater the resolution available and hence the greater the volume of data that can be stored on a single disc. Currently, ir radiation is frequency doubled into the visible region for use in data storage applications. Third harmonic generation, giving uv radiation, could further increase

the potential density of data storage. In other fields, green and blue radiation solid state sources are needed for low power colour visual display technology in conjunction with the red lasers commonly available. Solid state lasers based on crystals are smaller, more efficient and rugged with longer lifetimes than conventional gas lasers. Nonlinear optical materials are also used in fibre-optic and electro-optic applications, where optical pulses can be transmitted on picosecond or femtosecond scales rather than the nanosecond scale of conventional electronics.

This thesis describes work on the structure, chemistry and nonlinear optical properties of one such material, $KTiOPO_4$ (KTP). Section 1.2 is an introduction to the nonlinear optics necessary to understand such materials, section 1.3 is an overview of currently available NLO materials, section 1.4 describes the structure of $KTiOPO_4$, and section 1.5 explores some of the theories put forward to explain the excellent nonlinear optical properties of KTP.

1.2 Introduction to nonlinear optics

This section is an introduction to nonlinear optics, to explain terms used in the following chapters and to give a physical explanation for the phenomenon of second harmonic generation in crystals.

1.2.1 Second harmonic generation

In general when a material is subjected to an electric field, a dielectric polarisation ($\underline{P}$) is produced in the material, given

by:

$$\underline{P} = \varepsilon_o\{\chi^{(1)}\underline{E} + \chi^{(2)}\underline{E}^2 + \chi^{(3)}\underline{E}^3 + \ldots\}$$

where $\chi^{(n)}$ is the nth order susceptibility coefficient,

ε_o is the permittivity in a vacuum and

$\underline{E}$ is the electric field vector.

The magnitudes of these nonlinear susceptibility coefficients are such that only with the high field strength obtainable using laser radiation will any nonlinear optical effects be observed. Terms greater than third order ($\chi^{(3)}$) are rarely of similar magnitude to the second order terms so can be neglected.

Expressing the incident electromagnetic radiation in the form $\underline{E} = \underline{E}_1\cos(k_1x-\omega_1t) + \underline{E}_2\cos(k_2x-\omega_2t)$, the induced polarisation becomes:

$$\begin{aligned}\underline{P} &= \varepsilon_o[\chi^{(1)}(\underline{E}_1\cos(k_1x-\omega_1t)+ \underline{E}_2\cos(k_2x-\omega_2t)) \\ &\quad + \chi^{(2)}(\underline{E}_1\cos(k_1x-\omega_1t)+ \underline{E}_2\cos(k_2x-\omega_2t))^2+\ldots] \\ &= \varepsilon_o[\chi^{(1)}\underline{E}_1\cos(k_1x-\omega_1t) + \chi^{(1)}\underline{E}_2\cos(k_2x-\omega_2t) \\ &\quad + \chi^{(2)}[\underline{E}_1^2\cos^2(k_1x-\omega_1t) + \underline{E}_2^2\cos^2(k_2x-\omega_2t) \\ &\quad + 2\underline{E}_1\underline{E}_2\cos(k_1x-\omega_1t)\cos(k_2x-\omega_2t)]+\ldots] \\ &= \varepsilon_o\{\chi^{(1)}\underline{E} \\ &\quad + \tfrac{1}{2}\chi^{(2)}(\underline{E}_1^2+\underline{E}_2^2) \\ &\quad + \tfrac{1}{2}\chi^{(2)}(\underline{E}_1^2\cos(2k_1x-2\omega_1t)+ \underline{E}_2^2\cos(2k_2x-2\omega_2t)) \\ &\quad + \chi^{(2)}\underline{E}_1\underline{E}_2[\cos((k_1-k_2)x-(\omega_1-\omega_2)t) + \\ &\qquad \cos((k_1+k_2)x-(\omega_1+\omega_2)t)] \\ &\quad +\ldots\}\end{aligned}$$

This represents a linear term, a d.c. polarisation term, second harmonic radiation at frequencies $2\omega_1$ and $2\omega_2$, plus the sum and difference components at $\omega_1\pm\omega_2$. Examples of the higher order effects[4], which have not been expanded out, are the third order Kerr effect and coherent anti-Stokes Raman radiation.

In this equation for the polarisation, the electric field amplitude, $\underline{E}$, is a vector and the second order susceptibility, $\chi^{(2)}$, a tensor, so using the alternative notation for tensors, the quadratic term in the polarisation can be written as:

$$\underline{P}_i = \varepsilon_o\Sigma_{j,k}\,\chi_{ijk}\underline{E}_j\underline{E}_k \qquad \text{where } i,j,k=1,2,3$$

The second order susceptibility $X_{ijk}^{(2)}$ can be written in terms of second order nonlinear optical coefficients d_{ijk}. If the propagation direction is along the i direction, the d_{ijk} subscripts can be contracted to d_{ij}, because no physical significance can be attached to an exchange of $\underline{E}_j$ and $\underline{E}_k$, (components perpendicular to the propagation vector) giving: xx=1, yy=2, zz=3, yz=zy=4, xz=zx=5, xy=yx=6 (known as the piezoelectric contraction[23]). With the polarisation and electric field vectors written in terms of their components relative to cartesian coordinates, the quadratic term in the polarisation expression becomes:

$$\begin{matrix} P_x \\ P_y \\ P_z \end{matrix} = \begin{matrix} d_{11} & d_{12} & d_{13} & d_{14} & d_{15} & d_{16} \\ d_{21} & d_{22} & d_{23} & d_{24} & d_{25} & d_{26} \\ d_{31} & d_{32} & d_{33} & d_{34} & d_{35} & d_{36} \end{matrix} \begin{matrix} |\underline{E}_x \quad | \\ |\underline{E}_y \quad | \\ |\underline{E}_z \quad | \\ |2\underline{E}_y\underline{E}_z | \\ |2\underline{E}_x\underline{E}_z | \\ |2\underline{E}_x\underline{E}_y | \end{matrix}$$

The number of second order nonlinear optical coefficients d_{ij} which are non-zero is limited by the symmetry of the crystalline lattice. In a centrosymmetric structure, where $\underline{P}(\underline{E}) \equiv \underline{P}(-\underline{E})$, this becomes $\varepsilon_o \Sigma_{j,k} X_{ijk} \underline{E}_j \underline{E}_k \equiv \varepsilon_o \Sigma_{j,k} X_{ijk} (-\underline{E}_j)(-\underline{E}_k)$ which can only be satisfied if the coefficients d_{ij} are all zero. Therefore a material must crystallise with a non-centrosymmetric structure to exhibit second order effects. This requirement enables the observation of SHG from a material to be used as a test for a noncentrosymmetric structure.[104] The converse, absence of SHG indicating the presence of a centre of symmetry, does not apply because the nonlinear optical coefficient may be vanishingly small but non-zero. In general, the number of non-zero matrix elements in an acentric point group decreases with increasing symmetry, for example triclinic crystals having all 18 d_{ij}'s non-zero while orthorhombic mm2 crystals have 5 non-zero (d_{15}, d_{24}, d_{31}, d_{32} and d_{33}).

1.2.2 Microscopic physical origin of nonlinear optical behaviour[3,4]

Crystals can be considered to be built up from microscopic building units such as tetrahedra, octahedra, axially symmetrical bonds or molecules. The macroscopic susceptibility $\chi^{(2)}$ may be related to the microscopic second order hyperpolarisability β of such a unit by the expression:

$\chi^{(2)} = (1/V)\Sigma\beta(u)$, where the summation over u is over all the building units within the unit cell of volume V. In cartesian coordinates this becomes:

$\chi_{IJK}^{(2)} = \Sigma_u\Sigma_{ijk}\cos\theta_{Ii}(u)\cos\theta_{Jj}(u)\cos\theta_{Kk}(u)\beta_{ijk}(u)$

$\theta_{Ii}(u)$ is the angle between the macroscopic I axis and the i axis of the building unit.

The optical polarisation of materials is due to the outer valence electrons of these building units, electrons which are more readily displaced by the electromagnetic field:

$\underline{P}(t) = -Nex(t)$ where N = density of electrons
e = electronic charge
x(t) = deviation of the electron from its equilibrium position.

The movement of the electrons is affected by the direction, magnitude and frequency of the applied electric field and the nature of the potential well in which the electrons lie.

In a symmetrical potential well, the potential energy of the electrons is given by $V(x) = (m/2)\omega^2x^2 + (m/4)\gamma x^4 + \ldots$ Only even power terms appear in the expression because in a symmetric field $V(x) \equiv V(-x)$. The restoring force on the electron

$$F = -\frac{\delta V(x)}{\delta x} = -m\omega^2x - m\gamma x^3 - \ldots$$

The absence of second order terms explains why centrosymmetric crystals do not display second order nonlinear effects.

In an asymmetrical crystal the potential energy at x is not equal to that at -x so the potential energy expression contains odd powers of x, $V(x) = (m/2)\omega^2x^2 + (m/3)\beta x^3 + (m/4)\gamma x^4 + \ldots$ The restoring force on the electron then becomes:

$$F = -\frac{\delta V(x)}{\delta x} = -m\omega^2x - m\beta x^2 - m\gamma x^3 - \ldots$$

and the material can show nonlinear optical behaviour.

1.2.3 Phase-matching

An electromagnetic wave travelling through a nonlinear optical medium induces a polarisation that is a nonlinear function of the electric field amplitude. This nonlinear polarisation radiates another electromagnetic wave with a frequency $\omega = \omega_1 \pm \omega_2$ (where ω_1 and ω_2 are the two components of the fundamental radiation), which propagates at a velocity $v = \omega/k = c/n(\omega)$, (where k is the wave vector and $n(\omega)$ the refractive index). However, due to normal dispersion effects, i.e. the dependence of the refractive indices (n) on frequency (ω), the propagation velocity of the second harmonic (at 2ω; $\omega_1=\omega_2$) will be different to that of the fundamental (at ω), so the microscopic contributions from atoms at different positions in the crystal will destructively interfere, severely limiting the efficiency of second harmonic generation (SHG). To obtain appreciable second harmonic intensity, the velocities of the fundamental and second harmonic must be synchronised, i.e. the difference between their wave vectors:

$\Delta k = k(\omega_1 \pm \omega_2) - k(\omega_1) - k(\omega_2)$, (or $\Delta k = k(2\omega) - 2k(\omega)$ for SHG), should be minimised, a condition known as phase-matching. The

interference between the waves when not phase-matched is described by the factor:

$\frac{\sin^2(\Delta kl/2)}{(\Delta kl/2)^2}$ in the equation of the second harmonic.[5] Two adjacent peaks in this interference pattern are separated by $2\pi/l_c$, where l_c $(=\pi/\Delta k)$ is known as the coherence length. This is a measure of the maximum size of crystal through which the second harmonic components interfere constructively, and thus of the theoretical maximum effective crystal length of a given material, (after which the second harmonic intensity decreases).

The phase-matching condition $\Delta k=0$ may be achieved in birefringent crystals, in which there is anisotropy in the refractive index. A propagation direction can be chosen in which the refractive indices for the two orthogonally polarised propagation modes are different. Birefringent crystals can be illustrated by an optical ellipsoid, which is defined by the three principal axes of the dielectric susceptibility tensor:

$$\frac{x^2}{n_x^2(\omega)} + \frac{y^2}{n_y^2(\omega)} + \frac{z^2}{n_z^2(\omega)} = 1$$

using the convention that $n_x \geqslant n_y \geqslant n_z$. Crystals may be classified into three classes by their optical properties[6]

i) Isotropic. Three crystallographically equivalent mutually orthogonal directions, e.g. cubic; this gives rise to an optical sphere.

ii)Uniaxial. Two or more crystallographically equivalent directions in one plane but not in the isotropic class e.g. hexagonal, trigonal or tetragonal classes with the plane containing the equivalent directions perpendicular to the 6-fold, 3-fold or 4-fold axes. One dielectric principal coincides with this direction while the other two may be any orthogonal pair in the perpendicular plane, leading to an optical spheroid, $\varepsilon_x=\varepsilon_y\neq\varepsilon_z$ (where ε is the relevant dielectric

susceptibility)

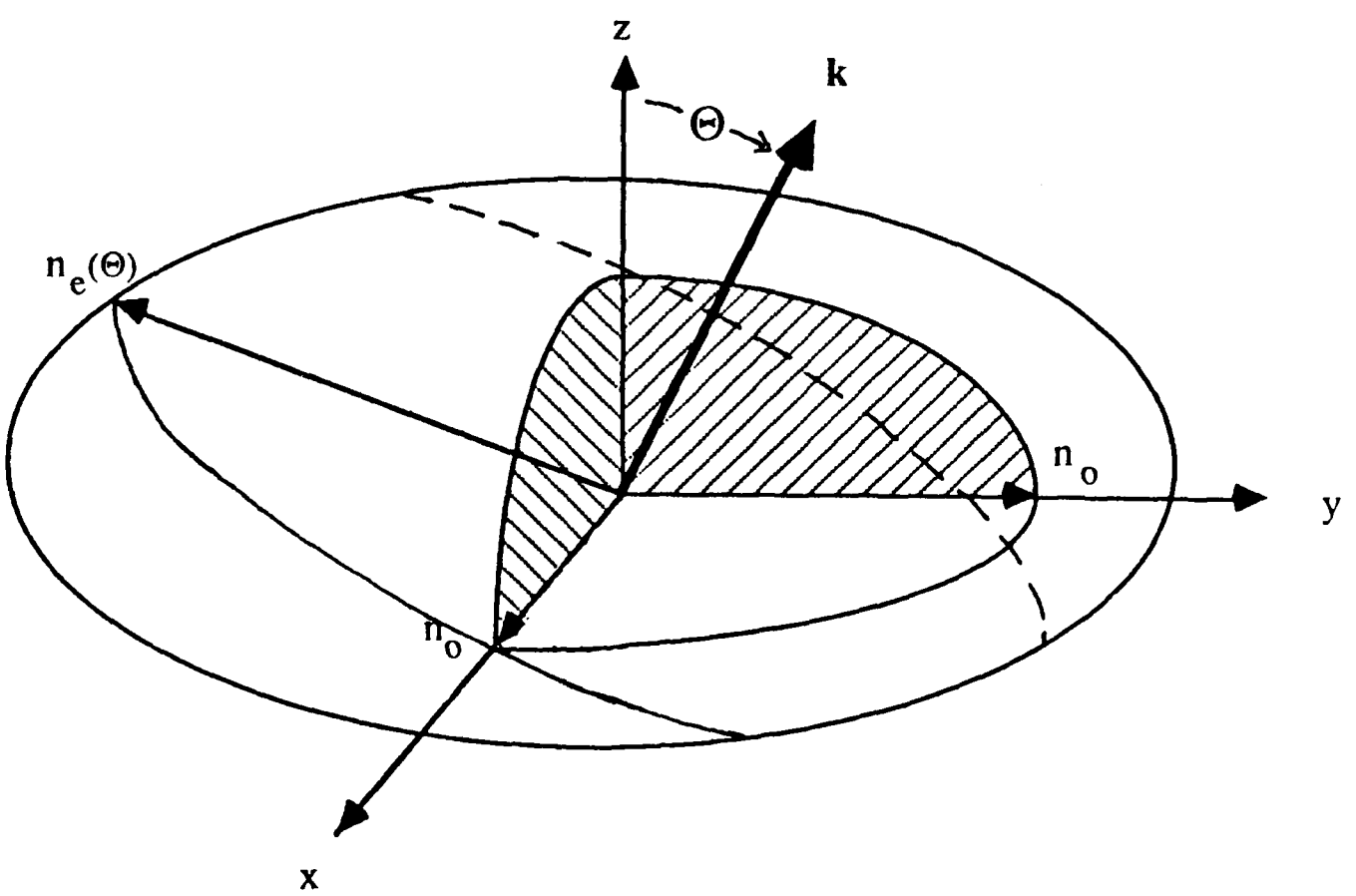
iii)Biaxial. No two crystallographically equivalent directions exist, e.g.orthorhombic, monoclinic or triclinic crystal systems. The optical directions may or may not be determined by the symmetry of the crystal and they may be wavelength dependent. This can be described as an optical ellipsoid.

Uniaxial birefringent crystals[7]

In uniaxial crystals, two of the principal axes of the dielectric susceptibility are equal, so the index ellipsoid becomes a spheroid (Figure 1.2.I), spherical with respect to the optical axis, and the equation becomes

$$\frac{x^2 + y^2}{n_o^2(\omega)} + \frac{z^2}{n_e^2(\omega)} = 1$$

Figure 1.2.I. The optical spheroid of a uniaxial birefringent crystal showing ordinary n_o (θ independent) and extraordinary $n_e(\theta)$ refractive indices.



In the diagram the plane perpendicular to the wave vector $\underline{k}$ which contains the origin and intersects the index ellipsoid defines n_o and n_e, the ordinary and extraordinary refractive indices. The ordinary refractive index n_o is independent of propagation while the extraordinary refractive index

$$n_e(\omega,\theta) = \left(\frac{\cos^2\theta}{n_o^2(\omega)} + \frac{\sin^2\theta}{n_e^2(\omega)}\right)^{-1/2}$$

If $n_e > n_o$ the crystal is said to be optically positive as is the case in the spheroid of Figure 1.2.I.

There are two types of phase-matching (Figure 1.2.II): type I, where for some angle θ_m(I), $n_e(2\omega,\theta_m) = n_o(\omega)$; and type II where at a different (larger) angle θ_m(II), $n_e(2\omega,\theta_m) = \frac{1}{2}[n_e(\omega,\theta_m) + n_o(\omega)]$.[7] These equations are for a negative uniaxial crystal; for a positive crystal they would be $n_o(2\omega) = n_e(\omega,\theta)$ and $n_o(2\omega) = \frac{1}{2}[n_e(\omega,\theta_m) + n_o(\omega)]$. The critical phase-matching angles can be calculated from the refractive indices by substituting the expression for n_e into the equations for negative phase-matching above:

Type I $$n_o(\omega) = \left(\frac{\cos^2\theta_m}{n_o^2(2\omega)} + \frac{\sin^2\theta_m}{n_e^2(2\omega)}\right)^{-1/2}$$

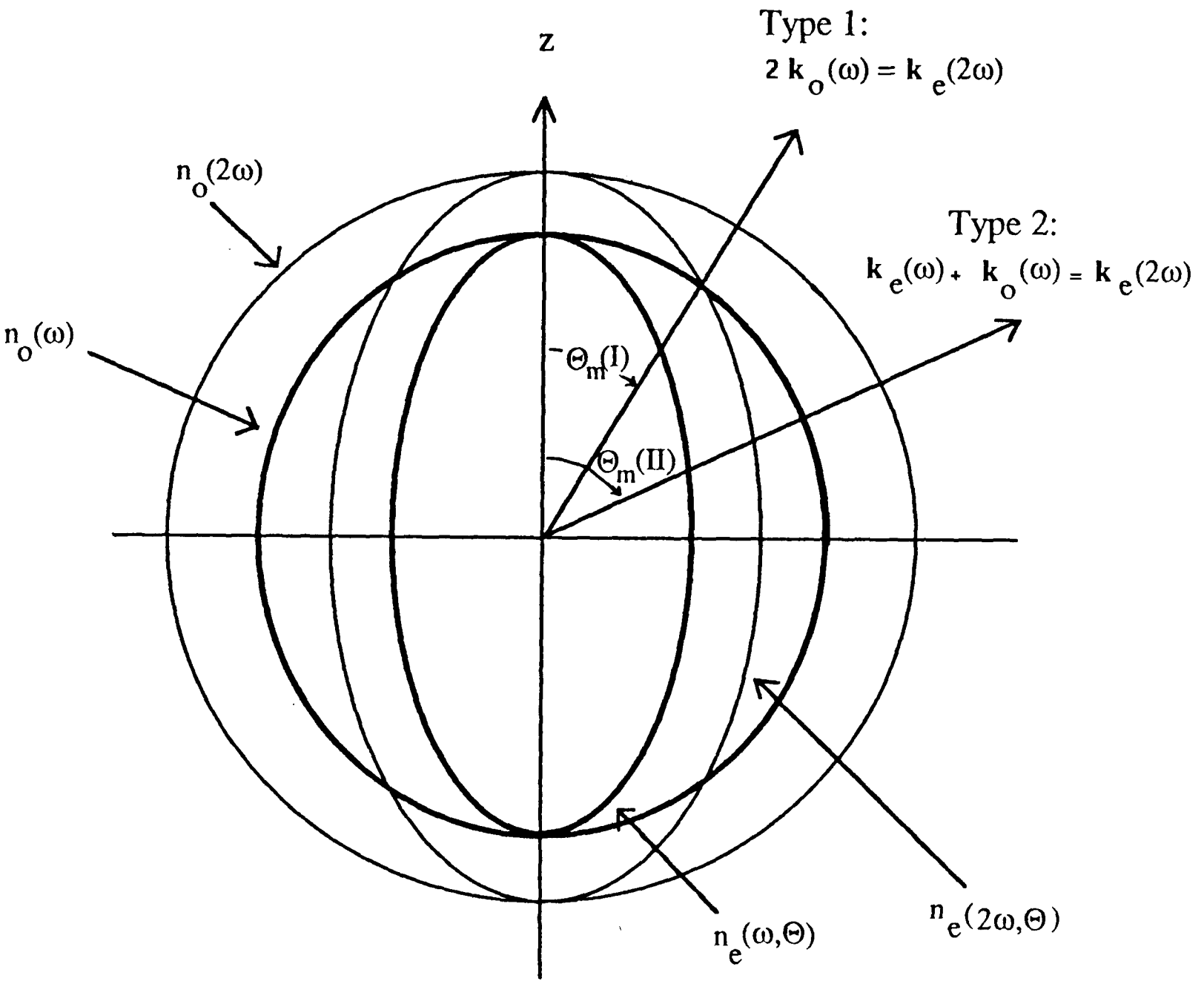
Type II $$\left(\frac{\cos^2\theta_m}{n_o^2(2\omega)} + \frac{\sin^2\theta_m}{n_e^2(2\omega)}\right)^{-1/2} = \frac{1}{2}\left(n_o(\omega) + \left(\frac{\cos^2\theta_m}{n_o^2(\omega)} + \frac{\sin^2\theta_m}{n_e^2(\omega)}\right)^{-1/2}\right)$$

Similar expressions can be derived for positive uniaxial phase-matching crystals.

Biaxial birefringent crystals[8]

The phase-matching direction in biaxial crystals is described by the intersection of index surfaces at the fundamental and second harmonic frequencies. In well-behaved systems, i.e. where $n_z(2\omega) > n_z(\omega)$, $n_y(2\omega) > n_y(\omega)$, $n_x(2\omega) > n_x(\omega)$,

Figure 1.2.II. The yz projection of the normal index surface for ordinary and extraordinary rays in a negative uniaxial crystal.



$n_z(2\omega) > n_y(2\omega) > n_x(2\omega)$ and $n_z(\omega) > n_y(\omega) > n_x(\omega)$, there are thirteen distinct phase-matching loci dependent on the order of magnitude of their indices (Hobden's classes).[8] For instance $KTiOPO_4$, has refractive indices:

λ	530μm	1064μm
n_x	1.7787	1.7400
n_y	1.7924	1.7469
n_z	1.8873	1.8304

so that it is a member of Hobden's biaxial crystal class 7[8] (i.e. $n_z(2\omega) > n_z(\omega) > n_y(2\omega) > n_x(2\omega) > n_y(\omega) > n_x(\omega)$, $n_x(2\omega) < \frac{1}{2}(n_x(\omega) + n_z(\omega))$ and $n_y(2\omega) > \frac{1}{2}(n_y(\omega) + n_z(\omega))$.

1.2.4 Walkoff[7]

The Poynting vector $\underline{P}(\omega)$ indicates the direction of power flow in an electromagnetic wave passing through the crystal and is perpendicular to the optical ellipsoid at its intersection with the wave vector $\underline{k}$ (Figure 1.2.III). Therefore, in Type I phase-matching $\underline{P}(\omega)$ is collinear with $\underline{k}(\omega)$ and $\underline{k}(2\omega)$ but not with $\underline{P}(2\omega)$ which is perpendicular to $n_e(2\omega)$ at $\theta_m(I)$. This difference in Poynting vector direction causes "beam walkoff", the separation of the incident and generated electromagnetic waves, which severely limits SHG efficiency. The angle between the Poynting vectors is given by[4]:

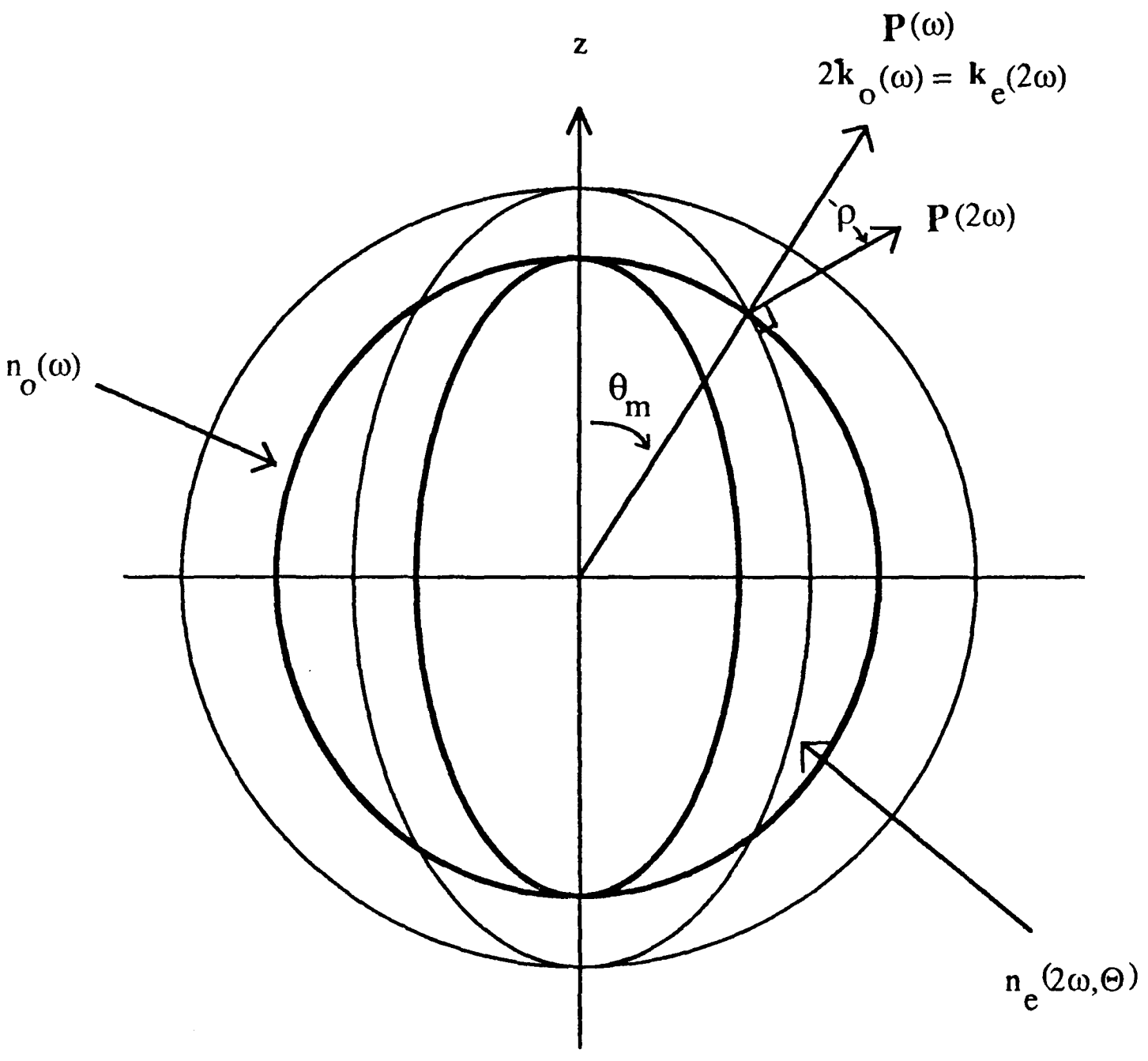
$$\rho = \tan^{-1}\left(\frac{1}{2} n_o^2(\omega)\left(\frac{1}{n_e^2(2\omega)} - \frac{1}{n_o^2(2\omega)}\right)\sin 2\theta_m\right)$$

Walkoff can be eliminated when the condition known as non-critical phase-matching is achieved.

1.2.5 Non-Critical Phase-matching

In practice the laser beams used for SHG are not perfectly collinear, but have a small finite divergence. This means that there is an angular range $\Delta\theta$ about the phase-matching angle θ_m

Figure 1.2.III, The index surface for a negative uniaxial crystal showing the Poynting vector $\underline{P}(\omega)$.



where $\Delta k \neq 0$. The expressions for the wave mismatch $\Delta k \neq 0$ in terms of θ are:[27]

Type I negative

$$\Delta \underline{k} = -(\omega/c) n_o^3(\omega) [n_e^{-2}(2\omega) - n_o^{-2}(2\omega)] \sin 2\theta_m . \Delta\theta$$

positive

$$\Delta \underline{k} = -(\omega/c) n_e^3(\omega,\theta) [n_e^{-2}(\omega) - n_o^{-2}(\omega)] \sin 2\theta_m . \Delta\theta$$

Type II negative

$$\Delta \underline{k} = -(\omega/c) \{ (\tfrac{1}{2} n_e^3(\omega,\theta_m) [n_e^{-2}(\omega) - n_o^{-2}(\omega)] + n_e^3(2\omega,\theta_m) [n_e^{-2}(2\omega) - n_o^{-2}(2\omega)] \} \sin 2\theta_m . \Delta\theta$$

$$\sim (-\omega/2c) n_o^3(\omega) [n_e^{-2}(2\omega) - n_o^{-2}(2\omega)] \sin 2\theta_m . \Delta\theta$$

positive

$$\Delta k = -(\omega/2c) [2n_o(2\omega) - n_o(\omega)] [n_e^{-2}(\omega) - n_o^{-2}(\omega)] \sin 2\theta_m . \Delta\theta$$

In type I phase-matching, there is a linear variation of $\Delta \underline{k}$ with $\Delta\theta$ when $\theta_m \neq 0$, reduced by a factor of 2 in type II phase-matching. When $\theta_m \neq 0$, known as critical phase-matching, walkoff will be detrimental to second harmonic output.

As the structure of a material distorts with temperature, the refractive indices and degree of birefringence are temperature dependent. If θ_m can be brought to 90° by adjustment of the refractive indices using this temperature dependence, the $\underline{k}$ and $\underline{P}$ vectors become collinear with crystal axes and the expressions for Δk in terms of θ are:

Type I

negative $\Delta k = -(\omega/c) n_o^3(\omega) [n_e^{-2}(2\omega) - n_o^{-2}(2\omega)] \Delta\theta^2$

positive $\Delta k = -(\omega/c) n_e^3(\omega,\theta_m) [n_e^{-2}(\omega) - n_o^{-2}(\omega)] \Delta\theta^2$

TypeII

negative $\Delta k \sim -(\omega/2c) n_o^3(\omega) [n_e^{-2}(2\omega) - n_o^{-2}(2\omega)] \Delta\theta^2$

positive $\Delta k = -(\omega/2c) [2n_o(2\omega) - n_o(\omega)] [n_e^{-2}(\omega) - n_o^{-2}(\omega)] \Delta\theta^2$

The beam divergence, $\Delta\theta$, now has a smaller, quadratic effect on Δk and there is no walkoff as the Poynting vectors are collinear with the wave vectors, so 90° phase-matching is known as "non-critical". The acceptance angle $\delta\theta$ can be calculated by setting $\Delta k = 2\pi/l_c$ in the above equations, this being the first minimum in the second harmonic power output.

If the crystal is critically phase-matched, the angle θ can be adjusted to cope with a change in refractive index caused by temperature fluctuations. However, adjustment in the case of 90° phase matching would be detrimental so the temperature must be controlled to maintain efficient second harmonic generation.

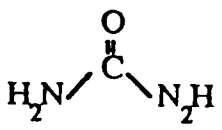
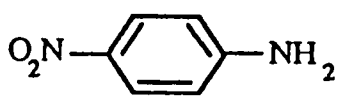
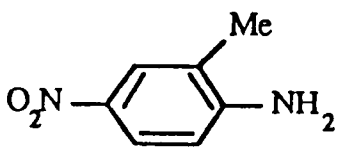
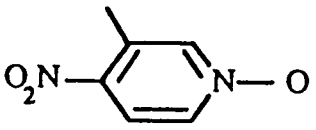
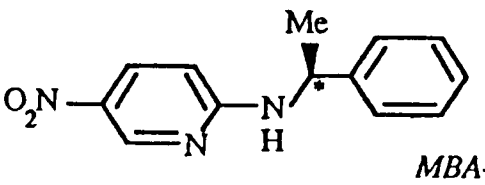
1.3 Nonlinear optical materials

The first requirement of a candidate material for nonlinear optical applications is that it must crystallise in a noncentrosymmetric space group. Almost as important is that the material should be phase-matchable (i.e. have reasonable birefringence) since this can increase the efficiency by a factor of 10^4. The material should also have adequate nonlinear optical coefficients, (figure of merit d^2/n^3), optical transparency and homogeneity. However, to survive the operating environment, physical properties such as mechanical strength, thermal stress resistance, fabrication ability (coating, polishing) and chemical stability are equally important. For use with high power lasers, materials should have low absorption at the required wavelengths and good thermal conductivity to avoid changes in properties with internal temperature; large temperature and angular bandwidths over which phase matching can occur; and a fair degree of fracture toughness.

1.3.1 Organic nonlinear optical materials

In general, organic nonlinear optical materials have a larger nonlinear optical figure of merit, d^2/n^3, than inorganic materials. These high values permit significant second harmonic generation, even in thin films. In addition, the relatively high laser damage threshold, low refractive indices (which reduce the loss due to scattering) and low operating power combine with the low cost of material synthesis to make organic nonlinear optical materials a subject of considerable research interest (Table 1.3.1).

Table 1.3.1: Selected nonlinear optical properties of some organic and inorganic materials

		SHG (c.f. urea)	SHG cutoff (nm)	$\beta(10^{-30}$esu)	d^2/n^3	Damage threshold GW/cm^2
Organic						
	*urea*		200 [1]	0.45 [1]	1.6 [2]	5 at 1064nm [4] 3 at 532 nm
	*p-NA*	0	470 [1]	35 [1]		
	*MNA*	22 [1] 80 [2]	480 [1]	42 [1]	~2000 [5]	0.2 at 1064nm [5]
	*POM*	13 [1]	410 [1]	5 [1]	15 [2]	2 at 1064 nm [4] 0.15 at 532 nm (0.27) [2]
	*MBA-NP*	25 [1] 81 [2]	430 [1]		13 [2]	0.12 to 0.5 [2]
Inorganic						
$KTiOPO_4$			990 [3]		32 [2]	15 [3]
β–BaB_2O_4			411 [3]		2.9 [2]	13.5 [3]
$LiNbO_3$			1080 [3]			0.12 [3]

1. Twieg R.J., Jain K., *A.C.S. Symposium Ser.*, 233, *Nonlinear optical properties of Organic and polymeric materials* , ed Williams D.J., 57, (1983).
2. Sherwood J.N., *Phil. Trans. R.Soc. Lond. A* , 330, 127, (1990).
3. Cheng L.K., Bosenberg W.R., Tang C.L., *Prog. Crystal. Grow. Charac.*, 20, 9, (1990).
4. Chen C.-T., Liu G.-Z., *Ann. Rev. Mater. Sci.* , 16, 203, (1980).
5. Levine B.F., Bethea C.G., Thurmond C.D., Lynch R.T., Bernstein J.L, *J. Appl. Phys.* , 502523, (1979).

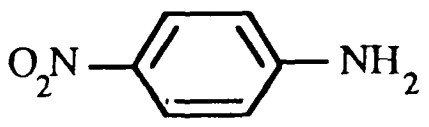
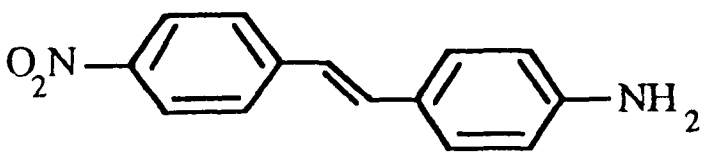
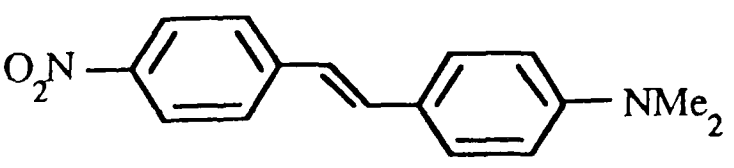
However, the mechanical and physical properties of these organic materials are inferior to those of inorganic materials; and large crystals of high optical quality are more difficult to produce. The crystals are often deliquescent, and other physical properties can be highly temperature dependent. The absorption of hydrogenous organic materials can lower the wavelength of the upper end of the transmission region to the point where the material cannot be used for the generation of visible radiation. This effect can be alleviated to some extent through substitution of deuterium or halogens for H. An improvement in the SHG figure of merit can increase the value of the uv cutoff wavelength (as seen in Table 1.3.1), thus reducing the transmission region further, and limiting the usefulness of the material. Due to these poor physical properties, few practical nonlinear devices have been fabricated from bulk organic nonlinear optical materials to date, although thin film devices are possible.

Design of organic nonlinear optical materials

Organic materials tend to form molecular crystals rather than extended solids, because the intermolecular forces are much weaker than the intramolecular forces and the molecules retain their identity. Under these conditions the macroscopic susceptibility $\chi^{(2)}$ can be more exactly described as a superposition of the molecular hyperpolarisability β than is the case in extended solids. A molecule can therefore be designed with appropriate features which are more likely to be carried through into the macroscopic structure. Due to the diversity of possible organic structures, new nonlinear optical organic materials can be readily designed and synthesised.

To produce second harmonic generation in organic molecules, the incoming oscillating electromagnetic wave must induce a large electronic perturbation in a low energy excited state; that is, a change in dipole moment.[9] This requirement is satisfied by intramolecular charge transfer systems consisting of: donor - delocalised system - acceptor where the donor and acceptor groups polarise the delocalised electrons, producing a large dipole moment. Delocalised regions of valence electron orbitals are found in conjugated and aromatic organic molecules, where typical electron donors are OCH_3, NH_2 and NMe_2 and acceptors CN and NO_2.[10] The microscopic hyperpolarisability of an organic molecule can be augmented through a number of factors: an increase in the electronegativity difference between the donor and acceptor groups, an increase in the area over which the π electrons are delocalised, and a greater change in dipole moment on excitation.[11] These effects are illustrated using the prototype molecule p-nitroaniline (pNA) in Table 1.3.2.[12]

Table 1.3.2 An example of the design of organic NLO materials

	β(x10^{-30}esu)	Reason for increased SHG
	16.2-34.5	p-nitroaniline, prototype
	225-295	extended π electron delocalisation
	450	increased electro-negativity difference between substituents

Reference: Williams D., *Advances in Chemistry series* , 218, eds Bowden M.J., Turner S.R., 297 (1988).

The other vital condition for a large macroscopic susceptibility, $\chi^{(2)}$, is that the molecule must crystallise in a noncentrosymmetric space group. However, molecules with a large dipole moment tend to crystallise in centrosymmetric space groups, the individual molecules aligning in an antiparallel fashion so that the dipole moments cancel.[13] For instance pNA crystallises in the centrosymmetric space group $P2_1/n$. Various methods have been devised to control the molecular orientation and produce a noncentrosymmetric crystal structure. In some cases this can be achieved by the addition of a substituent which breaks the symmetry, but does not affect the nonlinear optical properties. By substitution of a methyl group on the 2 position of pNA, the 2-methyl-4-nitroaniline (MNA) molecule crystallises in the noncentrosymmetric space group Cc with the NLO properties of the molecule almost unchanged[14] (Table 1.3.1). Hydrogen bonds have also been used to constrain the dipole direction.[15]

A material without a permanent dipole moment would be more likely to crystallise in a noncentrosymmetric space group. The molecule could still have a significant molecular hyperpolarisibility if the charge-transfer excited state has a large moment. This strategy was used to design the nonlinear optical material 3-methyl-4-nitropyridine-1-oxide[16] (POM, Table 1.3.1).

Altering the structure of a nonlinear optical material may be detrimental to the magnitude of its SHG ability and to its physical properties. Another approach to the production of effective organic nonlinear optical materials has been to include the active molecule in a host species[17] such as a zeolite[18] or polymer.

Polymeric nonlinear optical materials[19,20,21]

Polymers have been used to fix the orientation of molecules with a large nonlinear hyperpolarisability β, to produce a noncentrosymmetric structure. Such polymers must have uniform birefringence, low scattering loss, transparency in the required spectral region and stability in the operating environment to be suitable for use in a practical nonlinear optical material. The polymer/molecule mixture is heated above the polymer glass transition temperature, T_g, then an external field is applied to align the dipoles before cooling in the presence of a residual field. A high glass transition temperature is required to prevent relaxation of the dipoles under ambient conditions.

The active constituents may be incorporated into the polymer either as additives or as pendant groups from the main polymer chain. Guest-host systems[12,22] are the most readily available, but the magnitude of the nonlinear optical effect in these materials is constrained by the limited solubility of organic material in polymers, the possibility of organic phase separation, non-uniform dispersion of the active molecules and their possible migration. If the nonlinear optical fragment is chemically bound to the polymer, these drawbacks are alleviated.[23,24] The nonlinear-optically active unit is covalently bonded to a side chain spacer which is attached to the polymer background. This rigid attachment confers stability on the system and raises T_g. Further rigidity can be introduced by cross-linking the polymer chains to bind the nonlinear optical species at more than one site.[25]

Another approach to molecular orientation is to build the active species into Langmuir-Blodgett films, where the high

degree of order can produce large nonlinear optical susceptibility coefficients.[26]

1.3.2 Inorganic nonlinear optical materials

In general, inorganic nonlinear optical materials have superior physical properties to organic materials, so are more commonly used in bulk SHG applications despite the lower d^2/n^3 figure of merit. The choice of inorganic material depends on the fundamental wavelength used.

a) Materials used in the infra-red

The majority of materials available which can be used for frequency conversion in the infrared are chalcopyrites such as $AgGaS_2$ and $CdGeAs_2$ which are negative uniaxial Type I phase-matching materials. Optical parametric oscillation (a strong pump wave at ω_3 causing simultaneous generation of radiation at ω_1 and ω_2 where $\omega_3 \rightarrow \omega_1 + \omega_2$) in $AgGaS_2$ has been used to provide a tunable infrared source from 1.2 to 10μm with Nd:YAG radiation as the pump.[27,28] Radiation with a wavelength of 0.566μm has been produced by upconversion in $AgGaS_2$ (the conversion of a low frequency infrared wave to a higher frequency by mixing with a strong beam at an intermediate frequency ($\omega_1 + \omega_2 \rightarrow \omega_3$)).[29] A tunable source of infrared radiation from 8.7 to 11.6μm has been achieved through downconversion.[31]

Table 1.3.3 Properties of IR nonlinear materials $AgGaS_2$ and $AgGaSe_2$

	$AgGaS_2$	$AgGaSe_2$
Transparency range (μm)	0.49-13	0.71-18
nonlinear coefficients (pm/V)	18(5)	37(6)-43
refractive indices at 10.6μ		
n_o	2.34	2.5915
n_e	2.29	2.5585
phase-matching angle (^{o})	71.6-67.5	55-57.5
damage threshold (MW/cm^2)	3-25	12-40
phase-matching range (μm)	2-13	3-13

references for $AgGaS_2$ [27,28,30,31,32,33] and $AgGaSe_2$ [7,34,35]

$AgGaSe_2$[34] has larger nonlinear optical coefficients and a larger transparency range than $AgGaS_2$ (Table 1.3.3), and wavelengths further into the ir (7 to 15μm) have been achieved by frequency mixing.[36]

The most commonly available laser in the infrared is the CO_2 gas laser, (with a fundamental wavelength of 10.6μm), the second harmonic of which can be generated through $CdGeAs_2$ with 27% efficiency (if the material is cooled to 77K).[7] Tl_3AsSe_3 can also be used for SHG of 10.6μm (CO_2) radiation, for which it has a marginally greater damage threshold ($32MW/cm^2$).[37] In general the chalcopyrites compounds have large nonlinear optical coefficients and a wide phase-matching range, but their optical quality and damage resistance is poor.

b) Materials used in the ultra-violet

There are only two materials in common use for frequency conversion in the ultraviolet, Urea and β-BaB_2O_4.

Urea is hygroscopic, so must be immersed in oil (which tends to absorb uv) whilst in operation. Both type I and type II phase-matching are possible, although type I is more efficient.[38] Wavelengths between 0.238 and 0.85μm are

phasematchable[39,39] but the optical damage threshold is not very high,[39,40] and decreases with exposure to laser radiation (1GW/cm^2 for one shot, 180MW/cm^2 for multiple exposure).[39]

β-BaB_2O_4 (BBB or BBO) has a higher damage threshold (2-13.5GW/cm^2 at 1.06μm) than urea, has good optical quality and is not deliquescent. The nonlinear coefficients are higher than those of urea (d_{eff} = 1.94(7)pm/V[39] compared with d_{14} = 1.4pm/V[38]) and BBB has a wider transmission region. The structure of BBB contains $B_3O_6^{3-}$ planar groups which have conjugated π orbital systems, stacked perpendicular to the c axis, with the Ba ions sandwiched between planes.[41] Chen et al[42] showed that these groups have large microscopic hyperpolarisabilities analogous to the delocalised π electron systems of organic materials. The major limitation to the use of β-BaB_2O_4 as a uv material is the difficulty of producing large crystals of good optical quality, but SHG down to 204.8nm has been demonstrated, and sum frequency generation to 201.1nm.[44]

c) Materials used in the near-infrared to visible

Several materials have been discovered which are suitable for frequency conversion in the near-infrared -visible region, with research effort having been focused on the second harmonic generation of the common Nd:YAG laser's fundamental at 1.064μm.

KH_2PO_4 (KDP) is transparent from 0.21 to 1.5μm and large crystals can be grown with excellent optical and dielectric quality (although hygroscopic). The properties of KDP can be tailored to different applications through the preparation of isomorphs; (KD_2PO_4 (KD*P), $NH_4H_2PO_4$ (ADP) and CsH_2AsO_4 (CDA) among others have been characterised[7]), to provide efficient second harmonic generation of a number of sources. The nonlinear

coefficients and refractive indices are relatively low (KDP d_{36}=0.38pm/V)[44], but KDP has a high optical damage threshold (0.4 - 17GW/cm²)[7] enabling the material to be used in high power applications.

$LiNbO_3$[45] can be grown in large crystals of high optical quality[46], but has a low optical damage threshold of only 0.12GW/cm².[7] The damage resistance can be increased by doping the growth melt with at least 4.5 atomic% MgO.[47] The birefringence of $LiNbO_3$ is temperature sensitive: the noncritically phase-matched wavelength increases with temperature, from 1.064μm at -8°C to 3.8μm radiation at 550°C. MgO doping of $LiNbO_3$ increases the birefringence so that the phase-matching temperature for 1.064μm radiation in MgO:$LiNbO_3$ is increased to 107°C.[44]

$KNbO_3$ is also biaxial, which allows flexibility in the phase-matching conditions. The optical damage threshold of $KNbO_3$ is an order of magnitude greater than that of $LiNbO_3$, although the growth of high quality crystals is more difficult.[48,49] The greater birefringence of $KNbO_3$ permits shorter wavelengths to be obtained under ambient conditions, making $KNbO_3$ one of only a few materials able to give blue radiation. At room temperature, the 1.064μm wavelength is critically phase-matched, but noncritical phase-matching of this wavelength can be achieved by increasing the temperature to 181±2°C.[50] The temperature tuning properties of $KNbO_3$ enable noncritical phase-matching of wavelengths between 0.986 and 1.06μm along the a axis (using d_{31}) by raising the temperature from 22 to 180°C and wavelengths between 0.838 and 0.95μm by propagating parallel to the b axis (using d_{32}) between -36 and 180°C.[50,51,52] $KNbO_3$ has been used for SHG of Nd:YAG (1.064μm) and $Al_xGa_{1-x}As$

semiconductor lasers (0.840-0.950μm fundamentals).[52]

$LiIO_3$ has a wide transmission range (0.3 to 6μm),[53,54,55] but a low damage threshold (0.13-0.5GW/cm^2).[56,57] The nonlinear coefficients of $LiIO_3$ are similar to those of $LiNbO_3$,[44] but the refractive indices are smaller, giving $LiIO_3$ a larger SHG figure of merit (d^2/n^3).

The nonlinear optical properties of these materials are compared with those of $KTiOPO_4$ in Table 1.3.4.[57] For SHG of Nd:YAG 1.064μm radiation, KTP has the best combination of properties, a large figure of merit, high damage threshold, low sensitivity to temperature or angular displacements and small walkoff angle.

Table 1.3.4 Comparison of selected nonlinear optical properties of materials at a wavelength of 1.064μ.[57]

	$KTiOPO_4$	β-BaB_2O_4	$KNbO_3$	$LiNbO_3$	$LiIO_3$	KH_2PO_4
phase-matching region (μm)	1-2.5	0.4-3.3	0.4-5	0.4-5	0.3-5.5	0.2-1.5
d^2/n^3(cf KDP)	62	13	270	23	40	1
damage threshold (GW/cm^2)	1-10	1-10	0.35	0.05	0.5	0.2-10
angular bandwidth (mrad cm)	27-70	1	45	5-25	0.8	3.6
walkoff (mrad)	5	60	0	9-0	75	23
Temperature bandwidth (^{o}C)	30	37	0.3	0.6	50	6-25

The nonlinear optical properties of KTP are summarised in Table 1.3.5. Commercially available KTP crystals are of high optical quality, and are chemically and mechanically stable. KTP has a high laser damage threshold and low absorption allowing

its use in high power applications. In addition, the large nonlinear optical coefficients of KTP and the low threshold power required for second harmonic generation permit its use in low power devices such as diode-pumped lasers where the pump powers are of the order of mW.

Although both Type I and Type II phase-matching are possible in KTP, the latter is more efficient. Noncritical phase-matching occurs at 0.99 and 1.08μm in the xy plane. From 1.5 to 2.5μm the phase-matching angle θ is almost constant in both the xz and yz planes, giving wavelength noncritical phase-matching in the xy plane. The Type II interaction in the yz plane is phase-matchable from 0.99 to 3.5μm, but propagation in this direction is more angle dependent.[63]

However, the phase-matchable wavelength range of KTP is somewhat restricted. Modification of the KTP structure might achieve higher nonlinear optical coefficients and alter the phase-matching properties to access different wavelength regions.

Table 1.3.5 The nonlinear optical properties of $KTiOPO_4$, relating to the SHG of 1.064μm radiation propagating in the xy plane

nonlinear optical coefficients (pm/V)	d_{21} 6.5[58]		
	d_{32} 5.0[58]		
	d_{33} 13.7[58]		
	d_{24} 7.6[58]	3.3[44]	
	d_{15} 6.1[58]	2.6[44]	
	d_{eff} 7.4[58]	3.2[44]	1.3-3.4[59]
Refractive indices			
at 1.064μm (ω)	n_x 1.7381[60]	1.7400[61]	1.7367[71]
	n_y 1.7458[60]	1.7469[61]	1.7395[71]
	n_z 1.8302[60]	1.8304[61]	1.8305[71]
at 0.532μm (2ω)	n_x 1.7785[60]	1.7787[61]	
	n_y 1.7892[60]	1.7924[61]	
	n_z 1.8894[60]	1.8873[61]	
Temperature coefficients of refractive indices ($\times10^{-5}$, $^oC^{-1}$)		Δn_x 1.1[67]	1.9[66]
		Δn_y 1.3[67]	2.5[66]
		Δn_z 1.6[67]	3.7[66]
θ, phase matching angle in xy plane relative to x	23.2-25.2^o [44,59,60,61,62]		
Thermal bandwidth	22-30^{o}C[57,59,60,67,71]		
Angular bandwidth	11-70^o [57,59,67,69,71]		
Spectral bandwidth	4.5-28Åcm[57,59,60,67,71]		
Walkoff	1-5mrad[57,67]		
Transmission range	0.35-4.5μm[67]		
Phase-matchable range	0.99-2.5μm[67,70]		
Damage threshold	1-15GW/cm^2 [57,64,65,69]		
Threshold power	0.1MW[68]		
Conversion efficiency	50-55%[59,60,69]		

1.4 The structure of $KTiOPO_4$.

The synthesis of $KTiOPO_4$ (KTP) was first reported by Ouvrard,[72] who described it as being "biaxial, birefringent and probably monoclinic." The powder X-ray pattern of KTP was indexed on an orthorhombic cell by Masse et al. in 1971.[73]

KTP crystallises in the space group $Pn2_1a$, with unit cell dimensions: a=12.814(6), b=10.616(6), c=6.404(2)Å.[74,75] There are two formula units per asymmetric unit (and four asymmetric units in the unit cell), resulting in two crystallographically independent K, Ti and P sites. All the atoms sit on general positions, making the structure very versatile with respect to isomorphous substitution.

The PO_4 tetrahedra and TiO_6 octahedra form a three dimensional framework with the K atoms occupying cavities in the structure. Zigzag chains of alternating TiO_6 and PO_4 groups run parallel to all three axes. Figure 1.4.I is a projection of the unit cell of the KTP structure down the c axis. The zigzag chains parallel to the a and b axes can be seen at approximately x=0.25, 0.75 and y=0.25, 0.75 respectively.

The TiO_6 octahedra are also linked together by bonds to O(9) and O(10), forming $-Ti(1)O_6-Ti(2)O_6-Ti(1)O_6-$ helical chains parallel to [011] and [01-1] (Figure 1.4.II). The helix is produced by the octahedra linking together alternately *cis*- and *trans*- in the chains.

Each octahedron is distorted, containing one short "titanyl" bond (<1.75Å) *trans* to a long (>2.10Å) bond, with four bonds of medium length forming the equatorial plane. The Ti(2) octahedron forms *trans* linkages to Ti(1) so that the long Ti(2)-O(10) bond is opposite the titanyl Ti(2)-O(9) bond and both the distorted

Figure 1.4.I. A projection of the unit cell of $KTiOPO_4$ along [001].

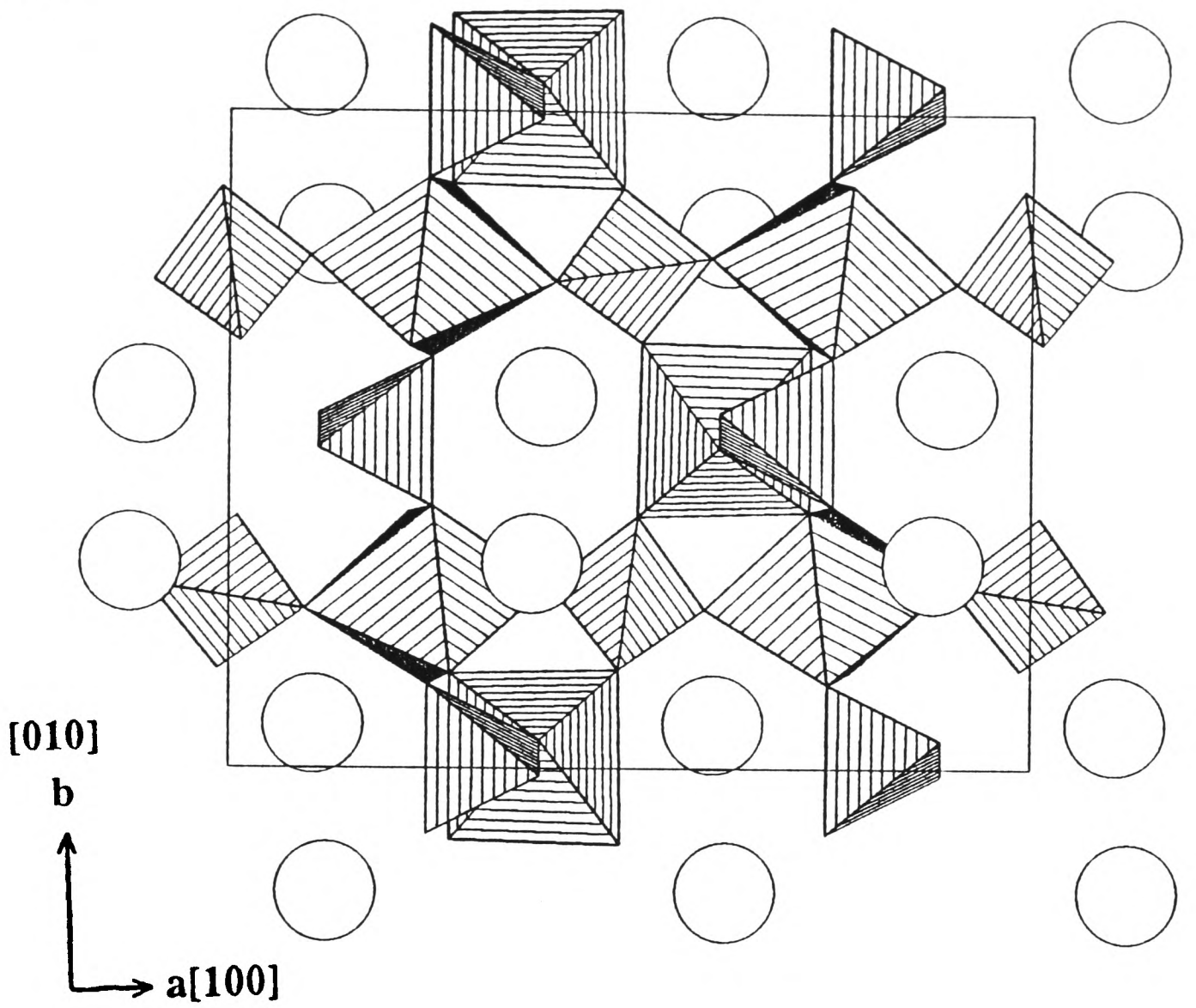
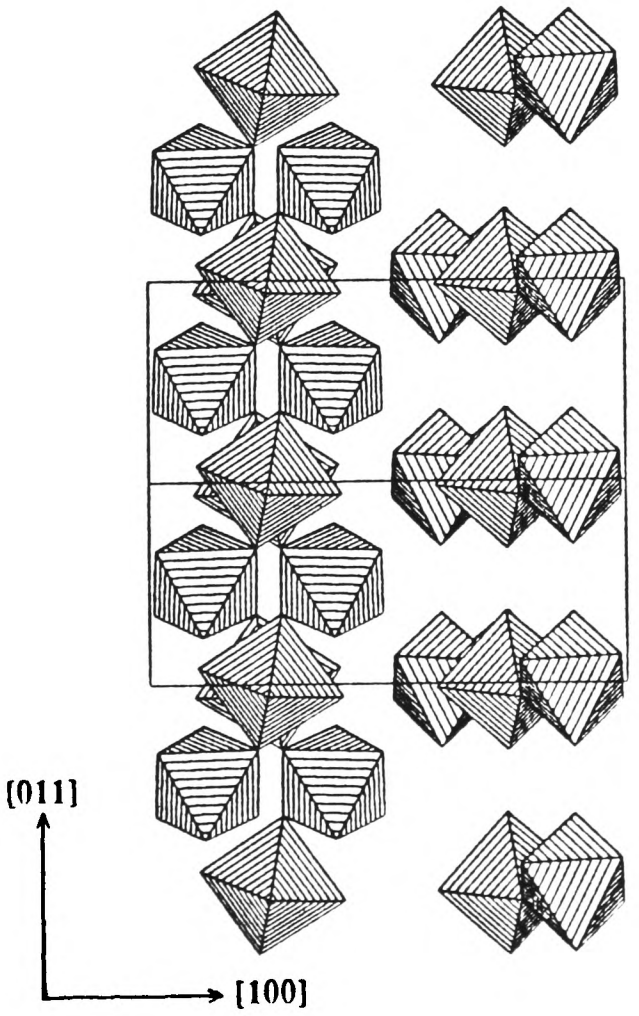
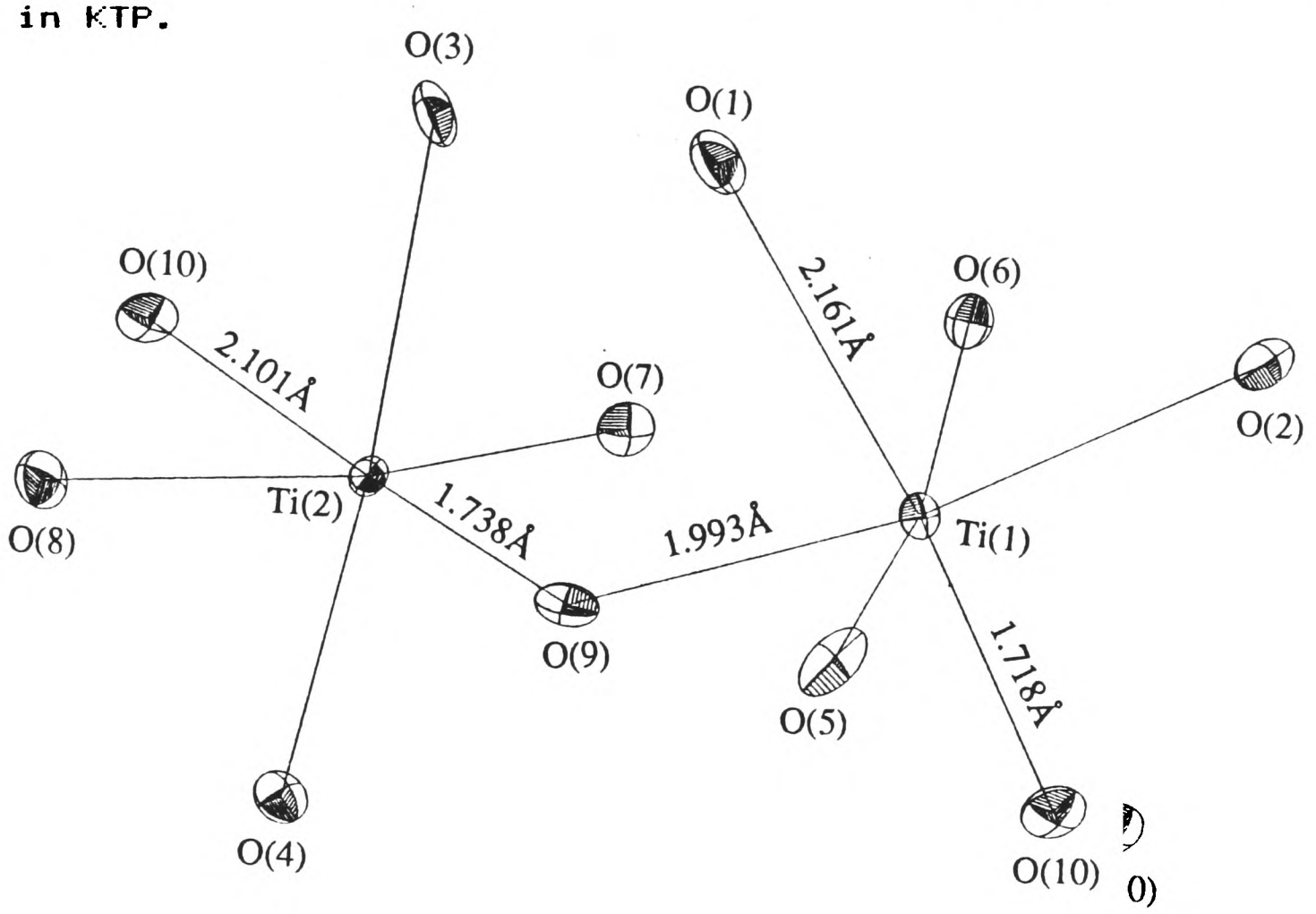


Figure 1.4.II The helices of TiO_6 octahedra in KTP, viewed down [01-1]



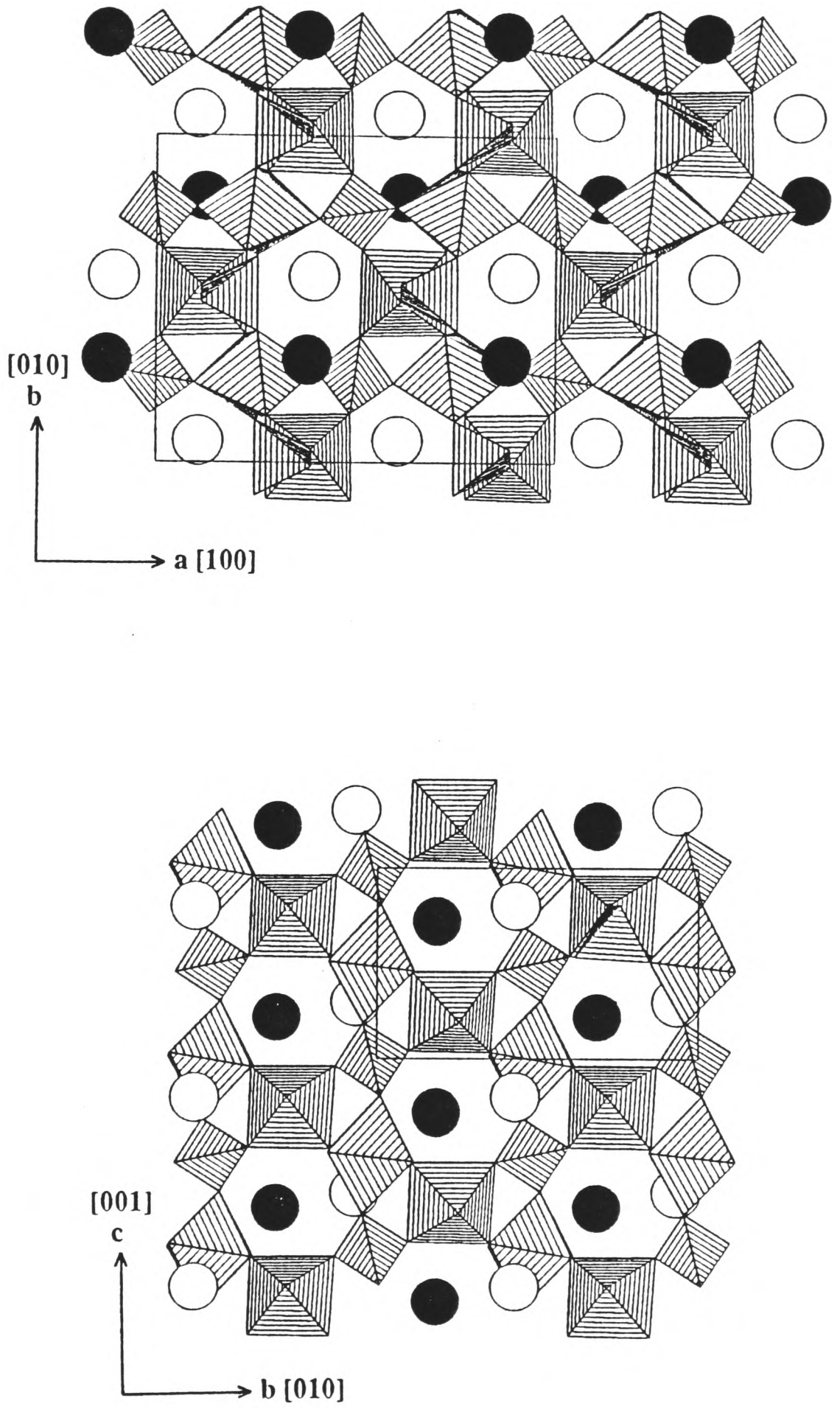
Ti-O bonds are contained within the helical chain. However the $Ti(1)O_6$ octahedra form *cis*-linkages so that although the titanyl Ti(1)-O(10) is part of the octahedral chain, the long Ti(1)-O(1) opposite to it interacts with a phosphate group.

Figure 1.4.III The oxygen coordination around the two Ti sites in KTP.



The K ions occupy one dimensional channels parallel to [100] and [001]. Figure 1.4.IVa shows a larger view of the structure down the c axis. The K(1) atoms (filled circles) occupy channels parallel to the a axis while the K(2) atoms (open circles) occupy channels parallel to the c axis (perpendicular to the plane of projection). The channels are defined by distorted hexagonal windows of O atoms. Figure 1.4.IVb, a partial view of the structure down the a axis, is perpendicular to the view in Figure 1.4.IVa. The K(2) cations now appear parallel to the TiO_6-PO_4-TiO_6- chains along c, while the K(1) atoms occupy channels perpendicular to the plane of projection.

Figure 1.4.IV. a) A projection of the KTP structure along [001], b) a partial projection along [100], with K(1) represented by filled circles, and K(2) by open circles.



The open framework of KTP allows cation diffusion through the structure. However this diffusion is highly anisotropic,[185] the resistivity along the polar, b, direction (~ $4\times10^{8}\Omega$cm) being considerably less than that in the ac plane[150,164] (10^{11}–$10^{12}\Omega$cm). The value of the conductivity varies depending on the method of crystal growth and the impurities present. The anisotropic ionic conductivity has enabled KTP to be used as a substrate for the formation of channel waveguides.[150,152]

1.5 Structure-property relationships in nonlinear optical materials

The accommodating structure of $KTiOPO_4$ raises the possibility of tuning its nonlinear optical properties through substitution chemistry. A major drawback to modelling the nonlinear optical properties is that KTP has 37 different bonds to oxygen and therefore 37 different microscopic hyperpolarisibilities which must be modelled theoretically in order to fully understand the evolution of the nonlinear optical properties. All nonlinear optical models currently used have predictive limitations due to the problem of using the small number of model parameters to predict the behaviour of a complex material with many observable parameters. A study of the dependence of the hyperpolarisability β on the substitution of each atom in turn in the KTP isostructural solid solution series should improve the available theories or create new theories with better predictive power.

Two models have been used to relate the structure of KTP isomorphs to their nonlinear optical properties: the bond charge model of Levine[76] and Chen's anionic group model.[9]

1.5.1 Bond Charge model

In the formation of a covalent bond there is a build-up of charge in the bonding region. This bond charge q is weakly bound and mobile compared to that in the free atom, especially in bonds containing d electrons, which have a small binding energy and significant delocalisation.[77] This charge sits in an asymmetric potential well, the asymmetry arising from the differences in electronegativity and atomic radius of the bonding atoms. Under the influence of a potential, the motion of the charge in the asymmetric well gives rise to the microscopic hyperpolarisability. The macroscopic susceptibility $\chi^{(2)}$ is given by the geometric superposition of the hyperpolarisabilities β in the material as a whole:

$\chi^{(2)} = \Sigma_{\mu} G_{ijk}{}^{\mu} N_b{}^{\mu} \beta^{\mu}$ for bonds of type μ where $N_b{}^{\mu}$ is the number of such bonds per cm^3 and $G_{ijk}{}^{\mu}$ is the geometric factor relating the crystallographic coordinate axes to those of the bond (see section 1.2.2).

The microscopic hyperpolarisability depends on the bond length: $\beta = \beta_o (d/d_o)^{\sigma}$ where β_o is the hyperpolarisability at the average bond length d_o and the power factor σ can be calculated from the measured susceptibility.[57,78] For covalent bonds, β increases with bond length ($+\sigma$), while for ionic bonds β decreases ($-\sigma$).

This model works well for a large number of simple materials.[76] In ferroelectric materials such as $BaTiO_3$ there is near cancellation of the microscopic hyperpolarisabilities, and the nonlinear d coefficients are proportional to the difference between the long and short bonds in the distorted TiO_6 octahedra. The nonlinear optical properties of KTP could therefore also be due to the distorted octahedra.

The bond charge model applied to KTP

Zumsteg et al.[79] used the bond charge model to investigate the nonlinear optical properties of KTP. The cation-oxygen bonds were considered to contribute little due to their high degree of ionicity. The result obtained using simple regular TiO_6 and PO_4 species in the model was an order of magnitude too small, the high degree of covalency in the titanyl Ti-O bond not having been taken into account. This implies that the titanyl bond is the major contributing factor in the hyperpolarisability.

The bond charge model was also used by Hansen et al.[80] to explore the nonlinear optical properties of KTP. In an electron deformation density study the PO_4 group appeared regular, but there was a significant increase in electron density in the short titanyl bond when compared to the other Ti-O bonds. Therefore a single β value for P-O bonds, one Ti-O value for the equatorial bonds and a separate Ti=O value for the titanyl bond were used in their calculations. The long Ti-O bond and the K-O bonds were assumed to have a negligible effect due to their high ionic character. In order to explain the observed nonlinearity, the short Ti-O bond had to have a β value approximately 30 times that of the medium bonds.

This dependence on bond length, introduced into the model to take account of systems with π bonding, did work for some ferroelectric materials, but the values of σ calculated for various BO_6 ferroelectrics cover a range that is too large for crystals of similar type: σ = 2.86, 0.74, 0.37 for $KTaO_3$, $SrTiO_3$ and $BaTiO_3$ respectively. This unsatisfactory large variation in bond nonlinearity dependent on an assumption of ionicity led to the development of another model for nonlinear optical properties in materials.

1.5.2 The anionic group theory[9,42]

Photons incident on a nonlinear optical material are not absorbed, but only perturb the structure; the electrons remaining confined to the ground state. This means that short range forces are important in the nonlinear optical properties, as the electrons are confined to certain delocalised regions of valence electron orbitals. The nonlinear susceptibility coefficient is caused by a localised effect of the incident radiation on clusters of orbitals, the anionic group in inorganic crystals (for instance MO_6, PO_4 and IO_3 groups) or the molecule in molecular crystals. The two major assumptions of this theory are that:[9,42]

1. the macroscopic nonlinear susceptibility results from the geometric superposition of the microscopic hyperpolarisability of the relevant groups and is independent of the cation and

2. the microscopic hyperpolarisability can be calculated from the localised molecular orbital wave function of the anionic groups. A large distortion of MO_6 groups, the existence of a lone pair, and planar structures with asymmetric conjugated π orbitals were identified as features causing a large β and hence large nonlinearity in a material.

In molecular orbital theory a perturbed electronic state can be described by a mixture of possible states; the transition moments containing terms of the form $\langle g|r|e\rangle$ which mix the ground state with excited states in which there could be a high degree of charge reorganisation, giving rise to a large dipole moment and hyperpolarisability. The electromagnetic perturbation of the system can be said to induce a virtual transition to the low-lying excited state, the dipole moment and β of which can be

calculated from the localised electronic orbitals.[81]

The conclusions of the anionic group theory were that the cation played no role in the nonlinear optical properties, that the larger the deformation of a MO_6 group the larger the hyperpolarisability, and when two adjacent anionic groups share an O atom, the nonlinear coefficients depend only on these MO_6^{n-} groups.

The anionic group theory applied to KTP

Stucky et al. used the anionic group theory to explain the nonlinear optical behaviour of KTP and its isomorphs.[57] Instead of using an isolated TiO_6 octahedron, the distorted -Ti-O-Ti-O- chains were considered to be the underlying cause of the large susceptibility coefficients. The bond length alternation within the chains was ascribed to a second order Jahn-Teller distortion, coupling the nonbonding levels at the top of the oxygen p band with Ti-O antibonding levels in the metal d band.

Mixing of O $p\pi$ with metal $d\pi$ orbitals produces bonding, nonbonding and antibonding orbitals of g, u and g symmetry with respect to inversion. Perturbation theory allows the mixing of g and u orbitals in an asymmetric distortion, which is accompanied by the incorporation of charge-transfer character into the valence orbitals. This distortion is energetically favoured, as it stabilises the bonding orbitals at the expense of the antibonding orbitals.[57,81]

Evidence for the importance of both the charge-transfer excited state and the Ti-O bonds was provided in molecular orbital calculations performed by Jarman et al.[82] The highest occupied orbital contained an important Ti $d\pi$-$p\pi$ (titanyl

oxygen) component, while a charge transfer component was indicated between these orbitals, through which charge passed down the conjugated chain.

This theory has been applied to several KTP isomorphs. $KSnOPO_4$ (KSP) has a negligible SHG output[e3] because the Sn 4dπ orbitals are filled, so the ground state can only mix with excited state Sn orbitals of much higher energy. This increased band gap means that the degree of mixing and therefore of charge transfer character are lower, providing less stabilisation on distortion. This decreases the contribution of the MO_6 group to the second order susceptibility $\chi^{(2)}$ and significantly lowers the SHG output.

Using the anionic group theory,[e7,e1] it is proposed that when cations of low coordination number or greater electronegativity are substituted for K, the cation-framework interaction increases, reducing the delocalisation in the Ti-O-Ti-O- chains and thereby reducing $\chi^{(2)}$. This effect explains the severe reduction of SHG output on Ag substitution, Ag having both a larger electronegativity and lower coordination number than K. A less severe reduction is seen on substitution of Na, since Na has similar electronegativity to K, but lower coordination.[e4]

1.6 The substitution chemistry of $KTiOPO_4$

The atoms in the KTP structure sit on general positions, making the structure very versatile with respect to isomorphous substitution. This has been reviewed recently by Stucky et al.[57]

K can be replaced in the TiO_6-PO_4 framework by Rb[58,153], Na,[84,91] Ag,[84,186] Tl[186] and NH_4.[158,186] Substitution of

Ti by Ge,[166,169] V,[170,186] Sn[83,168] and partially by Ga, Al, Mg, Cr and Nb[178,181] have been demonstrated. Metals in other oxidation states can be accommodated in the Ti(IV) sites by simultaneous substitution of a charge balancing ion, for example $KGa_{0.5}Nb_{0.5}OPO_4$,[57] $KMg_{0.33}Nb_{0.66}OPO_4$[57] and $KFePO_4F$.[169] P has been substituted by As to form $MTiOAsO_4$ compounds (M=K,[150] Rb, Tl, Cs,[155,173] and Na[84]). The presence of As enlarges the framework, allowing the formation of Zr-containing isomorphs; $MZrOAsO_4$ (M=Rb, Cs, NH_4).[57] Tetravalent anionic groups substituting for PO_4^{3-} have been charge-balanced by substitution of Sb(V) for Ti, forming $KSbSiO_5$ and $KSbGeO_5$.[171,172]

The structure of KTP contains two formula units per asymmetric unit, so the possibility exists of complete substituent ordering over the two available sites. However the majority of previously reported structural work has concentrated on fully substituted materials. Complete ordering of 50% substituted isomorphs should enable the selective modification of the optical properties to be correlated with alteration of one site in the structure, and with only one variable changing between structures, the modelling of the nonlinear optical properties should be more readily accessible.

This thesis describes an investigation into the structure and properties of partially substituted $KTiOPO_4$ isomorphs. Chapter two covers the experimental techniques used in this work, Chapters three and four are concerned with substitution for K, Chapter five with substitution for Ti and P in the framework and Chapter six with substitution of both K and Ti simultaneously. Chapter seven is a partial investigation of the doping of Cr

into the K_2O-TiO_2-P_2O_5 phase diagram. Second harmonic generation measurements on the $KTiO(P_{1-x}As_x)O_4$ solid solution are presented in Chapter five.

CHAPTER TWO

2.1 Synthetic Techniques

2.1.1 Solid State Synthesis

The majority of materials in this work were made by conventional solid state synthetic methods. Stoichiometric quantities of the reagents were weighed out and ground together in an agate pestle and mortar. If nitrates or ammonium phosphates were among the reagents, the mixture was left overnight in a vented oven at 250°C to decompose these materials. After grinding, the mixture was heated at a temperature between 750°C and 800°C to form a poorly crystalline version of the final product. This was necessary because some reagents melted before the desired synthesis temperature was reached. The final firing took place at 950°C for three days, with intermediate grinding to ensure complete mixing.

2.1.2 Flux Crystal Growth

Single crystals of KTP derivatives were prepared by flux methods[85] rather than from a melt as KTP decomposes below its melting temperature. The growth of KTP crystals from a number of fluxes has been well documented[86,87,88], with various additives (for example WO_3), being added to reduce the viscosity of the melt in order to obtain higher quality crystals. The flux composition used in this work was the composition recommended by Iliev et al.[89,90]: $0.46K_2O + 0.27P_2O_5 + 0.27TiO_2$ (mole ratios). The required proportions of starting materials were mixed, then added to a 20cc platinum crucible at temperatures up to 850°C. To produce large, high quality crystals there needs to

be as large a growth region as possible in the crucible. To obtain the maximum depth, the powder had to be melted into the crucible since the volume of powder required to fill the crucible was greater than the crucible volume. The temperature program followed was:

1. Dwell at 1000°C for 24 hours,
2. Cool to 700°C at 3°/hour and
3. Cool to room temperature at 25°/hour.

This was designed to let the flux mixture equilibrate at a temperature above the melting point when the liquid was transparent, then to cool the crucible slowly through the nucleation temperature of KTP, (around 850°C for this composition). When cold the crucible and contents were boiled in distilled water to remove the glassy "$K_6P_4O_{13}$" flux. The crystals obtained after filtration and drying were transparent or yellow in colour.

2.1.3 Ion Exchange

When the flux or solid state methods proved impossible, cation-exchanged KTP isomorphs were prepared by ion exchange of powders or crystals of KTP.[9,13] Because the temperature of formation is much lower, thermodynamically unstable materials may be obtained through ion exchange which are not accessible by solid state techniques. The required molar ratio of cation nitrate:KTP (for example 10:1 in sodium exchange) was weighed out and heated for periods of time up to two weeks at 350°C in a pyrex beaker. The nitrate was removed by boiling in distilled water and the crystals obtained by filtration. The filtrates were analysed by atomic absorption spectroscopy in Amoco Research Center's Analytical department.

2.2 Analytical Techniques

2.2.1 Powder X-ray diffraction

The first step in the analysis of the reaction products was to take an X-ray diffraction pattern of the material to give information on sample purity and crystallinity. The instrument available for routine work was a Philips PW1710 diffractometer interfaced to a Philips TP200 microcomputer, using Cu K_α radiation (λ = 1.5418Å). The detector was a high efficiency, Xe-filled proportional counter. The sample was ground, then placed into the rectangular indentation on the top surface of an aluminium sample plate and flattened with a glass slide. The plate was then clipped into the sample housing. The housing rotates by an angle of θ degrees as the detector rotates by 2θ to preserve the focusing geometry so that the diffraction pattern can be measured. The scan parameters are entered into the control system via the computer, with a typical run being from 10° to 70° in 2θ, collected at 0.05° per second. The d-spacings, 2θ positions and integrated intensities of any peaks found were sent to the printer.

Once the peak list had been obtained, known phases were identified using the JCPDS[92] powder diffraction file (PDF). Powder patterns may be retrieved either by compound name or PDF card number. Alternatively the PDF may be searched for a match to strong lines in the observed pattern and for a match to compounds of elements known to be present.

If the cell parameters and Laue group of a constituent phase are known, the list of d-spacings attributable to that phase may be generated using the program DSPACE[93]. Alternatively, if the crystal structure of the phase or an isomorphous phase is known,

the complete powder pattern with intensities, d-spacings and 2θ positions can be calculated using LAZY PULVERIX[94]. When the peaks in a phase have been indexed using one of the above programs, CELLREF[95] can be used to refine the cell parameters using the observed hkl and 2θ values. This involves an iterative least-squares refinement of the function:

$M = \Sigma w(\sin^2\theta_{obs} - \sin^2\theta_{calc})^2$ where w is a weighting factor (usually left at the default value of 1).

2.2.2 Analytical electron microscopy

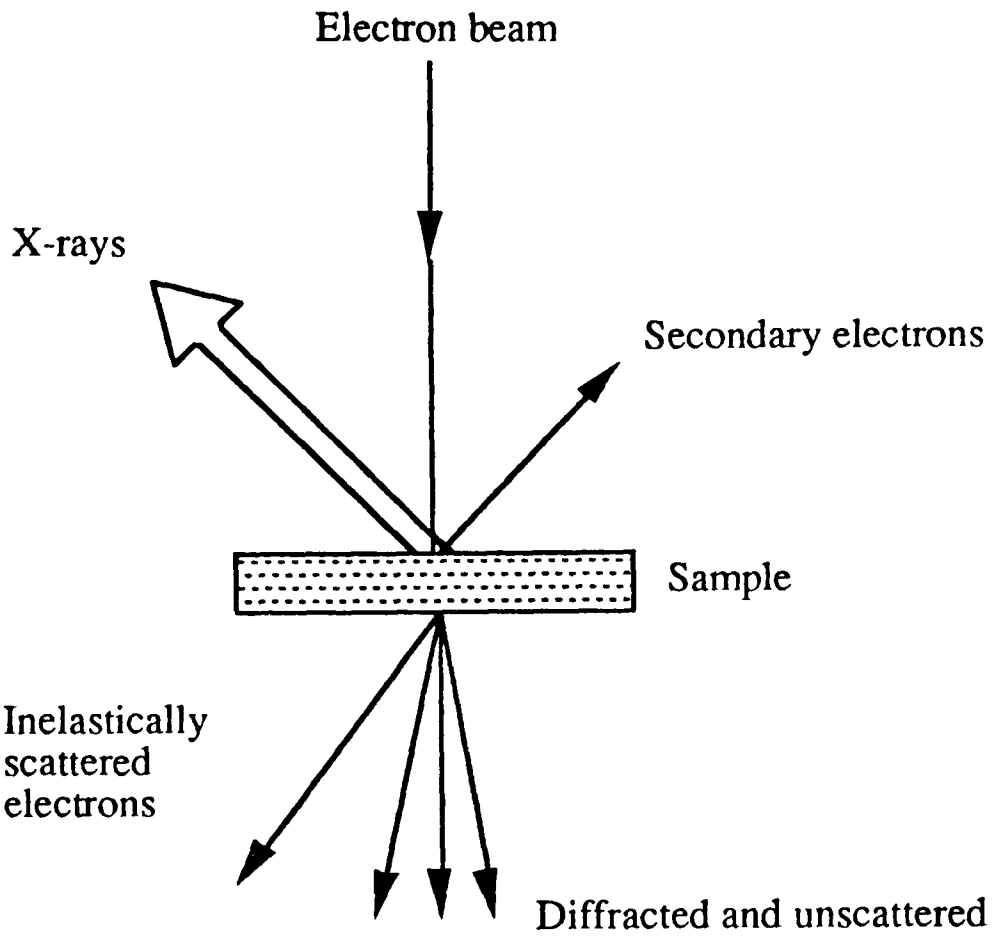
Analytical electron microscopy was used to determine the microscopic composition of the sample. To prepare a sample for electron microscopy, about 50mg of material was ground with an agate pestle and mortar. The powder was transferred to a sample vial to which $1cm^3$ of chloroform was added. The vial was then placed in an ultrasonic bath to break up powder agglomerates and form a suspension of the material. After approximately ten minutes the vial was removed from the bath and allowed to stand in order to let the larger particles settle out. A copper sample grid was placed on a piece of filter paper, a few drops of the sample suspension were placed on to the grid, and the sample was ready for analysis once the chloroform had evaporated. The sample grid was a 3mm diameter copper ring surrounding a square copper grid which was coated with a holey Formvar (polyvinylformal) film and sputter coated with carbon. The carbon provides a conducting layer to prevent charge build up.

The instrument used for analysis was a JEOL JEM2000FX analytical electron microscope.[96] It was operated in transmission mode for these analyses. An electron beam from the

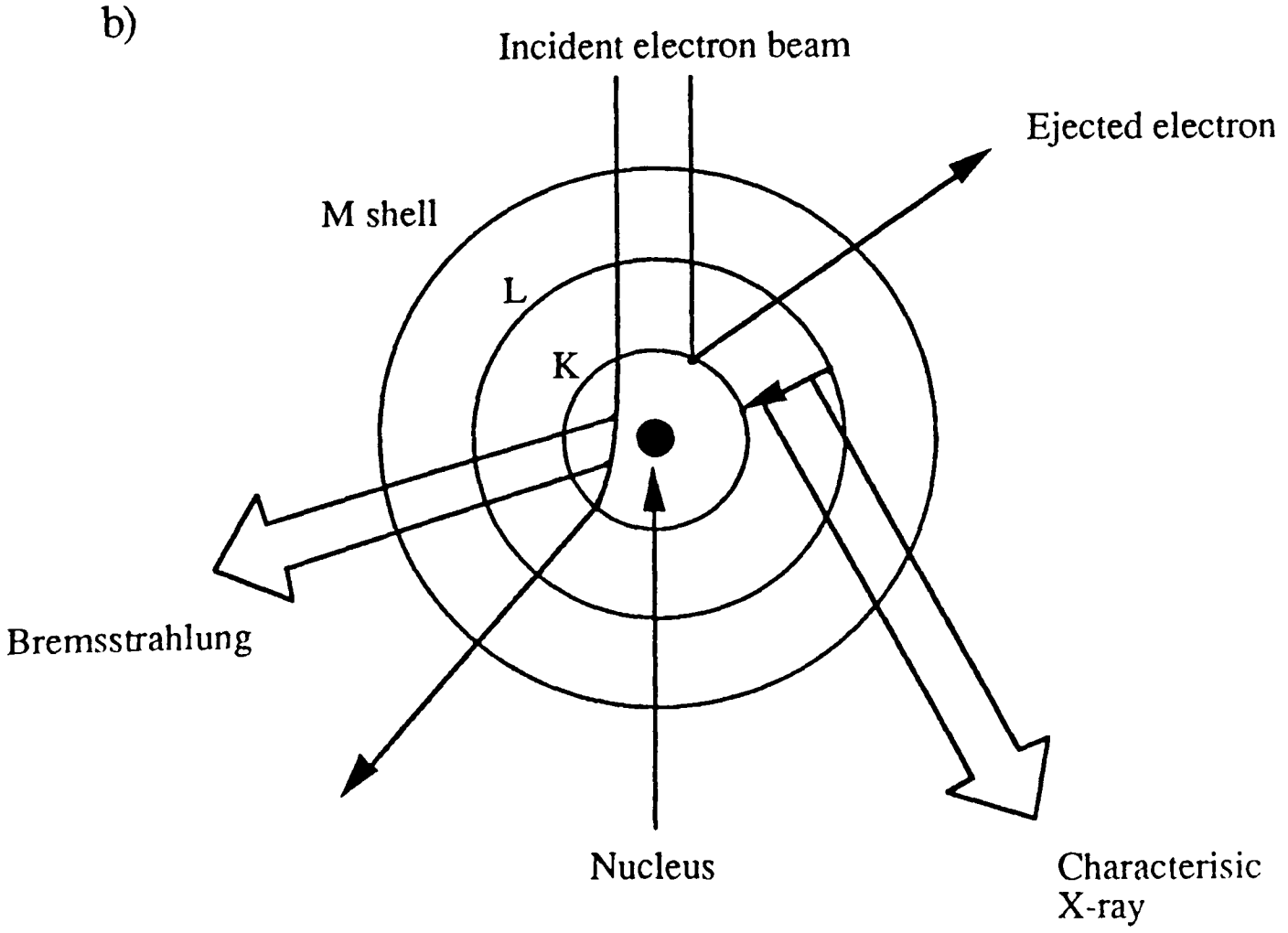
Figure 2.2.1a The main processes taking place at a sample under a high energy electron beam.

Figure 2.2.1b Production of characteristic X-rays and Bremsstrahlung background radiation in an atom.

a)



b)



LaB_6 filament was accelerated through a potential of 200kV, giving a wavelength of 0.025Å. Electromagnetic lenses focused the beam on to the specimen. The electrons can be diffracted by the lattice, but are also of high enough energy to eject core electrons (fig. 2.2.1a). The X-rays emitted as the atom relaxes after the ejection of a core electron are of a wavelength characteristic of the element (fig. 2.2.1b). The X-rays are detected at a high take-off angle by a Tracor Northern energy dispersive X-ray detector (EDS)[97], with a thin beryllium window. The window absorbs low energy X-rays so elements lighter than sodium cannot be analysed with this detector. Typical magnifications used in this work were 68,000 to 80,000x, with spot sizes varying between 4 and 6 (that is, between 10^{-7} and 10^{-8}m); dead-times were kept below 30%. Each microcrystallite was analysed for 100 to 300s depending on the concentration of the element of interest. The detector output was fed into a multi-channel analyser and displayed as a histogram with energy resolution of about 150eV. The intensities of X-ray peaks and the spectrum could be printed out for later interpretation.

On average, twenty crystallites were examined for each sample. These were chosen to be as thin as possible since, in the thin-crystal limit, the absorption and fluorescence effects should be negligible.[98,99] Under these conditions, for two elements x and y in the sample, the ratio of their concentrations, c_x and c_y, is related to the intensities of the characteristic X-rays I_x and I_y obtained from the analytical microscopy, by the equation:

$$\frac{c_x}{c_y} = k_{xy}\frac{I_x}{I_y}$$

The proportionality constant, k_{xy}, can be obtained by using the intensity ratio from a sample of known composition and is

specific for a given detector on a given microscope. Since each element may have a number of characteristic lines, $k_{x,y}$ refers to a specified pair of emission lines. If an element has more than one characteristic emission in the energy range being studied, the ratio of the peak intensities at these wavelengths may provide a measure of the absorption of the sample and the thickness of the microcrystallite. In the KTP work the only available ratio was the K(K_α) / K(K_β) in which absorption of the K(K_β) emission by Ti and P is 20% lower than that of the K(K_α) line so the ratio can be used to check the absorption. However, the difference in absorption is small, so the ratio will not be very sensitive to sample thickness.

Table 2.2 Mass absorption coefficients of Ti and P for the K(K) emissions in units of $10^3 cm^2/g$.[100]

	Ti	P
K(K_α)	256.8	870.3
K(K_β)	206.4	697.2

2.3 Single Crystal X-ray Diffraction

2.3.1 Data Collection

Crystals selected for data collection were less than 0.5mm in all dimensions so that they would be completely bathed in the X-ray beam and absorption effects would be minimised. The crystals were examined under a polarising microscope and only those that showed uniform birefringence, (indicative of the absence of twinning), were selected.

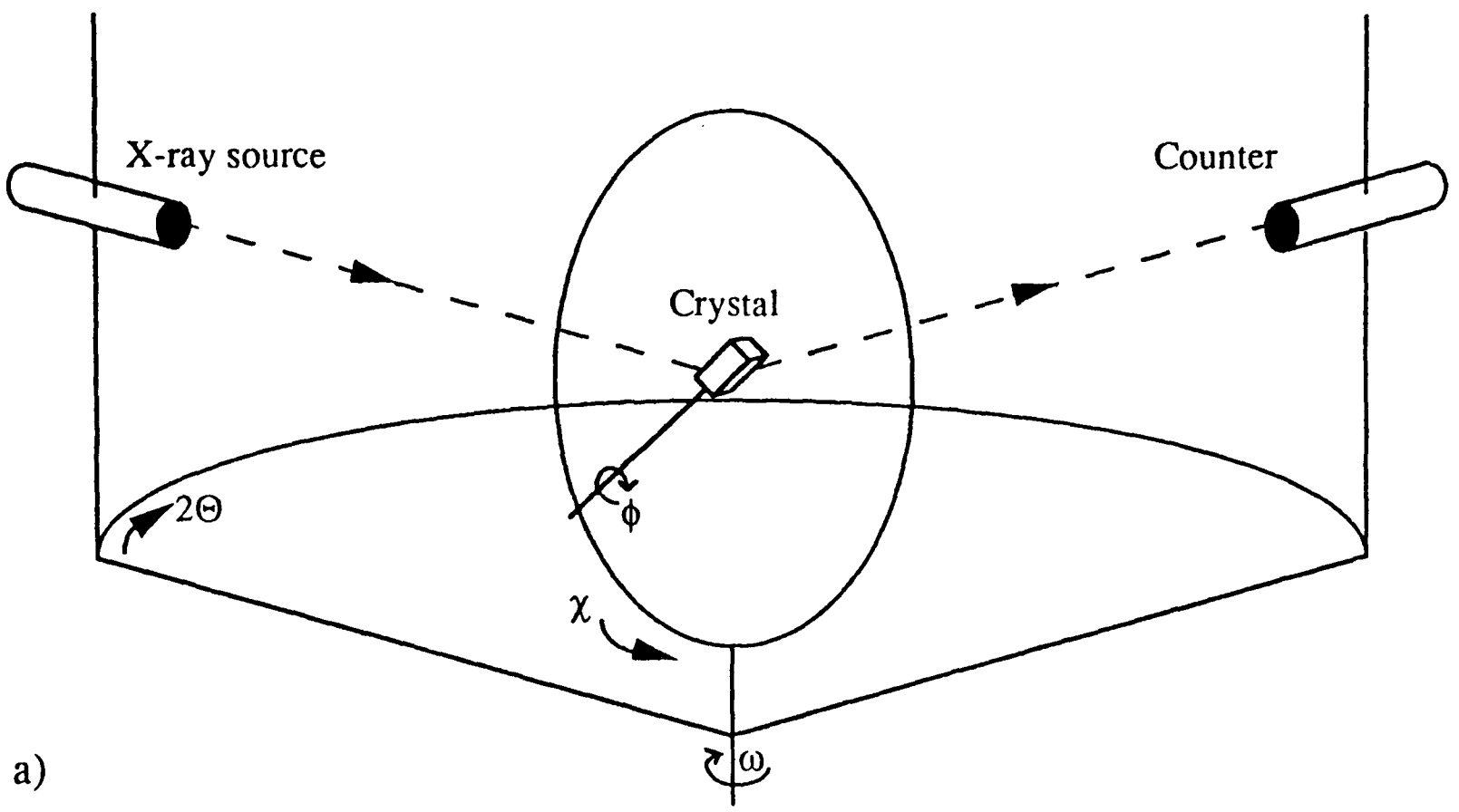
The crystal was then mounted on a thin glass fibre using Super Glue (cyanoacrylate adhesive). Axes indicated by the

crystal form were not absolutely aligned with the fibre axis to avoid multiple reflections being measured by the diffractometer. Preliminary Weissenberg[101] photographs were taken to determine the cell and space group and to ensure that the crystal was not twinned nor split. Crystal quality is more easily determined by photographic methods where all possible diffraction spots are shown rather than by using a diffractometer where the counter only samples a limited portion of reciprocal space.

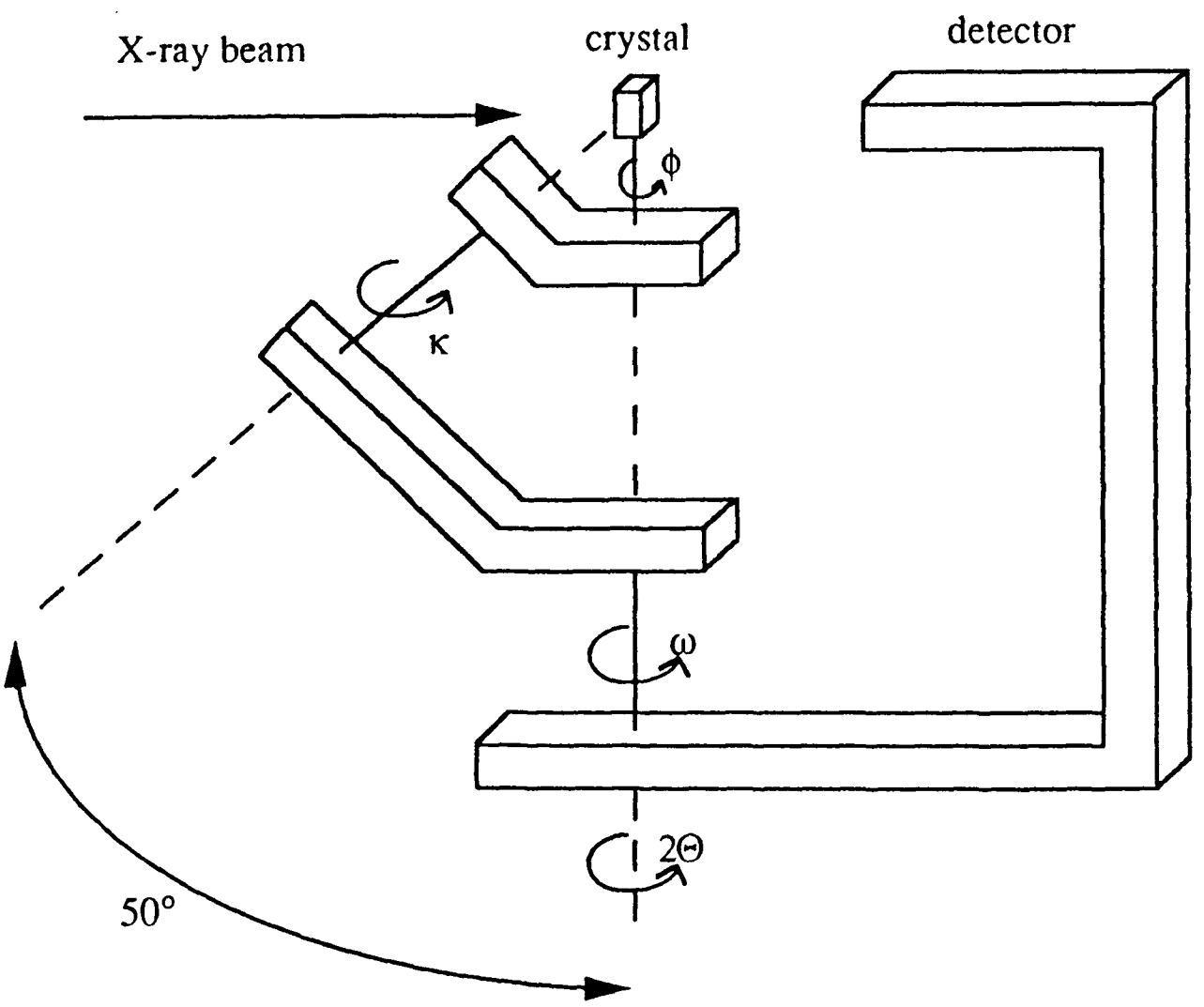
Single crystal data collection[102] was carried out on an Enraf-Nonius CAD4-F diffractometer controlled by a PDP11/23 minicomputer, using Mo K_α radiation (λ = 0.71069Å). This diffractometer uses Kappa geometry where the χ circle perpendicular to the ω axis of a conventional four-circle diffractometer has been replaced by an arm rotating about a κ axis at 50° to the ω axis (Figure 2.3.1). The Kappa geometry provides a more open environment so ancillary equipment such as a low temperature apparatus may be used more easily.

After the crystal was positioned at the centre of the diffractometer, a complete ϕ rotation photograph was taken. All the crystals examined diffracted strongly to give clear spots at high χ and θ. For this reason, 25 high angle reflections (typically θ>20°) were measured from the rotation photograph to use as starting positions in the orientation matrix determination, rather than obtaining initial reflections using a blind search method. The routine PHOTO searched for these reflections and centred them before the angles were centred more accurately using DETTH. The final reflection positions were used as input to INDEX, which automatically produced an orientation matrix and unit cell. The cell was always presented as the reduced cell, so the Niggli matrix, cell and reflection indices

Figure 2.3.1. A comparison of (a) the conventional Eulerian geometry diffractometer and (b) the Kappa geometry of the CAD4.



a)



b)

were examined in an attempt to find a more conventional cell with the full symmetry of the reciprocal lattice. When appropriate the orientation matrix was changed and the reflections reindexed to match the new cell.

To obtain a more precise cell, high angle reflections were selected, well spread in reciprocal space and of fairly high intensity. High angle reflections are used because the Mo $K_{\alpha 1}$ and $K_{\alpha 2}$ wavelengths are resolved at high 2θ, and the peak positions can therefore be obtained with greater precision. The use of symmetry equivalents enables the Laue symmetry of the reciprocal lattice to be checked. These reflections were centred using DETTH[102] as before and the cell refined using linear least squares methods.

All data were collected using $\omega/2\theta$ scans. The functions describing the horizontal variable aperture and ω scan angle are of the form $x + y\tan\theta$, containing a constant term and a term that increases with $\tan\theta$ as the $K_{\alpha 1}$,$K_{\alpha 2}$ splitting increases and broadens the peak width. The actual value of the latter term depends on the wavelength used (e.g. the scan angle increases by $0.35\tan\theta$ when using Mo radiation). The constant terms depend on the mosaic spread of the crystal and the primary beam divergence. These scan parameters were chosen from scans of a few intense low angle reflections well distributed in reciprocal space, so that the whole peak and some background on either side were collected.

Three reflections of moderately high intensity and medium 2θ values in different regions of reciprocal space were chosen as standards. The intensities of the standards were checked every hour of X-ray exposure time and data collection was halted if a measured intensity dropped below 75% of its initial value. The

orientation of these reflections was monitored every 250 reflections. If the scattering vector deviated from its calculated position by more than 20%, the orientation matrix was redetermined automatically.

A prescan of each reflection was carried out at 6.7°/minute, with the scan widths extended by 25% on either side of the peak to determine the background. The first 16 points of the scan are taken as the left background (BGL), the next 64 as peak intensity I_{pre} and the last 16 are the right background (BGR). The net intensity is given by:

$$I = \frac{I_{pre} - 2(BGL + BGR)}{\text{scan speed}}$$

with standard deviation:

$$\sigma(I) = \frac{(I_{pre} + 4(BGL + BGR))^{1/2}}{\text{scan speed}}.$$

The $\sigma(I)/I$ value is then compared with values of σ_p and σ_f defined in the data collection parameters. If $\sigma(I)/I$ is greater than σ_p (typically 0.3), then the reflection is unobserved and is flagged as being weak. If $\sigma(I)/I$ is less than or equal to σ_f (typically 0.1), the prescan data is sufficient, a final slower scan is not necessary. For all other reflections, the speed for the final scan is given by the prescan speed multiplied by $\frac{(\sigma(I)/I)^2}{\sigma_f}$, with the maximum time for any given reflection being sixty seconds, the ratio being designed to bring the $\sigma(I)/I$ value closer to the desired σ_f.

Data were collected in zigzag fashion through shells of reciprocal space until the majority of reflections were unobserved. Friedel pairs were collected when the structure was known to be non-centrosymmetric. The order of data collection was chosen so that the indices corresponding to the longest cell axis varied most quickly to minimise the data collection time.

Finally a few reflections with χ close to 90° were chosen for azimuthal scans. These scans rotate a diffraction plane about its normal and the crystal about the axis connecting the reciprocal lattice point with the reciprocal lattice origin, collecting data every 5° in ϕ to use in a semi-empirical absorption correction.

2.3.2 Data Reduction

The process of data reduction converts the raw intensity I_{hkl} into the more useful structure factor $|F_{hkl}|$ according to the equation:

$$|F_{hkl}| = \sqrt{(kI_{hkl}/Lp)},$$

where L is the Lorentz correction,

p is the polarisation correction and

k is a factor depending on the crystal size, beam intensity and incident wavelength which is incorporated in the scale factor once the structure is determined.[103]

The polarisation factor $p = \frac{1}{2}(1 + \cos^2 2\theta)$, is independent of the method used for data collection.[104] It arises because although X-rays with the electric vector $\underline{E}$, parallel to the reflecting plane are reflected by an amount proportional to the electron density in the plane, those X-rays with $\underline{E}$ perpendicular to the plane have a reflected intensity proportional to both the electron density and $\cos^2 2\theta$. This last term tends to zero as 2θ tends to 90°, so up to half the reflected intensity may be lost and the residual reflected beam will be partially polarised. This effect is further complicated by the use of single crystal monochromators which polarise the radiation incident on the sample.

The Lorentz correction is purely geometrical and depends on

the method of data collection. It takes account of the variation in time taken for a reciprocal lattice point to pass through the Ewald sphere, which depends on the direction it approaches the sphere and its position in reciprocal space. For 4-circle diffractometers the Lorentz correction is given by $L = 1/\sin\theta$.

The standard reflections used to monitor intensity during data collection could be used to scale the data if an intensity decrease had occurred, for instance a reduction in reflection intensity due to crystal decay. This scaling may be performed by linear interpolation, or polynomial curve fitting.

Absorption is a serious source of error in X-ray data. The intensity of a transmitted beam is given by $I = I_o e^{-\mu\tau}$ where τ is the thickness of the sample. The amount of absorption can be reduced by using molybdenum instead of copper radiation as the absorption coefficient μ decreases with decreasing wavelength. Molybdenum radiation has the disadvantage that it is less intense than copper radiation for the same power rating, and at the shorter wavelength reflections occur closer together in reciprocal space which can increase the severity of peak overlap. The absorption correction to be applied to spherical or cylindrical crystals is tabulated in the International Tables Vol II.[C1052] In a rigorous approach for other crystal forms, the precise measurement of crystal dimensions is required, which can be difficult (especially if the crystal is contained in a Lindemann capillary). The semi-empirical method used in this work[C1062] involved choosing two or three reflections with χ close to 90°, and measuring azimuthal scans. The intensity variation as a function of ϕ forms a transmission surface from which the transmission of incident and diffracted beams can be calculated.

Finally, in the data reduction process, systematically absent reflections were removed and those for which $I < 3\sigma(I)$ were excluded from the analysis.

2.3.3 Structure refinement

Isomorphic materials for all structures studied were known, so starting models were taken from the literature and refined using difference Fourier and full matrix least squares techniques. These were carried out on the DEC 3800 MicroVAX in the Chemical Crystallography laboratory, using the Oxford CRYSTALS [107] package. Complex neutral atom scattering factors were taken from volume IV of the International Tables[113], and were corrected for anomalous dispersion towards the end of the refinement. An overall secondary extinction parameter[108] was refined.

The polar space group $Pn2_1a$ in which KTP crystallises has a floating origin along y. In CRYSTALS this is fixed by constraining the centre of gravity of the y parameters of all heavy atoms, using the function $\Sigma_n a\delta z_n = 0$ where a = 1 for heavy atoms and 0 for light atoms.[109] To determine the polarity of the non-centrosymmetric structures, the Flack polarity parameter[110] x was refined, where

$|F_{hkl}(x)|^2 = (1-x)|F_{hkl}|^2 + x|F_{-h-k-l}|^2$. When the coordinates and the crystal have the same polarity x = 0 and when they are opposed, (and the chirality of the crystal structure should be reversed), x = 1. A value between 0 and 1 could indicate merihedral twinning.

The function minimised in least squares refinement is:

$$M = \Sigma w_{hkl}(|F_o| - |F_c|)^2$$

with unit weights w_{hkl} until the final stages of the refinement. In a good weighting scheme the average value of $w\Delta^2$ (where $\Delta = |F_o| - |F_c|$), should be a constant when the set of $w\Delta^2$ are analysed in a systematic fashion e.g. against $|F_o|$ or $\sin\theta/\lambda$. The weighting scheme used for all refinements in this work was the "Robust-Resistant" refinement[1111] where:

$$w = w'\{1 - (\Delta(F)/6\Delta(F)_{med})^2\}^2 \text{ and}$$

$$w' = 1/[A_oT'_o(x) + A_1T'_1(x) + \ldots A_{np-1}T'_{np-1}(x)]$$

The parameters A_i are the coefficients of a Chebyshev series[1112] in $T'_i(x)$, where x is $F_c/F_c(max)$. The weight w' is altered to give w by an expression giving the confidence in Δ, so that if the Δ calculated is more than 6 times that calculated in the Chebyshev series, it is classified as an outlier. This function minimises the variation of $\langle w\Delta^2 \rangle$ with $|F_o|$. Only three parameters (np = 3) were used in the Chebyshev series, as increasing the number did not improve the fit against $|F_o|$.

The overall goodness-of-fit is measured by residuals. The traditional unweighted R-factor is given by:

$$R = \frac{\Sigma||F_o| - |F_c||}{\Sigma|F_o|} = \frac{\Sigma|\Delta|}{\Sigma|F_o|}$$

Random positioning of atoms would give R = 0.59 for non-centrosymmetric systems, (but routine structures should achieve values of R below 0.1).[1013]

The weighted R,

$$wR = \left(\frac{\Sigma w\Delta^2}{\Sigma wF_o^2}\right)^{1/2}, \text{ is related to the function minimised}$$

in the least squares refinement. Comparison of wR values in the Hamilton R-ratio test is used as an indicator of the significance of changes in the model.[1113]

2.4 Powder Diffraction

In contrast to single crystal methods in which the intensity of individual diffraction spots can be measured throughout the three dimensional reciprocal space, in powder diffraction this 3D information is condensed into a 1D profile with considerable loss of information due to peak overlap. In some cases the overlap may be unavoidable (e.g. (4,3,2) and (-4,3,2) occur at the same d-spacing in point group 4/m, but are inequivalent), and in others it is purely accidental. The latter problem can be reduced to some extent by the use of high resolution powder diffractometers but can not be eliminated entirely. Inevitably the number of singly indexed peaks is greatly reduced in a powder experiment compared to a typical single crystal study, particularly in low symmetry materials, those with large unit cells and in samples containing impurity phases. For this reason, single crystals are normally preferred to powders for structure solution and classical least-squares refinement.

Despite the drawbacks in the analysis of powder diffraction data, the use of powder samples has advantages besides the obvious consideration that crystals may be difficult to grow. For the study of structural evolution with pressure, temperature or time, powdered samples are preferable since the experimental conditions of interest may cause fracture or domain formation during phase transitions or chemical reactions. In addition, powder diffraction can be conveniently used for the characterisation of structural modifications to materials of known structure; for example the effect of dopants, solid solution formation or adsorption of species into the structure, as the composition of powders can often be more readily

controlled during synthesis. The development of the Rietveld method (section 2.5) has meant that the intensity information contained in overlapping peaks can be used in the refinement of known structural types making low symmetry structures accessible through powder diffraction techniques.

2.4.1 Neutron versus X-ray diffraction[114,115]

Neutron diffraction is complementary to that of X-rays. X-rays are scattered from the electron cloud of an atom, so the amplitude of the signal obtained is proportional to the atomic number, Z, of the element. The wavelength of the X-rays used is similar to the dimensions of the electron cloud, so as the angle between the incident and scattered waves increases, X-rays scattered from an electron in one part of the atom will be increasingly out of phase with those scattered from electrons in other regions. Therefore the amplitude of the X-ray signal decreases as $\sin\theta/\lambda$ increases. This decrease is described by the atomic scattering factor f_x.

In contrast, neutrons are scattered from the nucleus and, as nuclear dimensions are much smaller than the wavelength of the radiation, there is no variation with θ. Consequently, diffraction peaks can be detected at higher values of 2θ with neutrons. The amplitude of neutron scattering from most nuclei is within an order of magnitude, unlike the rapid rise with Z seen with X-rays. This enables the determination of light atom positions in the presence of heavy atoms[116].

The neutron scattering cross-section is given by $\sigma = 4\pi b^2$, which is equal to the flux of scattered neutrons divided by the incident neutron flux. Each isotope of an element has a characteristic scattering length b, so the coherent scattering

amplitude for an element is the average over the various isotopes, weighted by their natural abundances.[117] Changing the ratio of isotopes present changes the diffraction pattern which can give valuable extra information about the position of the atom within the structure. The scattering amplitude of X-rays is a linear function of Z, so X-ray diffraction patterns contain more information about heavy than light atoms while the variation of neutron scattering factors with Z is almost random. This provides contrast between neighbouring elements in the periodic table not seen with X-rays.

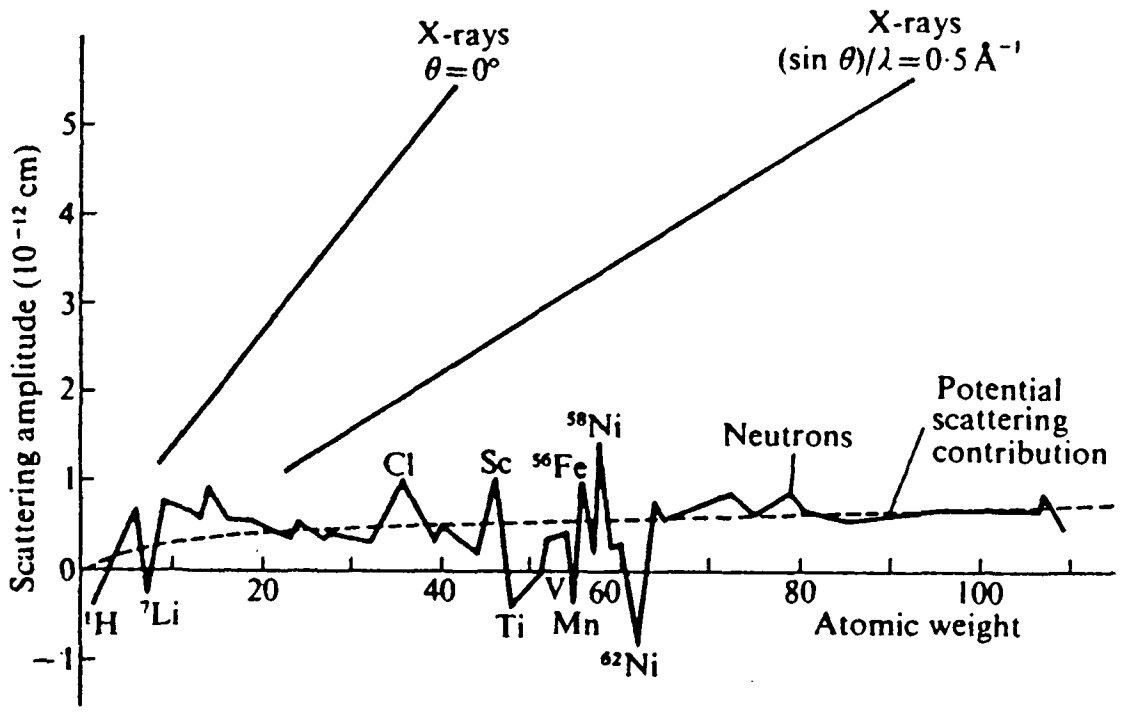


Fig. 2.4.1 The variation of neutron and X-ray scattering amplitudes with atomic weight.

In general, the absorption of neutrons is four orders of magnitude less than that of X-rays (with the exception of the absorption of materials containing elements such as B and Cd), which means that neutrons have much greater penetrating power, allowing the use of special sample environments. Neutrons may be used for non-destructive testing of materials due to this penetrating ability. However larger samples have to be prepared for neutron diffraction experiments than in X-ray work, mainly

because the neutron flux is smaller than that from X-ray sources.

The Gaussian peak shape obtained in constant wavelength neutron experiments is much simpler than that produced by laboratory X-ray sources where the peak measured is a compound of the $K_{\alpha 1}$ and $K_{\alpha 2}$ reflections and has low angle asymmetry. The complicated nature of the X-ray powder diffraction peak shape meant that Rietveld analysis of X-ray data developed more slowly than that of neutron diffraction data.

Neutrons can be used to determine the magnetic structure of materials due to the interaction of the electron spin with that of the neutron.[114] The interaction of the magnetic vector of X-rays with matter is much weaker and magnetic X-ray studies are much less common as a result.[118,119]

2.4.2 Neutron Diffraction Techniques[120-122]

Constant Wavelength. Neutrons are produced in a reactor, pass

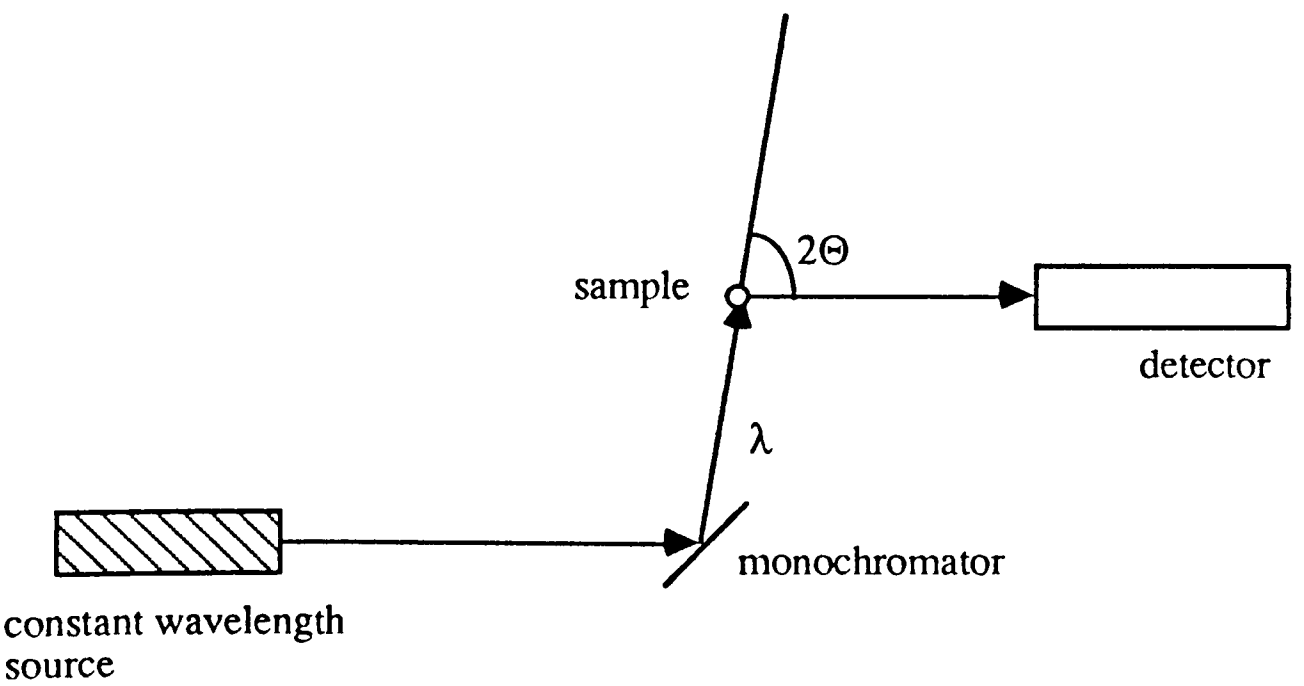


Fig 2.4.2 A schematic diagram of a constant wavelength diffraction experiment

through a moderator, then are guided towards the diffraction apparatus. The beam hits a monochromator which is a single crystal of, for example, highly mosaic germanium. The selected wavelength neutrons then impinge on the sample and the detector scans through 2θ to detect the diffracted beam. Thus by varying θ for fixed λ, d is found through Bragg's Law: $d = \lambda/2\sin\theta$.

Time-of-Flight (TOF). Neutrons are produced in a pulsed beam, either by chopping the flux output from a reactor, or by accelerator-based protons causing spallation of neutrons from a heavy metal target. In these diffractometers, the detector is at a fixed 2θ angle and the whole range of neutron wavelengths is used so that the Bragg condition for all reflections will be satisfied by some wavelength. Since the beam is pulsed, the wavelength can be determined by the time taken for the neutrons to reach the detector, fast neutrons having shorter wavelengths; and the whole pattern is measured at once. The wavelength is given by $\lambda = h/mv = ht/mL$ where t is the time of flight, m is the neutron mass and L is the length of the neutron flight path.

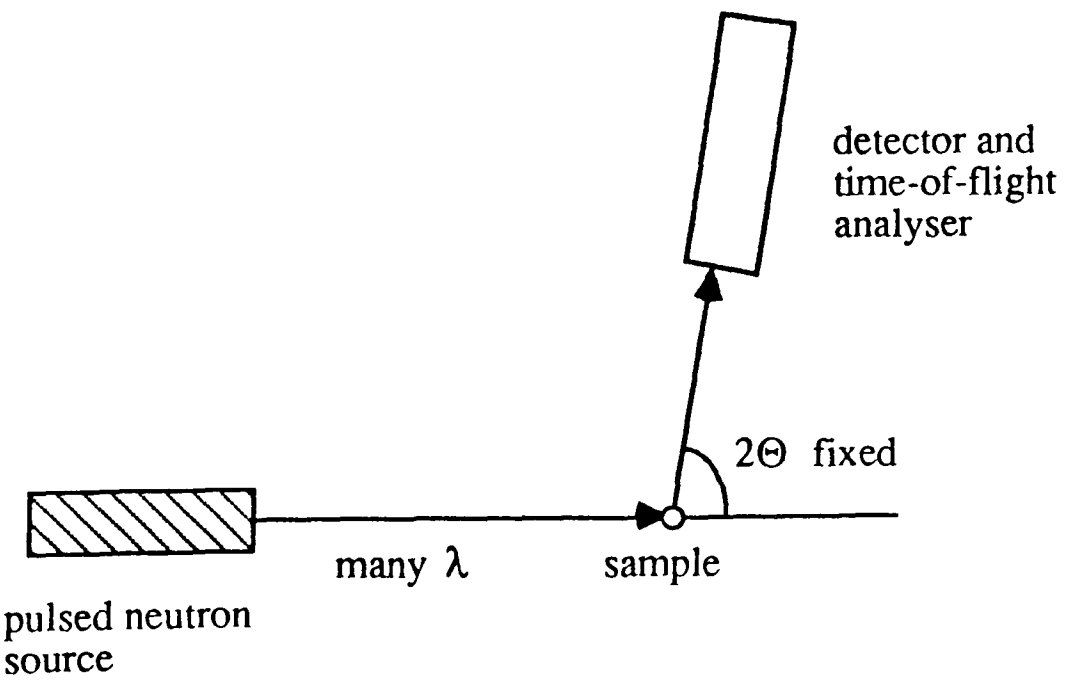


Fig 2.4.3 A schematic diagram of a time-of-flight neutron diffraction experiment.

Substitution into Bragg's Law gives $d = \{h/(2mL\sin\theta)\}t$. The resolution of a time-of-flight diffractometer is given by:

$$\frac{\Delta d}{d} \sim \left(\frac{(\Delta t)^2}{t^2} + (\Delta\theta\cot\theta)^2 + \frac{(\Delta l)^2}{l^2}\right)^{1/2}$$

where Δt is the uncertainty in the measured TOF, t, and Δl is the uncertainty in the flight path l. Increasing the flight path improves the resolution due to the $\Delta l/l$ term, a feature exploited by HRPD in the Rutherford Appleton Laboratory[123] which has a flight path of 96m and a resolution of $\Delta d/d = 4.5\times10^{-4}$. Due to the θ term the resolution increases as a function of the detector 2θ angle, $\Delta d/d$ being 0.008 at 60°, 0.004 at 90° and 0.002 in the backscattering detectors of GPPD at Argonne National Laboratory, (see below), independent of the value of d.

The constant wavelength method uses only a fraction of the total available neutron intensity, but results in a simple Gaussian peak shape and a smoothly varying background. The time-of-flight method uses the whole white beam but the background fluctuates markedly so the fitting is difficult, even with a complex polynomial. However the time-of-flight apparatus accommodates special environments (e.g. cryostats and furnaces) more readily since the detector does not move relative to the sample and only small incident and scattered neutron beam windows are required.

2.4.3 D2B, a constant wavelength neutron diffractometer[124,125]

The constant wavelength data used in this work were collected by Joanne Warner and David Perkins on the high resolution powder diffractometer D2B at the Institut Laue Langevin in Grenoble.

This diffractometer receives a high flux beam of neutrons since the 200mm diameter beam tube insert only depletes the

reactor flux by 2% to 3%. The primary horizontal collimation is carried out by a Soller collimator, and the beam is focused to 40mm at the sample position by a laminated squashed-germanium crystal monochromator. The sample is contained in a sealed vanadium can, vanadium being used because of its very low coherent scattering length (b = -0.038×10^{-12}cm). The detector consists of a bank of 64 collimators and counters situated at 2.5° intervals, so that a complete scan covering the full 160°

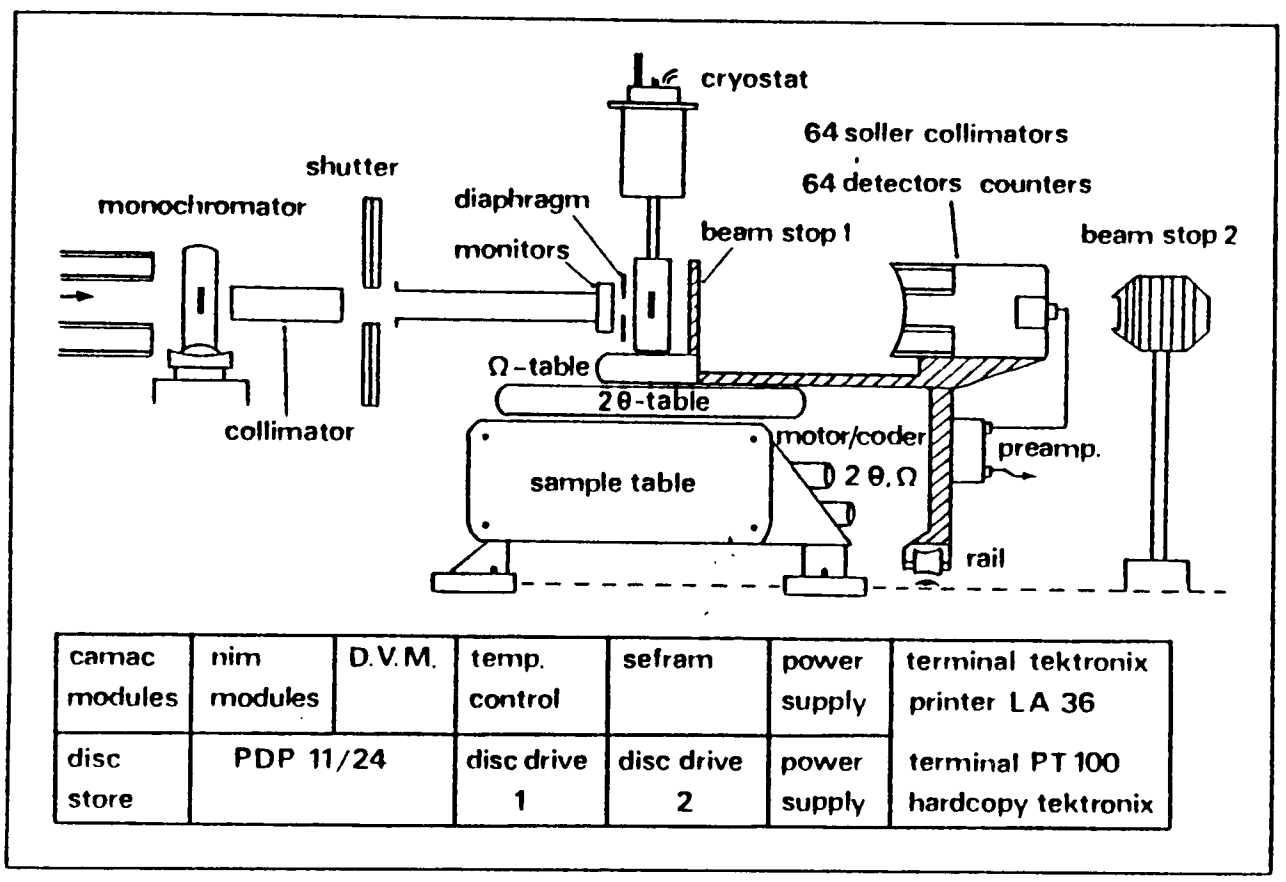


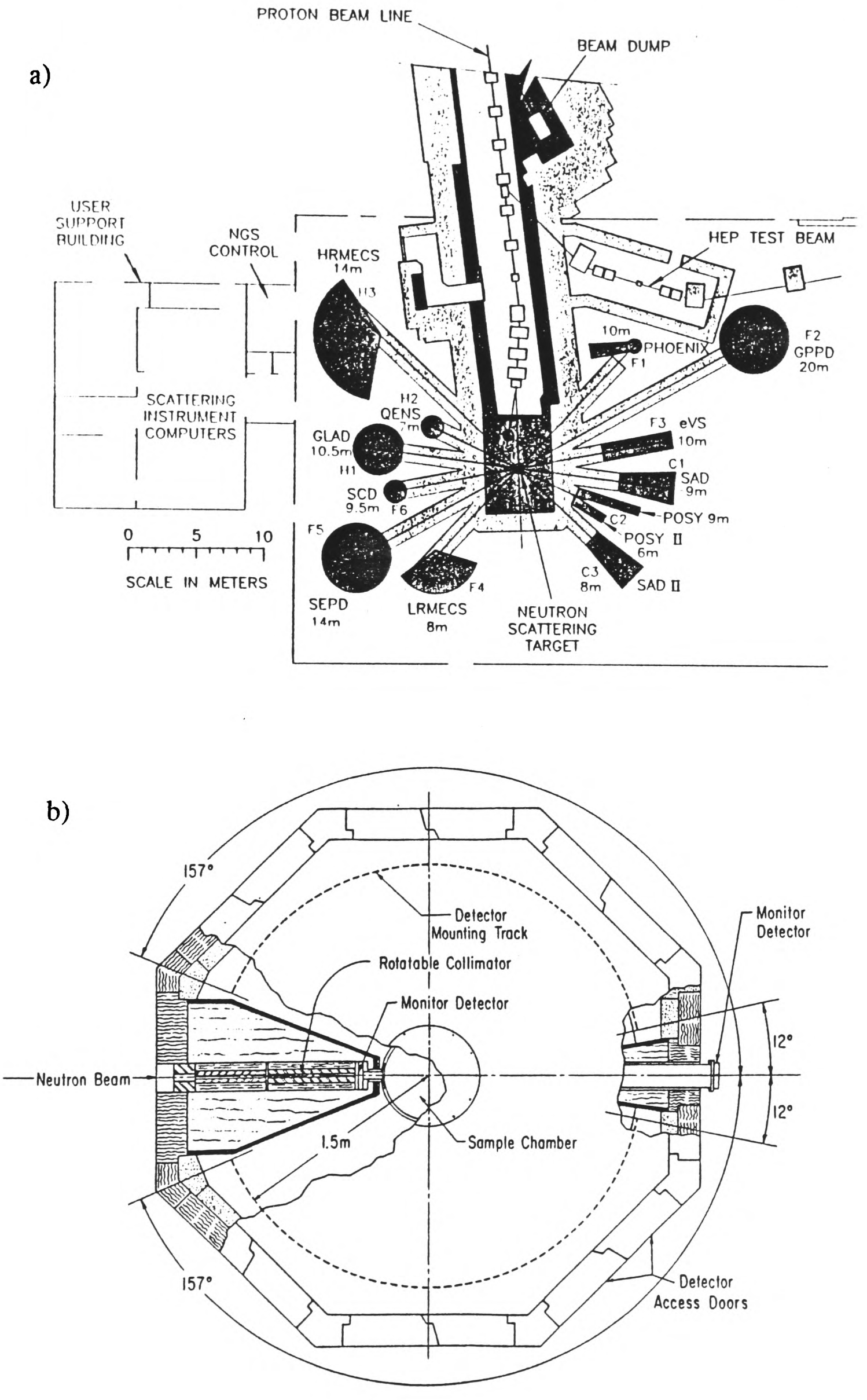
Fig. 2.4.4 Schematic diagram of D2B (I.L.L. User guide)

scattering range can be covered in 100 detector steps of 0.025°. The system is controlled by a PDP11/24 computer. There is no neutron guide tube so shorter wavelength radiation can be used, but this may introduce the possibility of higher order contamination of the wavelength selected by the monochromator, (that is the ($\lambda/3$) or other harmonic wavelengths), which must be allowed for in the raw data correction procedures.

2.4.4 GPPD A Time-Of-Flight Neutron Diffractometer[126,127]

The time-of-flight neutron data presented in this work were collected using the General Purpose Powder Diffractometer at the Intense Pulsed Neutron Source (IPNS), Argonne National Laboratory near Chicago, Illinois. Protons accelerated to 450MeV in the synchrotron impinge on an enriched-Uranium target and produce neutrons by spallation, (i.e. the induced fission of heavy elements on impact of high energy particles). The proton accelerator is pulsed at 30Hz so the neutrons are produced in bursts, which after being slowed in the moderator, have wavelengths between 0.2 and 5Å. The distance between the source and sample is 20m and the detector banks are 1.5m from the sample. The detectors are He-filled cylindrically-shaped proportional counters and they are placed in banks at 0°, 15°, 30°, 60°, 90° and 148° in 2θ. Data from the corresponding $\pm 2\theta$ banks of detectors are summed to double the data collection rate. The samples are contained in cylindrical vanadium cans and about $5cm^3$ of powder is required to fill the can. The resulting TOF powder diffraction pattern is superimposed on the incoherent intensity distribution of white radiation. A typical run lasts 8 hours, but preliminary indications of the crystallinity of the sample and its ability to diffract can be seen in the pattern obtained after a few minutes.

Figure 2.4.5. a, The experimental hall at IPNS, b, a schematic diagram of the General Purpose Powder Diffractometer (GPPD).



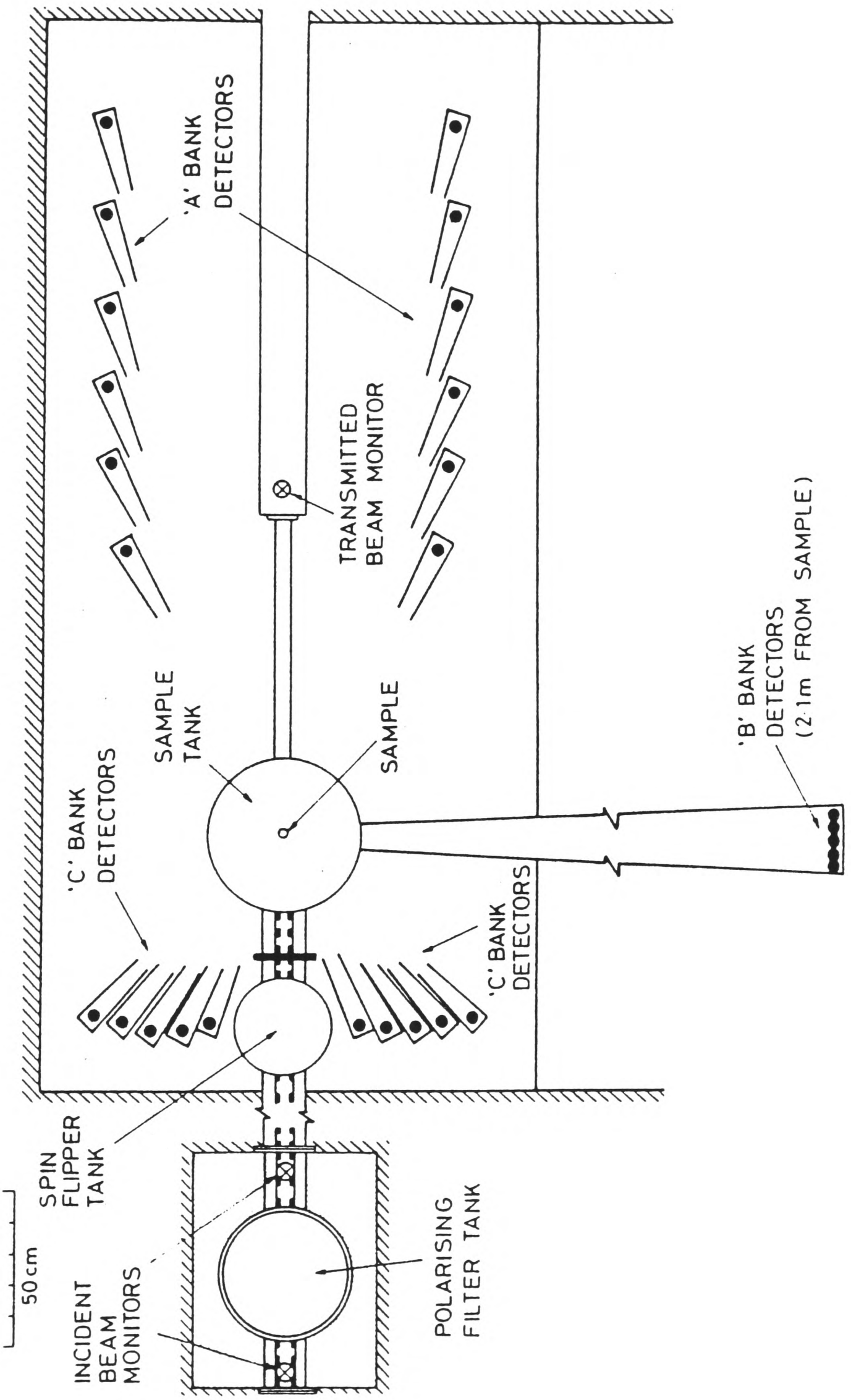
2.4.5 POLARIS, a TOF neutron powder diffractometer[123,128]

The time-of-flight neutron diffraction data from Cr-doped KTP powders were collected on the high intensity, medium resolution POLARIS diffractometer at the Rutherford Appleton Laboratory. The ISIS spallation neutron source is similar to that at IPNS. The POLARIS sample position is 12m from the moderator, with a beam cross-section of 36x24mm at that point. This 12m distance from moderator to sample in POLARIS gives a resolution that is a factor of ten less than that achieved by HRPD with its 95m flight path. The 42 ^{3}He gas detectors are arranged in banks of constant resolution. The resolution of the A-bank ($14<2\theta<30^o$) is dominated by the $\Delta\theta\cot\theta$ term and constant resolution in this bank is achieved by increasing the distance (l) of the successive detectors from the sample while decreasing θ. The resolution of the B-bank ($88<2\theta<92^o$) is constant as the detectors are at approximately the same angle and distance from the sample. In the C-bank ($135<2\theta<158^o$) the $\cot\theta$ term in the resolution equation is negligible, leaving only the $\Delta t/t$ and $\Delta l/l$ terms. Individual detectors are summed using the known sample to detector distance and 2θ value for each detector to calculate the time-focusing.

This is in contrast to GPPD where the detectors are arranged in a circle around the sample and the variation in TOF values across a bank is compensated by time-focusing:

$t_1 = t_o \sin\theta_o / \sin\theta_1$ where t_o and $\sin\theta_1$ refer to a reference bank. The high flux of POLARIS enables a diffraction pattern to be collected in 3 hours compared to the 8 hours necessary on GPPD.

Figure 2.4.6 A schematic diagram of the POLARIS diffractometer.



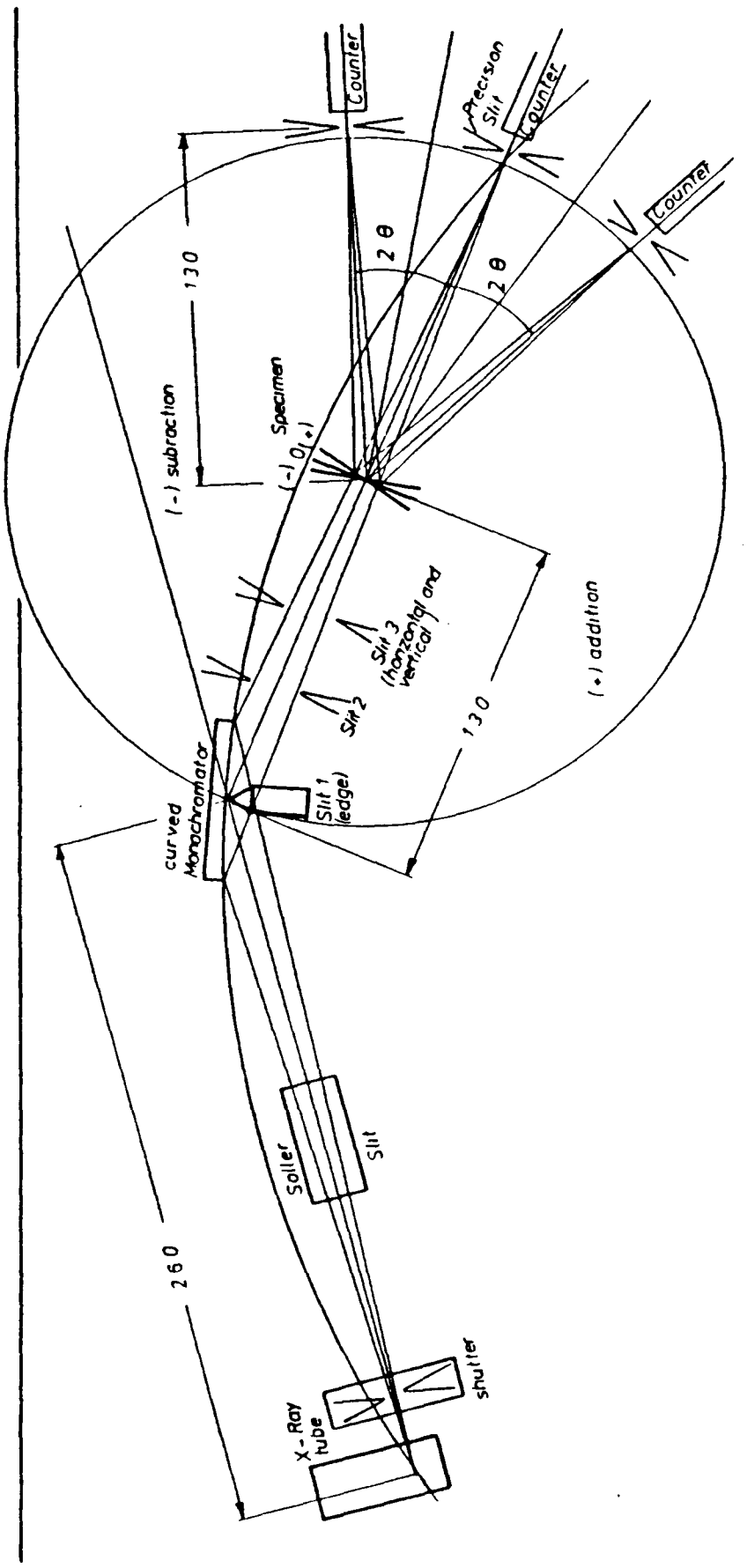
2.4.6 A Stoe STADI-P diffractometer

High resolution X-ray powder diffraction data were collected in the Clarendon laboratory on a Stoe Stadi-P diffractometer.[129] The diffractometer operates in transmission mode. A sample of approximately 50mg was ground and spread between two circular acetate foils using grease to ensure the foils adhered together. The foils were screwed into a circular mask which fed into the rotating sample holder. An initial scan was carried out using the scintillation counter to monitor the intensity with and without the sample in place. If the absorption was too great with the sample in place, another slide was prepared containing less sample.

A schematic diagram of the Stadi-P diffractometer operating in the transmission mode is shown in figure 2.4.6. The X-ray beam travels through a computer-controlled shutter and Soller collimator in a 26mm guide tube before impinging on a curved germanium monochromator which selects the Cu $K_{\alpha 1}$ wavelength. Slit 1 is a knife-edge which reduces the scatter of unwanted wavelengths from the monochromator, while slits 2 and 3 define the width and height of the focused beam arriving at the sample. The sample is rotated to reduce the preferred orientation effects that are common in flat plate geometry and improve the powder averaging of the sample.

A position-sensitive detector is used to collect the diffracted beam. Each photon entering the detector ionises the gas producing electrons which are attracted to the highly charged anode. On arrival they generate an electrical charge in the delay line from which the photon position is determined, and the pulse amplified and stored. Data are collected in 2θ scans with step widths of 0.014° and a resolution of 0.06° in 2θ.

Fig 2.4.6 The geometry of the STOE Stadi-P diffractometer in focusing monochromatic beam transmission mode.



2.5 The Rietveld Method

In the least squares refinement of models with single crystal data the observed intensity of the separate Bragg reflections, I_o is used in the minimization function:

$$M=\Sigma w_{hkl}(I_o-I_c)^2$$

where $I_c = \alpha|F_c|^2$. However, if the total integrated intensity of the overlapping peaks obtained in powder diffraction data is used in a least squares refinement, the information about the separate reflections contained in the peak shape is lost. Rietveld[130], recognising that the peaks obtained in constant wavelength neutron diffraction could be described by a Gaussian peak shape with a simple variation of full width at half maximum (FWHM) across the diffraction pattern, suggested the use of profile intensities instead of integrated intensities in modelling powder data. The derivation of the Rietveld method made possible the study of low symmetry crystal systems by powder methods.

In this description[131] the kth reflection makes a contribution y_{ik} to the observed profile at a position $2\theta_i$,

$$y_{ik} = \alpha m_k L_k S_k^2 \frac{2\sqrt{\ln 2}}{\Gamma_k\sqrt{\pi}} \times \exp[-4\ln 2\{(2\theta_i-2\theta_k)/\Gamma_k\}^2]$$

where α is the proportionality constant or scale factor,

m_k is the multiplicity of the reflection,

L_k is the Lorentz correction,

S_k^2 is the sum of nuclear and magnetic structure factors $= F_k^2 + J_k^2$,

Γ_k is the full width at half maximum height,

θ_i is the observed profile position and

θ_k is the calculated position of the Bragg peak.

At positions where more than one reflection contributes to a

profile point, the total profile intensity is given by a summation over all the Bragg peaks that are within 1.5 full widths at half-maximum of their calculated positions:

$Y_i = \Sigma_k y_{i,k}$, a distance beyond which the intensity of a Gaussian peak is negligible although the number of half-widths can be refined in most Rietveld codes. The function minimised in Rietveld refinement is therefore:

$M = \Sigma_i w_i (Y_i(obs) - Y_i(calc))^2$.

2.5.1 The Generalised Structure Analysis System (GSAS)[132]

All Rietveld refinements in this work were carried out using the GSAS suite of programs. Within GSAS, multiple data sets may be used in the refinement of a model. The different detector banks of the TOF diffractometer provide complementary information. The backscattering detector banks have the highest resolution (largest θ), but the low angle bank covers the larger d-spacing range. Multiple data set refinement allows both these properties to be harnessed. Combined use of X-ray and neutron diffraction data is also possible in GSAS, so the complementary properties of these techniques may be exploited fully. Neighbouring element contrast and light atom positions can be determined from the neutron data, together with an independent determination of heavy atom positions and occupancies obtained from the X-ray data.

The use of multiple phases is important in powder work as samples are rarely synthesised in pure form, unreacted starting materials or side-products often being present. These impurity phases may reduce the quality of fit to the data by a considerable amount so that the properties under investigation

(e.g. occupancies and temperature factors) cannot be reliably determined for the major phase. In GSAS these impurity peaks may be modelled, provided the structure of the impurity phase is known.

The Bragg intensities are calculated using

$Y_{p,h} = S_{p,h}F_{p,h}^2K_{p,h}H(\Delta T)$

where $S_{p,h}$ is the scale factor,

$F_{p,h}$ is the nuclear structure factor,

$K_{p,h}$ contains the geometric corrections (extinction, absorption, preferred orientation, reflection multiplicity, Lorentz and polarisation corrections) and

$H(\Delta T)$ is the value of the peak shape function for a reflection at a profile point T differing from its calculated position $T_{p,h}$ by a distance ΔT.

The subscripts p,h indicate for which phase and data set (or histogram) the Bragg intensities are being calculated.

2.5.1.1 Peak positions

For constant wavelength data the peak positions are calculated using Bragg's Law and corrected for diffractometer zero-point errors. For time-of-flight data the position $T_{p,h}$ is given by:

$T_{p,h} = DIFCd_p + DIFAd_p^2 + ZERO$ where DIFC, DIFA and ZERO are refinable parameters characteristic of a given counter bank of a diffractometer and are initially determined using a standard sample.

2.5.1.2 Profile functions

The profile function describing data collected from a spallation time-of-flight neutron source is non-gaussian and asymmetric.[133] It is modelled by the convolution of two exponentials (one describing the rise in intensity and another the decay) with a Gaussian peak shape:

$$H(\Delta T) = N[e^{u}\mathrm{erfc}(y) + e^{v}\mathrm{erfc}(z)]$$

where

$$N = \alpha\beta/2(\alpha+\beta)$$

$$u = \tfrac{1}{2}\alpha(\alpha\sigma^2 + 2\Delta T)$$

$$v = \tfrac{1}{2}\beta(\beta\sigma^2 - 2\Delta T)$$

$$y = (\alpha\sigma^2 + \Delta T)/\sqrt{2\sigma^2}$$

$$z = (\beta\sigma^2 - \Delta T)/\sqrt{2\sigma^2}$$

and erfc(x) is the complementary error function $(2/\sqrt{\pi})\int_x^\infty \exp(-t^2)dt$[134]. α and β are the coefficients for the rise and decay exponentials and σ^2 is the Gaussian variance. These coefficients depend on the d-spacing:

$\alpha = \alpha_o + \alpha_1/d$,

$\beta = \beta_o + \beta_1/d^4$ and

$\sigma^2 = \sigma_o^2 + \sigma_1^2 d^2 + \sigma_2^2 d^4$ + asymmetric broadening terms.

α and β are determined by the diffractometer while the σ terms are sample dependent, σ_1^2 being a measure of strain broadening and σ_2^2 a measure of particle size broadening.[104]

For constant wavelength neutron data a Gaussian profile shape is adequate, but for X-ray data a pseudo-Voigt is more successful:

$$H(\Delta T) = \sum_{i=1}^{n} g_i F(\Delta T')$$ where

$F(\Delta T) = \eta L(\Delta T', \Gamma) + (1-\eta)G(\Delta T', \Gamma)$,

$\Delta T'$ is the difference in 2θ between a peak position and the measured profile point,

η is a mixing coefficient and Γ is the FWHM.

The Gaussian variance[135] is given by:

$\sigma^2 = U\tan^2\theta + V\tan\theta + W + P/\cos^2\theta$ (the last term being the Scherrer coefficient for Gaussian broadening) and the Lorentzian coefficient

$\gamma = (X + X_e\cos\phi)/\cos\theta + (Y + Y_e\cos\phi)\tan\theta + Z$, giving the parameters U, V, W, P, X, Y and Z to be refined to fit the peak shape (the $\cos\phi$ terms describe the anisotropy). Strain broadening varies with $\tan\theta$, so U, V and Y measure strain while X and P are measures of size broadening which varies as $1/\cos\theta$. W and Z are constant terms, only one of which can be non-zero.

2.5.1.3 Background function

The background function used was a cosine Fourier series with up to twelve refinable coefficients:

$I_b = B_1 + \Sigma_{j=2,12}\ B_j\cos(P(j-1))$ where P for CW data is the 2θ value and for TOF is the time multiplied by 180/maximum time.

2.5.1.4 Goodness of fit parameters

The goodness of fit of the final refinement to the data can be measured by a variety of parameters.

The profile R-factor $R_p = \dfrac{\Sigma|Y_o - Y_c|}{\Sigma Y_o}$

The weighted profile R $R_{wp} = \dfrac{\sqrt{\Sigma w(Y_o - Y_c)^2}}{\sqrt{\Sigma_w (Y_o)^2}}$

The Bragg R-factor $R_I = \dfrac{\Sigma|I_o - I_c|}{\Sigma I_o}$

and $\chi^2 = \dfrac{\Sigma w(Y_o - Y_c)^2}{N_{obs} - N_{var} + N_{constraints}} = \dfrac{(R_{wp})^2}{(R_{exp})^2}$

where Y_i is a general intensity data point at an angle θ_i and I is the total integrated intensity of a peak. In a precise and accurate refinement, the weighted profile R would be the same as the expected R. A high value of R_{wp} indicates errors in the

lattice, peak shape, zero point and instrumental parameters, or an incorrect structural model. R_I is a measure of the quality of the structural fit since it relates to peak area so is insensitive to errors in peak shape and is often used in statistical analyses of the model. However it can be affected by a variety of factors unrelated to the structural model, so R_{wp} is the preferred measure of quality of fit.

2.6 Bond valence calculations[136]

The first concepts of bond valency were introduced by Pauling[137] who defined the mean bond strength, s, as the valency of a cation divided by its coordination number. The valency of an atom was defined as the number of electrons taking part in chemical bonding and is approximately equal to the sum of the individual bond valences.

Two formulae have been devised to calculate bond valences:

$s = (r/r_o)^{-N}$ [138,139] and $s = \exp\{(r_o-r)/B\}$ [140]

where N and B are constants, differing for each cation-anion pair, and r_o is the length of the cation-anion bond for unit valence. These parameters have been fitted empirically using structures reported in the Inorganic Crystal Structure Database and are tabulated in references [138 to 140]. The B parameter was found to vary little from one atom pair to another and a value of 0.37(5) could be used in the majority of cases. This discovery enabled the second expression to be readily used since only r_o has to be determined for each ion pair.

The atomic valency $V_i = \Sigma_j s_{ij} = \Sigma_j \exp((r_o-r_{ij})/B)$ where s_{ij} is the strength of the bond between the cation i and anion j. If an atomic valency differs by more than 5% from its theoretical value in a well refined structure it may indicate that the structure is incorrect. Alternatively it might be an indication of hydrogen bonds or solvent molecules that have been previously undetected. In a solid solution of atoms of different valency but similar scattering power, the atomic valency parameter can help determine the site occupancy as the ion of lower valency generally has longer bonds. Anomolously high bond valences may indicate disorder in the structure

since disorder modelled as large thermal motion will give short apparent bond lengths and a large valence parameter. In the present work, bond valence calculations according to the second equation have been used to help elucidate the cation ordering in the structures of KTP isomorphs.

2.7 Measurement of nonlinear optical coefficients

To determine the second harmonic generating (SHG) efficiency of a new nonlinear optical (NLO) material the coefficients d_{ijk} must be measured. The second harmonic intensity measured in experiments is proportional to d^2/n^3 where n is the refractive index of the material and d is the effective d_{ijk} for the material. This ratio is often used to compare the SHG ability of different materials.

The majority of nonlinear measurements are performed relative to some standard (e.g. crystalline quartz or potassium dihydrogen phosphate (KDP)), since absolute values are difficult to determine. The most reliable measurements are carried out on single crystal samples, using a large crystal which is precisely cut and polished in the correct orientation. If more than one non-zero d_{ijk} exists, then for a complete characterisation several crystals are needed, cut in the different orientations.

2.7.1 Methods of measuring nonlinear optical coefficients using crystals

i)Phase-matched Second Harmonic Generation [141,142]. Relative measurements of d_{ijk} may be obtained by recording the

power of the second harmonic P(2ω) as the crystal is rotated through the index-matching directions. The nonlinear coefficient is calculated from the ratio of the maximum P(2ω) to the laser power P(ω) squared.

ii)Maker fringe technique [143-145]. Varying the angle of incidence of the fundamental on a plane-parallel crystal specimen changes the path length through the sample. The second harmonic intensity oscillates with the thickness z, producing interference fringes. The coherence lengths can be calculated from the separation of the fringe minima and the nonlinear optical coefficients from least-squares fitting of the fringe envelope.

iii)Wedge technique [146]. Maker fringes can also be formed by the translation of a wedge-shaped sample through a laser beam.

iv)Spontaneous parametric emission [147]. Absolute d values may be obtained from the ratio of the spontaneous parametric emission power to the incident power at known temperature and wavelength. An advantage of this technique is that the angular alignment and temperature of the crystal are less critical because phase-matching is not necessary.

2.7.2 Measuring Second Harmonic generated from powders

Single crystals of new materials may be difficult to produce in a large enough size or optical quality for nonlinear optical testing. However powder samples can be used to obtain a qualitative measure of a sample's SHG ability relative to a standard such as crystalline quartz. (A quartz single crystal is used to obtain a reproducible reference

signal for calibration of the powder samples.) In a powder, second harmonic intensity will be generated in each microcrystallite, but these components will not bear any phase relationship to one another. The signal observed is weighted by the coherence lengths which, in general, will not be the same in all directions. The output also depends on whether the material is phase-matchable, whether it is transparent at both the fundamental and second harmonic frequencies, and on the magnitude of the nonlinear optical coefficients.

The powder test was initially designed by Kurtz and Perry,[148] who defined five classes of materials:

Phase-matchable

Class A: Refractive indices > crystalline quartz ($n \geqslant 1.9$)

Class B: Refractive indices < crystalline quartz ($n \leqslant 1.6$)

Not phase-matchable

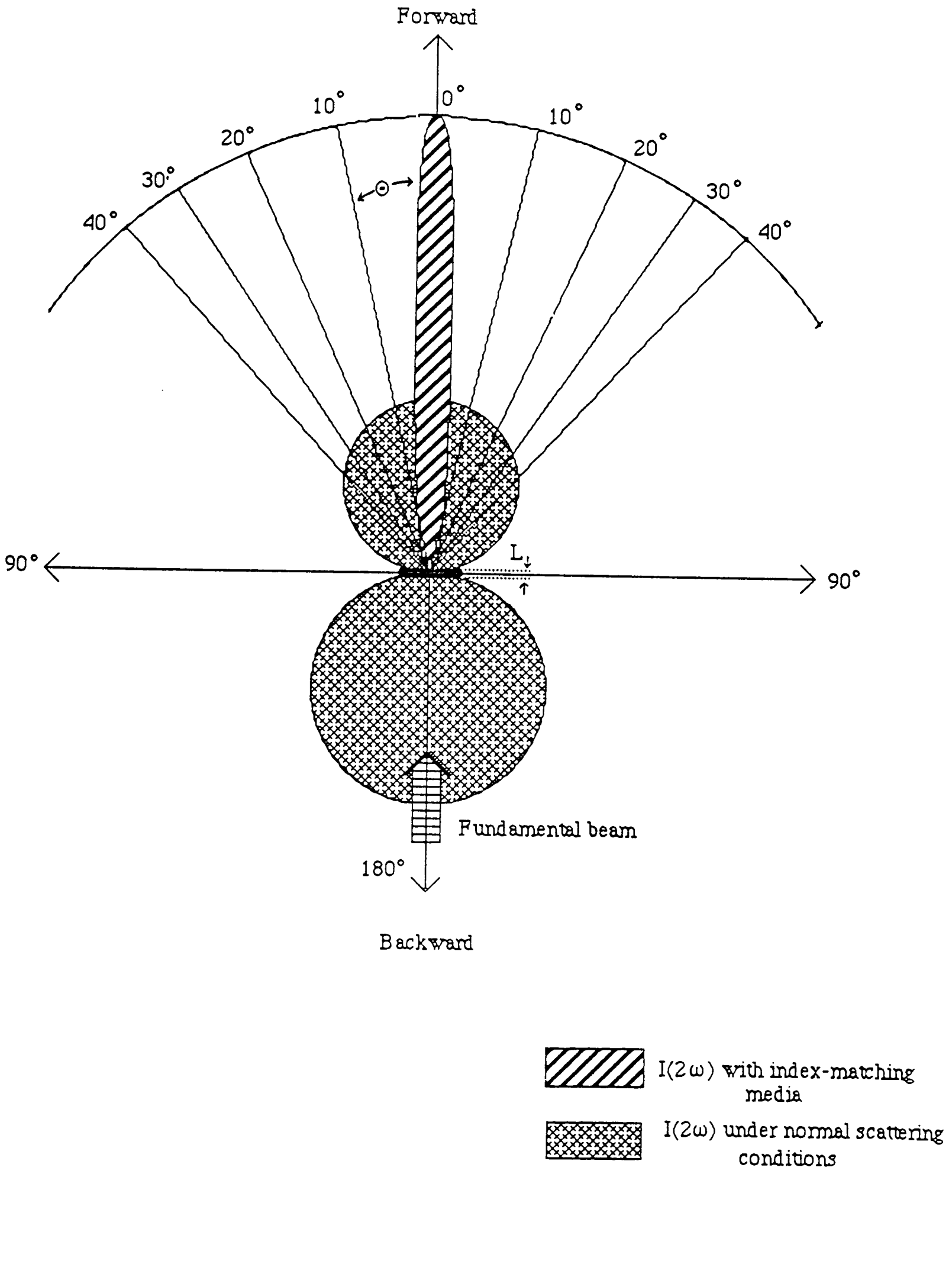
Class C: Refractive indices > crystalline quartz ($n \geqslant 1.9$)

Class D: Refractive indices < crystalline quartz ($n \leqslant 1.6$)

Class E: Centrosymmetric

To obtain a powder average in the sample, the particle size should be considerably smaller than the thickness of the sample, which in turn should be less than the beam diameter. The angular distribution of the second harmonic generated is proportional to $\cos\theta$, the angle of deviation from the fundamental direction (Fig.2.7.I). However, the lobes of $I(2\omega)$ are not identical and as the particle size of samples decreases the area of the lobe in the backscattering direction increases while that in the forward direction decreases; it is thus important to measure both. If the particles are immersed in a fluid of similar refractive index, the scattering of

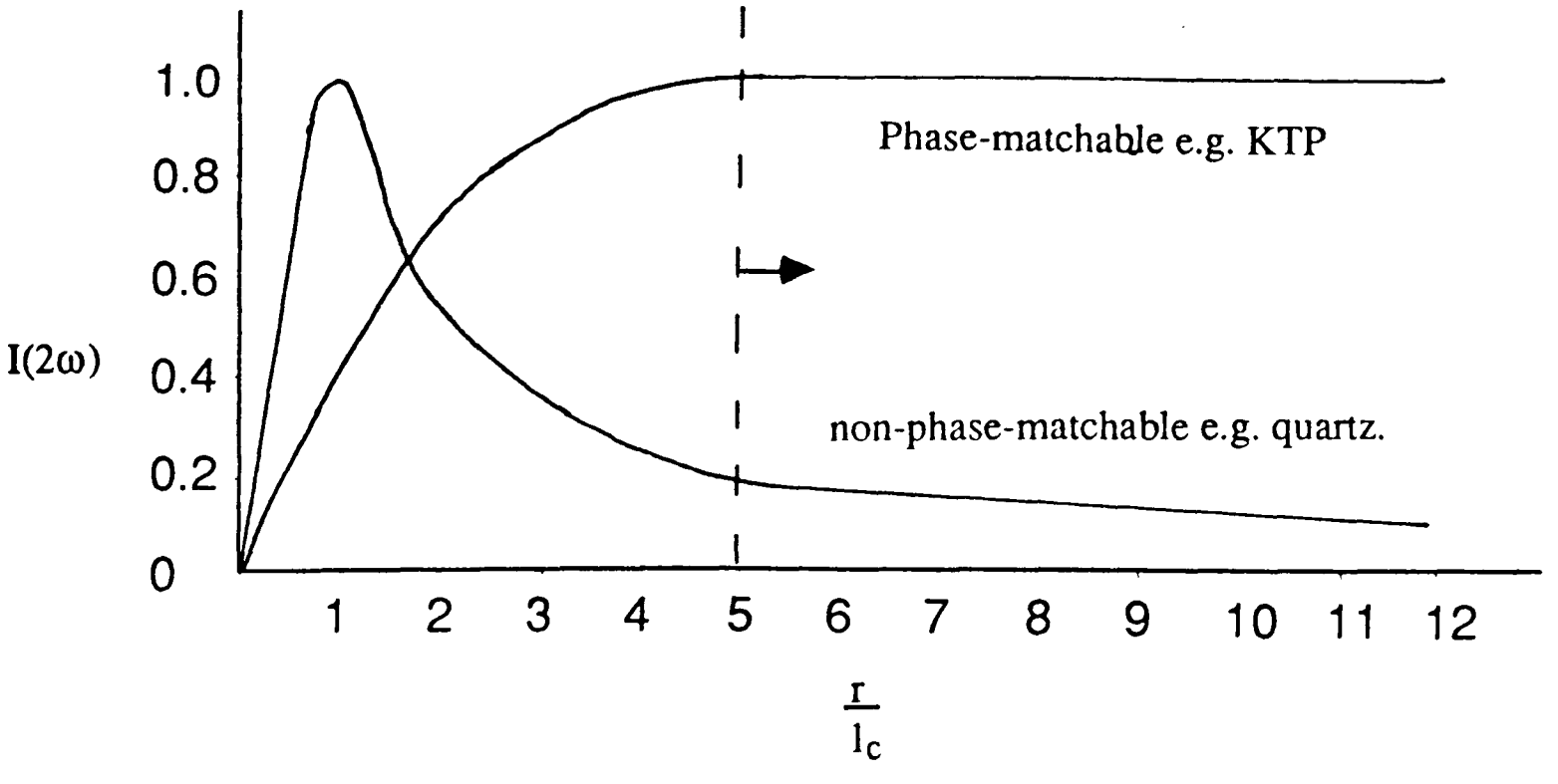
Figure 2.7.I Angular distribution of second harmonic radiation generated in a powder sample



radiation is reduced because the majority of air-crystal interfaces are removed.[149] Under these conditions, the second harmonic radiation is produced in a narrow cone in the forward direction, making an accurate measurement of the total second harmonic intensity possible.

The second harmonic intensity is proportional to the thickness of the sample, i.e. directly proportional to the number of particles present. The dependence of $I(2\omega)$ on the average particle size, r, is different for phase-matchable and non-phase-matchable materials. If the material is in the latter category the $I(2\omega)$ increases with particle size, reaching a maximum at $r=l_c$; and when $r>l_c$, the second harmonic intensity initially rapidly decreases with the particle size, then falls off more gradually. The second harmonic intensity from phase-matchable materials rises more slowly with particle size, levelling off at $r \sim 5l_c$, after which the intensity is independent of particle size (Fig. 2.7.II).

Figure 2.7.II Graph of the dependence of SHG intensity on powder particle size.



2.7.3 Preparation of KTP derivatives for SHG measurements

Ideally, single crystals of $KTiOPO_4$ (KTP) derivatives would be used to test the intensity of second harmonic radiation produced relative to a standard KTP sample, but crystals of good optical quality are difficult and expensive to produce and this method has only been used for the As-substituted $KTiOAsO_4$ (KTA)[150]. The single crystal measurement in itself is difficult and for a comparison of many materials the powder test is more convenient[57,147,151], since effort is not expended in producing a single crystal of an isomorph with poor SHG ability. However, in order to test the phase-matched second harmonic generated from powders, the particle size must be considerably greater than the coherence length so that the relative second-harmonic does not depend on small differences in particle size.

The most reliable method of forming a particular member of a solid solution isomorphous with KTP is by high temperature solid-state synthesis, but this involves repeated cycles of heating and grinding which results in particle sizes of about 5μm, i.e. less than the coherence length (which usually lies in the 1 to 10μm region). Such powders can only be used to measure the un-phase-matched SHG ability of a material. Phase-matchable powder samples are prepared by the careful grinding of single crystals of high optical quality (which can often be obtained, but in a size too small for single crystal measurements).

2.7.4 Second Harmonic Generation Testing

Each crystalline sample was carefully ground and sieved to collect the fraction between 106μm and 212μm, larger than the coherence length but small enough to allow a powder average orientation within the incident radiation spot size. This fraction was then funnelled into a 1mm quartz cuvette whilst tapping to ensure optimum packing. The cuvettes used were transparent in the near infra-red and visible regions. This was the mounting method used by Kurtz and Perry.[148] More recently it has been proposed that dispersal of powders of organic materials in pressed KCl discs reduces the second harmonic intensity differences between samples caused by the difficulty of achieving a constant packing density.[149] For these organic materials the KCl also acts as an index-matching medium, but for KTP, which has refractive indices of the order of 1.8, there are no readily available transparent media (liquid or solid) that are also resistant to laser damage. The following experiments were therefore performed without the benefit of having the second harmonic intensity channelled into the forward direction.

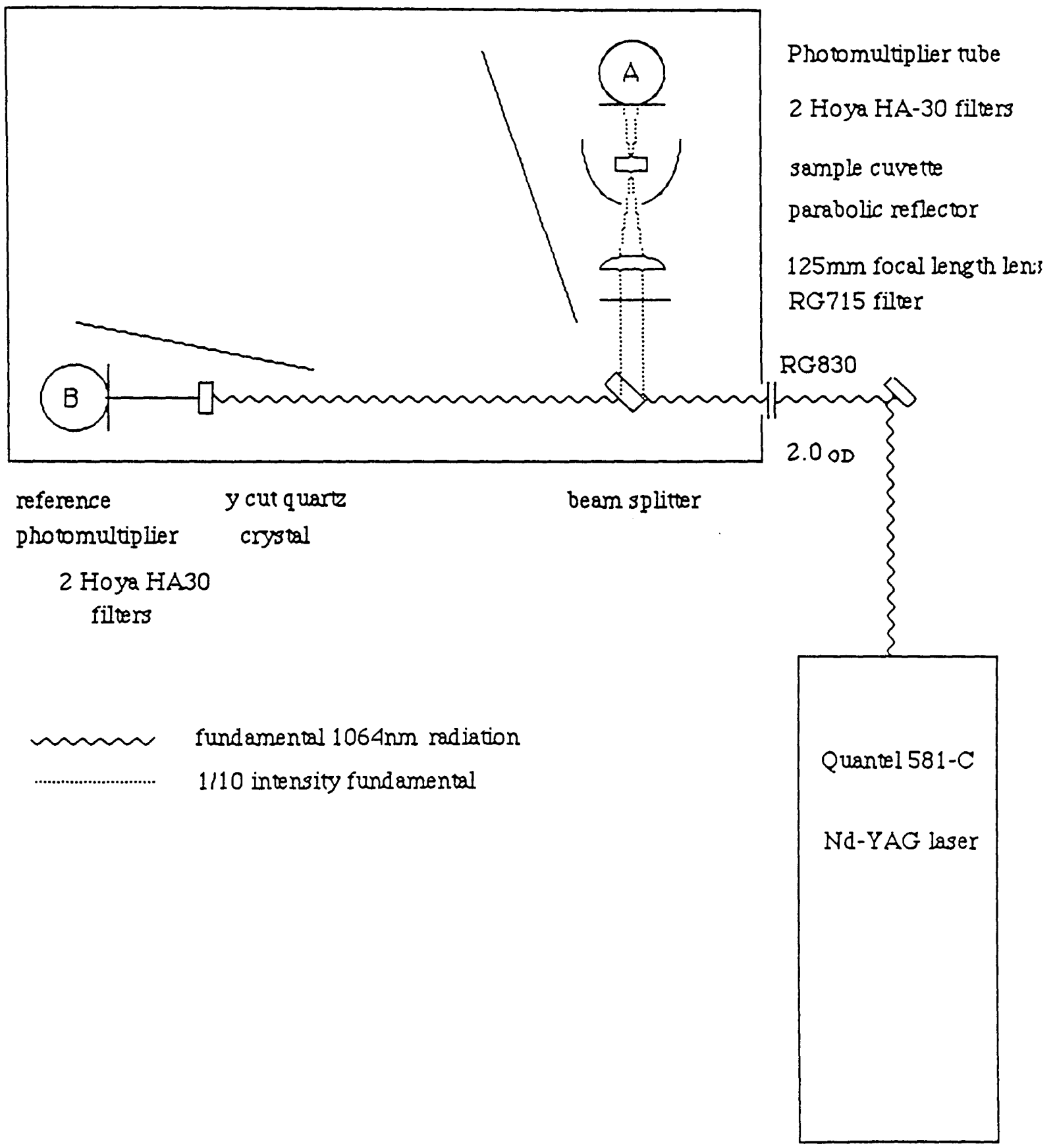
Apparatus for the second harmonic generation experiments

The fundamental ir radiation used was the 1064nm output of a Quantel 581-C Nd:YAG laser. This passed through a long focal length lens to counteract beam divergence before entering the black box constructed around the rest of the apparatus to exclude stray light (Fig. 2.7.III). To remove visible light from the incident beam, a RG830 filter was put in the box

window, together with a neutral density filter to reduce the amount of radiation incident on the photomultiplier tubes. Within the box, the beam was split so that approximately one tenth travelled towards the sample cuvette, with the remaining nine tenths incident on a y-cut quartz crystal reference. To obtain a reproducible reference point, the position of the quartz crystal was adjusted to obtain the maximum signal in the photomultiplier tube B. The components of the radiation incident on the sample cuvette were combined by a 125mm focal length lens, and passed through a parabolic reflector positioned to direct more of the second harmonic intensity emitted in the backwards direction into the photomultiplier tube A. The photomultiplier tubes were insensitive to infra-red radiation, but to avoid the risk of spurious signals due to the sheer intensity of the residual infra-red radiation, each photomultiplier tube was protected by two HOYA HA30 filters. The RG715 filter in the sample path serves to exclude back-reflected 532nm light from the quartz crystal. As a final precaution, black card was strategically placed between the sample and reference regions to avoid the detection of the other's signal.

When several materials were being compared, a single measurement consisted of a reading from cuvettes packed with each of these samples. At least ten such measurements were taken in each experiment. This cyclic measurement method was used to eliminate time-dependent effects on the readings, e.g. the change in reference intensity as the quartz crystal absorbs the infra-red radiation, and its temperature increases, changing the refractive indices.

Figure 2.7.III Schematic diagram of the apparatus used in SHG experiments.



The output from the photomultiplier tubes was collected on a Stanford Research boxcar averager (Model SR250), which could be attached to an oscilloscope, chart recorder or digital meter. The readings quoted are 10A/|B| i.e. ten times the sample reading divided by the reference. All results obtained are relative SHG values; single crystals of good optical quality are required for absolute measurements.

A reference was necessary to normalise the signal with respect to fluctuations of the incident intensity. As the second harmonic intensity depends on the square of the fundamental Nd:YAG intensity, the fundamental radiation could not be used directly as a reference. However using the second harmonic from a quartz crystal provided a square-dependent reference signal of reproducible intensity without electronic manipulation.

CHAPTER THREE

3.1 Introduction

The $KTiOPO_4$ (KTP) structure can be described as a host-guest framework in which the potassium cations sit in the channels of the TiO_6-PO_4 framework. These cations can be replaced, either during synthesis or by ion exchange after KTP synthesis. The ionic conductivity of KTP is significant, allowing rapid ion-exchange in molten salts. It has been shown that the cation diffusion is highly anisotropic, being significantly greater along the [010] direction. This latter property has led to the use of KTP in optical waveguides,[152] as there is very little exchange in the perpendicular directions at the 350° temperature used in waveguide formation.

Many cations have been substituted for K : Rb[79,153], Tl[73] and NH_4 form complete solid solutions with nearly unchanged nonlinear optical properties (showing that the framework has not been greatly affected by the substitution), while Cs and Ag can only be partially accommodated by the KTP framework. Framework substitution can have a marked effect on the cation exchange properties. For instance, substitution of As for P in the XO_4 tetrahedra increases the cavity size, so the maximum Ag occupancy decreases from 85% to 50%, and that of Cs is increased to 100%.[154] Rb, NH_4 and Tl still form complete solid solutions.[155]

The less thermodynamically stable cation-substituted KTP isomorphs (for example those containing Na or Ag) have sharply reduced ability to generate second harmonic radiation, while isomorphs that can be synthesised directly (Rb, Tl, NH_4) have

nonlinear optical properties indistinguishable from KTP. An investigation of the differences between these structures may lead to a greater understanding of the relationship between the structure and nonlinear optical properties.

3.1.1 Previous cation substitution into KTP

The Na-exchanged KTP isomorph (known as β-$NaTiOPO_4$) cannot be formed by direct synthesis, $Na_4TiO(PO_4)_2$, $NaTi_2(PO_4)_3$ and α-$NaTiOPO_4$ are formed preferentially in high temperature synthesis.[156] α-$NaTiOPO_4$ (α-NTP) is centrosymmetric and isomorphous with titanite, $CaTiSiO_5$.[157] The $K_{1-x}Na_xTiOPO_4$ solid solution members can be prepared by solid state synthesis only up to the x=0.65 point, after which the α-NTP and x = 0.65 solid solution member are formed in varying proportion. However β-$NaTiOPO_4$ can be formed by ion exchange of KTP in a large excess of molten $NaNO_3$.[57] The SHG intensity measured from the $K_{1-x}Na_xTiOPO_4$ solid solution members stays at a high level, comparable with that of KTP, until x = 0.65, (the point at which β-NTP becomes the less thermodynamically stable phase), above which the intensity drops off, falling to one tenth that of KTP when x = 1.[64] The asymmetry of the bonds around Ti, thought to be responsible for the large nonlinear optical coefficients, is not significantly changed by Na substitution across the solid solution range, so the decrease in SHG must be caused by a more subtle distortion of the framework. For instance, the close coordination of Na(1) and Na(2) to O(9) decreases the Ti(1)-O(9)-Ti(10) bond angle from 135.5° to 130.8°. The coordination numbers of cations within the β-NTP channels, six and five, are smaller than in KTP, (where the values are eight and nine on the two different sites), an indication that the

framework does not relax to accommodate the smaller cation.

Substitution of Ag for K in KTP takes a similar path to Na exchange, although the maximum substitution possible by solid state methods is only 50%, and even by ion exchange Ag only substitutes up to the $K_{0.15}Ag_{0.85}TiOPO_4$ member under conditions that retain the crystallinity.[57,84] The α-ATP phase formed preferentially at high Ag concentrations is again isomorphous with titanite. The coordination around the Ti atom is little altered from that in KTP, but the coordination numbers of the Ag^+ ions are only five and four, with short Ag-O bond lengths. The shortest Ag-O bond is to O(9), which decreases the Ti(1)-O(9)-Ti(2) bond angle to 129.5°, and the SHG intensity drops still further to only five times that of quartz.

The NH_4-substituted species has very similar TiO_6 coordination and comparable SHG properties to KTP itself. However, the large nonlinear coefficients can be markedly reduced by the gas phase desorption of NH_3, which takes place with retention of crystallinity under 10^{-5} mmHg vacuum at 223°C[158] In the formation of $(NH_4H)(TiOPO_4)_2$, the NH_3 is lost selectively only from the smaller $NH_4(1)$ site. The Ti-O(9) bond lengths in this isomorph become almost equal, removing the bond length asymmetry of alternate octahedra in the TiO_6 chain and giving the O(9) atom a bond valence sum of only 1.07. This suggests that the H^+ is bonded to O(9) and protonation of every other link in the helix is responsible for the reduction in SHG to six times that of quartz. It would also explain the reduction in the Ti(1)-O(9)-Ti(2) bond angle to 127.4°, which is even smaller than that seen in β-ATP.

This previous work indicates that the TiO_6-PO_4 framework is fairly rigid, since changing the nature of the guest cation does

not cause the channels to change substantially in size. However, the cations do have a second-order effect on the structure, as the second harmonic intensity decreases with complete substitution of Na or Ag. This is not accounted for in the theories of Levine[76,77] and Chen[93], which assume that only anionic groups are responsible for the large nonlinear coefficients of materials such as KTP, whereas in the β-ATP and β-NTP species the asymmetry of the Ti-O bonding within the TiO_6 groups is unchanged. The smaller cations coordinate strongly to the O(9) atom, (this is seen in the structure as a reduction in the asymmetry of the Ti-O-Ti bonds connecting octahedra), reducing the Ti-O microscopic susceptibility and therefore the second harmonic output. The smaller SHG signal emitted by β-ATP relative to β-NTP is explained by the high electronegativity of Ag which makes the Ag-O(9) bond more covalent.[84]

Structural analysis of intermediate members of these solid solutions would provide additional information on the correlation between structure and properties. Since the two K sites in KTP are different, as shown by the different cation coordination numbers, the possibility exists of preferential replacement of K on one of the sites. The site on which potassium is exchanged would depend on the relative sizes of the cations. This chapter reports the synthesis and characterization of cation-substituted KTP isomorphs.

3.2 Synthesis and characterisation of cation-substituted $KTiOPO_4$ isomorphs

3.2.1 Synthesis

The three alkali-metal cation substituted KTP isomorphs $K_{0.5}Na_{0.5}TiOPO_4$, $Na_{0.5}Rb_{0.5}TiOPO_4$ and $K_{0.5}Rb_{0.5}TiOPO_4$ were prepared by high temperature solid state synthesis according to the equations:

$$KH_2PO_4 + NaH_2PO_4 + 2TiO_2 \rightarrow 2K_{0.5}Na_{0.5}TiOPO_4 \quad (KNTP) + 2H_2O$$

$$Na_4P_2O_7.10H_2O + 2Rb_2CO_3 + 8TiO_2 + 6NH_4H_2PO_4 \rightarrow 8Na_{0.5}Rb_{0.5}TiOPO_4 \ (NRTP) + 6NH_3 + 2CO_2 + 19H_2O$$

$$Rb_2CO_3 + 2KH_2PO_4 + 4TiO_2 + 2NH_4H_2PO_4 \rightarrow 4K_{0.5}Rb_{0.5}TiOPO_4 \ (KRTP) + CO_2 + 2NH_3 + 5H_2O.$$

The starting materials were ground and heated at a final temperature of 950°C.

3.2.2 Characterisation

Preliminary X-ray powder patterns indicated that the samples were crystalline and that the KNTP phase occurred with TiO_2 (rutile) as an impurity phase. To determine the cation ratio in the compounds, samples were subjected to analytical electron microscopy.

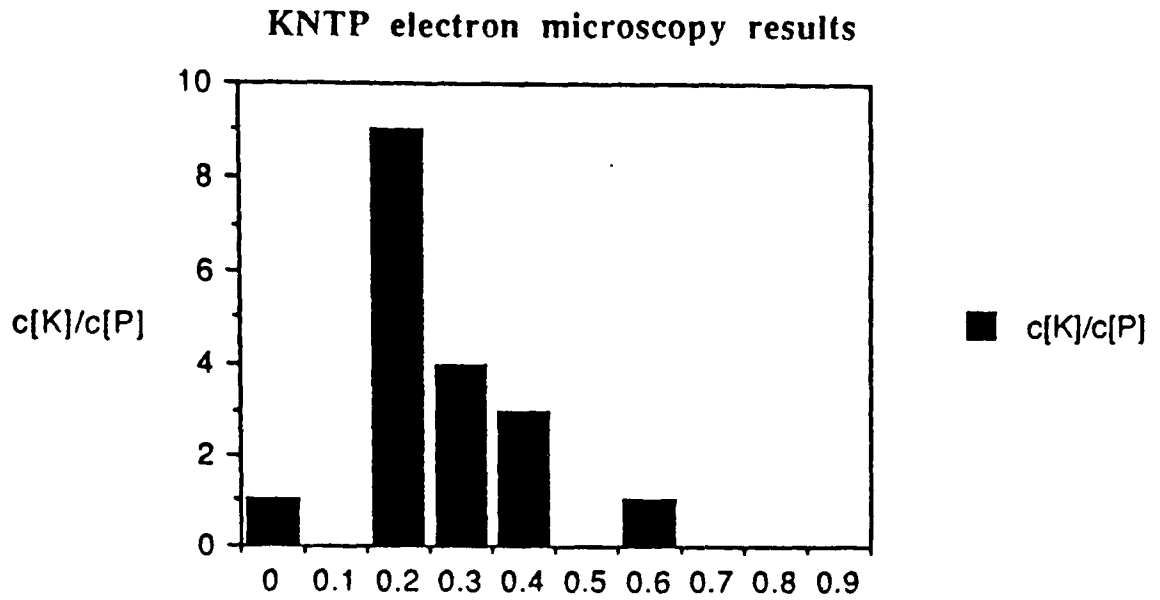
During the analysis of the KNTP sample it became clear that both Na and K were "boiling off" under the intense electron beam. This was demonstrated by the wide range of results obtained and by the marked reduction in the intensity of the

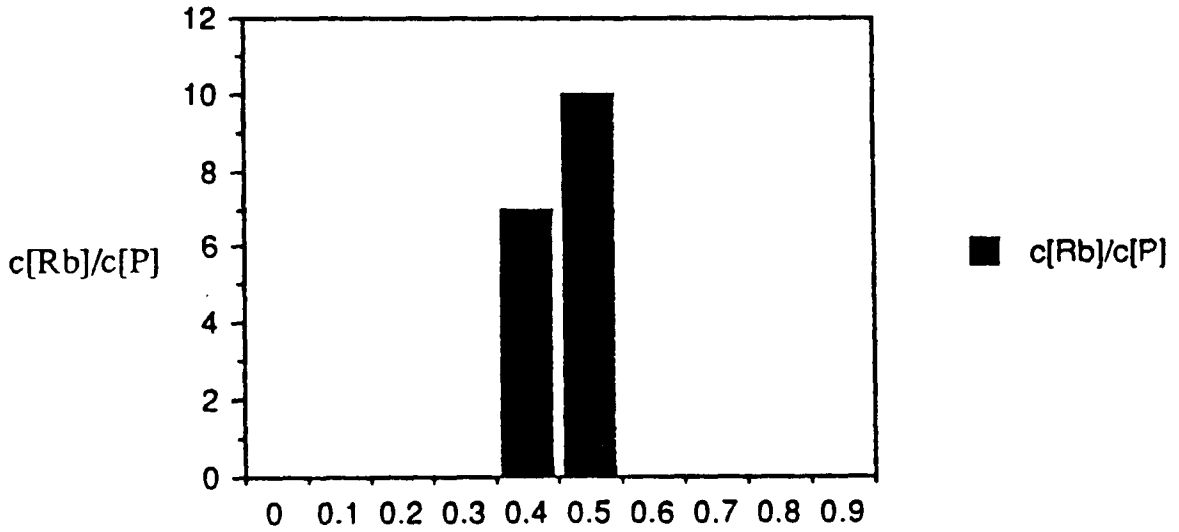
K(Kα) peak relative to the others when a crystallite was analysed twice. Analysis for Na was not attempted because Na(K_α) is at the limit of detection using the Be window detector and the intensities obtained were unreliable. The cation loss may have been facilitated by the channel structure of KTP and probably affected the measurement of the KTP standard used in the analysis. The mean value of the K:P ratio for the 18 crystallites sampled was 0.32(6), and the results are shown in histogram form in Figure 3.2a. X-ray fluorescence measurements carried out by the Amoco Research Center's analytical department indicated that the sample contained 50%K, in line with the starting composition.

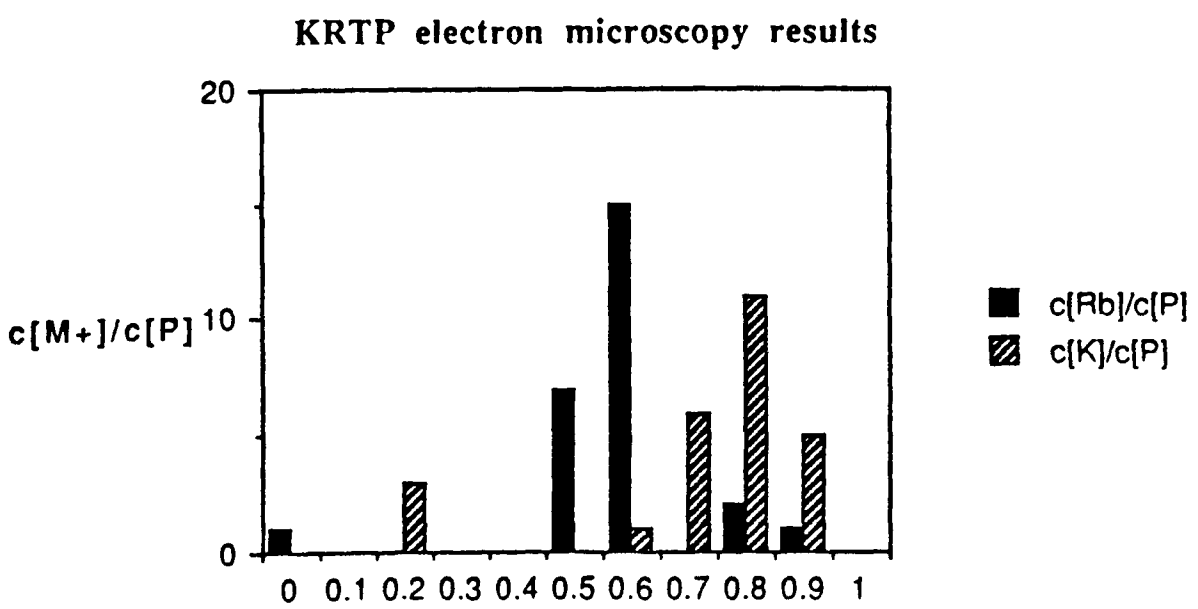
The analysis of NRTP proved more straight-forward, since the Rb cations were much more stable under the electron beam. The mean Rb:P ratio over 17 samples was 0.51(3), in agreement with the target composition, and the results of the analysis are presented in Fig. 3.2b. The presence of the Na(K_α) was only rarely detected.

When both K and Rb were present, as in KRTP, the unreliability of analysis for K in KTP isomorphs was demonstrated. The mean Rb:P ratio over 20 crystallites was 0.54(4), whereas the K:P ratio was 0.68(10), which was inconsistent with both the target composition and the Rb:P ratio. The histograms are shown in Fig. 3.2c. The K:P value is enhanced because the minimum possible spot size was used to avoid loss of potassium. However the K:P standard used to calculate the concentration of K had been measured under more normal conditions where the intensity of the K(K_α) peak would have been reduced.

Figure 3.2 Histograms of analytical electron microscopy results on cation-exchanged KTP isomorphs:a) KNTP, b) NRTP, c) KRTP.







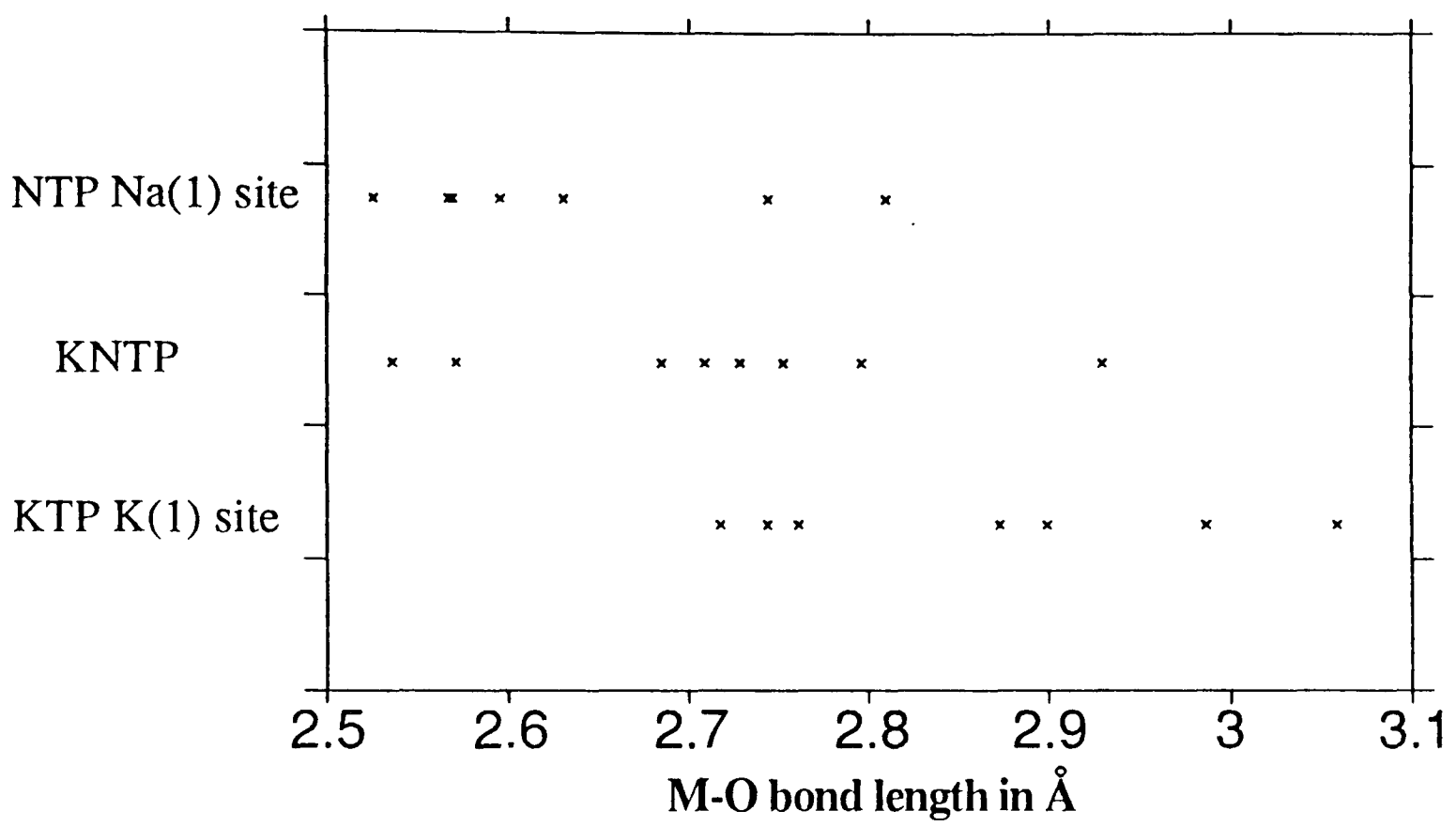
3.3 Determination of the crystal structure of $K_{0.5}Na_{0.5}TiOPO_4$ (KNTP)

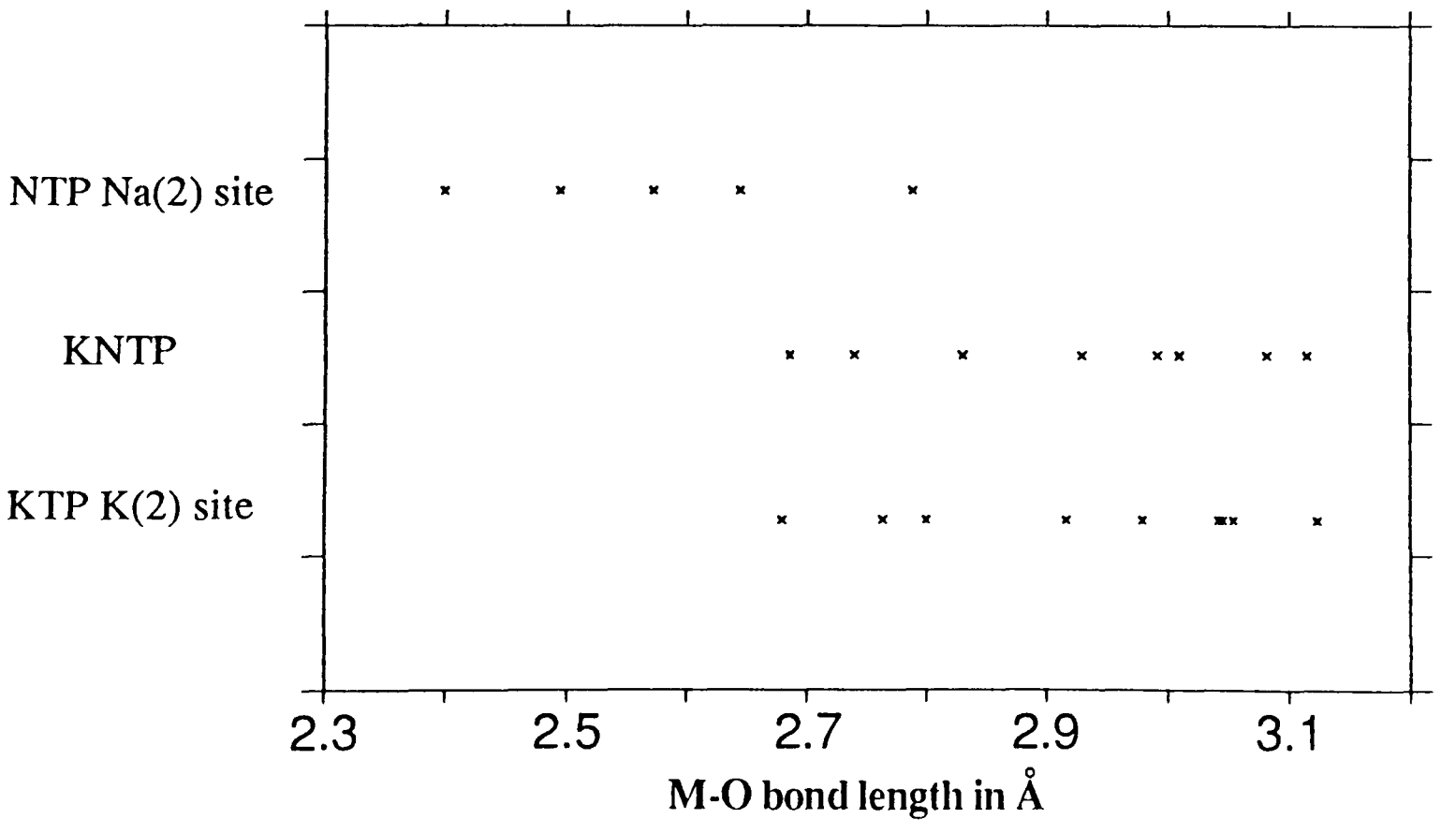
Time-of-Flight neutron powder diffraction data from KNTP were collected at room temperature on the General Purpose Powder Diffractometer (GPPD) at the Intense Pulsed Neutron Source (IPNS), Argonne National Laboratory, run number 3866. Data from both the 90° and 148° banks were used in the analysis.

The starting model was taken from a single crystal structure of KTP[159], and refined using the RIETVELD code developed at Argonne.[160] This gave a reasonable final model, but the neutron scattering factors for Na (0.363×10^{-14}m) and K (0.367×10^{-14}m) are too similar for these elements to be distinguished using neutron diffraction alone. A plot of the cation-oxygen bond distances against those of the solid solution end-members KTP and β-NTP is shown in Fig. 3.3.I. The range of Na-O bonds in β-NTP and K-O bonds in KTP overlap, so the nature of the cation ordering over the two sites cannot be precisely determined from bond lengths alone. However the range of K(2)-O in KNTP matches the bond length range of K(2) in KTP almost exactly, implying that K(2) contains K as the majority cation, while K(1) contains mostly Na.

To investigate this hypothesis, an X-ray data set was collected on the STOE Stadi-P diffractometer in the Clarendon Laboratory. Using GSAS, the model was refined using both the X-ray and neutron diffraction data, the neutron data to provide accurate atomic coordinates (of both light and heavy atoms) and the X-ray data to allow stable refinement of the cation occupancies over the two sites. A crystal structure of TiO_2 (rutile) was taken from the literature[161] and used to model

Figure 3.3.I A Comparison of cation-oxygen bond lengths in KNTP with those in the parent compounds β-NTP and KTP.





the impurity phase in the sample, with its atomic coordinates unrefined.

When the KNTP atomic coordinates were refined, the P-O bond lengths spread over a range 1.51 to 1.58Å, much larger than that seen in KTP itself (1.523(4) to 1.551(4)Å). [74] Uncertainty in the geometry of the PO_4 tetrahedra would make the geometry of the whole framework less accurate, including that of the TiO_6 octahedra, which are thought to be responsible for the large nonlinear coefficients. In order to obtain more precise values of the Ti-O bond lengths and angles without directly restricting the Ti-O bonds themselves, soft constraints were applied to the P-O bonds, restricting them to a value of 1.54(1)Å. The Ti(1) y coordinate was not refined to fix the origin along the y direction.

The thermal parameters of each atom type were constrained to be the same and refined isotropically. Without this constraint the values of the oxygen thermal parameters varied from 0.004(1) to 0.012(2)$Å^2$, while those for the different heavy atoms were the same within the experimental errors. The total occupancy on each site was constrained to be unity.

Even with all these constraints, there were large differences between the observed and calculated X-ray diffraction intensities. Several preferred orientation axes were tried in an attempt to improve the difference map. The axes chosen also had an effect on the occupancy of the Na and K on the cation sites. Incorrect preferred orientation axes were partially compensated for by increasing the occupancy of the major cations. For instance, using the [011] axis increased the K content of the K(2) site from 1.05(7) to 1.24(7). Use of the [042] axis left the cation occupancies at 1.05(7) Na in Na(1) and 1.13(8) K in

K(2), (compared with 1.23(7) and 1.05(7) respectively when no preferred orientation was modelled), and the coefficient, which indicates the effective sample compression along the preferred orientation axis, was significantly different from 1 (0.76(1)). The (042) axis was therefore used in the subsequent refinement.

The X-ray data were excluded between 5 and 15°, as the slope of the background was too steep to be modelled well and only one small peak was predicted in the excluded region. The data collection parameters are given in Table 3.3.1, atomic coordinates in Table 3.3.2 and selected bond distances and angles in Table 3.3.3. The final profile plots are given in Figure 3.3.II.

Table 3.3.1 Data collection and analysis of $K_{0.5}Na_{0.5}TiOPO_4$

Data Collection	Neutron data		X-ray data
Diffractometer	GPPD, Argonne National Lab. 90°	148°	Stoe Stadi-P Cu $K\alpha_1$
Data range	3.84-30.5ms	4-30.5ms	5-85°2θ
Step size			0.02°
No. of reflections	2215	2233	336
Total observations	11586	-	-
Sample shape	10mm vanadium can		flat plate
R_I (%)	2.07	2.22	20.7
R_p (%)	2.64	2.91	11.39
wR_p (%)	3.61	4.75	14.39
$R_{expected}$ (%)	1.79	3.44	18.75
χ^2(combined)	2.132	-	-

Model refinement

phase 1: $K_{0.5}Na_{0.5}TiOPO_4$
space group $Pn2_1a$
unit cell a=12.75613(7), b=10.60426(6), c=6.31869(4)Å
V=854.725(6)Å^3

phase 2: TiO_2 (rutile)
space group $P4_2/mnm$
atomic and cell parameters were taken from the Inorganic Crystal Structure Database and not refined.

Scattering lengths/10^{-14}m K:0.367, Na:0.363, Ti:-0.344, P:0.513, O:0.5805

No. of parameters 99

Function minimised $M=\Sigma[w(Y_o-Y_c)^2]$, $w = 1/Y_o$

neutron model
Background: 8 term cosine fourier series
Peak shape: Gaussian convoluted with double exponential 90° bank σ_1:118(2) σ_2:1.7(3),
148° bank σ_1:45(2) σ_2:-1.9(4)

X-ray model
Background: 3 term cosine fourier series
Peak shape: pseudo-Voight U:0,V:0, W:9.5(9),
X:-0.2(5), Y:4(1), Z:0,
asym: 3.2(2), shift:0.005(12)

Table 3.3.2 Atomic positions and isotropic temperature factors ($Å^2$) for $K_{0.8}Na_{0.8}TiOPO_4$.

	x	y	z	$100U_{iso}$	occupancy
Ti(1)	0.3721(2)	0.0000	0.4911(8)	0.37(6)	
Ti(2)	0.2489(4)	0.2515(7)	0.2699(7)	0.37(6)	
P(1)	0.4959(3)	0.2627(6)	0.3363(2)	0.47(3)	
P(2)	0.1839(1)	0.5123(6)	0.4998(7)	0.47(3)	
Na(1)	0.3528(3)	0.2898(6)	0.7689(7)	3.39(13)	0.96(7)
K(1)	0.3528(3)	0.2898(6)	0.7689(7)	3.41(12)	0.04(7)
Na(2)	0.1030(4)	0.0687(7)	0.6776(8)	3.39(13)	-0.05(8)
K(2)	0.1030(4)	0.0687(7)	0.6776(8)	3.41(12)	1.05(8)
O(1)	0.4810(2)	0.1521(5)	0.4939(5)	0.80(2)	
O(2)	0.5064(3)	0.3870(5)	0.4648(4)	0.80(2)	
O(3)	0.3997(2)	0.2782(6)	0.1898(4)	0.80(2)	
O(4)	0.5941(2)	0.2434(6)	0.1975(5)	0.80(2)	
O(5)	0.1171(3)	0.5377(5)	0.3031(4)	0.80(2)	
O(6)	0.1103(3)	0.4869(6)	0.6866(5)	0.80(2)	
O(7)	0.2556(3)	0.6275(6)	0.5290(6)	0.80(2)	
O(8)	0.2567(3)	0.3972(6)	0.4600(6)	0.80(2)	
O(9)	0.2253(3)	0.6409(6)	-0.0363(6)	0.80(2)	
O(10)	0.2242(3)	0.3855(6)	0.0296(6)	0.80(2)	

Table 3.3.3 Selected bond lengths (Å) and angles (°) in $K_{0.5}Na_{0.5}TiOPO_4$

		KNTP	KTP			KNTP	KTP
Ti(1)	-O(1)	2.129(5)	2.161(4)	Ti(2)	-O(3)	2.010(6)	2.037(3)
	-O(2)	1.979(5)	1.957(4)		-O(4)	1.987(6)	1.979(3)
	-O(5)	2.016(5)	2.047(4)		-O(7)	2.012(6)	1.966(4)
	-O(6)	1.942(6)	1.900(4)		-O(8)	1.959(6)	1.994(4)
	-O(9)	1.951(6)	1.993(4)		-O(9)	1.728(6)	1.738(4)
	-O(10)	1.744(5)	1.718(4)		-O(10)	2.103(6)	2.101(4)
*trans*Δ		0.385	0.443			0.375	0.363
P(1)	-O(1)	1.551(3)	1.523(4)	P(2)	-O(5)	1.531(3)	1.541(4)
	-O(2)	1.554(3)	1.550(4)		-O(6)	1.532(3)	1.533(4)
	-O(3)	1.546(3)	1.549(4)		-O(7)	1.538(3)	1.551(4)
	-O(4)	1.543(3)	1.547(4)		-O(8)	1.553(3)	1.543(4)
K(1)	-O(1)	2.798(5)	2.900(4)	K(2)	-O(1)	2.741(6)	2.679(4)
	-O(2)	2.932(6)	2.743(4)		-O(2)	2.991(5)	2.979(4)
	-O(3)	2.729(5)	2.717(4)		-O(3)	3.081(6)	3.046(4)
	-O(5)	2.710(5)	2.874(4)		-O(4)	3.011(5)	3.125(4)
	-O(7)	2.752(5)	3.059(4)		-O(5)	2.830(6)	2.799(4)
	-O(8)	2.571(5)	2.762(4)		-O(7)	2.928(6)	2.917(4)
	-O(9)	2.684(6)	2.987(4)		-O(8)	3.114(6)	3.044(4)
	-O(10)	2.536(6)	2.717(4)		-O(9)	2.685(7)	2.765(4)
					-O(10)	3.083(6)	3.055(4)
mean		2.71(12)	2.84(12)			2.94(15)	2.93(14)

	β-NTP	KNTP	KTP
Ti(1)-O(9)-Ti(2)	129.5(6)	134.8(3)	135.5
Ti(1)-O(10)-Ti(2)	133.8(6)	132.6(3)	132.9

Figure 3.3.IIa Observed (dots), calculated (continuous curve) and difference plots of the GPPD 148th data for $K_{0.6}Na_{0.6}TiOPO_4$.

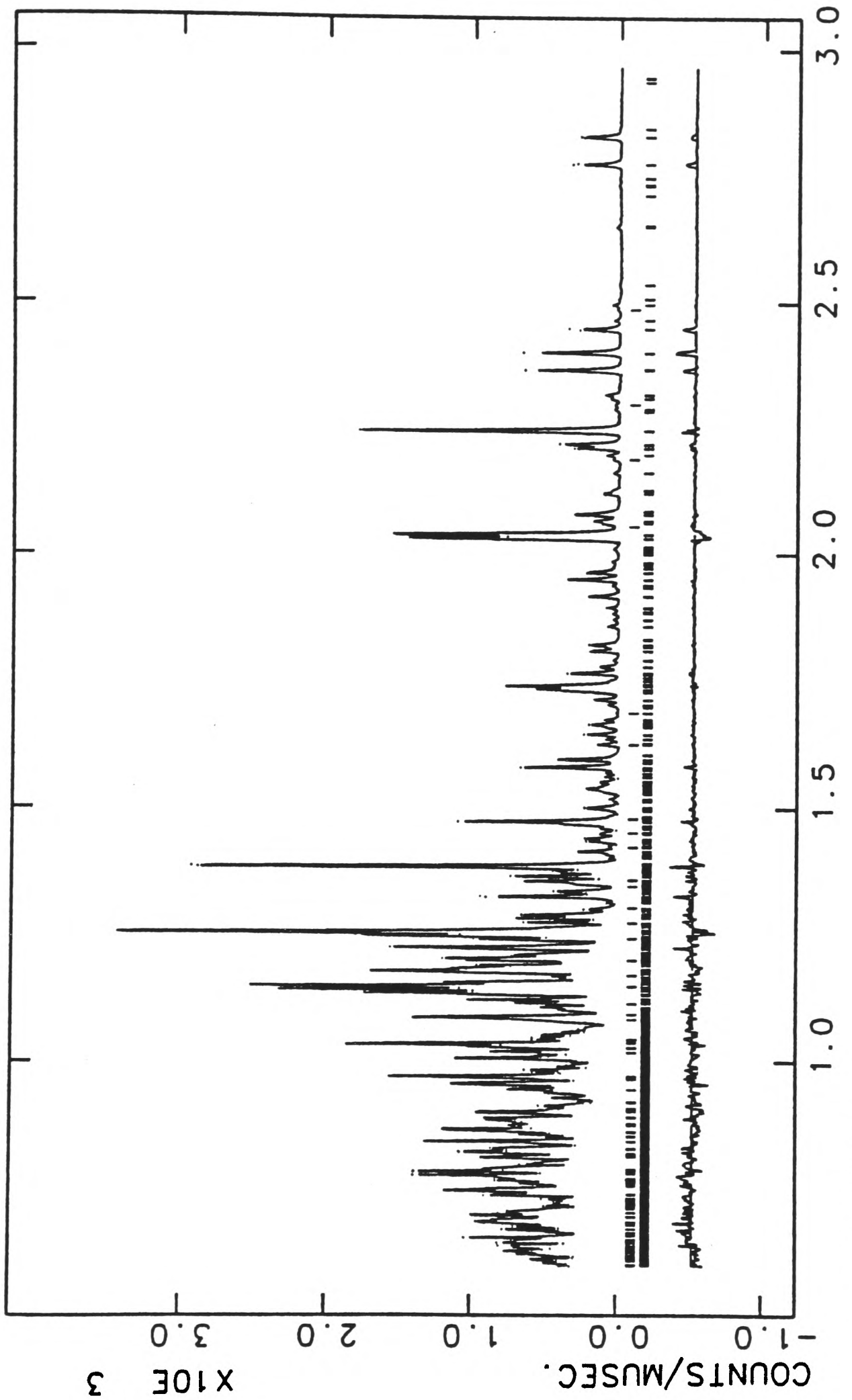


Figure 3.3.IIb Observed (dots), calculated (continuous curve) and difference plots of the GPPD 90° data for $K_{0.5}Na_{0.5}TiOPO_4$.

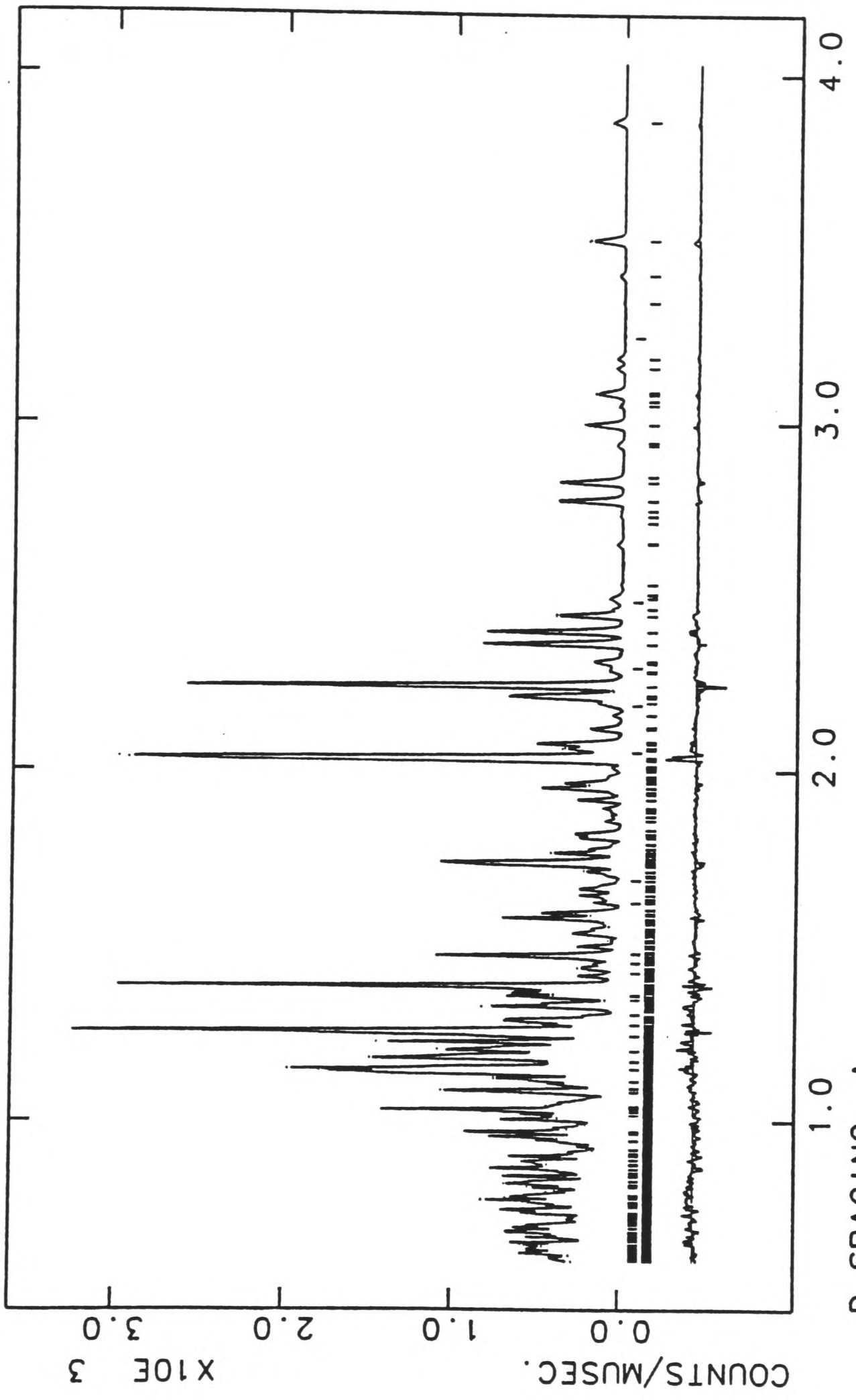
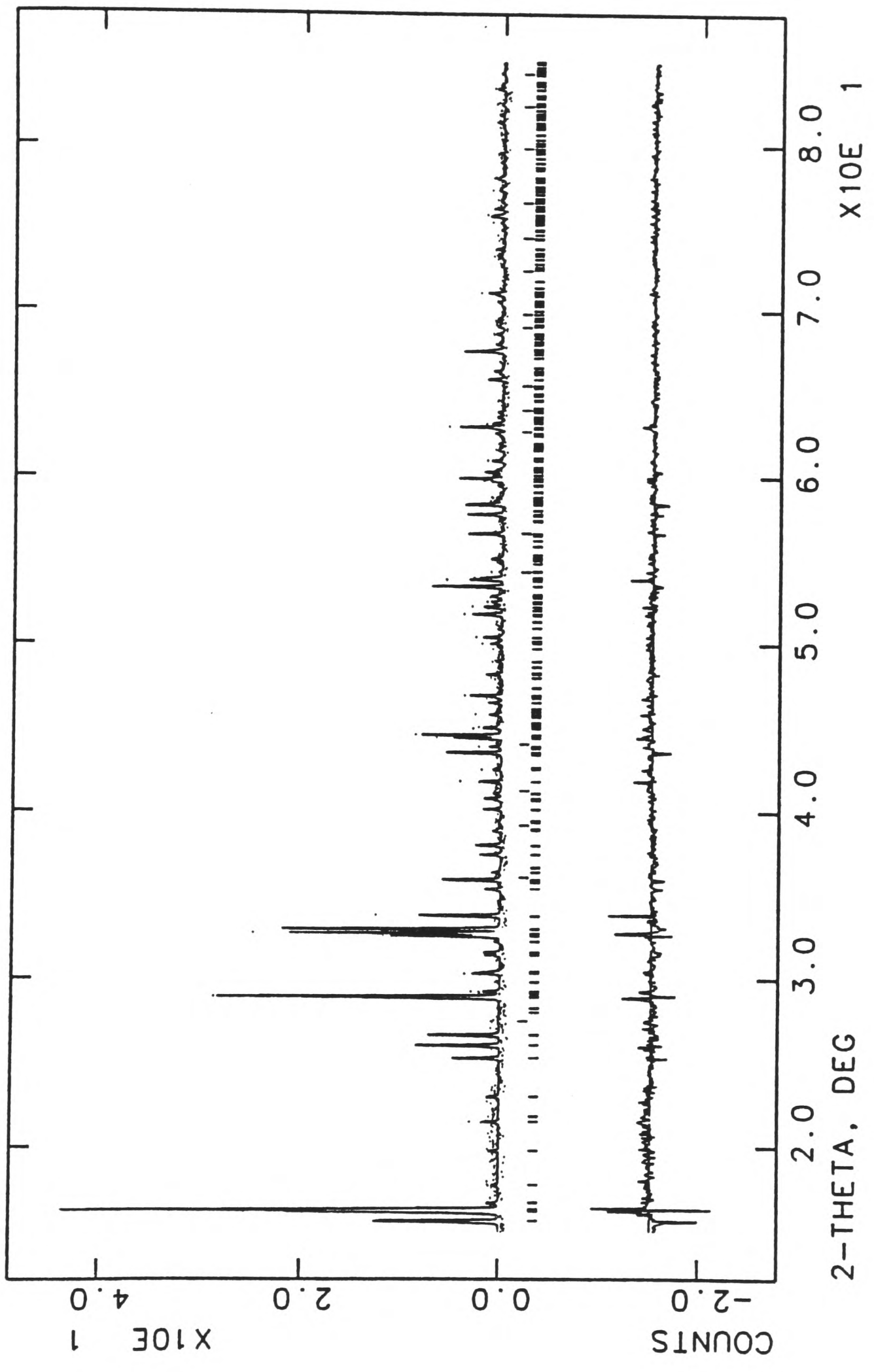


Figure 3.3.IIc Observed (dots), calculated (continuous curve) and difference plots of the X-ray data for $K_{0.5}Na_{0.5}TiOPO_4$.



Discussion

The KNTP structure has been shown to be isomorphous with the solid solution end members KTP and β-NTP, through a combined analysis of X-ray and neutron diffraction data. There is complete ordering over the two cation sites, sodium substituting preferentially into the smaller K(1) site. This ordering is reflected in the bond lengths, those around the K(1) site in KNTP being shorter than the corresponding bonds in KTP, while the average K(2) bond in KNTP is very similar to that in KTP.

When the cation distribution was fixed so that there were equal amounts of sodium and potassium on each site, the R_p of the X-ray data only increased from 11.39 to 11.83%, indicating that the X-ray data are not very sensitive to the cation ordering. The total occupancies obtained, K = 0.55(8) and Na = 0.45(8) are in good agreement with the synthetic target composition of $K_{0.5}Na_{0.5}TiOPO_4$.

^{31}P magic angle spinning n.m.r spectra of β-NTP, KNTP and KTP, and ^{23}Na m.a.s.n.m.r. spectra of β-NTP and KNTP were collected by Jon Owen (Figure 3.5.III).[162] The ^{31}P spectra all show only two distinct resonances, implying that the cations are fully ordered, and the ^{31}P shift is also sensitive to the cation composition. The ^{23}Na quadrupolar lineshape in KNTP could be simulated using a single Na site, implying that only one of the two sites contains Na. This is in contrast to the broad featureless peak, caused by the superposition of the lines from the two crystallographically distinct Na sites, which is obtained in the spectrum of β-NTP. These results provide further confirmation of the site occupancies obtained from structural refinement.

Bond valence calculations[136] corroborate the cation

ordering found in the diffraction experiment (Table 3.3.4), the highest sodium valence being on site 1 and the lowest potassium valence on site 2. Both the K(1) and K(2) sites are too large for Na, even in the β-NTP solid solution end member, showing that the framework is rigid and cannot distort sufficiently to accommodate smaller cations. The valence of K(1) increases from KTP to KNTP indicating that the cavity may have slightly decreased in size. In KNTP the atoms are fully ordered so the scattering will be dominated by the major cation at each site. As the cations are constrained to be on the same site, the minor cation may be represented at a position at which it would not actually be found, giving non-ideal valence parameters.

Table 3.3.4 Bond valence parameters for KNTP and the solid solution end members KTP and β-NTP.

	K(1)	Na(1)	K(2)	Na(2)
β-NTP		0.76		0.65
KNTP	1.42	0.77	1.13	0.69
KTP	1.23		1.12	

The final bond lengths obtained in the PO_4 tetrahedra cover a similar range to those in KTP, indicating that the restraints were working, and that the bonds were not constrained too rigidly. The Ti-O bonds are relatively unaffected by cation substitution; the asymmetry of the octahedra as measured by Δ, (the difference between the longest and shortest Ti-O bonds), does not decrease in a systematic fashion across the solid solution. The drop in SHG output seen by Phillips et al.[ce4] must be caused by a more subtle effect of the cation change on the TiO_6 octahedra.

3.4 Determination of the crystal structure of $Na_{0.5}Rb_{0.5}TiOPO_4$ (NRTP)

Constant wavelength neutron powder diffraction data were collected on D2B in the Institut Laue Langevin, Grenoble by Joanne Warner and David Perkins. The data were analysed using the program GSAS. The neutron scattering lengths of sodium and rubidium are sufficiently different, (0.363×10^{-14}m, 0.708×10^{-14}m respectively), that a joint neutron and X-ray diffraction data analysis was not required to elucidate the cation ordering over the two sites. The P-O distances were restrained to be within 1.54(1)Å and the Ti(1) y parameter was not refined to fix the floating origin. The thermal parameters for each atom type, and for all the cations, were constrained to be the same. The total occupancy of each cation site was fixed at unity. The data collection parameters are given in Table 3.4.1, the atomic coordinates in Table 3.4.2 and selected bond distances and angles in Table 3.4.3. The final profile plot is given in Figure 3.4.I.

Table 3.4.1 Data collection and analysis of $Na_{0.5}Rb_{0.5}TiOPO_4$

Neutron Data collection

Diffractometer	D2B, I.L.L., Grenoble
Data range	2θ = 14-160°
Step size	0.02°
Wavelength	1.59434Å
No. of reflections	904
Total observations	2927
Sample can	10mm vanadium
R_I(%)	3.93
R_p(%)	5.15
wR_p(%)	7.16
$R_{expected}$(%)	3.13
χ^2	5.365

Model refinement

Space group	$Pn2_1a$
Unit cell	a=12.8272(6), b=10.6050(5), c=6.3347(3)Å
	V=861.8(1)Å^3
Scattering lengths/10^{-14}m	Rb:0.708, Na:0.363, Ti -0.344,
	P:0.513, O:0.5805
No. of parameters	66
Background	3 term Fourier series
Peak shape	Gaussian U:93(4), V:-190(10), W:276(5),
	asymmetry:14.2(4), shift: -26(2)

Table 3.4.2 Atomic coordinates and isotropic temperature factors ($Å^2$) for $Na_{0.5}Rb_{0.5}TiOPO_4$.

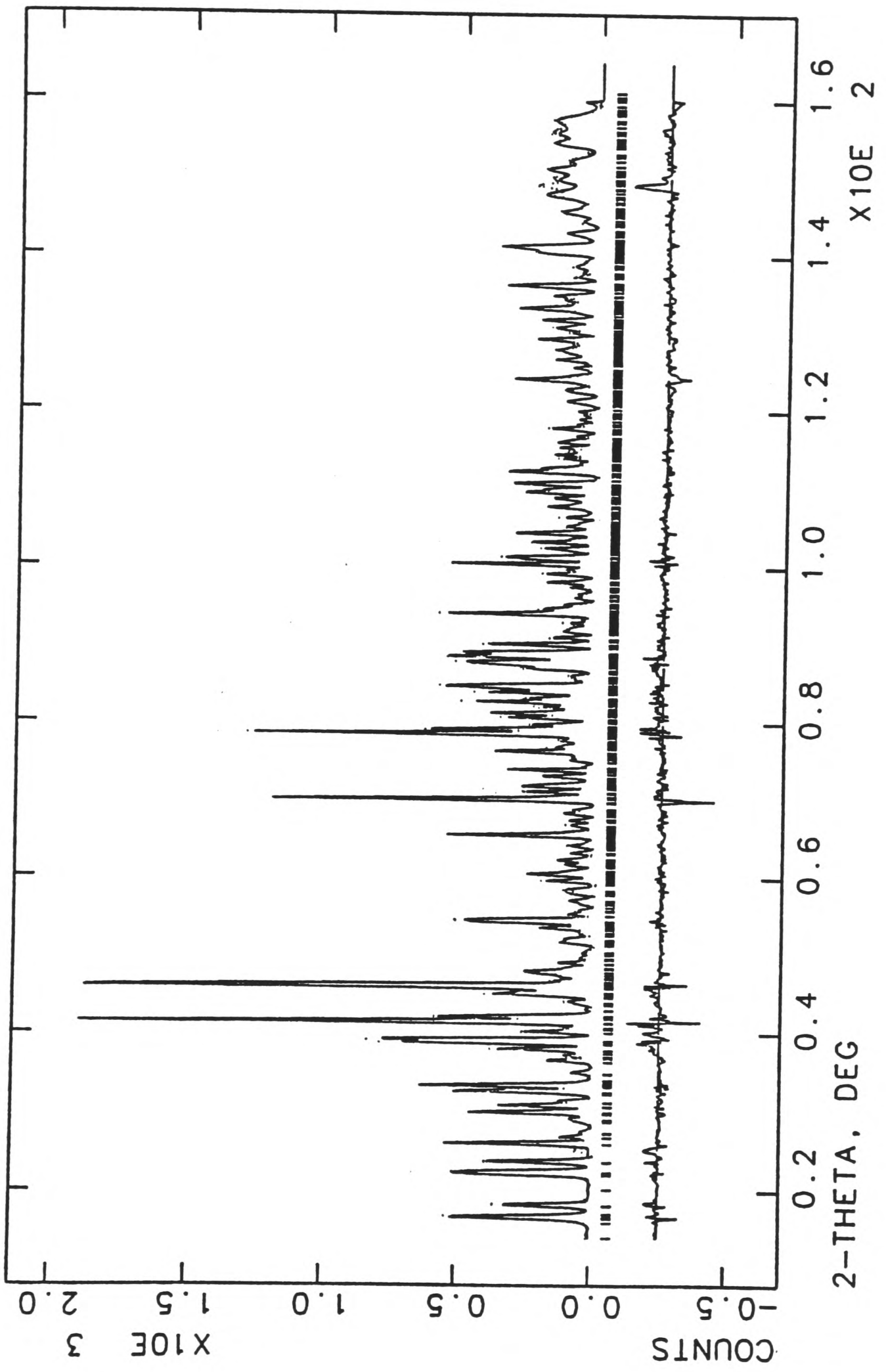
	x	y	z	$100U_{iso}$	occupancy
Ti(1)	0.3729(6)	0.000	0.4700(14)	0.55(12)	
Ti(2)	0.2508(10)	0.2645(16)	0.2467(14)	0.55(12)	
P(1)	0.4972(4)	0.2680(9)	0.3357(5)	0.28(6)	
P(2)	0.1855(3)	0.5194(9)	0.4858(8)	0.28(6)	
Na(1)	0.3511(9)	0.2972(12)	0.744(2)	2.9(2)	0.97(3)
Rb(1)	0.3511(9)	0.2972(12)	0.744(2)	2.9(2)	0.03(3)
Na(2)	0.0983(5)	0.0744(10)	0.6618(10)	2.9(2)	0.04(3)
Rb(2)	0.0983(5)	0.0744(10)	0.6618(10)	2.9(2)	0.96(3)
O(1)	0.4859(5)	0.1494(10)	0.4755(10)	0.88(3)	
O(2)	0.5116(6)	0.3831(9)	0.4842(10)	0.88(3)	
O(3)	0.4041(5)	0.2896(11)	0.1859(8)	0.88(3)	
O(4)	0.5975(5)	0.2541(10)	0.2027(8)	0.88(3)	
O(5)	0.1214(5)	0.5451(9)	0.2861(7)	0.88(3)	
O(6)	0.1093(5)	0.4936(10)	0.6698(8)	0.88(3)	
O(7)	0.2517(4)	0.6393(9)	0.5175(9)	0.88(3)	
O(8)	0.2599(5)	0.4084(9)	0.4437(9)	0.88(3)	
O(9)	0.2191(5)	0.6528(10)	-0.0485(10)	0.88(3)	
O(10)	0.2280(6)	0.3960(90	0.0142(9)	0.88(3)	

Table 3.4.3 Selected bond distances (Å) and angles (°) in $Na_{0.5}Rb_{0.5}TiOPO_4$

		NRTP	KTP			NRTP	KTP
Ti(1)	-O(1)	2.14(1)	2.161(4)	Ti(2)	-O(3)	2.02(1)	2.037(3)
	-O(2)	1.95(1)	1.957(4)		-O(4)	2.00(1)	1.979(3)
	-O(5)	2.06(1)	2.047(4)		-O(7)	1.97(1)	1.966(4)
	-O(6)	1.92(1)	1.900(4)		-O(8)	1.97(1)	1.994(4)
	-O(9)	2.00(1)	1.993(4)		-O(9)	1.80(1)	1.738(4)
	-O(10)	1.72(1)	1.718(4)		-O(10)	2.05(1)	2.101(4)
Δ		0.28	0.275			0.25	0.363
P(1)	-O(1)	1.545(3)	1.523(4)	P(2)	-O(5)	1.533(3)	1.541(4)
	-O(2)	1.552(3)	1.550(4)		-O(6)	1.546(3)	1.533(4)
	-O(3)	1.542(3)	1.549(4)		-O(7)	1.542(4)	1.551(4)
	-O(4)	1.546(3)	1.547(4)		-O(8)	1.539(4)	1.543(4)
K(1)	-O(1)	2.89(1)	2.900(4)	K(2)	-O(1)	2.826(9)	2.679(4)
	-O(2)	2.79(1)	2.743(4)		-O(2)	3.205(9)	2.979(4)
	-O(3)	2.88(1)	2.717(4)		-O(3)	3.024(9)	3.046(4)
	-O(5)	2.71(1)	2.874(4)		-O(4)	2.993(8)	3.125(4)
	-O(7)	2.75(1)	3.059(4)		-O(5)	2.854(8)	2.799(4)
	-O(8)	2.53(1)	2.762(4)		-O(7)	3.042(9)	2.917(4)
	-O(9)	2.57(1)	2.987(4)		-O(8)	3.098(9)	3.044(4)
	-O(10)	2.55(1)	2.717(4)		-O(9)	2.818(8)	2.765(4)
					-O(10)	3.069(9)	3.055(4)
mean		2.71(14)	2.84(12)			3.00(13)	2.93(14)

	NRTP	KTP	β-NTP	RTP[1892]
Ti(1)-O(9)-Ti(2)	134.5(6)	135.5	129.5(6)	137.1(4)
Ti(1)-O(10)-Ti(2)	131.3(6)	132.9	133.8(6)	134.4(4)

Figure 3.4.I Observed(dots) and calculated (smooth curve) neutron diffraction pattern of NRTP. Difference curves on the same scale and reflection markers are also shown.



Discussion

Due to the smaller number of observed data available, the final model parameters are less well determined than those in the refinement of KNTP. In a test refinement cycle, the thermal parameters for the two cation types were allowed to refine separately. The cation occupancies and thermal parameters obtained were:

	Occupancy	U_{iso}
Na(1)	0.85(4)	0.06(1)
Rb(1)	0.15(4)	0.024(2)
Na(2)	0.11(3)	0.06(1)
Rb(2)	0.89(3)	0.024(2)

with only a minor decrease in wR_p from 7.16 to 7.10%. The Na thermal parameter has increased to a value that is too large, which is accompanied by a reduction in the cation ordering, implying that there is not enough information to determine the cation occupancies simultaneously with thermal parameters.

The cations in NRTP are approximately fully ordered over the two cation sites, Rb occupying the larger 9-coordinate site. This ordering is reflected in the bond lengths (Figure 3.4.II), the bonds around the K(2) site being too long to accommodate Na, and those around K(1) being too short for Rb. A bond valence calculation[136] carried out for NRTP gave bond valence parameters comparable to the respective solid state end-members for Na(1) and Rb(2), the cations which are proposed to be occupying those sites (Table 3.4.4). The values for Rb on the K(1) site and Na on the K(2) site are much less favourable and confirm that the cation would be unlikely to occupy those sites. A refinement where the cation occupancies were constrained to values of 0.5 increased the wR_p to 7.92%, reinforcing this conclusion.

Figure 3.4.II Comparison of cation-oxygen bond lengths in NRTP with those in the parent compounds β-NTP and RTP.

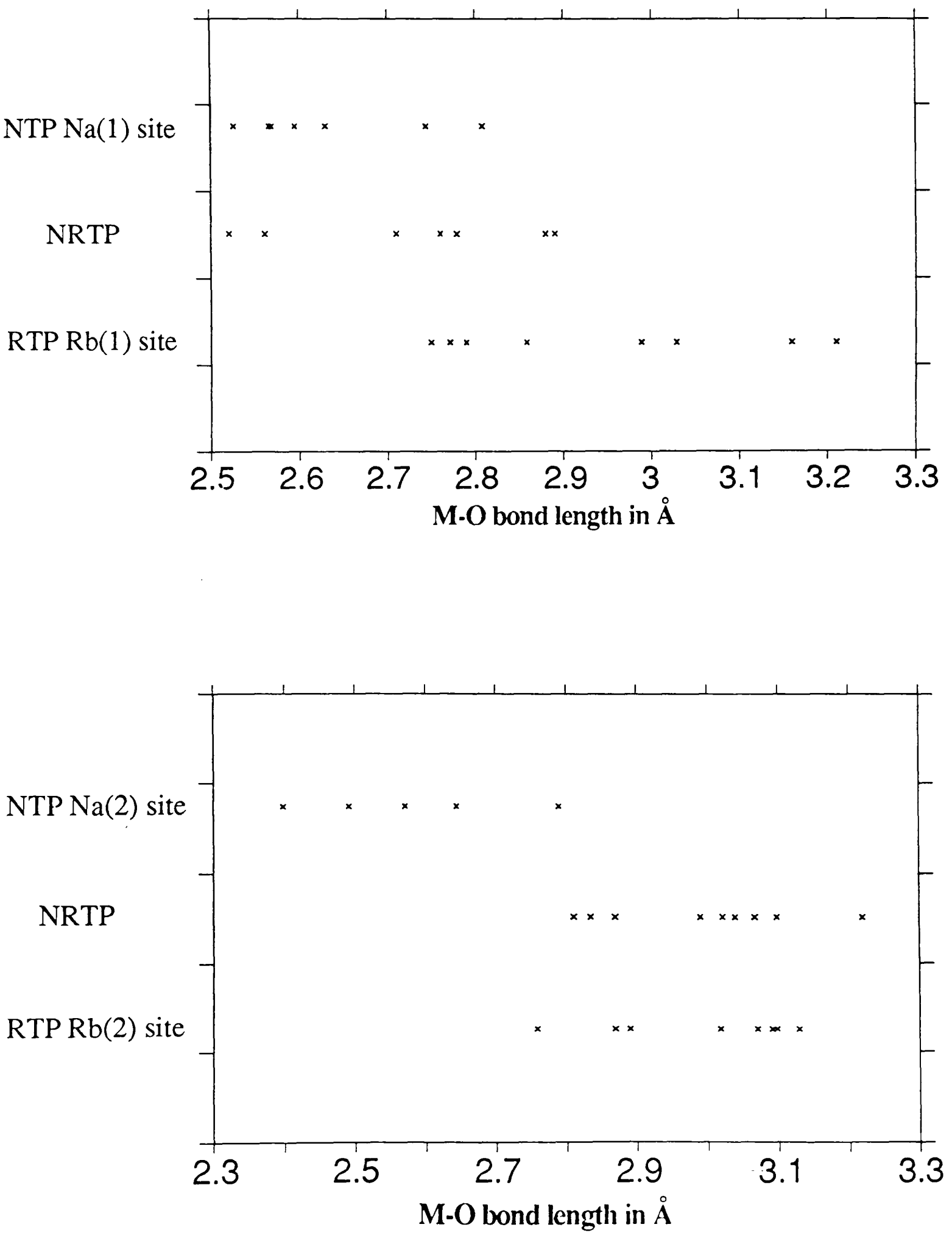


Table 3.4.4 Bond Valence parameters calculated for NRTP and the parent compounds β-NTP and RTP.

	Na(1)	Rb(1)	Na(2)	Rb(2)
β-NTP		0.76		0.65
NRTP	0.74	2.76	0.39	1.36
RTP		1.46		1.39

^{31}P and ^{23}Na m.a.s.n.m.r spectra collected from β-NTP, NRTP and RTP again confirmed the ordering seen in the powder diffraction work through similar features to those in the $K_{1-x}Na_xTiOPO_4$ series (Figure 3.5.III).[162]

The second harmonic generating ability of RTP is similar to KTP, so an analogy might be made between the $K_{1-x}Na_xTiOPO_4$ and $Na_xRb_{1-x}TiOPO_4$ solid solutions where Na substitutes into KTP and RTP. The distortion around Ti(2) measured by Δ seems to decrease on substitution of both Na and Rb into KTP, a phenomenon not seen in KNTP, and on this basis the SHG of NRTP would be expected to be less than that in KNTP. The Ti(1)-O(10)-Ti(2) bond angle decreases on substitution of Na into Rb, but this is not very significant in terms of the solid solution system as a whole because the decrease is not continued in β-NTP. However the magnitude of the Ti(1)-O(9)-Ti(2) angle is similar to that in KNTP and decreases further in β-NTP. This is another indicator of the distortion in the compound, but it provides contradictory information about the possible value of the nonlinear properties of this species relative to KNTP. Therefore the value of the second harmonic intensity produced by intermediate species cannot be readily predicted.

3.5 Determination of the crystal structure of $K_{0.5}Rb_{0.5}TiOPO_4$ (KRTP)

Time-of-flight neutron diffraction data were collected from a sample of KRTP on GPPD at IPNS, Argonne National Lab, run number 4742. Data from the 60°, 90° and 148° detector banks were used in the analysis. The data collection and refinement parameters are given in Table 3.5.1.

The KNTP structure obtained from the joint X-ray and neutron powder diffraction data was used as the starting model for the analysis of the KRTP data. However, as in the NRTP case, the neutron scattering lengths of K (0.367×10^{-14}m) and Rb (0.708×10^{-14}m) are sufficiently different that a joint analysis with X-ray data was not required to elucidate the cation ordering. The P-O bond lengths were restrained to be within 1.54±.01Å and the Ti(1) y coordinate was not refined to fix the floating origin along the y direction in $Pn2_1a$. The temperature factors were constrained to a single value for each atom type, and to a single value for both K and Rb cations. When individual cation thermal parameters were refined, those of K increased to 0.124(9) while those of Rb decreased to 0.008(1) and the ordering of the cations almost disappeared. Subsequently the temperature factors were constrained to a single parameter as these values were too extreme to allow the occupancy to refine to a sensible value.

The peak at d = 2.29Å and other smaller peaks in the diffraction patterns (final plots are given in Figure 3.5.I), revealed the presence of an impurity phase. A search of the Powder Diffraction File did not produce any suitable phases of

known structure, so the impurity was not modelled, and this is probably the cause of the majority of the peaks found in the final difference plots and the relatively large R-factors. The final atomic coordinates and thermal parameters are given in Table 3.5.2 and selected bond lengths and angles in Table 3.5.3.

Table 3.5.1 Data collection and analysis of $K_{0.5}Rb_{0.5}TiOPO_4$

Neutron Data collection

Diffractometer	GPPD, IPNS, Argonne National Lab., Il.		
Data Bank	148°	90°	60°
Data range(ms)	5.04-30.995	4.45-30.992	4.94-30.99
No. of reflections	4382	2543	682
Total observations	11109	-	-
Sample can	10mm vanadium		
R_I (%)	2.46	3.24	4.03
R_p (%)	3.16	3.51	4.70
wR_p (%)	5.24	5.44	6.86
$R_{expected}$ (%)	1.69	1.60	2.70
χ^2	9.562	-	-
Model refinement			
space group	$Pn2_1a$		
unit cell	a=12.8961(10), b=10.5929(8), c=6.4299(5)Å		
	V=878.4(2)Å^3		
Scattering lengths/10^{-14}m	K:0.367, Rb:0.708, Ti:-0.344,		
	P:0.513, O:0.5805		
No. of parameters	96		
Diffractometer coefficients			
	148°bank	90°bank	60°bank
DIFC	unrefined	7699(1)	5449(1)
DIFA	-3.0(2)	-0.9(3)	-1.0(2)
zero	-12.7(6)	-11.8(8)	-15(1)
Background	8 term Fourier series		
Peak shape	Gaussian convoluted with double exponential		
148°	σ_1:36(2), σ_2:0.7(5)		
90°	σ_1:114(4), σ_2:6.8(7)		
60°	σ_1:212(5), σ_2:3.7(6)		

Table 3.5.2 Atomic coordinates and isotropic temperature factors ($Å^2$) for $K_{0.5}Rb_{0.5}TiOPO_4$.

	x	y	z	$100U_{iso}$	occupancy
Ti(1)	0.3730(3)	0.0000	0.4889(12)	0.33(7)	
Ti(2)	0.2534(6)	0.2567(12)	0.2710(10)	0.33(7)	
P(1)	0.5005(4)	0.2611(8)	0.3342(4)	0.44(4)	
P(2)	0.1821(2)	0.5126(8)	0.4937(8)	0.44(4)	
K(1)	0.3825(5)	0.3111(8)	0.7752(8)	2.83(8)	0.71(2)
Rb(1)	0.3825(5)	0.3111(8)	0.7752(8)	2.83(8)	0.29(2)
K(2)	0.1033(4)	0.0754(8)	0.6834(8)	2.83(8)	0.29(2)
Rb(2)	0.1033(4)	0.0754(8)	0.6834(8)	2.83(8)	0.71(2)
O(1)	0.4831(3)	0.1484(7)	0.4824(8)	0.73(2)	
O(2)	0.5099(4)	0.3825(7)	0.4628(7)	0.73(2)	
O(3)	0.4042(3)	0.2832(8)	0.1928(7)	0.73(2)	
O(4)	0.5981(3)	0.2454(8)	0.1975(7)	0.73(2)	
O(5)	0.1105(3)	0.5340(8)	0.3081(6)	0.73(2)	
O(6)	0.1151(3)	0.4752(8)	0.6849(7)	0.73(2)	
O(7)	0.2530(4)	0.6282(7)	0.5374(8)	0.73(2)	
O(8)	0.2535(5)	0.3991(8)	0.4549(8)	0.73(2)	
O(9)	0.2231(5)	0.6386(8)	-0.0431(8)	0.73(2)	
O(10)	0.2213(5)	0.3831(8)	0.0309(8)	0.73(2)	

Table 3.5.3 Selected bond distances (Å) and angles (°) in $K_{0.5}Rb_{0.5}TiOPO_4$

		KRTP	KTP			KRTP	KTP
Ti(1)	-O(1)	2.118(7)	2.161(4)	Ti(2)	-O(3)	2.028(9)	2.037(3)
	-O(2)	1.981(7)	1.957(4)		-O(4)	2.016(9)	1.979(3)
	-O(5)	2.095(9)	2.047(4)		-O(7)	2.029(9)	1.966(4)
	-O(6)	1.978(9)	1.900(4)		-O(8)	1.917(10)	1.994(4)
	-O(9)	1.933(8)	1.993(4)		-O(9)	1.757(9)	1.738(4)
	-O(10)	1.756(7)	1.718(4)		-O(10)	2.085(9)	2.101(4)
Δ		0.362	0.443			0.328	0.363
P(1)	-O(1)	1.545(4)	1.523(4)	P(2)	-O(5)	1.526(4)	1.541(4)
	-O(2)	1.533(4)	1.550(4)		-O(6)	1.553(4)	1.533(4)
	-O(3)	1.557(4)	1.549(4)		-O(7)	1.554(4)	1.551(4)
	-O(4)	1.544(4)	1.547(4)		-O(8)	1.535(4)	1.543(4)
K(1)	-O(1)	2.864(7)	2.900(4)	K(2)	-O(1)	2.760(7)	2.679(4)
	-O(2)	2.704(8)	2.743(4)		-O(2)	3.088(6)	2.979(4)
	-O(3)	2.716(7)	2.717(4)		-O(3)	3.097(6)	3.046(4)
	-O(5)	2.945(8)	2.874(4)		-O(4)	3.041(6)	3.125(4)
	-O(7)	3.107(7)	3.059(4)		-O(5)	2.792(7)	2.799(4)
	-O(8)	2.806(8)	2.762(4)		-O(7)	2.988(8)	2.917(4)
	-O(9)	3.063(7)	2.987(4)		-O(8)	3.153(7)	3.044(4)
	-O(10)	2.758(9)	2.717(4)		-O(9)	2.753(8)	2.765(4)
					-O(10)	3.198(7)	3.055(4)
mean		2.87(14)	2.84(12)			2.99(16)	2.93(14)

	RTP	KRTP	KTP
Ti(1)-O(9)-Ti(2)	137.1(4)	136.4(5)	135.5
Ti(1)-O(10)-Ti(2)	134.4(4)	134.8(5)	132.9

Figure 3.5.I Observed(dots) and calculated(smooth curves) time-of-flight neutron diffraction patterns of KRTP. Difference curves are shown on the same scale. a)148° bank.

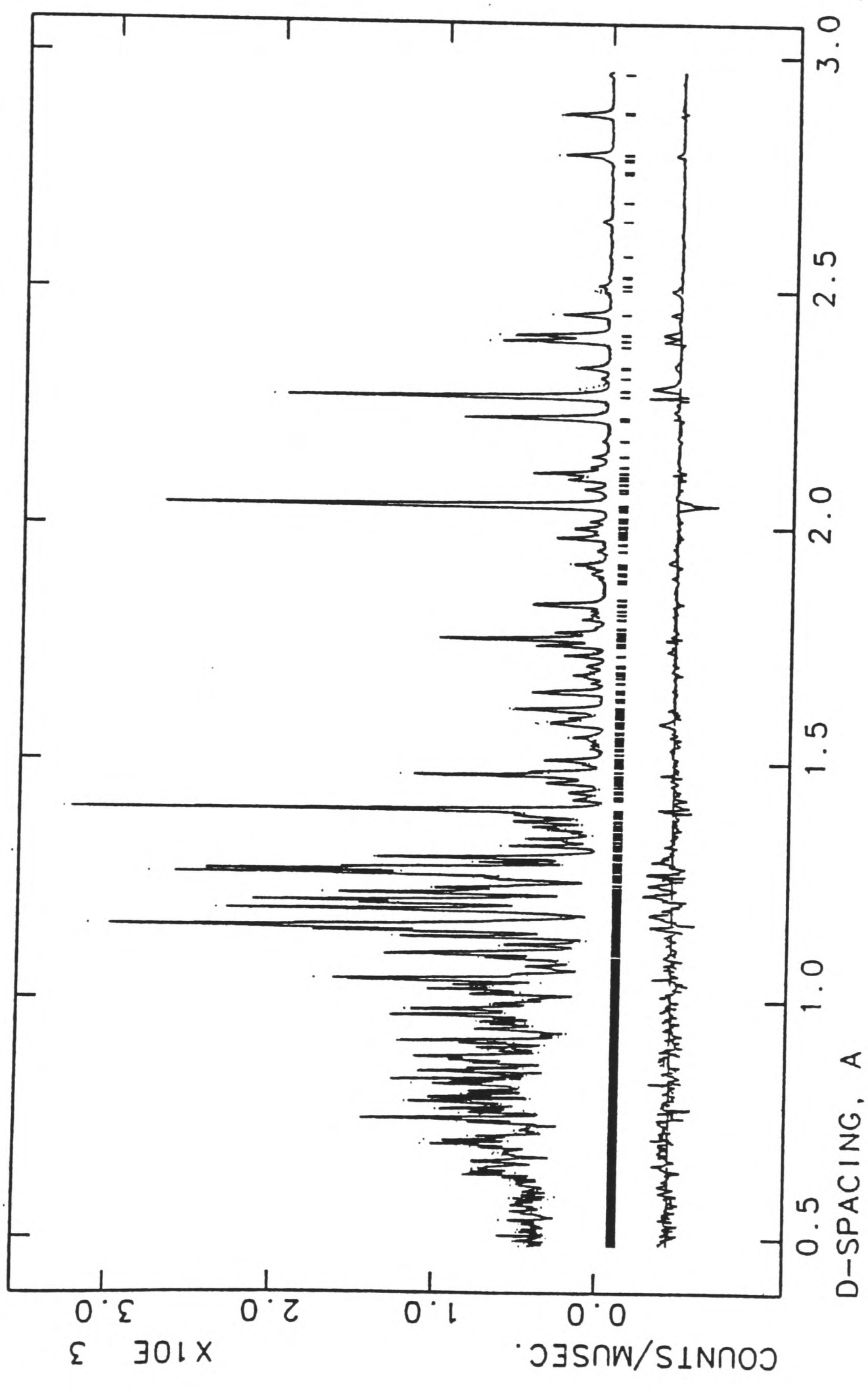


Figure 3.5.I Observed(dots) and calculated(smooth curves) time-of-flight neutron diffraction patterns of KRTP. Difference curves are shown on the same scale. b)90º bank.

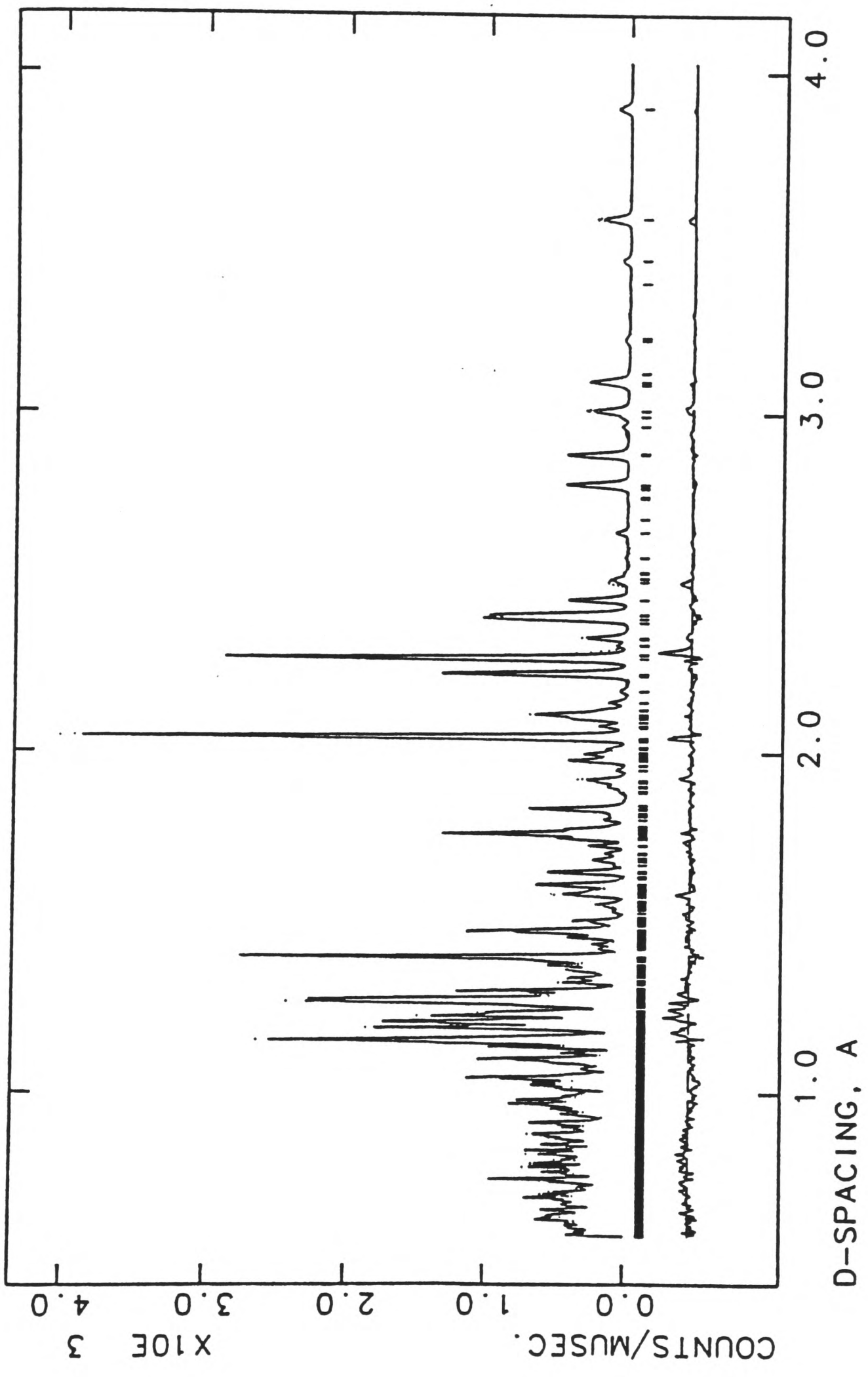
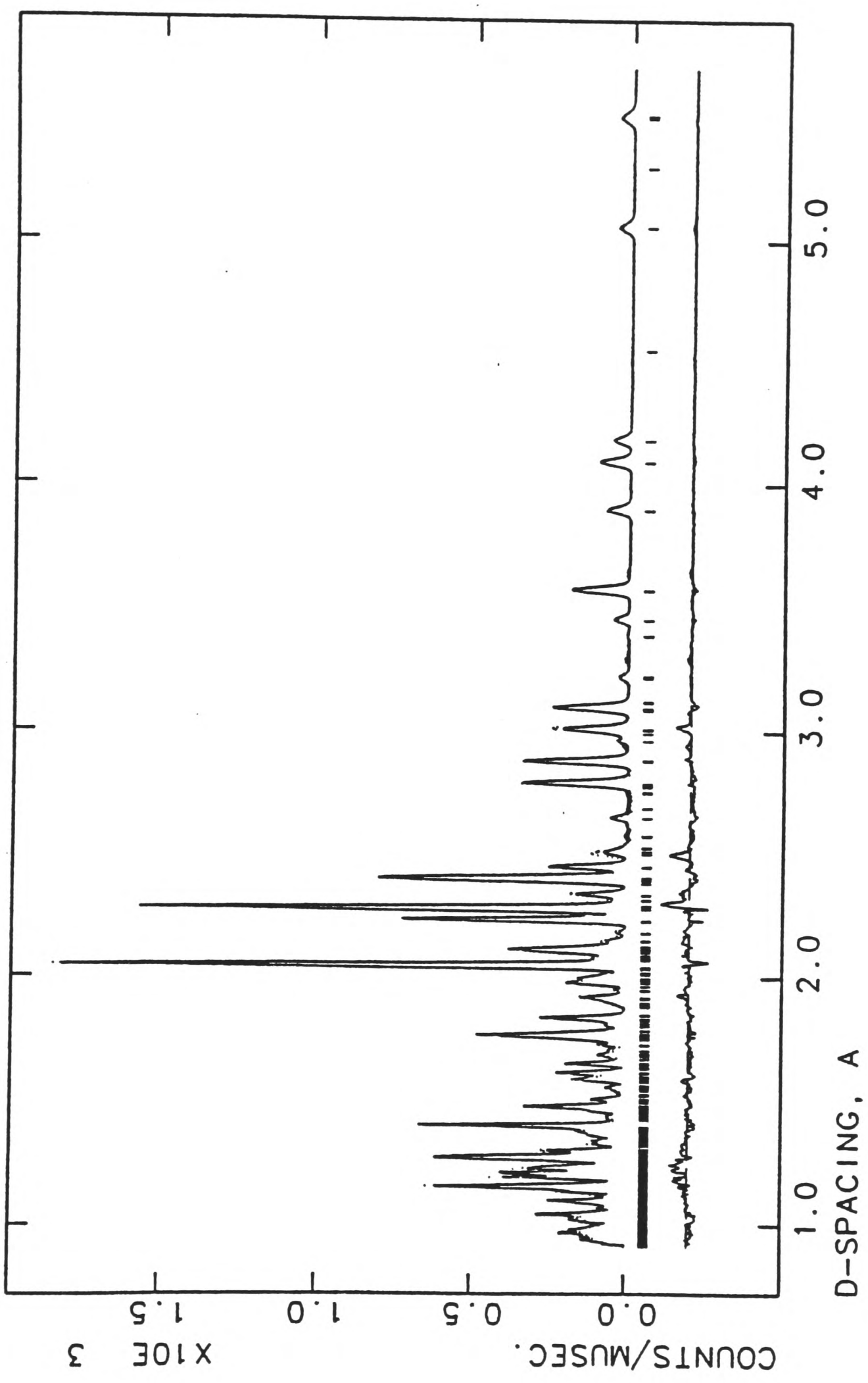


Figure 3.5.I Observed(dots) and calculated(smooth curves) time-of-flight neutron diffraction patterns of KRTP. Difference curves are shown on the same scale. c)60º bank.



Discussion

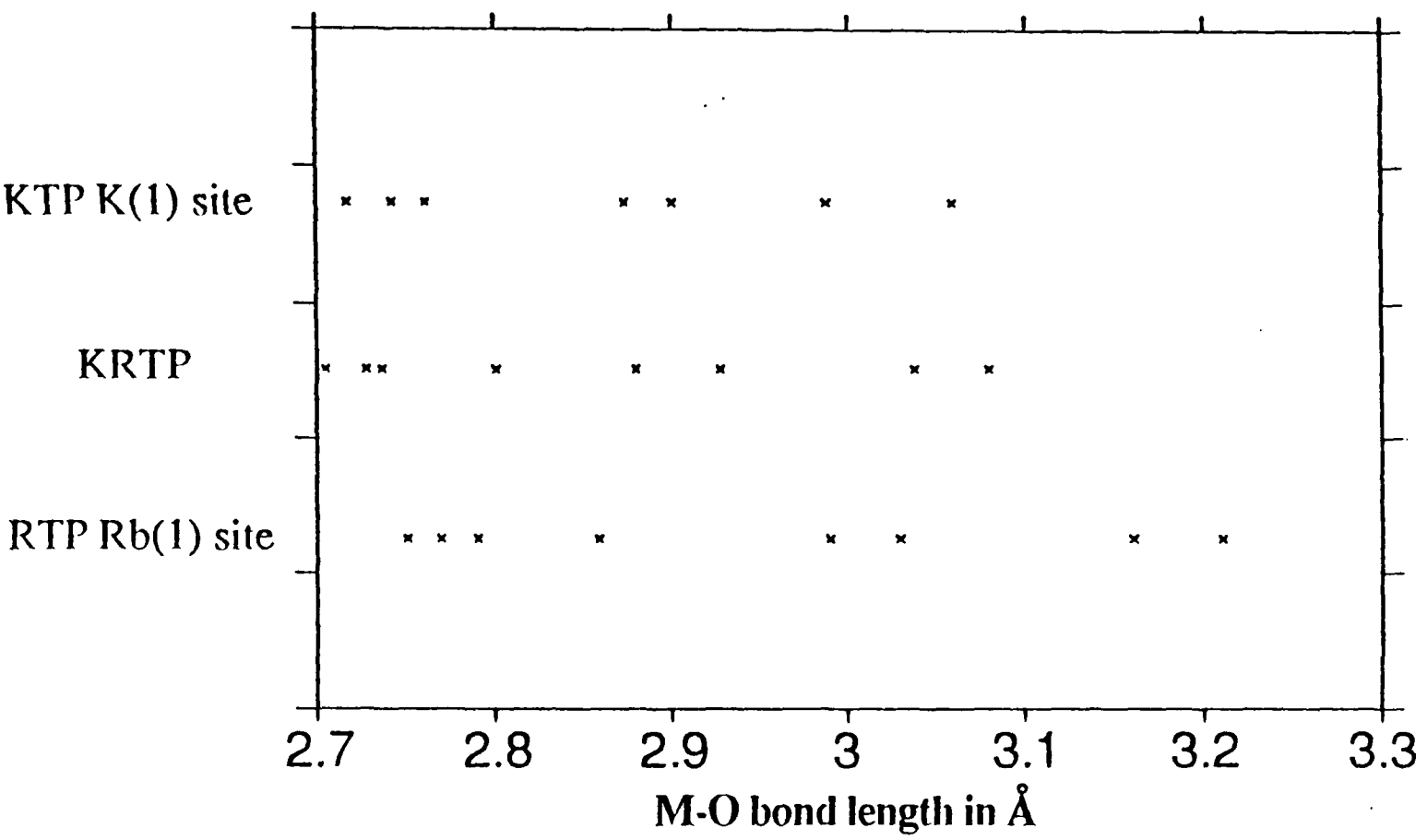
The structure of KRTP has been determined by neutron powder diffraction. The cations are only partially ordered over the two sites, 71% K occupying the smaller 8-coordinate K(1) site. The difference between the ionic radii of K^+ (1.33Å) and Rb^+ (1.47Å) is too small for the ordering to be complete, being less than that between Na (0.97Å) and K, or Na and Rb. This similarity in size will also cause K and Rb to have similar thermal characteristics as they occupy almost identical sites within the framework cavity. The cation-oxygen bond lengths of the parent compounds KTP and RTP cover a wide and almost totally overlapping range, confirming the similarity of the ions. However, the range of bond lengths around site 1 approximates more closely to that in KTP than that in RTP[159], and conversely for site 2 where the bond lengths are closer to those of RTP (Figure 3.5.II), as expected for the partially ordered model.

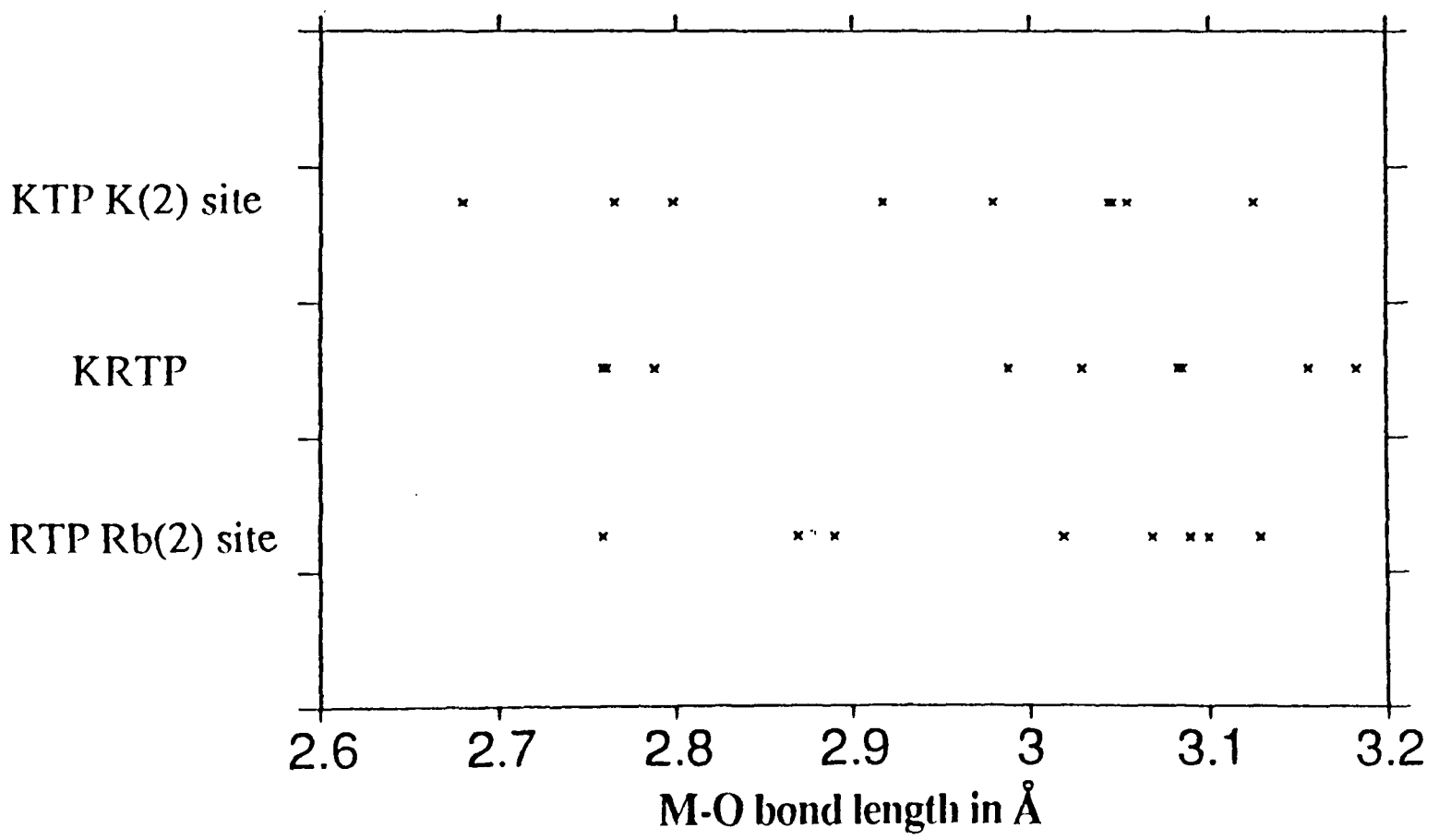
A bond valence calculation[136] indicates that the framework can adjust slightly to accommodate larger cations. Both sites are larger than those in KTP, and site 1 expands further in RTP. Site 2 is most favourable for substitution by both K and Rb, and the competition for this site ensures that the ordering is not complete. However the larger dimensions of

Table 3.5.4 Bond valence parameters calculated for KRTP and the two solid solution end members KTP and RTP.

	K(1)	Rb(1)	K(2)	Rb(2)
KTP	1.23		1.12	
KRTP	1.17	1.66	0.99	1.41
RTP		1.46		1.39

Figure 3.5.II Comparison of cation-oxygen bond lengths in KRTP with those in the parent compounds KTP and RTP.



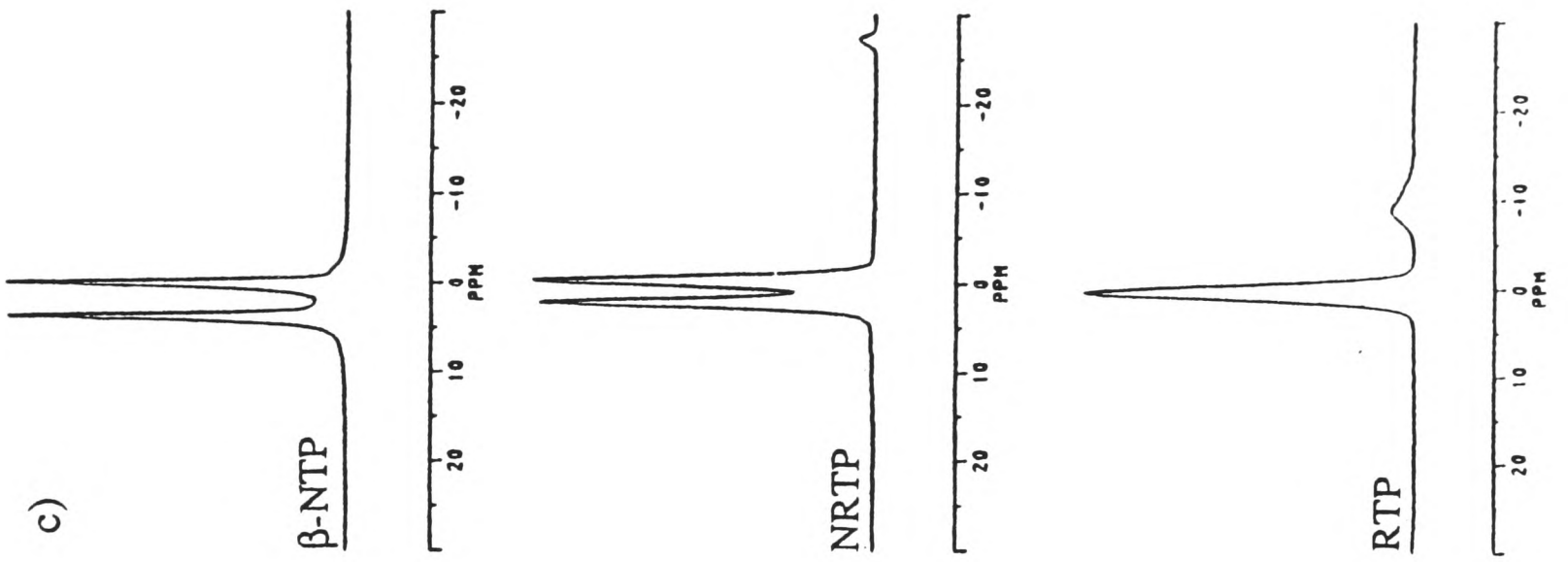


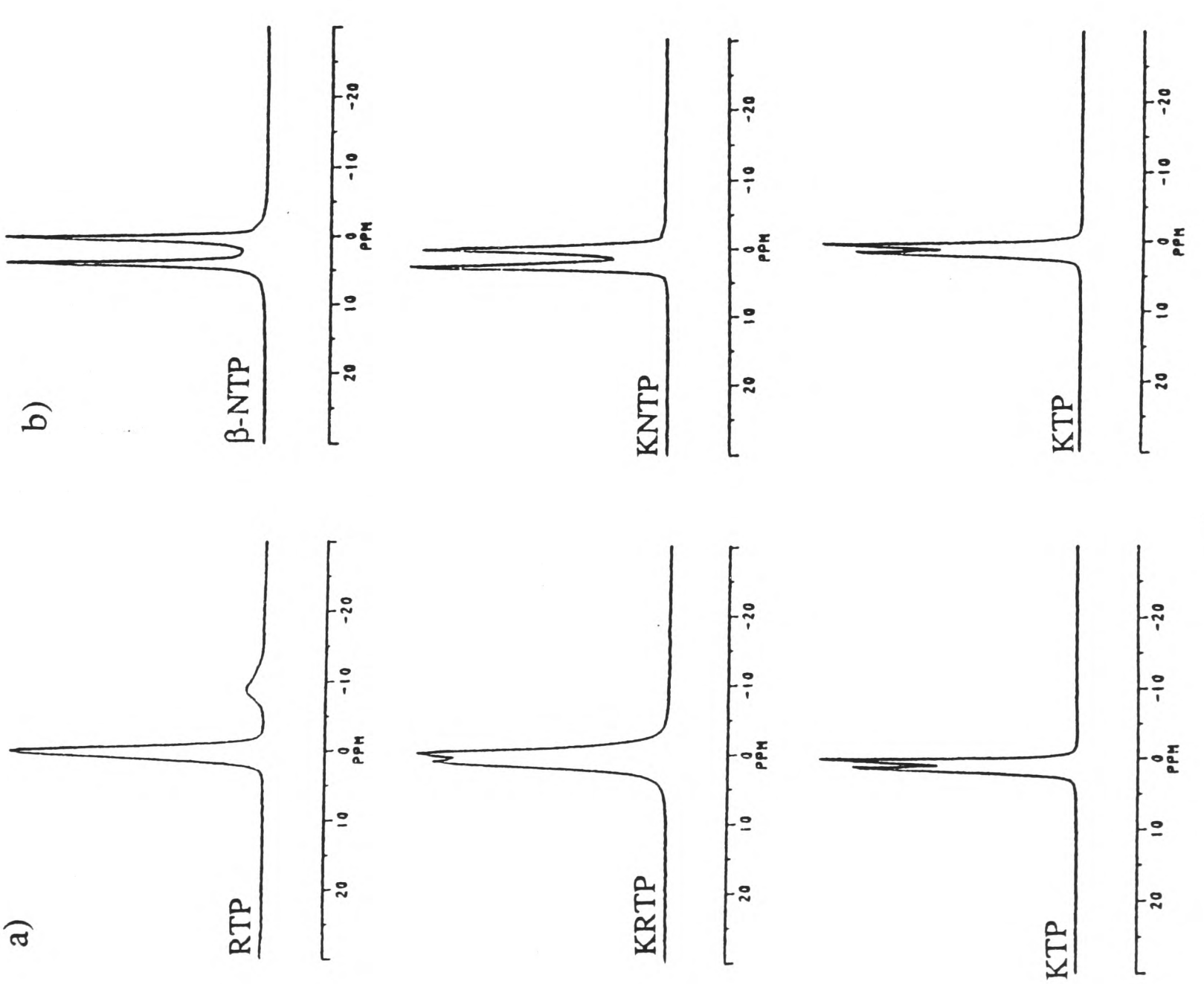
site 1 relative to KTP means that it is not unsuitable for K occupation, and the combination of these factors produces preferential but not complete substitution of Rb onto site 2.

The ^{31}P m.a.s.n.m.r spectrum of KRTP exhibits two resonances much broader than those measured in either of KNTP or NRTP (Figure 3.5.III).[162] This is interpreted as an indication that the ordering is not complete in this system, confirmation of the partial ordering found in the neutron powder diffraction study. Only one peak is observed in RTP, due to the similarity of the Rb(1,2)-P coordination and in KRTP the peaks are nearly merged, in contrast to the other $x = ½$ isomorphs where the resonances are almost totally resolved.

The TiO_6 distortion as measured by the difference between long and short Ti-O bonds decreases only marginally on Rb substitution into KTP, while the Ti(1)-O-Ti(2) angles increase on the substitution of the larger cation. The SHG measured from KRTP and RTP is unchanged from that in KTP[57], so an increase in these angles cannot have the same inhibiting effect on the SHG as seen when the angles decrease in β-NTP.

Figure 3.5.III.a) ^{31}P MASNMR spectra of KTP, KRTP and RTP, and for comparison; b) ^{31}P MASNMR spectra of KTP, KNTP and β-NTP and c) ^{31}P MASNMR spectra of RTP, NRTP and β-NTP. A $\pi/2$ pulse length of 3.5μs was used with a recycle time of 60s.





3.6 Discussion of alkali-metal cation exchange into $KTiOPO_4$

3.6.1 Cation bond valence calculations

A series of 50% substituted KTP isomorphs have been prepared and characterised by powder diffraction methods. Table 3.6.1 presents the cation valence sums[136] calculated from the atomic coordinates. The theoretical valency for all the cations is unity, a value which only K approaches, indicating that the TiO_6-PO_4 framework cannot readily distort to accommodate cations with ionic radii larger or smaller than K. Bond valence sum parameters for Na (ionic radius 0.97Å) are consistently less than one, even in the β-NTP parent compound where there are no larger cations to enlarge the channels; and conversely, Rb cations (ionic radius 1.47Å) have valences which are too high. The valence for a particular cation is approximately constant, indicating that the channel size is independent of cation radius. The most marked deviations from this are seen when the cation is in very low concentration, for example Na(2) and Rb(1) in NRTP. In these cases, the cation is depicted as being at the position of the cation that dominates the scattering, and the bond valence for both cations is calculated at that position. In reality the other cation would probably be in a more favourable position within the cavity with a valence comparable to that calculated in other isomorphs. The inflexibility of the framework is also shown by the reduction in the coordination number. The sodium ions have to move from a central position in the cavity to obtain sufficient interaction with oxygens in the walls because the framework does not contract.

Table 3.6.1 Cation valences in alkali-metal cation substituted KTP isomorphs.

	Na(1)	Na(2)	K(1)	K(2)	Rb(1)	Rb(2)
β-NTP	0.76	0.65				
KNTP	0.77	0.69	1.42	1.13		
NRTP	0.74	0.39			2.76	1.36
KTP			1.23	1.12		
KRTP			1.17	0.99	1.66	1.41
RTP					1.46	1.39

3.6.2 Correlation to nonlinear optical properties

The second harmonic generating ability of several of these materials has been measured by Stucky et al.[57]

a) $K_{1-x}Na_xTiOPO_4$

In the $K_{1-x}Na_xTiOPO_4$ series, the SHG remains roughly constant until x = 0.65, above which it falls off abruptly.[84] To correlate with this, a parameter affecting the nonlinear coefficients needs to remain constant in KTP and KNTP and change in β-NTP. The asymmetry of bonds within anionic groups such as TiO_6 has been postulated to be the major structural feature responsible for large nonlinear coefficients in inorganic compounds.[9,76,77] This can be described by Δ, the difference between the long and short Ti-O bonds (i.e. {Ti(1)-O(1)}-{Ti(1)-O(10)} and {Ti(2)-O(10)}-{Ti(2)-O(9)}). However these parameters do not change in a systematic fashion with the SHG (Table 3.6.2, Figure 3.6.II); in fact, β-NTP has more distorted $Ti(1)O_6$ octahedra than any other isomorph studied (Figure 3.6.I).

Table 3.6.2 The distortion (Δ) of TiO_6 octahedra in KTP isomorphs.

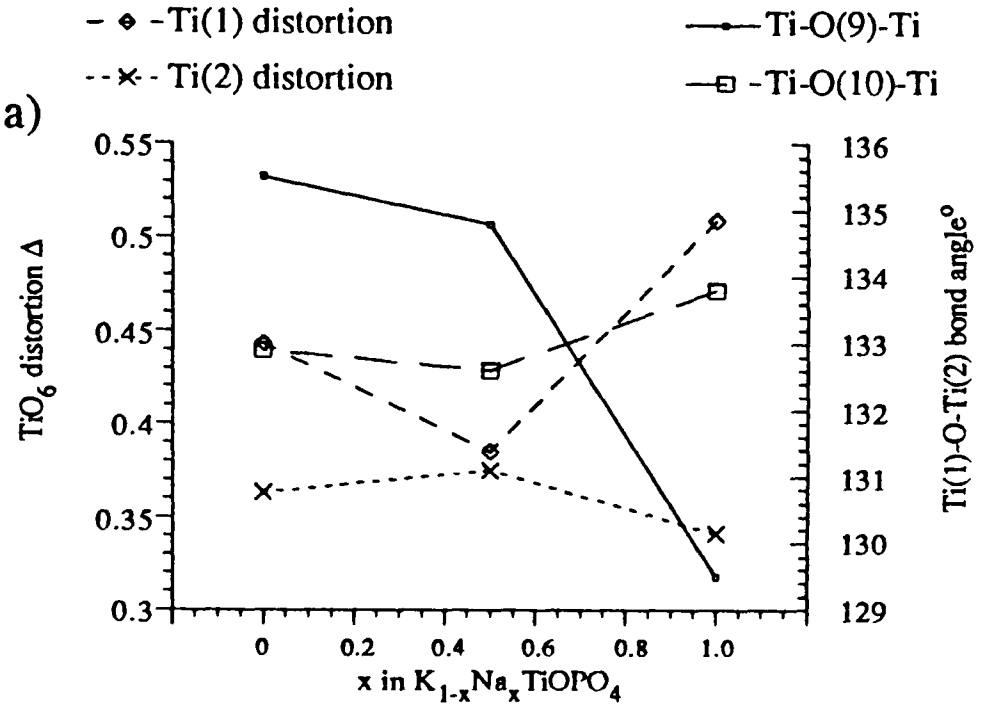
	KTP	KNTP	β-NTP
Ti(1)-O(1)	2.161(4)	2.129(5)	2.226(6)
-O(9)	1.993(4)	1.951(6)	2.005(8)
-O(10)	1.718(4)	1.744(5)	1.717(6)
Δ	0.443	0.385	0.509
Ti(2)-O(9)	1.738(6)	1.728(6)	1.758(6)
-O(10)	2.101(4)	2.103(6)	2.099(6)
Δ	0.363	0.375	0.341

	KTP	KRTP	RTP
Ti(1)-O(1)	2.161(4)	2.118(7)	2.133(7)
-O(9)	1.993(4)	1.933(8)	1.971(7)
-O(10)	1.718(4)	1.756(7)	1.711(7)
Δ	0.443	0.362	0.422
Ti(2)-O(9)	1.738(4)	1.757(9)	1.736(8)
-O(10)	2.101(4)	2.085(9)	2.098(8)
Δ	0.363	0.328	0.362

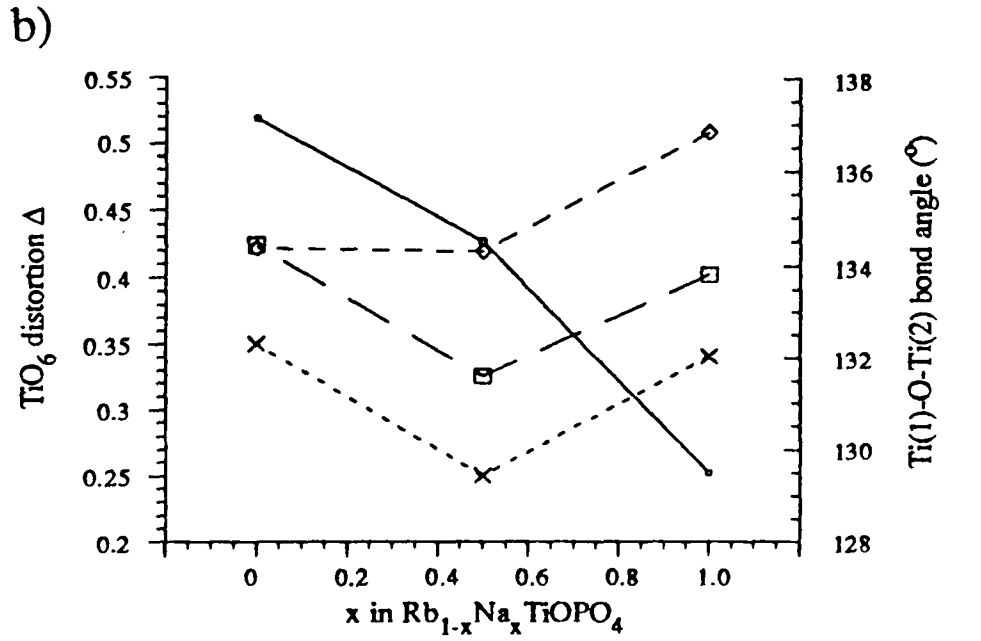
	RTP	NRTP	β-NTP
Ti(1)-O(1)	2.133(7)	2.14(1)	2.226(6)
-O(9)	1.971(7)	2.00(1)	2.005(8)
-O(10)	1.711(7)	1.72(1)	1.717(6)
Δ	0.422	0.42	0.509
Ti(2)-O(9)	1.736(8)	1.80(1)	1.758(6)
-O(10)	2.098(8)	2.05(1)	2.099(6)
Δ	0.362	0.25	0.341

Figure 3.6.I Graphs of TiO_6 distortion as measured by Δ and the Ti(1)-O-Ti(2) bond angle, against composition in a) $K_{1-x}Na_xTiOPO_4$, b) $Rb_{1-x}Na_xTiOPO_4$ and c) $K_{1-x}Rb_xTiOPO_4$.

a)



b)



c)

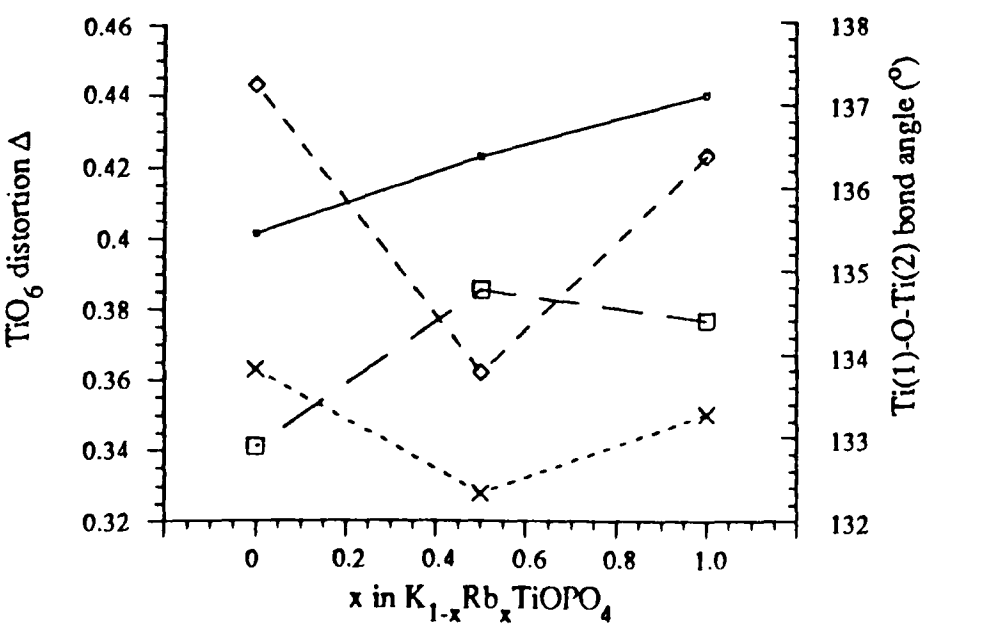
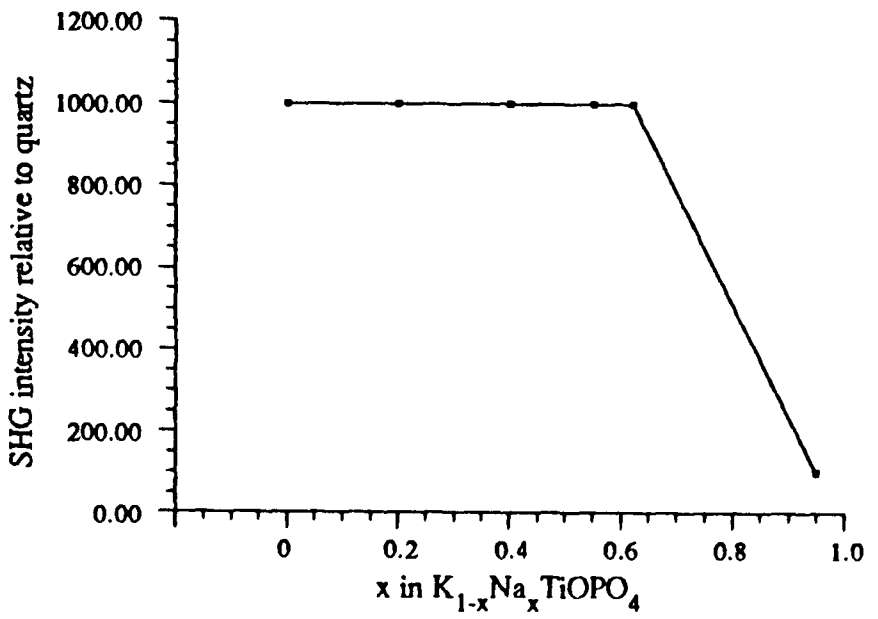
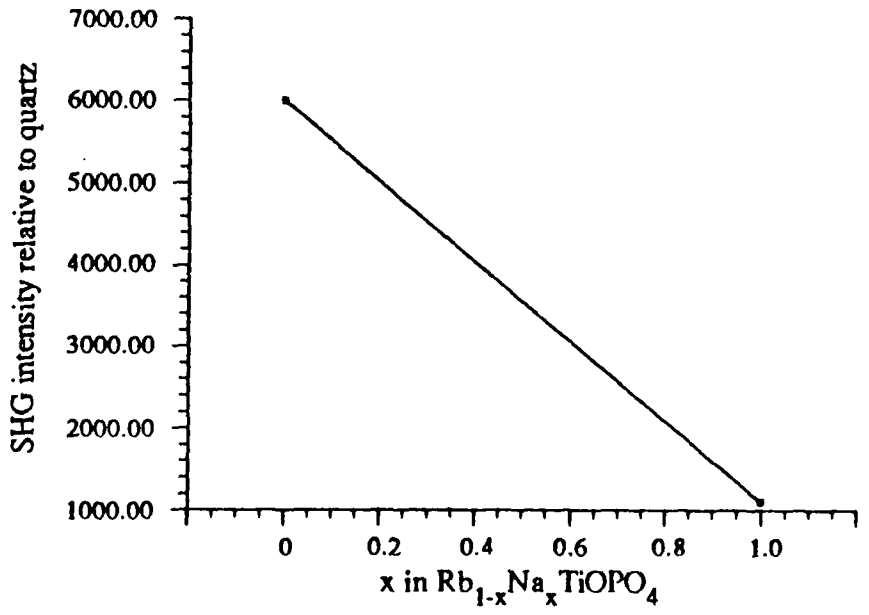


Figure 3.6.II Graphs of measured SHG intensity against composition in a)$K_{1-x}Na_xTiOPO_4$, b) $Rb_{1-x}Na_xTiOPO_4$ and c) $K_{1-x}Rb_xTiOPO_4$.

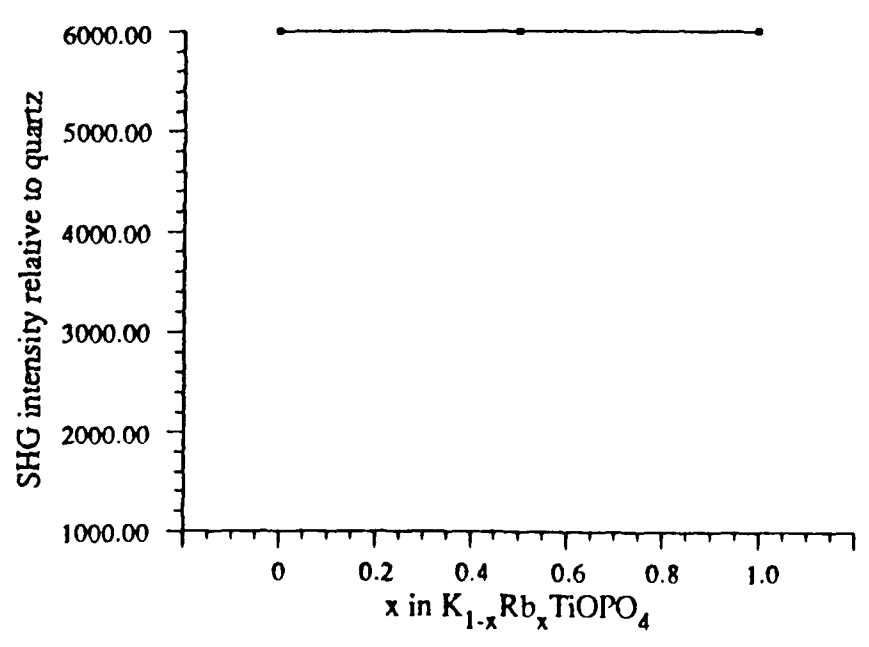
a)



b)



c)



The bond angles between octahedra will also affect the SHG since they will determine how the microscopic susceptibility of different TiO_6 octahedra add together to give the macroscopic susceptibility coefficient. The Ti(1)-O(10)-Ti(2) angle remains unchanged on Na substitution, but the Ti(1)-O(9)-Ti(2) angle changes from 135.5° in KTP through 134.8° in KNTP to 129.5° in β-NTP, mimicking the SHG behaviour, which drops slightly between KTP and KNTP then falls to a much lower value in β-NTP(Figure 3.6.Ia and Figure 3.6.IIa).

b) $K_{1-x}Rb_xTiOPO_4$

Similarly in the $K_{1-x}Rb_xTiOPO_4$ series, there is no significant trend in the Δ(Ti-O) values (Figures 3.6.Ic and 3.6.IIc), but this might be expected since there is no change in the SHG on Rb substitution.[67] The bond angles about both O(10) and O(9) increase slightly with Rb substitution:

	KTP	KRTP	RTP
Ti(1)-O(9)-Ti(2)	135.5	136.4(5)	137.1(4)
Ti(1)-O(10)-Ti(2)	132.9	134.8(5)	134.4(4)

This change in O(9) bond angle is only one third that seen in the Na-substituted series, but the SHG would be expected to increase if the SHG was a simple function of the angle between octahedra. The observation that the SHG remains constant while the angle increases from that in KTP indicates that it is only when the angle decreases and the cations are smaller than potassium that this angle is important in influencing the nonlinear optical properties. This may be because the smaller cation is able to interact more strongly with the titanyl oxygens and reduce the Ti=O bond order.

c) $Rb_{1-x}Na_xTiOPO_4$

The SHG output from intermediate members of the $Na_xRb_{1-x}TiOPO_4$ series has not been measured, although the relative effectiveness of the end members is known. The distortion of the Ti(2) octahedra shows no trend on substitution of Na into RTP, while the distortion of Ti(1) increases (Figure 3.6.Ib). However, the SHG output from β-NTP is very low, despite the large Ti-O bond asymmetry, so, as in the KNTP series, other factors are more important than this range of distortion. The Ti(1)-O(9)-Ti(2) bond angle decreases markedly on Na substitution and this decrease has been accompanied by a decrease in SHG output in the KNTP series independent of any change in the internal distortion of the octahedra.

	RTP	NRTP	β-NTP
Ti(1)-O(9)-Ti(2)	137.1(4)	134.5(6)	129.5(6)
Ti(1)-O(10)-Ti(2)	134.4(4)	131.3(6)	133.8(6)

The O(9) bond angle in NRTP is very similar to that in KNTP and KRTP, so the SHG output is probably comparable to that of KTP. However the reduction of the distortion around Ti(2) in NRTP may cause a further reduction in the nonlinear optical properties of this species.

From this work, it appears that the Ti(1)-O(9)-Ti(2) bond angle is more important in the determination of the large nonlinear optical coefficients than small reductions in the asymmetry of the Ti-O bonds.

3.6.3 Correlation of titanyl oxygen bond valencies with SHG

The bond valencies for the titanyl oxygens O(9) and O(10), calculated only from their bonds to titanium atoms, are given in Table 3.6.3. All the values are less than the theoretical value

Table 3.6.3 Titanyl oxygen bond valences in KTP isomorphs calculated only from their bonds to titanium.

	β-NTP	KNTP	NRTP	KTP	KRTP	RTP
O(9)	-1.77(5)	-1.93(2)	-1.63(3)	-1.86(4)	-1.89(6)	-1.92(3)
O(10)	-1.76(2)	-1.68(2)	-1.81(3)	-1.79(3)	-1.65(6)	-1.80(3)

of -2, indicating that there is a contribution to the oxygen valence from another source, in this case the cations. The bond valences of O(10) do not correlate with the nonlinear optical properties of the KTP isomorphs, that of KTP for example being lower than β-NTP, which produces a tenth the SHG intensity. However the variation in O(9) valence is more significant. In the KTP-KRTP-RTP series, the O(9) valences are approximately the same, as are the SHG properties. The KNTP and KTP O(9) valences are similar while that of β-NTP is smaller, which again correlates with the SHG output. The nonlinear optical properties of intermediate members of the RTP-NRTP-β-NTP series have not been measured, but the O(9) valence in RTP is higher than that of O(9) in β-NTP, in agreement with measurements carried out on these parent compounds. The bond valence of O(9) in NRTP is much less than in any other species, indicating that the atom has weaker Ti-O bonds and stronger interaction with the cations; the SHG output of NRTP is predicted to be less than that of any other cation-substituted isomorph.

The Ti(1)-O(9)-Ti(2) bond angle and the O(9) bond valence seem to correlate with the nonlinear coefficients in the cation-substituted solid solutions isomorphous with KTP. Substitution of a smaller cation reduces the SHG and the Ti(1)-O(9)-Ti(2) bond angle. An increase in this angle, for

example in the substitution of Rb, does not change the nonlinear optical properties, so the reduction may be caused by the closer interaction of the smaller cation of higher charge density with the titanyl oxygen atoms, reducing the strength of the bonds to titanium.

Extracts from this work have been published as the following papers:

1. Crennell S.J., Owen J.J., Grey C.P., Cheetham A.K., Kaduk J.A. and Jarman R.H., *J. Mater. Chem.*, 1, 113, (1991).
2. Crennell S.J., Cheetham A.K., Kaduk J.A. and Jarman R.H., *J. Mater. Chem.*, 1, 297, (1991).

CHAPTER FOUR

In chapter three, significant ordering was seen in KTP isomorphs, materials made by high temperature synthesis. Optical waveguides have been formed in KTP substrates through ion exchange at temperatures of approximately 350°C. The waveguide consists of a region of another isomorph in the bulk KTP, the structure of which could be important for the waveguide properties. However, features such as cation ordering found in isomorphs made at high temperature are not necessarily applicable to the structures of the waveguides prepared at 350°C. This chapter reports the structure of ion-exchanged KTP isomorphs prepared at temperatures comparable to those of waveguide formation in KTP.

4.1 Waveguide Formation

A crystal waveguide for the transmission of electromagnetic radiation is a channel or planar region on the surface of a nonlinear-optical material with a refractive index greater than that of the substrate. These can be prepared by etching a substrate surface or by ion exchange. Due to the difference between the refractive indices, any radiation in the guide undergoes total internal reflection at the interface between the channel and the substrate. Waveguides play an important role in optical communications, providing a range of switches, modulators and polarisation transforming devices.[163]

An electro-optic figure of merit for a nonlinear optical material, related to the bandwidth/ driving voltage ratio is given by n^3r/ε_{eff} where n is the refractive index, ε_{eff}, the

effective dielectric constant (= $\sqrt{\varepsilon_{11}\varepsilon_{33}}$) and r, the electro-optic constant for the material. Values for some important materials are given in Table 4.1.

Table 4.1 Comparison of the electro-optic properties of materials used in waveguide formation.[67]

	r(pm/V)	n	ε_{eff}	n^3r/ε_{eff}(pm/V)
KTP	35	1.86	13	17.3
$KNbO_3$	25	2.17	30	9.2
$LiNbO_3$	29	2.20	37	8.3
$Ba_2NaNb_5O_{15}$	56	2.22	86	7.1
GaAs	1.2	3.6	14	4.0

KTP has a figure of merit nearly twice that of other materials commonly used in waveguide formation.[152] The properties that make KTP suitable for SHG applications, e.g. high optical damage threshold and chemical stability, also make it a suitable substrate for waveguides.

As has been shown, KTP can form a large number of solid solutions with only minimal change in the nonlinear properties but with differing refractive indices. The K ions in KTP are mobile, so waveguides can be formed by ion exchange at relatively low temperatures. For instance, complete exchange of K by Rb gives a difference in refractive indices between waveguide and substrate, $\Delta n = 0.02$; or by Tl gives $\Delta n = 0.23$.[152] Such solid solutions can be made by direct ion exchange into a prepared KTP substrate. The ionic conductivity of KTP is highly anisotropic, with that along the [010] direction being 10^4 times larger than that in perpendicular directions.[164] Waveguides can be fabricated in y-cut

substrates where this anisotropy produces vertical channel walls with little diffusion in directions parallel to the [010]. However the actual value of the ionic conductivity varies from 10^{-10} to $10^{-6}\Omega^{-1}cm^{-1}$ depending on the method of KTP synthesis employed.[57]. This variation is caused by changes in the potassium nonstoichiometry from sample to sample. The presence of K vacancies will enhance the conductivity as the rate of K-ion hopping will increase[67], the loss of K and O being compensated for by the presence of Ti^{3+} ions. These latter ions have been detected in flux-grown KTP samples by electron paramagnetic resonance.[165]

Rb-exchanged waveguides have been fabricated in KTP by immersion of the polished substrate surface in a bath of molten rubidium nitrate. If a channel waveguide is required, the rest of the y-cut surface is covered with an approximately 500Å thick Al or Au mask prior to ion exchange.[152] After exchange, the refractive index measured at the waveguide surface is that of pure RTP, while the depth profile of Rb in the bulk indicates that the formation process is diffusion controlled. The properties of the waveguide produced appear independent of the temperature of the molten salt between 350 and 450°C, and of the diffusion time between 0.25 and 4 hours.[152] This is explained by an initial high ionic conductivity which decreases rapidly on Rb substitution as the ionic conductivity in RTP (which forms at the surface) is a factor of two less than that in KTP. This results in the rapid production of a waveguide of limited depth. The addition of a divalent ion to the molten nitrate increases the number of K ion vacancies in KTP and markedly increases the depth of the waveguide. For instance, the addition of 3% $Ba(NO_3)_2$ to the $RbNO_3$ melt increases the waveguide depth from

8μm to about 100μm.

KTP waveguides have been used in a variety of applications. One example is the Mach-Zehnder amplitude modulator (Figure 4.1).[166] In this device, a portion of the waveguide is split into two arms, and a voltage applied across one to change the refractive index so that when the waves recombine, the output intensity can be controlled by changing the amount of destructive interference.

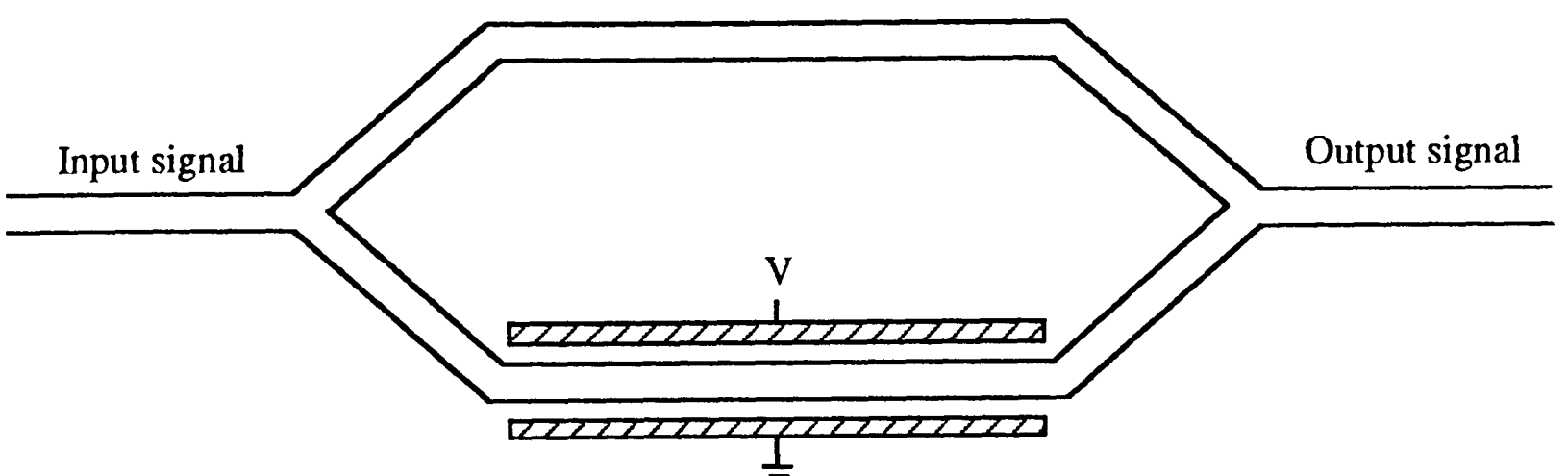


Figure 4.1. A schematic diagram of a Mach-Zehnder amplitude modulator.

Waveguides can be constructed in sections of length l_i and wave mismatch Δk_i so that the phase matching condition, $\Sigma l_i \Delta k_i$, is zero over the whole guide. This allows waveguides to generate second harmonic radiation from the fundamental without the temperature and angle tuning required in single crystal experiments.[167]

4.2 Synthesis and Characterisation of ion-exchange products

Waveguides are produced under low temperature conditions (i.e. ~ 350°C). The majority of previous structural work has however, been carried out on crystals synthesised by high

temperature hydrothermal or flux methods. In Chapter three, significant ordering was seen in KTP isomorphs prepared by high temperature solid state synthesis. To investigate the possibility of ordering of substituents in ion-exchanged KTP isomorphs and, by analogy, in waveguides, $K_{1-x}Rb_xTiOPO_4$ and $K_{0.5}Na_{0.5}TiOPO_4$ samples were prepared by ion exchange in KTP.

4.2.1 $K_{1-x}Rb_xTiOPO_4$

The ion-exchange isotherm of this solid solution has not been published despite its importance in waveguide formation. In a series of syntheses designed to explore the isotherm, KTP powder was mixed with $RbNO_3$ in molar ratios 1:5, 1:10 and 1:20.

After 48 hours at 350°C the mixtures were boiled in deionised water to remove the nitrates and the powders filtered and dried. Powder X-ray diffraction indicated that the products were pure $K_{1-x}Rb_xTiOPO_4$ phases with cell dimensions:

Ratio	a(Å)	b(Å)	c(Å)	V(Å^3)
1:5	12.899(3)	10.591(5)	6.450(3)	881.1(6)
1:10	12.933(4)	10.563(2)	6.459(1)	882.4(4)
1:20	12.943(2)	10.577(2)	6.454(1)	883.5(3)

Using the unit cell volumes of the known members of the solid solution, KTP (871.2), RTP (887.5)[1893] and KRTP from Chapter 3.5 (878.4), a graph of cell volume against composition can be constructed (Figure 4.2.I). The compositions predicted for the ion-exchange phases from this graph are:

Ratio	cell volume	x	x from A.A.
1:5	881.1(6)	0.63(4)	0.54
1:10	882.4(4)	0.71(4)	0.75
1:20	883.5(3)	0.78(4)	1.0

The results of atomic absorption spectroscopy (A.A.) carried out

by Amoco's Analytical department on the composition of the solid deduced from that of the nitrate washings are also presented. The two methods of analysis were not in very close agreement, but do indicate that the final phases contain a greater

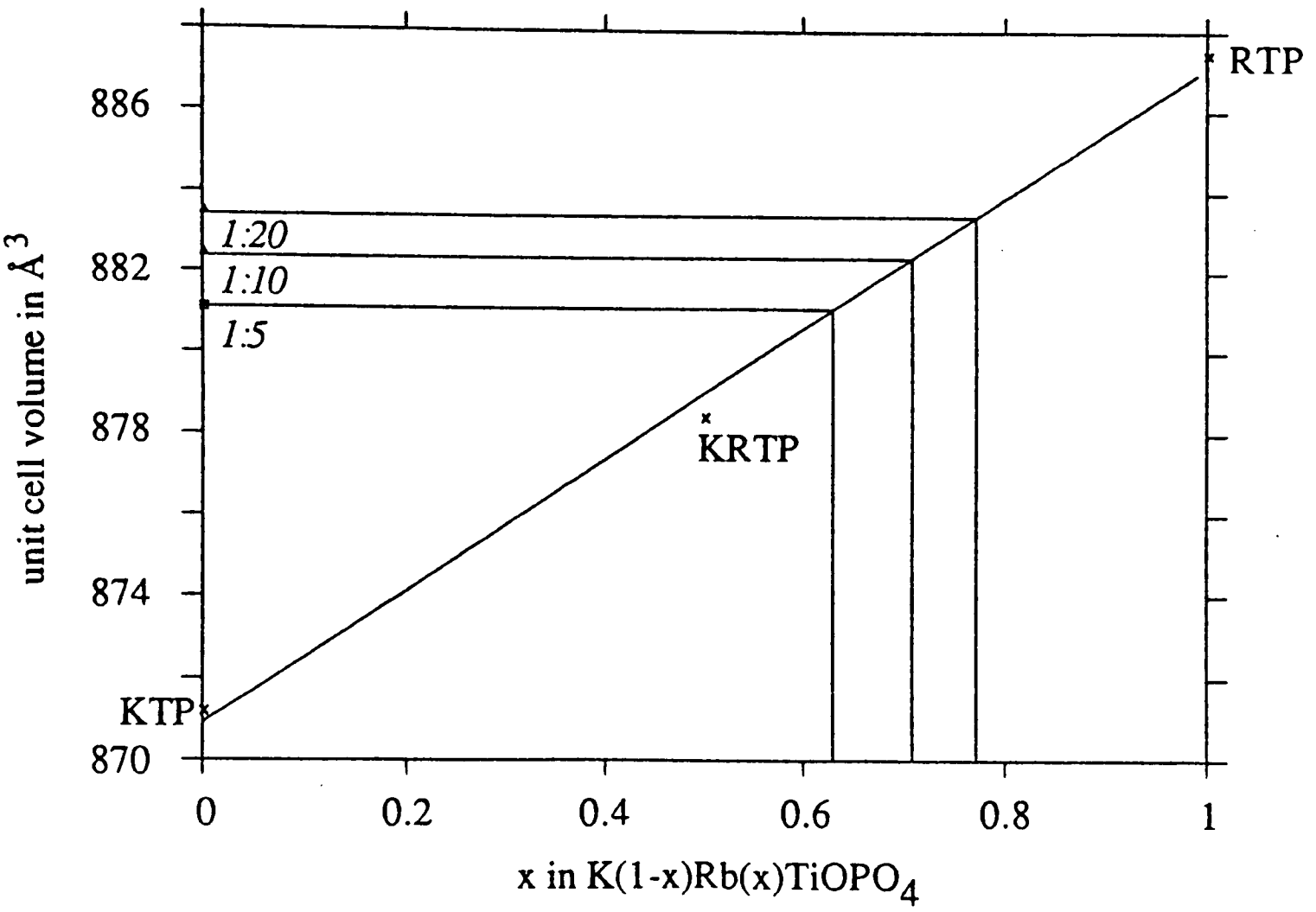


Figure 4.2.I A Vegard's Law plot of composition against volume in the $K_{1-x}Rb_xTiOPO_4$ series.

proportion of Rb than the desired x = ½ composition needed for comparison with the powder diffraction study (section 3.5). Higher KTP:$RbNO_3$ ratios, which would be required to form the x = ½ solid solution member, are not feasible because the volume of molten $RbNO_3$ would be too small to cover the KTP powder in the crucible, and ion exchange would not take place uniformly throughout the sample.

4.2.2 $K_{1-x}Na_xTiOPO_4$

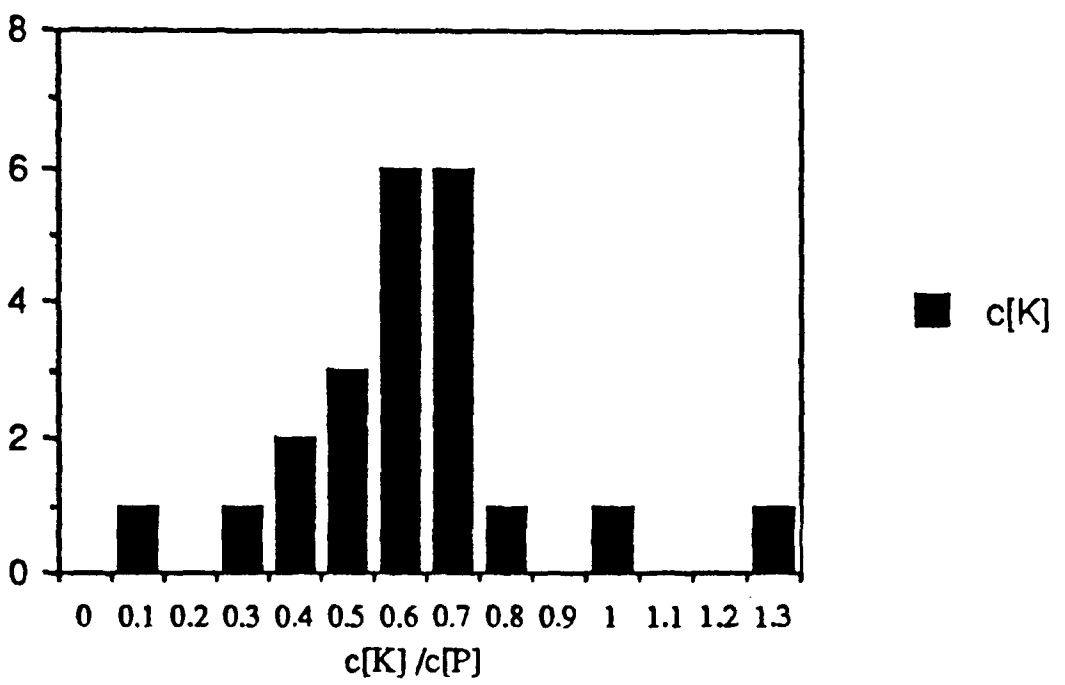
The nonlinear properties of this solid solution have been measured and show a considerable drop in second harmonic intensity after the x = 0.65 member.[84] The refractive indices of β-NTP have not been measured, but the inferior SHG properties mean the Na-doped isomorphs would probably not be used in commercial waveguide fabrication. However the system has been studied by ion exchange into KTP[91], and Na exchange appears considerably less facile than that of Rb, a large molar excess of $NaNO_3$, (approximately 100:1), is needed to obtain the β-NTP end-member. The KNTP system may form a more amenable system for the comparison between the structures of materials formed at low and high temperatures. Subsequent work indicated that a 10:1 $NaNO_3$:KTP ratio is required to obtain the x = ½ solid solution member.

i) exploratory powder syntheses.

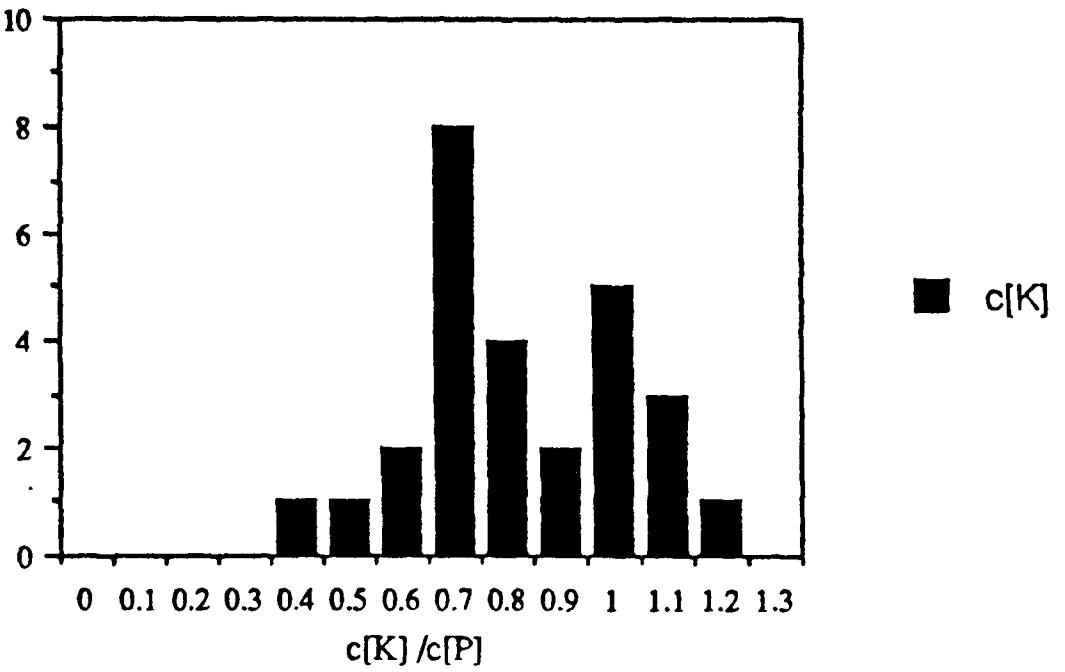
A sample of KTP was prepared by the standard solid state technique for use as the ion exchange starting material. Three 2g samples were mixed with a 10:1 molar excess of $NaNO_3$ and held in a Pyrex beaker at 350°C for 48 hours, 96 hours and two weeks respectively. The samples were boiled in deionised water, filtered and dried, then analysed with analytical electron microscopy using the K (K_α) emission. This emission was shown to unreliable in section 3.2, but it is the only available cation emission, so was used with the smallest possible electron beam spot size to minimise decomposition. Microscopy is more sensitive to the homogeneity of the sample than analysis based on the cell volume because the technique analyses individual crystallites rather than the bulk material.

Figure 4.2.II Analytical electron microscopy results on samples of KTP heated in molten $NaNO_3$ for periods of 48 hours, 96 hours and two weeks.

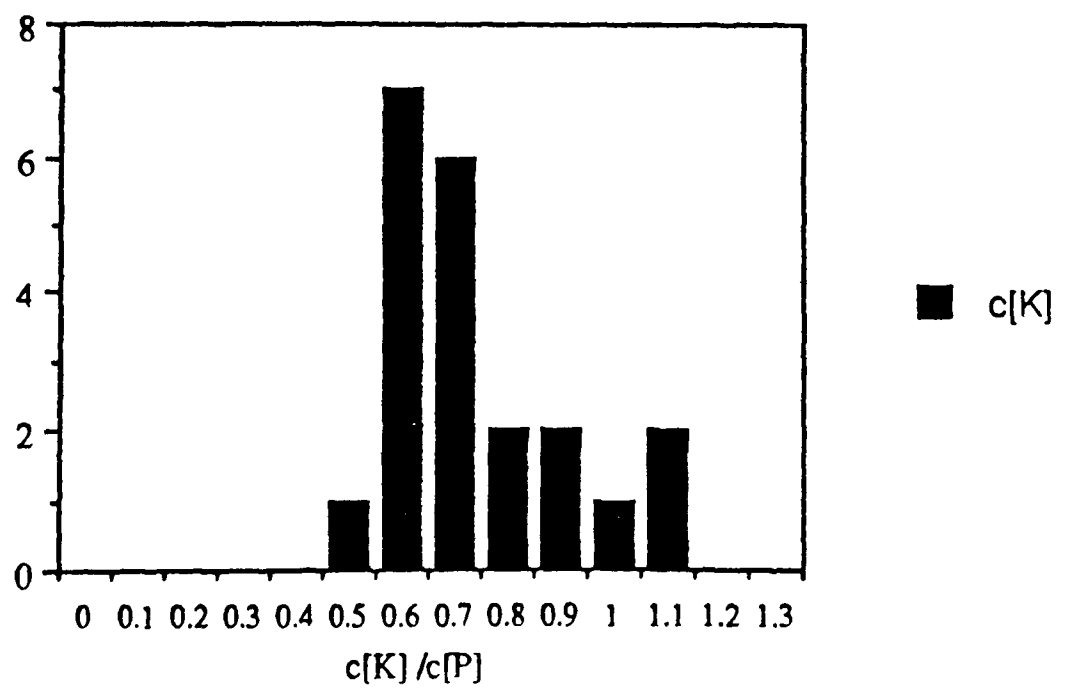
KTP after 48hrs in NaNO3



KTP after 96hrs in NaNO3



KTP after 14 days in NaNO3



The first sample (figure 4.2.II) contained crystallites covering a wide range of compositions (c_K = 0.57(6)c_P). This range contracts when ion exchange is allowed to continue, until after two weeks, the range of compositions obtained by analysis for K is only slightly greater than that in the sample prepared by solid state synthesis (Figure 3.2).

ii) single crystal ion-exchange.

In waveguide formation, exchange along the (010) direction seems to occur almost immediately to a depth of 10μm, but exchange in other directions takes place at a negligible rate at 350°C and the waveguide depth, even in the favourable direction, is limited. Although polycrystalline powders readily undergo cation exchange, 30-300μm crystals, when immersed in a 10:1 excess of $NaNO_3$ for 24 hours, appeared unchanged.[9,13] The crystals used in this work underwent ion exchange for two weeks to allow the mixture to attain equilibrium.

KTP crystals were prepared by the high temperature flux method. Powder X-ray diffraction patterns of ground crystals indicated that the product was pure KTP. 2g of these colourless, transparent crystals were mixed with a 10:1 molar excess of $NaNO_3$ and heated at 350°C in an alumina crucible for two weeks. After extraction from the reaction mixture, the crystals appeared white and opaque. To alleviate any chemical zoning, a portion of the crystals was annealed at 700°C for four days.

It was not possible to perform SHG measurements on these crystals because of the reduction in signal caused by the opacity, irrespective of the internal structure.

4.3 Single crystal X-ray diffraction study of an annealed $K_{0.5}Na_{0.5}TiOPO_4$ crystal

An annealed KNTP crystal of dimensions 0.13x0.22x0.30mm^3 was mounted and centred on an Enraf-Nonius CAD4 diffractometer as described in section 2.3. An interrupted SEARCH routine found 25 reflections from three regions of reciprocal space which were then centred and indexed on the orthorhombic cell

a=12.7319(16) b=10.6079(17) c=6.3076(16)A V=851.9(5)A^3.

Data collection, including all Friedel pairs, was carried out in shells from 0 to 55° in θ. After the shell at 40°, 25 high index reflections were centred and the unit cell refined to give:

a=12.7378(9) b=10.6081(14) c=6.3077(5)A V=852.3(2)A^3.

In the data reduction process, the data were corrected for Lorentz and polarisation effects. A semi-empirical absorption correction was carried out using azimuthal scans of the (3,0,1) and (5,-1,2) reflections with 80°<x<100°. Data reduction and all subsequent calculations were carried out using the CRYSTALS program[107] with complex scattering factors taken from the International Tables for Crystallography.[113] The data collection parameters are given in Table 4.3.1.

4.3.1 Structure refinement

Atomic coordinates for Ti and P were taken from the combined X-ray and neutron diffraction analysis of the KNTP powder synthesised by the high temperature solid-state method (section 3.3). The cation positions from this refinement were not used, as they presumably represent the average of the true K and Na positions within the framework cavity. However, after the Ti and P atomic coordinates had been refined, a difference Fourier map

Table 4.3.1 Data collection parameters for the annealed crystal.

molecular formula	$K_{0.43}Na_{0.57}TiOPO_4$
Formula weight	188.79
Crystal size	0.13x0.22x0.30mm^3
Crystal system	Orthorhombic
Unit cell/A	a = 12.7378(9) b = 10.6081(14) c = 6.3077(5)
V/A^3	852.3(2)
Space Group	$Pn2_1a$(33)
D_c/gcm^{-3}	2.960
F(000)	736
z	4
linear absorption coeff.	28.0512
X-radiation	MoK_α graphite monochromator
2θ max	110
scan type	ω-2θ
scan width	0.83 + 0.35tanθ
min, max scan	1.5,6.7
total data	11981
observed data	8180
I>nσ(I), n=	3
abs. correction min, max	1.00, 1.37
min, max h,k,l	0,0,0; 29,24,14
number of parameters	157
Weighting scheme	w[1-(ΔF/6σF)^2]^2
coefficients	6.56, -1.80, 5.11
$\Delta\rho$/eA^{-3}	1.78
Final shift/error	0.002
Final R = $\Sigma\Delta F/\Delta F_o$(%)	3.08
Rw = ($\Sigma w\Delta F^2/\Sigma wF_o^2$)$^{1/2}$(%)	3.70

gave a clear indication of the major K position (the K(2) site). The oxygens and Na (Na in the K(1) site), were identified through subsequent cycles of least squares refinement and difference Fourier syntheses, Na being distinguished from O on bond length criteria. The final refinement of all these atom coordinates and anisotropic thermal parameters gave an R-factor of 3.71%. However, two significant peaks were present in the difference Fourier map; one at 5.4e/A^3, close to Na, and a second smaller one at 2.2e/A^3 close to K. These were thought to be the positions of small amounts of K in the Na(1) cavity and Na in the K(2) cavity. The cation occupancy was restrained so that the total occupancy within a framework cavity was equal to unity and the positions of these minor cations were refined with isotropic thermal parameters. With this addition to the structure the R-factor dropped to 3.42% and the largest remaining peak in the difference Fourier map was only ρ = 1.8e/A^3. The polarity parameter refined to a value of 0.12(3) which is close to 0, the theoretical value for a structure of the correct stereoisomer. The only significant correlations observed were between the shifts of atomic y coordinates, the centre of origin of which was used to fix the floating origin along the y direction. After the application of the Tukey-Prince weighting scheme, final R-factors of 3.08% (Rw = 3.70%) were obtained. The final refinement parameters are given in Table 4.3.1, atomic coordinates and thermal parameters in Table 4.3.2 and selected bond lengths and angles in Table 4.4.3.

Table 4.3.2 Atomic coordinates for the annealed $K_{0.5}Na_{0.5}TiOPO_4$ crystal.

	x	y	z	occupancy	U_{iso} (Å^2)
Ti(1)	0.37298(1)	0.99779(8)	0.49372(2)		0.0049
Ti(2)	0.24527(1)	0.25018(8)	0.26508(2)		0.0050
P(1)	0.49540(2)	0.26205(8)	0.33875(5)		0.0053
P(2)	0.18392(2)	0.51134(8)	0.49832(5)		0.0053
K(1)	0.3801(8)	0.319(1)	0.783(2)	0.056(6)	0.023(2)
Na(1)	0.3489(1)	0.2819(1)	0.7677(2)	0.944(6)	0.0268
K(2)	0.09819(4)	0.06176(9)	0.6785(1)	0.810(4)	0.0196
Na(2)	0.1000(5)	0.0431(6)	0.778(1)	0.190(4)	0.030(1)
O(1)	0.48213(8)	0.1532(1)	0.4928(2)		0.0092
O(2)	0.50561(7)	0.3856(1)	0.4690(2)		0.0089
O(3)	0.39919(6)	0.2786(1)	0.1917(1)		0.0079
O(4)	0.59293(6)	0.2430(1)	0.1979(1)		0.0082
O(5)	0.11605(8)	0.5398(1)	0.3035(1)		0.0084
O(6)	0.11112(7)	0.4902(1)	0.6867(1)		0.0088
O(7)	0.25635(8)	0.6265(1)	0.5312(2)		0.0086
O(8)	0.25533(7)	0.3966(1)	0.4640(2)		0.0085
O(9)	0.22710(7)	0.6417(1)	-0.0354(1)		0.0079
O(10)	0.22419(7)	0.3858(1)	0.0270(2)		0.0089

Anisotropic thermal parameters (A^2x100) for the annealed crystal.

	U(11)	U(22)	U(33)	U(23)	U(13)	U(12)
Ti(1)	0.547(4)	0.451(4)	0.487(4)	0.062(4)	-.016(4)	-.042(4)
Ti(2)	0.474(4)	0.427(4)	0.619(4)	-.022(4)	-.032(3)	0.063(4)
P(1)	0.409(6)	0.520(8)	0.727(8)	0.048(7)	-.028(6)	-.092(6)
P(2)	0.700(7)	0.468(8)	0.481(7)	-.075(6)	-.017(7)	0.033(6)
Na(1)	4.40(8)	2.32(5)	1.99(4)	-.08(3)	-.36(4)	-.61(5)
K(2)	1.35(1)	2.59(2)	2.56(2)	0.20(2)	-.69(1)	0.13(1)
O(1)	0.98(3)	1.04(3)	1.18(3)	0.53(2)	0.30(2)	0.38(2)
O(2)	0.80(2)	0.81(2)	1.39(3)	0.42(2)	-.10(2)	-.22(2)
O(3)	0.52(2)	1.01(2)	0.98(3)	0.11(2)	-.11(2)	-.05(2)
O(4)	0.46(2)	1.02(3)	1.05(3)	-.11(2)	0.13(2)	-.00(2)
O(5)	1.15(3)	1.14(3)	0.51(2)	-.02(2)	0.14(2)	0.33(2)
O(6)	1.12(2)	1.14(3)	0.56(2)	0.02(2)	-.09(2)	0.22(2)
O(7)	1.14(3)	0.76(2)	1.00(3)	-.35(2)	-.24(2)	0.32(2)
O(8)	1.09(3)	0.71(2)	1.09(3)	0.34(2)	0.30(2)	0.31(2)
O(9)	0.85(2)	0.74(2)	0.90(2)	-.20(2)	0.01(2)	0.19(2)
O(10)	0.96(2)	0.79(2)	1.02(3)	0.14(2)	-.01(2)	0.28(2)

4.4 Single-crystal X-ray diffraction study of ion exchanged $K_{0.5}Na_{0.5}TiOPO_4$

A crystal that had not been annealed after ion exchange was mounted and centred on the Enraf-Nonius CAD4 diffractometer. An initial Polaroid photograph showed clear, sharp diffraction spots, indicating that the particle chosen was crystalline and that cation disorder had not severely broadened the reflections. 25 reflections were measured from the photograph and centred to find the orientation matrix. The high-angle reflections chosen for cell refinement in the annealed crystal data collection were centred, and least squares refinement of the initial orthorhombic cell gave:

a=12.7298(21) b=10.6073(13) c=6.3074(4)Å V=851.7(3)Å^3

Data were collected from 0 to 54° in θ and azimuthal scans were taken on the (-12,0,-1) and (-9,0,-1) reflections which had χ>80° for use in a semi-empirical absorption correction. A total of 12347 reflections were obtained after merging, of which 8904 were considered observed using the criteria $I>3\sigma(I)$. Data collection parameters are given in Table 4.4.1

4.4.1 Structure refinement

The structure of the annealed KNTP crystal was used as the starting model for the analysis of the ion exchanged crystal data. The positions of the small K(1) and Na(2) cations were unstable until they were removed and replaced by the two largest peaks from a difference Fourier map (which were close to the refined Na(1) and K(2) positions). The minor cations were refined with isotropic thermal parameters, while the other positions were refined anisotropically to give a final R-factor

of 4.53%. The largest peak in a final difference map was again the 1.8e/A^3 peak seen in the annealed crystal analysis, 1.2Å from P(2). The final refinement parameters are given in Table 4.4.1, atomic coordinates and thermal parameters in Table 4.4.2 and selected bond distances in Table 4.4.3.

4.5 Results and Discussion

Waveguide fabrication on KTP substrates involves exchange of K by Rb and Tl at a temperature of approximately 350°C. Previous structural work has been carried out on isomorphous materials prepared under high temperature hydrothermal, flux or solid state conditions, and the structural results are not necessarily applicable to the low temperature situation. In particular, it is not clear whether the cation ordering found in high temperature solid solutions is also a feature of the ion exchanged materials. Rb exchange into KTP took place too readily to permit the preparation of an ion-exchanged x = ½ solid-solution member for comparison with the earlier powder diffraction structure (section 3.5). However, after two weeks in molten $NaNO_3$, partially exchanged $K_{1-x}Na_xTiOPO_4$ crystals with x ~ ½ were obtained.

Using a graph of cell volume against composition that had been determined previously in a study of the ion exchange isotherm,[9,13] (Figure 4.5.I) the composition of the ion exchanged and annealed crystals can be estimated at $K_{0.45}Na_{0.55}TiOPO_4$ and $K_{0.43}Na_{0.57}TiOPO_4$ respectively. These values are in excellent agreement with those obtained through refinement of the cation occupancies (x = 0.58 and 0.57 respectively in $K_{1-x}Na_xTiOPO_4$).

Table 4.4.1 Data collection and refinement parameters.

molecular formula	$K_{0.45}Na_{0.55}TiOPO_4$
Formula weight	188.79
Crystal size	0.13x0.15x0.32mm^3
Crystal system	Orthorhombic
Unit cell/Å	a = 12.7298(21) b = 10.6073(13) c = 6.3074(4)
V/Å^3	851.7(3)
Space Group	$Pn2_1a$(33)
D_c/gcm^{-3}	2.942
F(000)	736
z	4
linear absorption coeff.	28.0706
X-radiation	MoK_α graphite monochromator
2θ max	108
scan type	ω-2θ
scan width	0.92 + 0.35tanθ
min, max scan	1.8,6.7
total data	12437
observed data	8904
I>nσ(I), n=	3
abs. correction min, max	1.16, 1.38
min, max h,k,l	0,0,0; 29,24,14
number of parameters	157
Weighting scheme	w[1-(ΔF/6σF)^2]^2
coefficients	9.8(2), -1.3(1), 7.9(2)
$\Delta\rho$/eÅ^{-3}	2.00
Final shift/error	0.08
Final R = $\Sigma\Delta F/\Delta F_o$(%)	4.53
Rw = ($\Sigma w\Delta F^2/\Sigma wF_o^2$)$^{1/2}$(%)	5.54

Table 4.4.2 Atomic coordinates for the ion exchanged $K_{0.8}Na_{0.8}TiOPO_4$ crystal.

	x	y	z	occupancy	$U_{iso}(A^2)$
Ti(1)	0.37293(2)	0.01073(9)	0.49432(3)		0.0051
Ti(2)	0.24501(1)	0.26288(9)	0.26564(3)		0.0052
P(1)	0.49518(3)	0.2751(1)	0.33889(6)		0.0055
P(2)	0.18385(3)	0.5243(1)	0.49875(6)		0.0054
K(1)	0.381(1)	0.327(1)	0.786(2)	0.0669(13)	0.026(3)
Na(1)	0.3488(2)	0.2950(2)	0.7686(2)	0.9332(13)	0.0271
K(2)	0.09840(5)	0.0747(1)	0.6793(1)	0.773(7)	0.0197
Na(2)	0.0989(6)	0.0581(7)	0.773(1)	0.227(7)	0.028(1)
O(1)	0.4822(1)	0.1664(1)	0.4931(2)		0.0096
O(2)	0.50553(9)	0.3985(1)	0.4683(2)		0.0094
O(3)	0.39902(8)	0.2914(1)	0.1922(2)		0.0080
O(4)	0.59272(7)	0.2559(1)	0.1978(2)		0.0088
O(5)	0.1157(1)	0.5526(1)	0.3047(2)		0.0087
O(6)	0.11130(9)	0.5033(1)	0.6870(2)		0.0087
O(7)	0.2566(1)	0.6393(1)	0.5316(2)		0.0088
O(8)	0.2552(1)	0.4093(1)	0.4642(2)		0.0089
O(9)	0.22728(9)	0.6545(1)	-0.0347(2)		0.0080
O(10)	0.2240(1)	0.3986(1)	0.0275(2)		0.0084

Anisotropic thermal parameters (A^2x100) for the ion exchanged KNTP crystal

	U(11)	U(22)	U(33)	U(23)	U(13)	U(12)
Ti(1)	0.609(5)	0.461(5)	0.488(5)	0.061(5)	0.014(4)	-.039(5)
Ti(2)	0.534(5)	0.436(5)	0.604(5)	-.025(5)	-.042(4)	0.070(5)
P(1)	0.462(9)	0.51(1)	0.72(1)	0.046(8)	-.013(7)	-.079(7)
P(2)	0.74(1)	0.47(1)	0.471(9)	-.066(7)	-.009(8)	0.019(7)
Na(1)	4.1(1)	2.47(7)	2.08(5)	-.11(5)	-.29(6)	-.66(7)
K(2)	1.36(2)	2.53(3)	2.53(3)	0.20(2)	-.64(2)	0.11(2)
O(1)	1.03(3)	1.03(3)	1.20(4)	0.51(3)	0.25(3)	0.36(3)
O(2)	0.85(3)	0.88(3)	1.39(4)	0.41(3)	-.08(3)	-.24(2)
O(3)	0.54(3)	1.04(3)	0.94(3)	0.16(3)	-.08(2)	0.01(2)
O(4)	0.57(2)	1.15(3)	1.07(3)	-.14(3)	0.08(2)	-.01(2)
O(5)	1.17(3)	1.19(4)	0.51(3)	0.02(2)	0.08(2)	0.27(3)
O(6)	1.09(3)	1.13(3)	0.56(2)	0.01(3)	-.06(2)	0.22(3)
O(7)	1.08(3)	0.78(3)	1.08(3)	-.37(3)	-.28(3)	0.26(2)
O(8)	1.17(3)	0.76(3)	1.05(3)	0.32(3)	0.28(3)	0.33(2)
O(9)	0.89(3)	0.73(3)	0.91(3)	-.23(2)	-.01(3)	0.22(2)
O(10)	0.92(3)	0.81(3)	0.96(3)	0.17(2)	0.02(3)	0.30(2)

Table 4.4.3 Selected bond distances (Å) in KNTP determined by single crystal and powder diffraction methods.

		ion exchanged	annealed	powder
Ti(1)	-O(1)	2.159(1)	2.1563(9)	2.129(5)
	-O(2)	1.967(1)	1.9656(9)	1.979(5)
	-O(5)	2.013(1)	2.0096(9)	2.016(5)
	-O(6)	1.951(1)	1.9494(8)	1.942(6)
	-O(9)	1.996(1)	1.9969(8)	1.951(6)
	-O(10)	1.727(1)	1.7283(9)	1.744(5)
Ti(2)	-O(3)	2.037(1)	2.0366(8)	2.001(6)
	-O(4)	1.954(1)	1.9556(7)	1.988(6)
	-O(7)	1.974(1)	1.9748(9)	1.907(6)
	-O(8)	2.000(1)	2.0007(9)	2.055(6)
	-O(9)	1.741(1)	1.7417(9)	1.796(6)
	-O(10)	2.097(1)	2.0971(9)	2.038(6)
P(1)	-O(1)	1.517(1)	1.5188(9)	1.550(3)
	-O(2)	1.548(1)	1.5520(9)	1.554(3)
	-O(3)	1.544(1)	1.5470(9)	1.546(3)
	-O(4)	1.541(1)	1.5404(9)	1.543(3)
P(2)	-O(5)	1.529(1)	1.5323(9)	1.531(3)
	-O(6)	1.521(1)	1.5237(9)	1.532(3)
	-O(7)	1.545(1)	1.5444(9)	1.537(3)
	-O(8)	1.536(1)	1.5349(9)	1.554(3)
K(1)	-O(1)	2.82(1)	2.85(1)	
	-O(2)	2.66(1)	2.64(1)	
	-O(3)	2.60(1)	2.62(1)	
	-O(5)	2.91(2)	2.96(1)	
	-O(7)	3.07(1)	3.10(1)	
	-O(8)	2.73(1)	2.70(1)	
	-O(9)	3.05(2)	3.07(1)	
	-O(10)	2.63(1)	2.609(9)	
	Na(1)	0.54(1)	0.57(1)	
Na(1)	-O(1)	2.787(2)	2.784(2)	2.787(5)
	-O(3)	2.748(2)	2.750(2)	2.729(5)
	-O(5)	2.620(2)	2.617(2)	2.709(5)
	-O(7)	2.698(3)	2.698(2)	2.752(5)
	-O(8)	2.564(2)	2.564(2)	2.571(5)
	-O(9)	2.612(3)	2.609(2)	2.684(6)
	-O(10)	2.529(2)	2.532(2)	2.537(6)

K(2)	-O(1)	2.721(1)	2.725(1)	2.741(6)
	-O(2)	2.927(2)	2.933(1)	2.992(5)
	-O(3)	3.006(1)	3.005(1)	3.082(6)
	-O(4)	3.059(1)	3.056(1)	3.010(5)
	-O(5)	2.783(5)	2.741(1)	2.829(6)
	-O(7)	2.969(1)	2.975(1)	2.928(6)
	-O(8)	3.127(2)	3.129(1)	3.114(6)
	-O(9)	2.732(1)	2.737(1)	2.685(7)
	-O(10)	3.085(1)	3.085(1)	3.083(6)
	-Na(2)	0.615(8)	0.661(7)	
Na(2)	-O(1)	2.389(8)	2.387(7)	
	-O(2)	2.481(8)	2.459(7)	
	-O(5)	2.776(7)	2.799(6)	
	-O(7)	2.607(7)	2.583(6)	
	-O(8)	2.720(8)	2.680(7)	

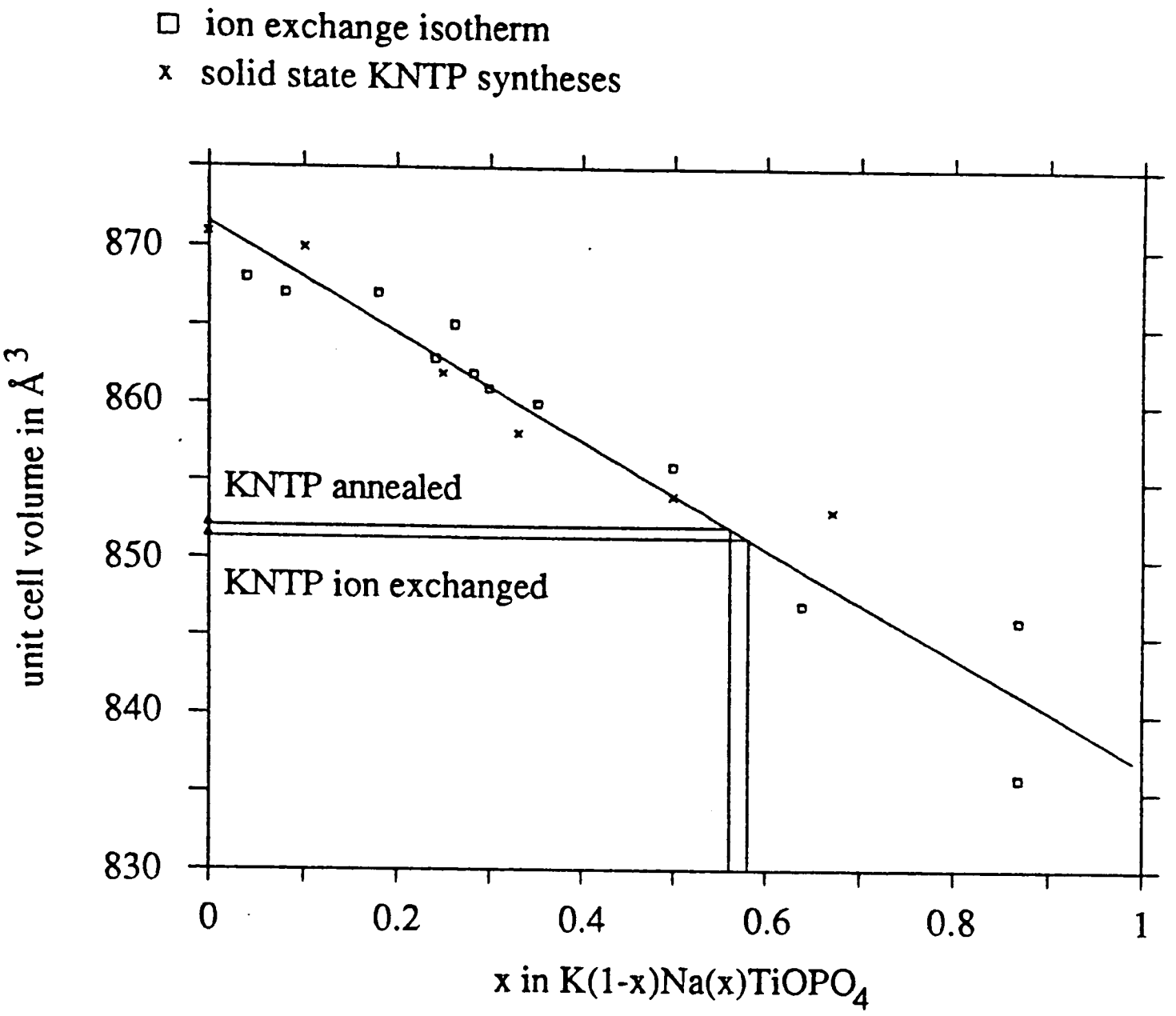
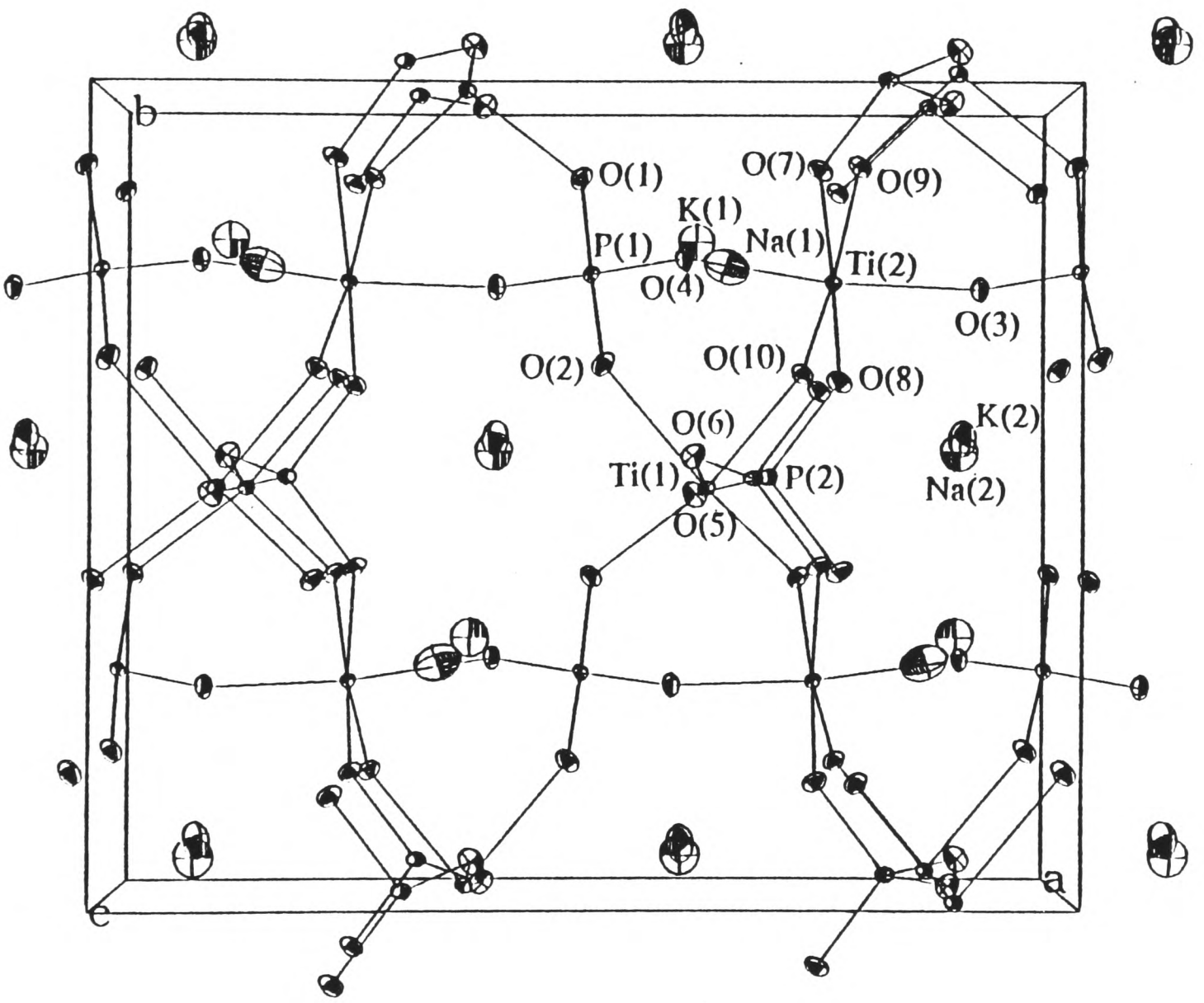


Figure 4.5.I A Vegard's Law plot of composition against unit-cell volume for the $K_{1-x}Na_xTiOPO_4$ solid solution.

The ion exchanged crystal diffracted X-rays out to 54° in θ and the structure obtained was well defined. These results indicate that the crystal was free from concentration gradients which would have introduced gross disorder into the structure. Annealing the crystal improved the precision, but did not materially alter the details of the structure.

The single crystal X-ray structure determinations of KNTP show that it is isomorphous with KTP (Figure 4.5.II). Even in the unannealed crystal there is almost complete ordering over the two cation sites, Na preferentially occupying the smaller

Figure 4.5.II A projection of the unit cell of $K_{1-x}Na_xTiOPO_4$, (where x = 0.5), along [001].

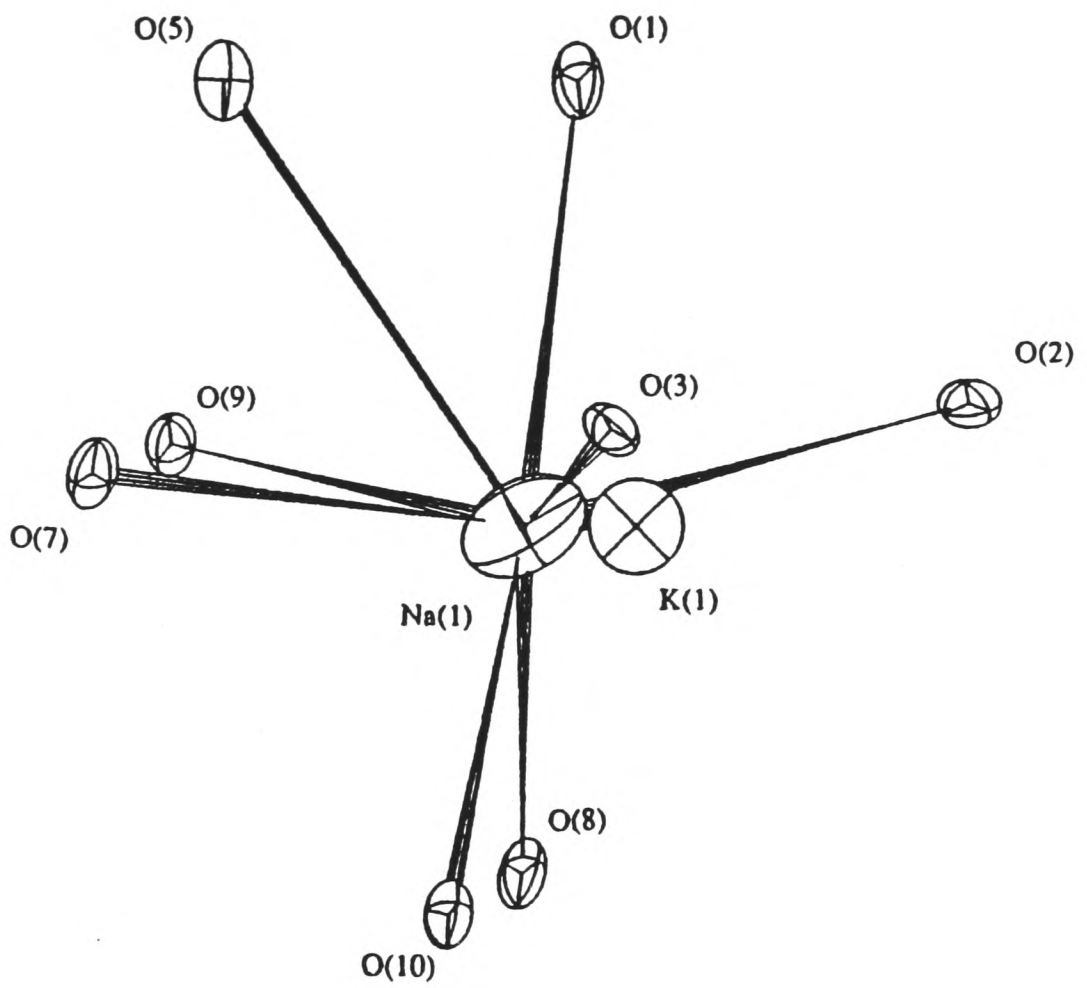


K(1) site and K occupying the K(2) site. This is in agreement with the cation ordering seen in the powder diffraction study of KNTP (section 3.3). The higher resolution of the single crystal study allowed the positions of minor cation sites to be located and refined independently within the cation cavity. It is clear that the ordering is not absolute, but that the powder diffraction study gives a reliable indication of the cation distribution. The nature of the cation substitution does not change between that in the ion exchanged crystal and that in the materials prepared at high temperature. Structure determination of materials prepared by conventional high temperature flux methods therefore appears to be a reliable indicator of the substitution taking place in waveguide formation.

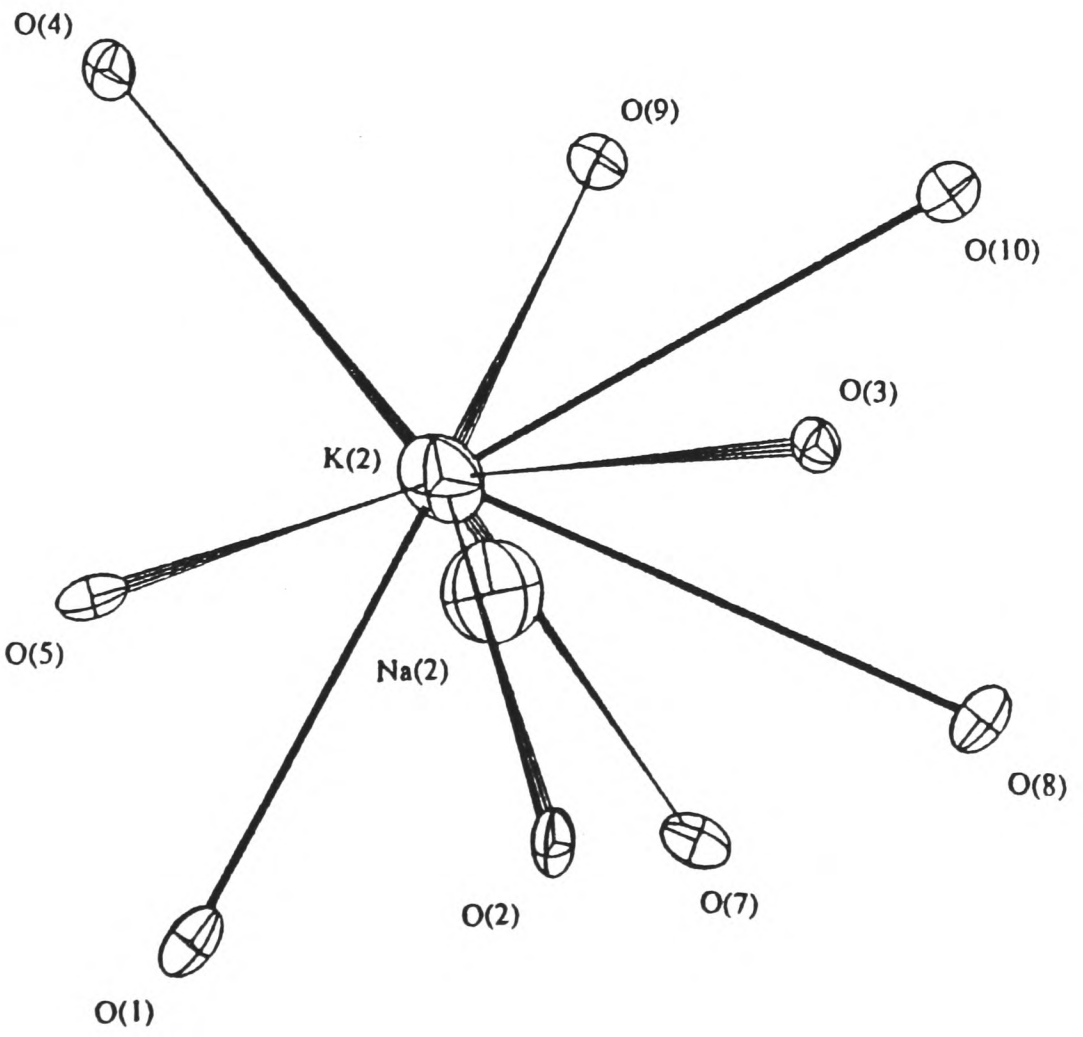
The oxygen coordination around the two cation sites is shown in Figure 4.5.III, where the isotropic cations are drawn without bonds for clarity. The positions of the oxygen atoms defining the framework cavity might be expected to change according to the size of the cation contained in the cavity. The shifted positions of the oxygens caused by 10% occupancy of the minor cations would contribute only 10% of the scattering, so would not be distinguished, even in the high resolution single crystal structure determination, but the disorder in the oxygen sites would lead to enhanced thermal parameters. The O anisotropic thermal parameters obtained (Tables 4.3.2 and 4.4.2) are very similar to those presented in a recent single-crystal X-ray study of KTP and $KSnOPO_4$[c143], so it would appear the framework is rather rigid and that the oxygens do not move to accommodate the different ionic radii of cations exchanged for K.

Figure 4.5.III Oxygen coordination around the cation sites; a) the Na(1) site and b) the K(2) site. The positions of the minor cations are also shown, refined with isotropic thermal parameters.

a)



b)



4.5.1 Bond valence calculations[15]

The results of bond valence calculations carried out on the cation-oxygen distances in the KNTP structures are presented in Table 4.5.1. In KTP, the K bond valence sums are close to the theoretical value of 1, but in β-NTP the valences are smaller than 1, indicating that the framework cannot relax sufficiently to accommodate Na (this may be the reason that NTP prefers to form in the α- modification). In the KNTP compounds, the major cations Na(1) and K(2) have bond valences very similar to those in the parent species. The Na(2) parameter in single-crystal KNTP is indistinguishable from that in β-NTP; that is the framework coordination of Na does not change on substitution of the larger K ion into the majority of the K(2) sites. The K(1) parameter is larger than expected, but the occupancy of this site (.06), may be too small for accurate determination of the K(2) position.

Table 4.5.1 Bond valence parameters of $K_{1-x}Na_xTiOPO_4$ and the solid solution end-members.

Structure	Site 1	Site 2	Reference
ion exchanged sample			
Na	0.77	0.74	section 4.4
K	1.45	1.14	
annealed sample			
Na	0.77	0.76	section 4.3
K	1.44	1.13	
β-$NaTiOPO_4$	0.79	0.73	[10]
$KTiOPO_4$	1.22	1.11	[16]
$K_{0.5}Na_{0.5}TiOPO_4$			
Na	0.76	0.52	section 3.3
K	1.75	0.99	

The bond-valence calculations indicate that the framework is rigid and that the channels do not distort significantly to accommodate cations of smaller ionic radii.

In the powder diffraction study of KNTP, the bond-valence parameters of the major cations are similar to those calculated in the single-crystal work. However, the K(1) parameter is much larger, and that of Na(2) much smaller, than the ideal value (1). In the powder structure determination, these sites could not be distinguished and their valence was calculated at the average cation position in the cavity. As the ordering is almost complete, the scattering is dominated by the major cation so the cation position obtained is very close to the ideal site of the major occupant, which in turn is ~ 0.6Å from the minor cation (see Table 4.4.3).

4.5.2 Correlation with SHG properties

The SHG properties of this solid solution have been measured in the powder form.[84] The SHG intensity remains high until the $x = 0.65$ solid solution member, after which it decreases, reaching a value one tenth that of KTP when $x = 1$. To correlate with this, a structural parameter must remain almost constant between KTP and KNTP, and change significantly between KNTP and β-NTP.

The large nonlinear coefficients are thought to arise mainly from the distorted TiO_6 octahedra, a measure of which is the difference between the longest and shortest Ti-O bonds, Δ. The distortion in the Ti(2) octahedron decreases marginally between KTP and KNTP and to a greater extent between KNTP and β-NTP as required, but the $Ti(1)O_6$ distortion is a maximum at β-NTP implying that this should give the highest SHG intensity. Other

possible structural indicators that have been put forward are the titanyl bond lengths, their bond valences (calculated using contributions from Ti only) and the angles between octahedra in the TiO_6 chains. Table 4.5.2 compares these parameters for four KTP isomorphs.

Table 4.5.2 Selected Ti-O structural parameters thought to correlate with nonlinear properties in KTP isomorphs.

	KTP	KNTP	β-NTP	AgTP[103]
Ti(1)-O(10)	1.718(4)	1.718(1)	1.717(6)	1.709(11)
Ti(2)-O(9)	1.738(4)	1.741(1)	1.758(6)	1.78(1)
Δ(Ti(1))	0.443(6)	0.432(1)	0.509(8)	0.519(10)
Δ(Ti(2))	0.363(6)	0.356(1)	0.341(8)	0.290(10)
Ti(1)-O(9)-Ti(2)	135.5	134.43(7)	130.8(3)	129.5(6)
Ti(1)-O(10)-Ti(2)	132.9	130.58(7)	132.3(3)	133.8(6)
O(9) valence	1.85(1)	1.83(1)	1.76(2)	1.67(5)
O(10) valence	1.76(2)	1.74(1)	1.76(2)	1.82(5)
SHG referred to KTP	1	0.1		0.001

The Δ(Ti(2)) (the difference between the longest and shortest Ti(2)-O bonds in the octahedron), Ti(1)-O(9)-Ti(2) bond angle, Ti(2)-O(9) bond length and O(9) bond valence correlate with the SHG intensity reported. This implies that cation substitution affects the O(9) atom and its role in the long-short alternation of Ti-O-Ti bonds in the helical chains of TiO_6 octahedra.

The KNTP species is almost fully ordered, with Na occupying K(1). The SHG intensity decreases after this point in the solid solution, so that it is the substitution of the smaller cation into the K(2) site that is accompanied by the reduction in nonlinear properties.

Table 4.5.3 Cation - oxygen bond lengths (A) and bond orders in the $K_{1-x}Na_xTiOPO_4$ solid-solution series.

	KTP		KNTP K(1)=Na, K(2)=K		β-NTP	
K(1)-O(9)	2.987(4)	0.099	2.612(3)	0.113	2.745(8)	0.078
-O(10)	2.717(4)	0.206	2.529(2)	0.137	2.525(7)	0.142
K(2)-O(9)	2.765(4)	0.181	2.732(1)	0.197	2.644(8)	0.103
-O(10)	3.055(4)	0.083	3.085(1)	0.076	-------	

Figure 4.5.IV shows the relationship of the cations in the K(2) cavity to the Ti-O_6 coordination. The bond orders of the cation-oxygen bond decrease on substitution of the smaller cation, so the effect of the cation on O(9) is not electronic, (that is, to weaken its titanyl bond by strengthening the Na-O interaction). However, the Na(2)-O(9) bond is shorter than the K-O bond, which may cause the Ti-O-Ti angle to decrease, (either through movement of the O(9) or repulsion of the Ti atoms), lowering the O(9) bond order through steric interactions. This angle increases to 137.1° in RTP, as expected for a larger cation.

4.6 Ramifications for powder refinements

In the light of the single crystal results, the powder data from Chapter three were reanalysed to ascertain whether they were sufficiently sensitive to detect the individual sites occupied by cations. Only in the NRTP case was the refinement stable and chemically reasonable, but the figures of merit were not significantly improved.

Figure 4.5.IV A view of the TiO_6 chains in the KNTP structure down the [001] direction, with O(9) atoms drawn as open ellipsoids, Na(2) as shaded circles and K(2) as shaded ellipsoids.

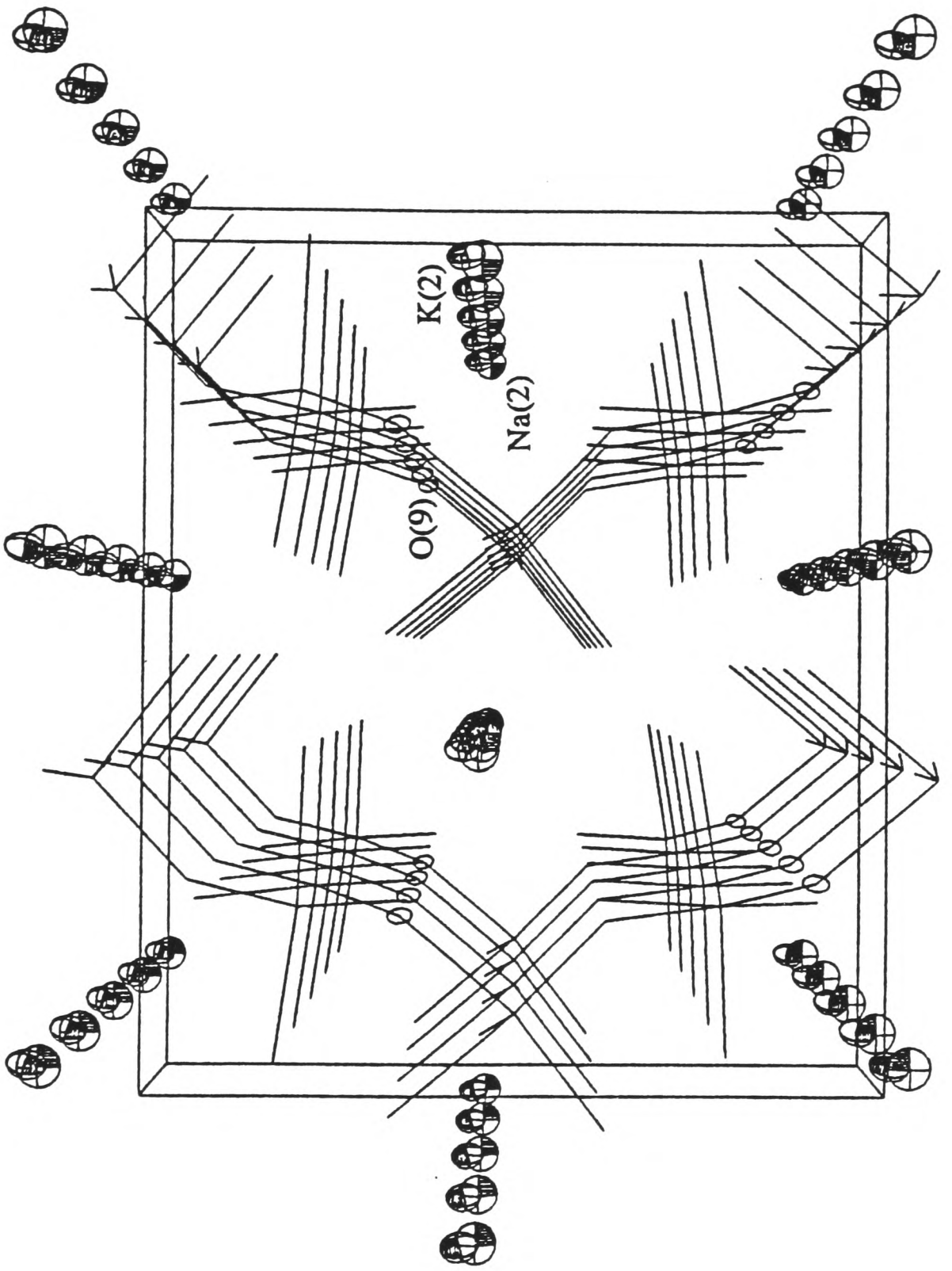


Table 4.6.1 Bond valence and refinement parameters for NRTP.

	Na	Rb	Na	Rb	χ^2	wR_p
fixed sites	0.74	2.58	0.39	1.36	5.253	7.10
separate sites	0.74	3.99	0.38	1.33	5.277	7.08

These results indicate that separate cation sites within a KTP cavity cannot, in general, be distinguished using powder diffraction data, even when the separate sites are known to exist from single-crystal work.

The results presented in this chapter have been accepted for publication in *Chem. of Mater.*.

CHAPTER FIVE

5.1 Introduction

Chapters three and four described the substitution of various cations into the cavities of the TiO_6-PO_4 framework of KTP, either during synthesis or by ion exchange into KTP, and the effect of this exchange on the framework. However the versatility of the KTP structure has been further demonstrated by the substitution for Ti, P and O in the framework itself.[57] Sn[168], Ge[169], Zr[57] and V[170] can be substituted for Ti during synthesis, while mixed valence materials such as $KFe_{0.5}Nb_{0.5}OPO_4$, $KMg_{0.33}Nb_{0.66}OPO_4$ and $KGa_{0.5}Nb_{0.5}OPO_4$[57] have also been synthesised. Metals in other oxidation states can also be charge balanced in the KTP structure by simultaneous substitution for other atoms in the framework, for example Sb(V) in $KSbOSiO_4$[171], $KSbOGeO_4$[172] and Fe(III) in $KFeOPO_4F$[57]. As yet, no substitution has been found to improve the nonlinear optical properties of KTP except the substitution of As for P[154,155,173] which, according to one report, increases the SHG figure of merit by a factor of 2.3.[150]

This chapter describes an investigation of the structure and properties of 50% framework-substituted KTP isomorphs prepared by both flux and solid state methods, Sn and Ge substituting for Ti and As for P. The nonlinear optical properties of $KTiO(P_{1-x}As_x)O_4$ were measured by the powder method and compared with the structural developments across the solid solution.

5.2 Sn substitution into KTP isomorphs

5.2.1 Synthesis of $MTi_{1-x}Sn_xOPO_4$ solid solutions

All Sn KTP isomorphs were made by solid state techniques since Sn was not incorporated into the KTP product from fluxes containing a mixture of TiO_2 and SnO_2. The reactions used were:

$$2KH_2PO_4 + TiO_2 + SnO_2 \rightarrow 2KSn_{0.5}Ti_{0.5}OPO_4 \text{ (KSTP)} + 2H_2O$$

$$Rb_2CO_3 + SnO_2 + TiO_2 + 2NH_4H_2PO_4 \rightarrow 2RbSn_{0.5}Ti_{0.5}OPO_4 \text{ (RSTP)} + CO_2 + 3H_2O + 2NH_3$$

Both samples were fired at 950°C for three days with daily grinding. Analytical electron microscopy carried out on the products confirmed their composition:

KSTP $c_{Ti} = 0.53(3)c_P$ RSTP $c_{Ti} = 0.59(4)c_P$

together with a SnO_2 (cassiterite) impurity revealed in preliminary X-ray diffraction patterns.

5.2.2 Powder diffraction study of KSTP

Room temperature neutron diffraction data were collected on the General Purpose Powder Diffractometer (GPPD) at Argonne National Lab. The starting model for the analysis was taken from a single crystal study of KTP[159] with the Sn occupying 50% of both Ti sites. The cassiterite structure was taken from the literature[174] and its parameters were not refined.

The neutron data were analysed using the RIETVELD code developed at Argonne. When the atomic coordinates were allowed to refine, the Ti(1) site was unstable and, since Ti(1) y was being used to fix the floating origin along y, every y coordinate had large e.s.d.s. The occupancy of Ti(1) had refined to (63%Ti + 37%Sn) which gave rise to a weighted average scattering length at this site of approximately zero:

b(Ti(1)) = (0.639 x −0.344) + (0.361 x 0.623) = 0.005×10^{-14}m.

A difference Fourier map calculated with Ti(1) removed did not reveal any scattering at that site, and the residuals and e.s.d.s on the coordinates of the other atoms did not increase in least squares cycles without Ti(1). Thus the neutron diffraction data was totally insensitive to the Ti(1) position.

To define this site, a combined neutron and X-ray data analysis was undertaken in GSAS, the X-ray data enabling the Ti(1) site to be located and precise Ti(1)-O bond lengths to be determined. The O(1) y parameter was used to define the origin along y, and a soft constraint was applied to the P-O bonds, restricting them to the range 1.540(5)Å in view of the large number of parameters in the refinement. Isotropic thermal parameters were restricted to a single value for each atom type and the total occupancy on each Ti site was constrained to be unity, but the overall composition was not constrained. The data collection parameters are given in Table 5.2.2.1, atomic coordinates and thermal parameters in Table 5.2.2.2 and selected bond lengths and angles in Table 5.2.2.3. The final profile plots are shown in Figure 5.2.2.I.

Discussion.

A precise determination of the structure of KSTP has been carried out by combined analysis of neutron and X-ray data. There is partial ordering over the two Ti sites, Ti preferentially occupying site 1 (63.9(4)%Ti, 36.1(4)%Sn; site 2 35.4(5)%Ti, 64.6(5)%Sn), giving an overall formula of $K(Sn_{0.503}Ti_{0.497})OPO_4$, in good agreement with the target composition. Sn preferentially occupies the less distorted *trans*-linking octahedra, presumably because the oxygens around

Table 5.2.2.1 Data collection and refinement parameters for $KSn_{0.5}Ti_{0.5}OPO_4$.

Data Collection	neutron		X-ray
Diffractometer	GPPD, Argonne National Lab. 90°	148°	Scintag PAD V Cu K_α
Data range Step	3.84-30.5	4-30.5ms	10-80°2θ 0.020,
Contributing reflections	3020	3056	646
Total number of Observations	11468 (for combined refinement)		
Sample can	V cylinder	V cylinder	flat plate
R_p %	2.81	3.46	9.35
wR_p %	4.28	6.45	12.01
$R_{expected}$ %	1.85	3.39	5.75
x^2(combined)	4.365		

Phase 1: $K(Sn_{0.5}Ti_{0.5})OPO_4$

Space group *P n 2₁ a*

Unit cell a=12.9764(3) b=10.6461(2) c=6.4669(1)Å
V=893.38(2)Å³

Phase 2: SnO_2 (cassiterite)[1174]

space group *P 4₂ 2₁ 2*

atom parameters and cell unrefined

Scattering lengths[1173] $\times 10^{-14}$m K:0.367 Ti:-0.344 Sn:0.6228 P:0.513 O:0.5805

Programs RIETVELD (neutron data only)
GSAS (combined neutron and X-ray)

No. of parameters 91

Neutron model background: 8 term cosine Fourier series
peak shape: Gaussian convoluted with double exponential
90° σ_1:407(7) σ_2:10(2)
148° σ_1:393(16) σ_2:35(4)

X-ray model background: 3 term cosine Fourier series
peak shape: Pseudo-Voigt
V:373(7) W:-67.4(7) X:6.38(8)
asym:2.83(7) shift:-1.098(7)

Table 5.2.2.2 Atom coordinates and isotropic thermal parameters of $K(Sn_{0.5}Ti_{0.5})OPO_4$

	x	y	z	U_{iso}(Å^2)	occupancy
Ti(1)	0.3749(3)	-.0062(12)	0.4988(15)	0.0105(16)	0.639(4)
Sn(1)	0.3749(3)	-.0062(12)	0.4988(15)	0.0101(9)	0.361(4)
Ti(2)	0.2478(6)	0.2389(11)	0.2533(11)	0.0105(16)	0.354(5)
Sn(2)	0.2478(6)	0.2389(11)	0.2533(11)	0.0101(9)	0.646(5)
P(1)	0.4960(4)	0.2457(6)	0.3420(4)	0.0049(5)	
P(2)	0.1781(2)	0.4899(8)	0.4995(13)	0.0049(5)	
K(1)	0.3795(5)	0.2917(8)	0.7785(10)	0.0231(12)	
K(2)	0.1093(6)	0.0565(9)	0.6971(10)	0.0231(12)	
O(1)	0.4837(5)	0.1319	0.4878(12)	0.0085(4)	
O(2)	0.5102(6)	0.3673(5)	0.4707(11)	0.0085(4)	
O(3)	0.4014(4)	0.2634(9)	0.1994(11)	0.0085(4)	
O(4)	0.5901(4)	0.2235(8)	0.2005(9)	0.0085(4)	
O(5)	0.1096(7)	0.5216(8)	0.3124(11)	0.0085(4)	
O(6)	0.1085(6)	0.4680(9)	0.6882(11)	0.0085(4)	
O(7)	0.2473(5)	0.6043(7)	0.5426(10)	0.0085(4)	
O(8)	0.2518(5)	0.3789(7)	0.4723(10)	0.0085(4)	
O(9)	0.2314(4)	0.6213(8)	-.0179(10)	0.0085(4)	
O(10)	0.2203(4)	0.3652(8)	0.0421(10)	0.0085(4)	

Table 5.2.2.3 Selected bond lengths (Å) in $K(Sn_{0.5}Ti_{0.5})OPO_4$ and KTP[743].

		KSTP	KTP			KSTP	KTP
Ti(1)	-O(1)	2.04(1)	2.161(4)	Ti(2)	-O(3)	2.04(1)	2.037(3)
	-O(2)	2.02(1)	1.957(4)		-O(4)	2.07(1)	1.979(3)
	-O(5)	2.06(1)	2.047(4)		-O(7)	1.98(1)	1.966(4)
	-O(6)	2.04(1)	1.900(4)		-O(8)	2.06(1)	1.994(4)
	-O(9)	1.94(1)	1.993(4)		-O(9)	1.96(1)	1.738(4)
	-O(10)	1.87(1)	1.718(4)		-O(10)	1.95(1)	2.101(4)
mean		2.00(3)	1.96(6)			2.01(2)	1.97(5)
Δ		0.19(1)	0.443(6)			0.12(1)	0.363(6)
P(1)	-O(1)	1.544(3)		P(2)	-O(5)	1.539(3)	
	-O(2)	1.550(3)			-O(6)	1.536(3)	
	-O(3)	1.547(3)			-O(7)	1.538(3)	
	-O(4)	1.544(3)			-O(8)	1.531(3)	
K(1)	-O(1)	2.874(9)	2.900(4)	K(2)	-O(1)	2.73(1)	2.679(4)
	-O(2)	2.74(1)	2.743(4)		-O(2)	3.10(1)	2.979(4)
	-O(3)	2.754(9)	2.717(4)		-O(3)	3.12(1)	3.046(4)
	-O(5)	2.89(1)	2.874(4)		-O(4)	3.136(8)	3.125(4)
	-O(7)	3.10(1)	3.059(4)		-O(5)	2.87(1)	2.799(4)
	-O(8)	2.74(1)	2.762(4)		-O(7)	2.95(1)	2.917(4)
	-O(9)	3.01(1)	2.987(4)		-O(8)	3.16(1)	3.044(4)
	-O(10)	2.790(9)	2.717(4)		-O(9)	2.59(1)	2.765(4)
					-O(10)	3.17(1)	3.055(4)
mean		2.86(13)	2.84(12)			2.98(20)	2.93(15)

Figure 5.2.2.Ia Observed (dots), calculated (continuous curve) and difference plots of the GPPD 148° data for $K(Sn_{0.5}Ti_{0.5})OPO_4$.

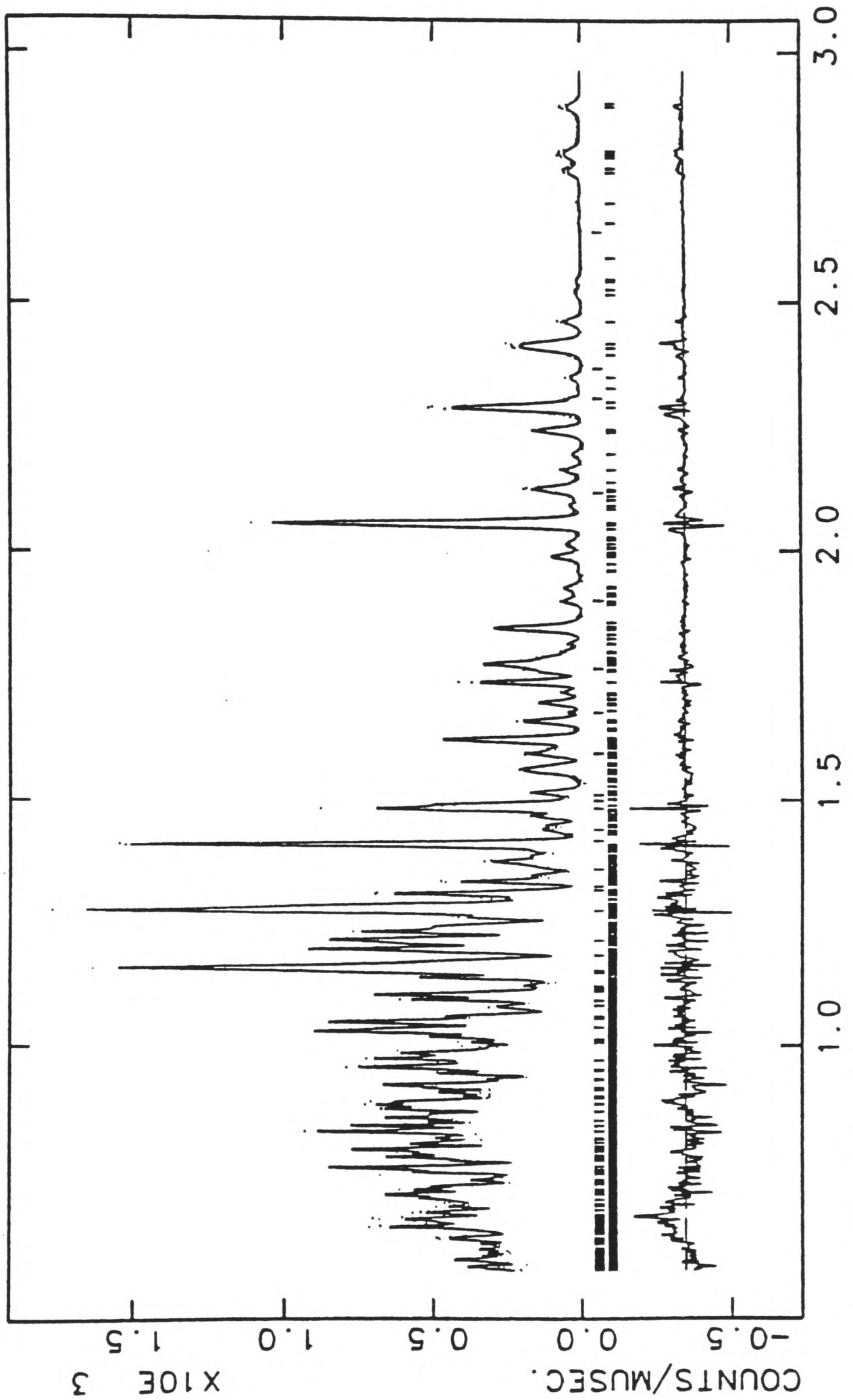


Figure 5.2.2.Ib Observed (dots), calculated (continuous curve) and difference plots of the GPPD 90° data for $K(Sn_{0.5}Ti_{0.5})OPO_4$.

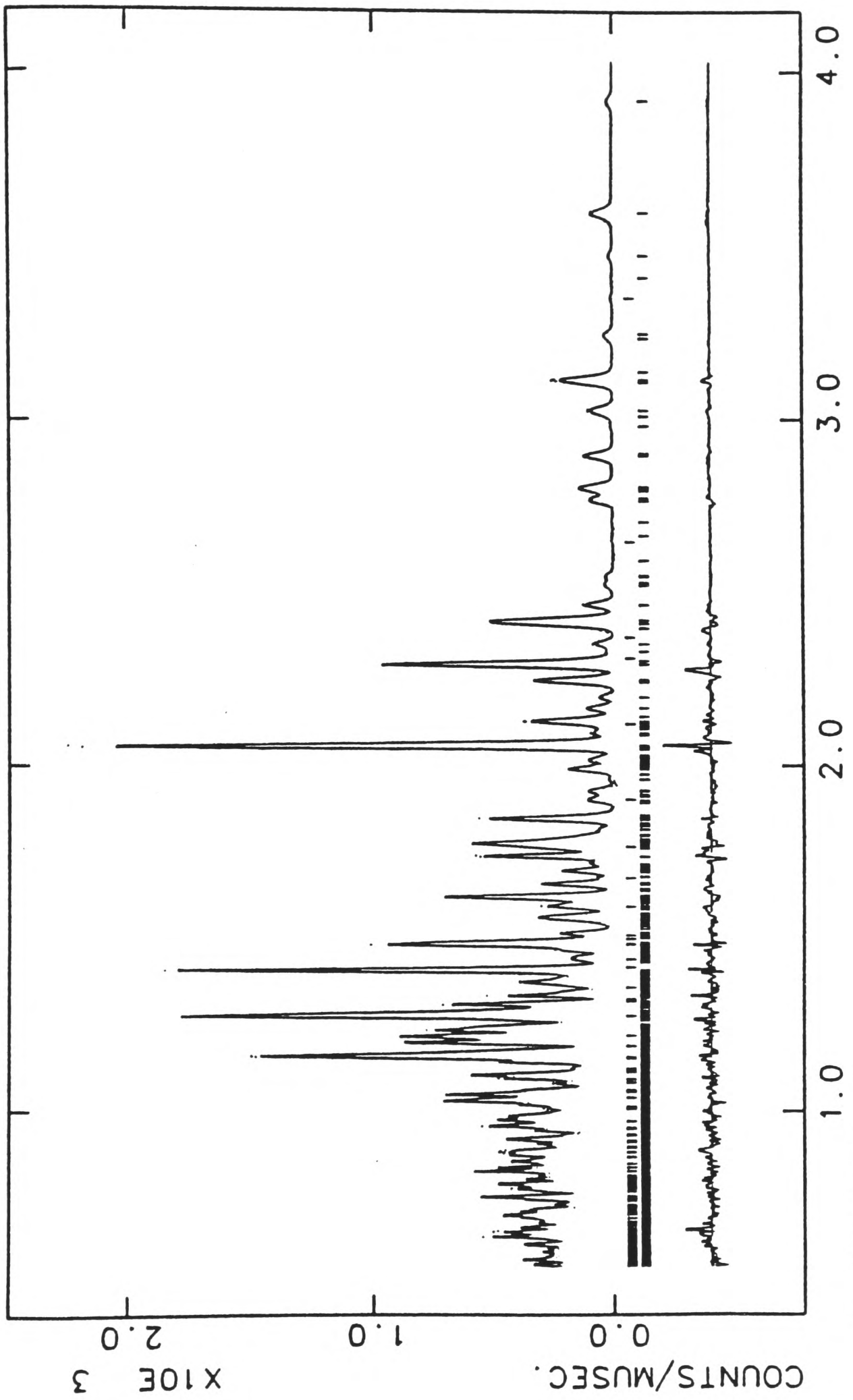
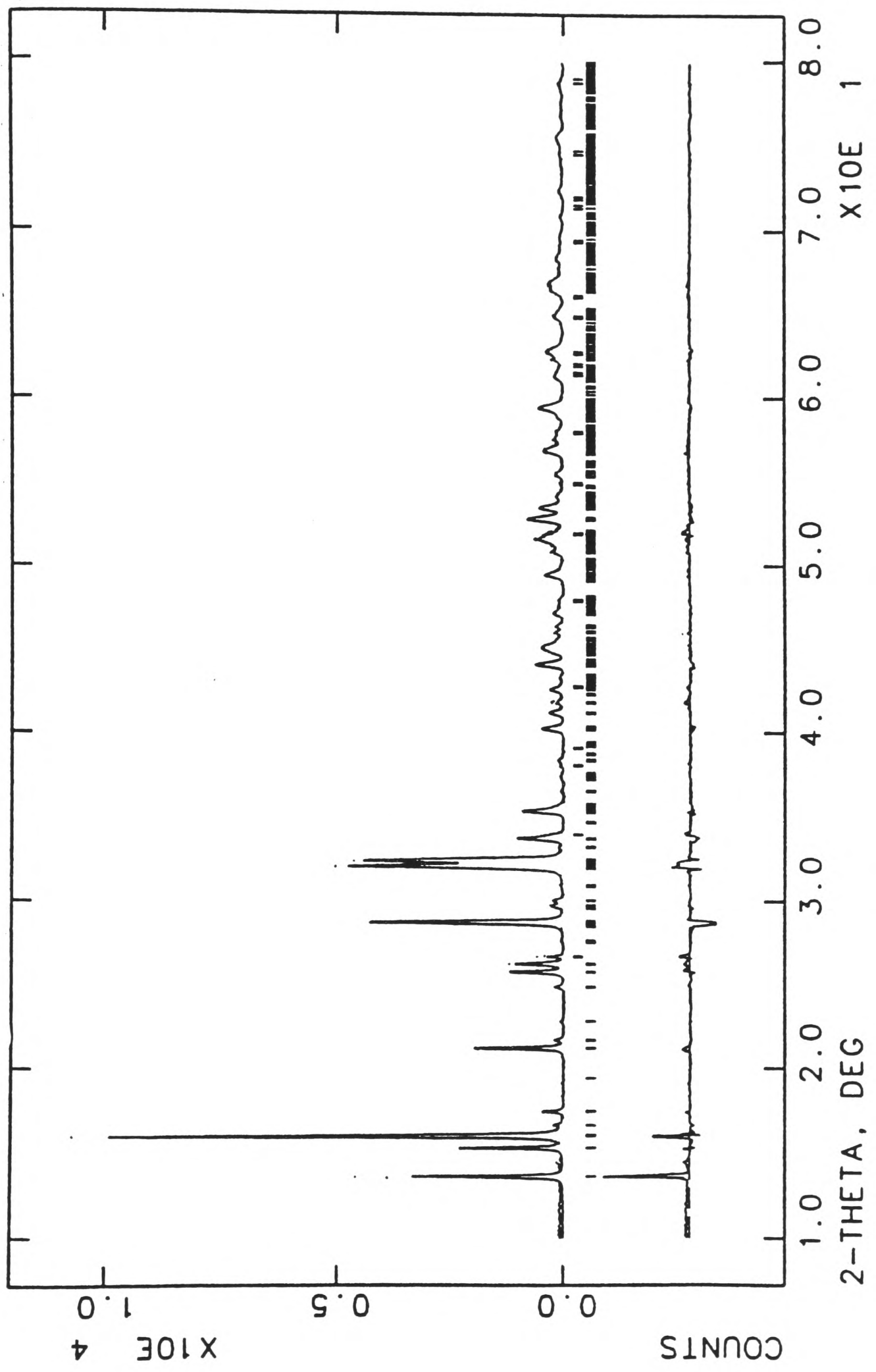


Figure 5.2.2.Ic Observed (dots), calculated (continuous curve) and difference plots of the X-ray data for $K(Sn_{0.5}Ti_{0.5})OPO_4$.



this site will more readily form a regular SnO_6 octahedron. The distortion of the TiO_6 octahedra has been suggested[175] to be ferroelectric in origin, stabilised by $d\pi$-$p\pi$ bonding between Ti and the bridging oxygens. The SnO_6 octahedra have been found to be regular in the pure Sn end member $KSnOPO_4$,[166] as the Sn 5d orbitals are too high in energy to permit $d\pi$-$p\pi$ bonding. The average bond lengths around the Ti(1) and Ti(2) sites are longer than in KTP as expected on substitution of the larger Sn atom, and the distortion around Ti(1), as measured by Δ, is marginally greater than that around Ti(2), in agreement with the greater proportion of Ti found in site 1. The marginal increase in K-O bond lengths is consistent with the increase in framework size.

The intensity of SHG measured from powdered materials in the $KSn_xTi_{1-x}OPO_4$ series has been measured,[175] and decreases with increasing Sn content until no SHG is observed at KSP when $x = 1$. The distortion within the TiO_6 octahedra and the alternation of long and short Ti-O bonds through the TiO_6 helices are thought to be responsible for the large nonlinear coefficients of KTP.[57] As Sn substitutes into the chains, the reduction in SHG can be explained by the gradual removal of both the charge-transfer character of the chain and the octahedral distortion as regular SnO_6 replace distorted TiO_6 octahedra. Since Sn substitutes preferentially into the Ti(2) site, the SHG should decrease rapidly to the point at which all these sites were filled with Sn, (when the alternation of long-short Ti-O bonds is removed throughout the structure), and then decrease more slowly to $x = 1$ when all octahedra are regular. Unfortunately the powder SHG measurements are not sufficiently precise to test this hypothesis.

5.2.3 X-ray powder diffraction study of $Rb(Sn_{0.5}Ti_{0.5})OPO_4$.

The X-ray powder diffraction data were collected on a STOE STADI-P diffractometer. The starting model was again taken from a single crystal diffraction study of KTP[743], with 50%Sn in each of the Ti sites. Due to the paucity of data, the thermal parameters were fixed at the values obtained for KSTP and not refined. The Ti/Sn(1) y parameter was not refined in order to fix the floating origin along y. Data collection parameters are given in Table 5.2.3.1, atom coordinates and thermal parameters in Table 5.2.3.2. The final profile plot is presented in Figure 5.2.3.I.

Discussion

The structure of RSTP has been determined by powder X-ray diffraction. The lack of neutron diffraction data means that all atom coordinates are imprecise, leading to large e.s.d.s on the bond lengths. Even with the P-O bond lengths constrained to lie within 1.54(1)A, the Ti-O values cover a considerably wider range than those in either KSTP or RTP, so conclusions cannot be reliably drawn about the level of residual TiO_6 distortion after 50% substitution by Sn.

Table 5.2.3.1 Ti-O bond lengths (A) in RSTP compared with KSTP and RTP[1593].

	RSTP	KSTP	RTP		RSTP	KSTP	RTP
Ti1-O1	2.13(6)	2.04(1)	2.133(7)	Ti2-O3	2.00(4)	2.04(1)	2.058(5)
-O2	1.97(4)	2.02(1)	1.950(7)	-O3	2.03(4)	2.07(1)	2.021(5)
-O5	2.09(4)	2.06(1)	2.081(8)	-O7	1.81(4)	1.98(1)	1.976(8)
-O6	2.21(5)	2.04(1)	2.029(8)	-O8	2.41(6)	2.06(1)	2.000(9)
-O9	2.09(6)	1.94(1)	1.971(7)	-O9	2.25(5)	1.96(1)	1.736(8)
-O10	1.79(6)	1.87(1)	1.711(7)	-O10	1.83(5)	1.95(1)	2.098(8)
mean	2.05(13)	2.00(7)	1.98(13)		2.1(2)	2.01(5)	1.98(12)
Δ	0.42(8)	0.19(1)	0.422(10)		0.58(8)	0.12(1)	0.36(1)

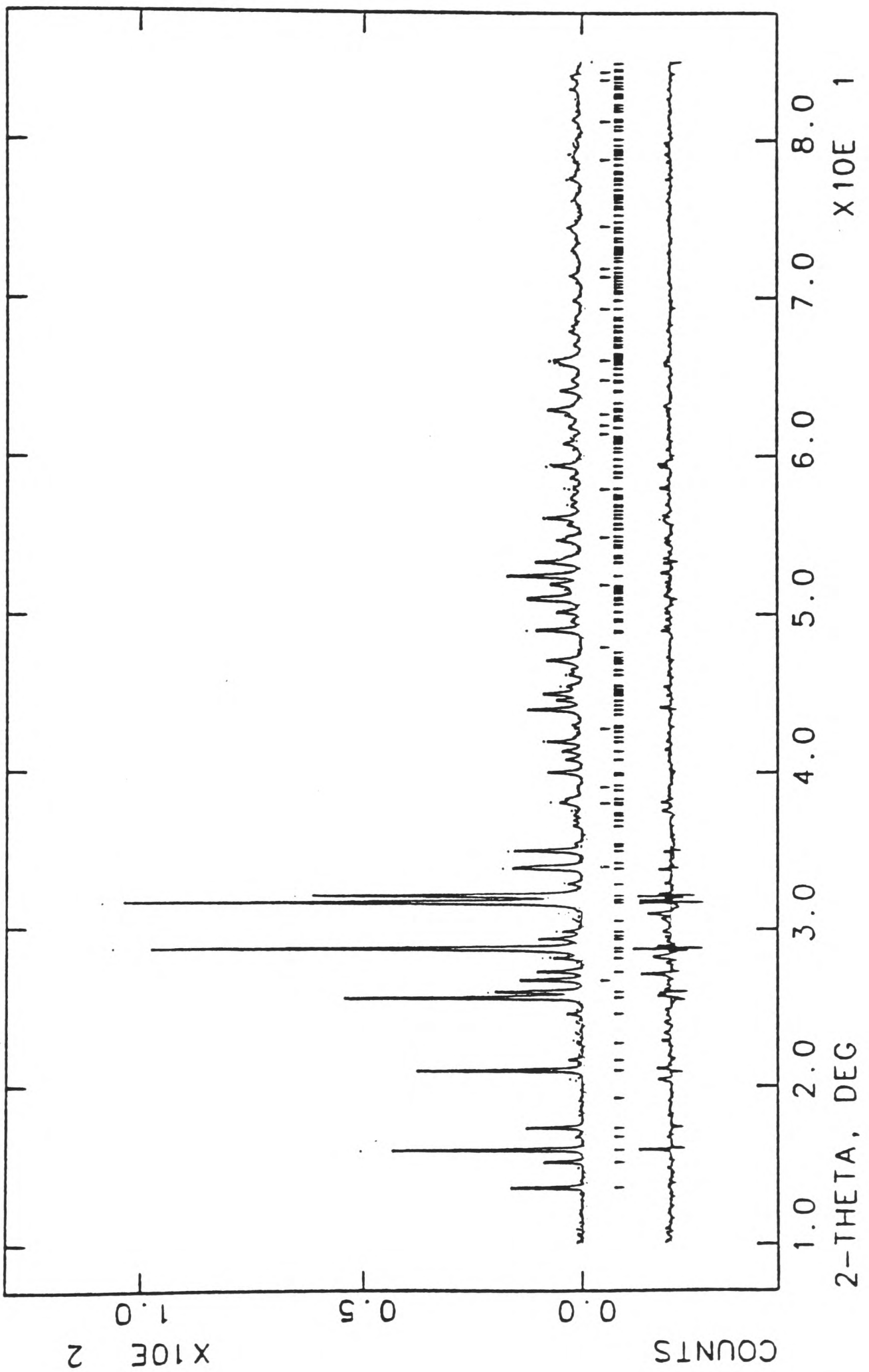
Table 5.2.3.2 Data collection and refinement parameters for $Rb(Sn_{0.5}Ti_{0.5})OPO_4$.

X-ray data collection	
Diffractometer	STOE Stadi-P
Radiation	Cu $K_{\alpha 1}$
Data range	5-80°2θ
Step	0.014°
Contributing reflections	357
Total number of observations	3757
R_p %	9.11
wR_p %	12.02
$R_{expected}$ %	12.89
x^2	0.884
Refinement parameters	
Space group	$Pn2_1a$
Unit cell	a=13.1316(9) b=10.6140(7) c=6.5655(5) V=915.1(2)
no.of parameters	69
background	5 term cosine Fourier series
Peak shape	Pseudo-Voigt GW:21.0(8) LX:-3.1(3) LY:35(1) asym .07(2)

Table 5.2.3.3 Atom coordinates and thermal parameters of $Rb(Sn_{0.5}Ti_{0.5})OPO_4$.

	x	y	z	$U_{iso}(A^2)$	occupancy
Ti(1)	0.3721(6)	0.000	0.5040(21)	.01	0.623(15)
Sn(1)	0.3721(6)	0.000	0.5040(21)	.01	0.377(15)
Ti(2)	0.2504(9)	0.2420(24)	0.2409(15)	.01	0.308(16)
Sn(2)	0.2504(9)	0.2420(24)	0.2409(15)	.01	0.692(16)
P(1)	0.4913(22)	0.252(4)	0.3332(30)	.0049	
P(2)	0.1728(16)	0.509(4)	0.513(5)	.0049	
Rb(1)	0.3843(10)	0.3210(17)	0.7837(15)	.023	
Rb(2)	0.1016(8)	0.0689(17)	0.6903(16)	.023	
O(1)	0.482(6)	0.147(4)	0.493(6)	.0085	
O(2)	0.526(5)	0.365(4)	0.462(8)	.0085	
O(3)	0.399(3)	0.275(6)	0.193(6)	.0085	
O(4)	0.596(3)	0.238(6)	0.231(7)	.0085	
O(5)	0.115(4)	0.540(5)	0.314(6)	.0085	
O(6)	0.098(4)	0.463(5)	0.678(7)	.0085	
O(7)	0.255(4)	0.602(4)	0.584(6)	.0085	
O(8)	0.247(3)	0.397(4)	0.509(11)	.0085	
O(9)	0.243(5)	0.635(5)	0.036(9)	.0085	
O(10)	0.206(4)	0.369(5)	0.076(9)	.0085	

Figure 5.2.3.I Observed (dots), calculated (continuous curve) and difference plots of the X-ray data from $Rb(Sn_{0.5}Ti_{0.5})OPO_4$.



However the data are sensitive to partial ordering over the two Ti sites in RSTP, Sn preferentially substituting onto site 2 (site 1: 62%Ti, 38%Sn site 2 31%Ti, 69%Sn). This degree of ordering is indistinguishable from that seen in KSTP, indicating that the substitution of the larger Rb cation into the cavities does not significantly alter the TiO_6-PO_4 framework.

Bond valence calculations[136]

Bond valence calculations have been carried out on KSTP, RSTP and the solid solution end-members for which structures have been reported (Table 5.2.3.4). The values for RSTP are unreliable due to the large e.s.d.s on bond lengths, but they follow the same trends as those for KSTP. The valence parameters for KTP, RTP and KSP are close to the ideal value of 4 for both Ti and Sn. However the valence parameters for Ti and Sn in KSTP seem to indicate that the sites are too large for Ti(IV) and too small for Sn(IV). In reality the individual sites are probably of the correct size for the ion contained within them, but the bond valence sums are calculated using the weighted average Ti-O and Sn-O bond lengths measured over the whole structure. The parameters obtained for the mixed species KSTP reflects the ordering obtained, since those of Ti(1) and Sn(2) are more favourable than those for Sn(1) and Ti(2). The greater amount of, for example Ti in site 1, will make the weighted average bond lengths obtained around site 1 closer to the ideal for Ti.

Table 5.2.3.4 Valence parameters calculated[136] for KSTP, RSTP and the solid solution end-members KTP[74], RTP[159] and KSP[168].

	Ti(1)	Sn(1)	Ti(2)	Sn(2)
KTP	4.17(2)		4.17(2)	
KSTP	3.77(5)	4.81(6)	3.58(5)	4.57(6)
RSTP	3.4(2)	4.4(3)	3.6(2)	4.6(3)
RTP		4.15(3)		4.05(4)
KSP		4.10(5)		4.12(5)

There is partial ordering over the two Ti sites in $M(Sn_{0.5}Ti_{0.5})OPO_4$ compounds, Ti preferentially occupying the more distorted Ti(1) site. This ordering of the TiO_6–PO_4 framework is unaffected by the exchange of Rb for K in the framework cavities.

5.3 A combined X-ray and neutron time-of-flight powder diffraction study of $KGe_{0.5}Ti_{0.5}OPO_4$.

A sample of $K(Ge_{0.5}Ti_{0.5})OPO_4$ (KGTP) was prepared by the high temperature solid state reaction:

$$K_2CO_3 + TiO_2 + GeO_2 + 2NH_4H_2PO_4 \rightarrow 2KGe_{0.5}Ti_{0.5}OPO_4 \text{ (KGTP)} + CO_2 + 2NH_3 + 3H_2O$$

The conditions under which the material could be prepared in a crystalline form were more restricted than for the other isomorphs. Calcination at 700°C was strictly necessary before final firing at 800°C, to prevent the powders from melting. The final heating temperature of 800°C is lower than had been used to produce the highly crystalline KTP solid solutions, but even after calcination, melting still took place at these higher temperatures. Analytical electron microscopy carried out on this sample (c_{Ti}=0.56(4)), was consistent with the $KTi_{0.5}Ge_{0.5}OPO_4$ target composition.

Time-of-flight neutron diffraction data were collected from KGTP on the GPPD diffractometer at Argonne National Lab., (run number 4743), and three banks of neutron data were included in the refinement. X-ray data were collected on a Philips diffractometer with Nicolet L11 automation using CuK_α radiation.

The structure of KSTP was used as the starting model in the Rietveld refinement of KGTP with Ge having an initial occupancy of 50% of each site. The total occupancy of each site was constrained to unity. The O(1) y coordinate was used to fix the floating origin along y, as the neutron scattering from the Ti(1) site more commonly used was close to zero. Restraints were applied to the P-O bond lengths, restricting them to the range 1.54(1)Å and thermal parameters were constrained to a single value for each atom type. When thermal parameters for Ti and Ge

were refined separately, those of Ti were larger, (0.02A^3), than those observed in other KTP isomorphs. Since Ge is considerably smaller than Ti (ionic radii 0.53, 0.68Å respectively), the thermal parameters may be an indication that the two atoms occupy different sites within the $(Ti/Ge)O_6$ octahedron. However, a difference Fourier map calculated with the Ti and Ge removed showed no clear positive and negative regions in the Ti(2) site that could be attributed to separate Ge and Ti sites. In subsequent refinements the thermal parameters of Ti and Ge were constrained to a single value.

X-ray data were added to the refinement to help define the Ti(1) site. The bond distances and angles improved markedly, and the presence of a GeO_2 impurity was revealed by a number of unindexed lines (Powder Diffraction File 36-1463). The structure of GeO_2 was taken from the literature[176], and used to model the impurity with the model parameters unrefined. The calculated peak shape for the neutron data appeared to be too broad, and not peaked enough to match the observed data. This indicated that the model used needed to be changed. A better fit was achieved by adding a Lorentzian component. This was modelled using the third GSAS time-of-flight neutron peak shape model, the convolution of a pseudo-Voigt with two exponentials. Final data collection and refinement parameters are given in Table 5.3.1, atom coordinates and thermal parameters in Table 5.3.2, selected bond distances and angles in Table 5.3.3, and final profile plots in Figure 5.3.I.

Discussion

The structure of KGTP has been refined using time-of-flight neutron and X-ray powder diffraction data. There is partial

Table 5.3.1 Data collection and refinement parameters for $K(Ge_{0.5}Ti_{0.5})OPO_4$.

Data collection	neutron			X-ray
Diffractometer	GPPD, Argonne National Lab.			Philips
	148°	90°	60°	Cu Kα
Data range	4.96-30.99	4.5-30.992	5-30.99ms	20-90 2θ
Contributing reflections	4367	3314	1201	776
Total number of observations	12873			
sample can	10mm vanadium can			flat plate
R_p %	3.70	4.08	4.72	9.63
wR_p %	5.43	5.72	6.68	12.35
R_I %	1.62	2.52	1.93	4.03
$R_{expected}$ %	1.6	1.51	2.57	4.46
χ^2	10.956			
Phase 1: $K(Ge_{0.5}Ti_{0.5})OPO_4$				
space group	$Pn2_1a$			
unit cell	a=12.6360(9), b=10.2895(7), c=6.3943(5)Å			
	$V=830.6(2)Å^3$			
Phase 2: GeO_2				
space group	$P3_22_1$			
atom parameters and cell unrefined				
Scattering lengths/10^{-14}m	K:0.367, Ge:0.8193, Ti:-0.3438, P:0.513, O:0.5805			
No. parameters	115			
Neutron model	Background: 8 term cosine Fourier series			
	Peak shape: Pseudo-Voigt convoluted with double exponential	148°	90°	60°
	σ_1	236(20)	136(14)	174(17)
	σ_2	-20(3)	14(2)	10(1)
	γ_1	40(1)	28.2(8)	17(1)
X-ray model	Background: 5 term cosine Fourier series			
	Peak shape: Pseudo-Voigt GW:39(7) LX:5(1) LY:42(4) asym.:11.9(7)			

Table 5.3.2 Atom coordinates and isotropic thermal parameters of $K(Ge_{0.5}Ti_{0.5})OPO_4$.

	x	y	z	$U_{iso}(Å^2)$	occupancy
Ti(1)	0.3679(6)	0.025(2)	0.496(3)	0.003(1)	0.767(4)
Ge(1)	0.3679(6)	0.025(2)	0.496(3)	0.003(1)	0.233(4)
Ti(2)	0.2459(7)	0.2834(9)	0.242(1)	0.003(1)	0.339(5)
Ge(2)	0.2459(7)	0.2834(9)	0.242(1)	0.003(1)	0.661(5)
P(1)	0.4971(5)	0.2708(5)	0.3366(4)	0.0034(5)	
P(2)	0.1831(2)	0.5382(7)	0.5093(9)	0.0034(5)	
K(1)	0.3811(7)	0.3429(9)	0.788(1)	0.016(1)	
K(2)	0.1128(7)	0.1034(8)	0.691(1)	0.016(1)	
O(1)	0.4819(4)	0.1497	0.4762(9)	0.0080(2)	
O(2)	0.5028(6)	0.3945(6)	0.4716(9)	0.0080(2)	
O(3)	0.3999(5)	0.2891(8)	0.189(1)	0.0080(2)	
O(4)	0.5959(5)	0.2536(8)	0.195(1)	0.0080(2)	
O(5)	0.1100(6)	0.5635(7)	0.320(1)	0.0080(2)	
O(6)	0.1139(6)	0.5027(7)	0.699(1)	0.0080(2)	
O(7)	0.2596(5)	0.6543(6)	0.535(1)	0.0080(2)	
O(8)	0.2549(5)	0.4227(6)	0.447(1)	0.0080(2)	
O(9)	0.2300(5)	0.6626(7)	-.053(1)	0.0080(2)	
O(10)	0.2221(5)	0.4019(7)	0.041(1)	0.0080(2)	

Table 5.3.3 Selected bond lengths (Å) and angles (°) in $K(Ge_{0.5}Ti_{0.5})OPO_4$, KTP[74] and KSTP.

		KGTP	KTP			KGTP	KTP
Ti(1)	-O(1)	1.93(1)	2.161(4)	Ti(2)	-O(3)	1.98(1)	2.037(3)
	-O(2)	2.12(1)	1.957(4)		-O(4)	1.96(1)	1.979(3)
	-O(5)	2.12(2)	2.047(4)		-O(7)	1.88(1)	1.966(4)
	-O(6)	1.93(2)	1.900(4)		-O(8)	1.94(1)	1.994(4)
	-O(9)	1.91(1)	1.993(4)		-O(9)	1.83(1)	1.738(4)
	-O(10)	1.72(1)	1.718(4)		-O(10)	1.80(1)	2.101(4)
Δ		0.40(3)	0.443(6)			0.18(1)	0.363(6)
mean		1.96(6)	1.96(6)			1.90(4)	1.97(5)
P(1)	-O(1)	1.544(3)		P(2)	-O(5)	1.546(3)	
	-O(2)	1.538(3)			-O(6)	1.538(3)	
	-O(3)	1.560(3)			-O(7)	1.544(3)	
	-O(4)	1.552(3)			-O(8)	1.548(3)	
K(1)	-O(1)	3.09(1)		K(2)	-O(1)	2.74(1)	
	-O(2)	2.59(1)			-O(2)	3.16(1)	
	-O(3)	2.637(9)			-O(3)	3.24(1)	
	-O(5)	2.881(9)			-O(4)	2.917(9)	
	-O(7)	3.068(9)			-O(5)	2.85(1)	
	-O(8)	2.82(1)			-O(7)	2.78(1)	
	-O(9)	3.19(1)			-O(8)	2.99(1)	
	-O(10)	2.65(1)			-O(9)	2.60(1)	
					-O(10)	3.092(9)	

	KGTP	KTP
Ti(1)-O(9)-Ti(2)	137.1(7)	135.5
Ti(1)-O(10)-Ti(2)	136.5(7)	132.9

Figure 5.3.Ia Observed (dots), calculated (continuous curve) and difference plots of GPPD 148° bank data on KGTP.

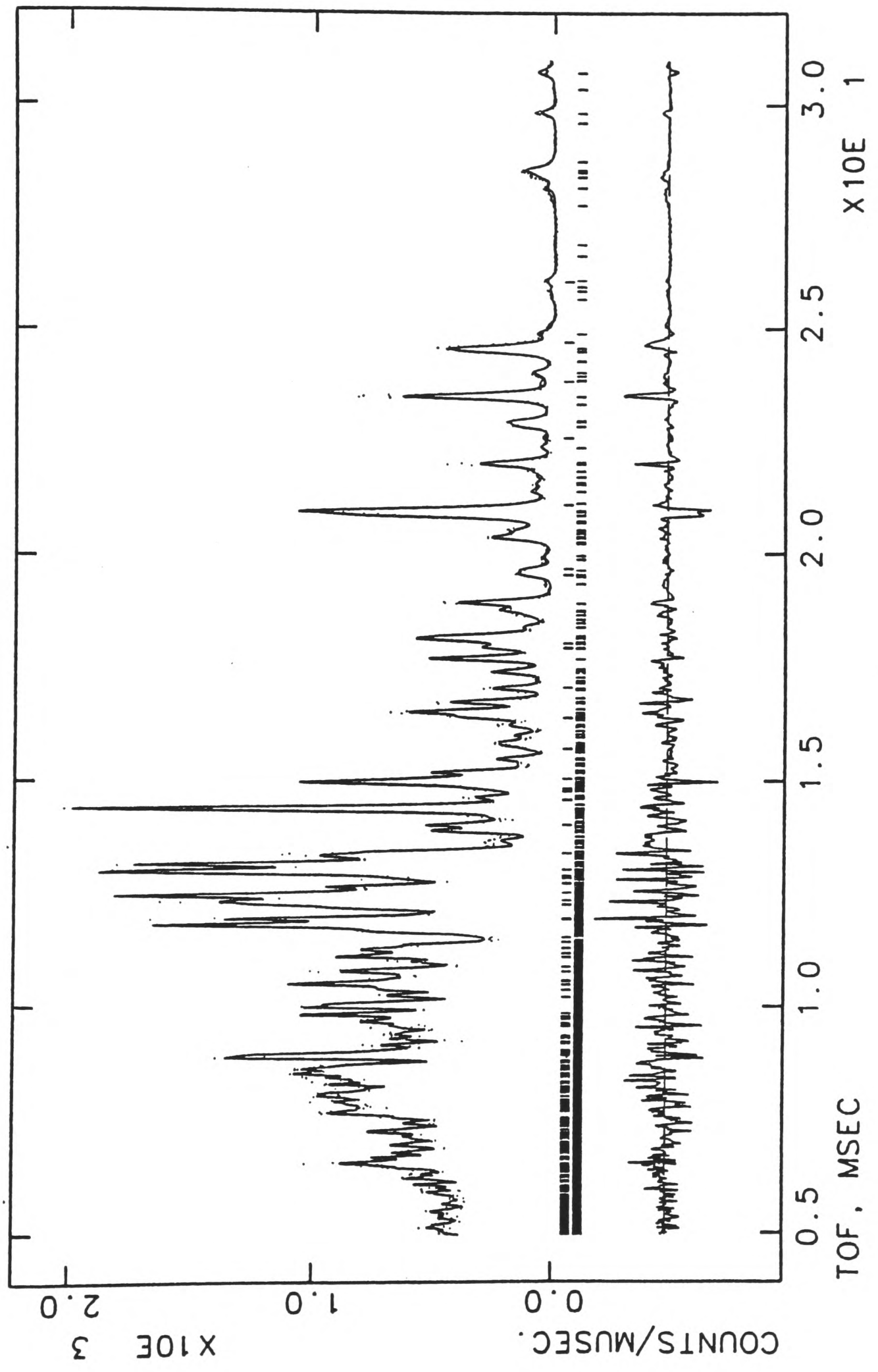


Figure 5.3.Ib Observed (dots), calculated (continuous curve) and difference plots of GPPD 90° bank data on KGTP.

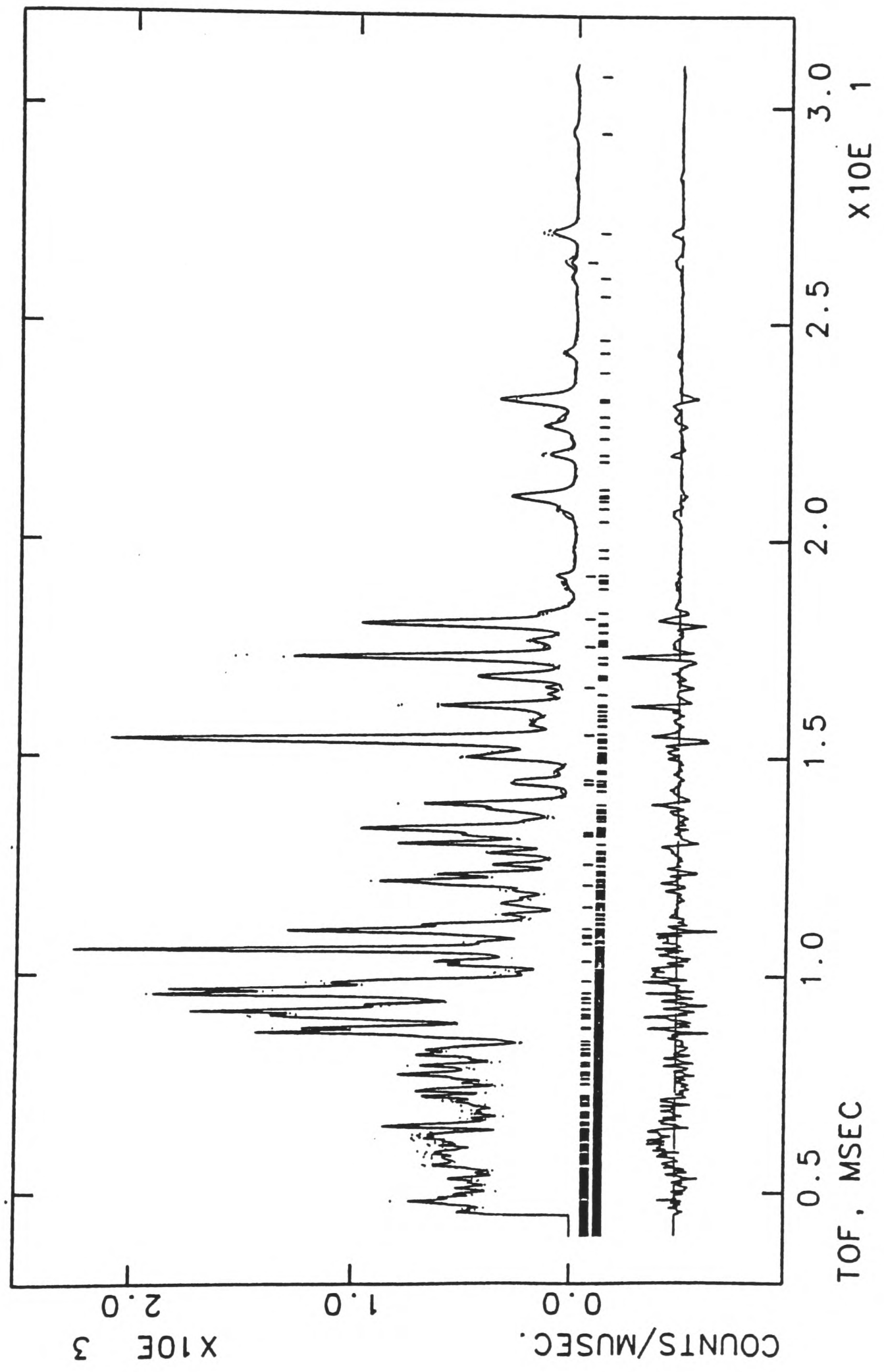


Figure 5.3.Ic Observed (dots), calculated (continuous curve) and difference plots of GPPD 60° bank data on KGTP.

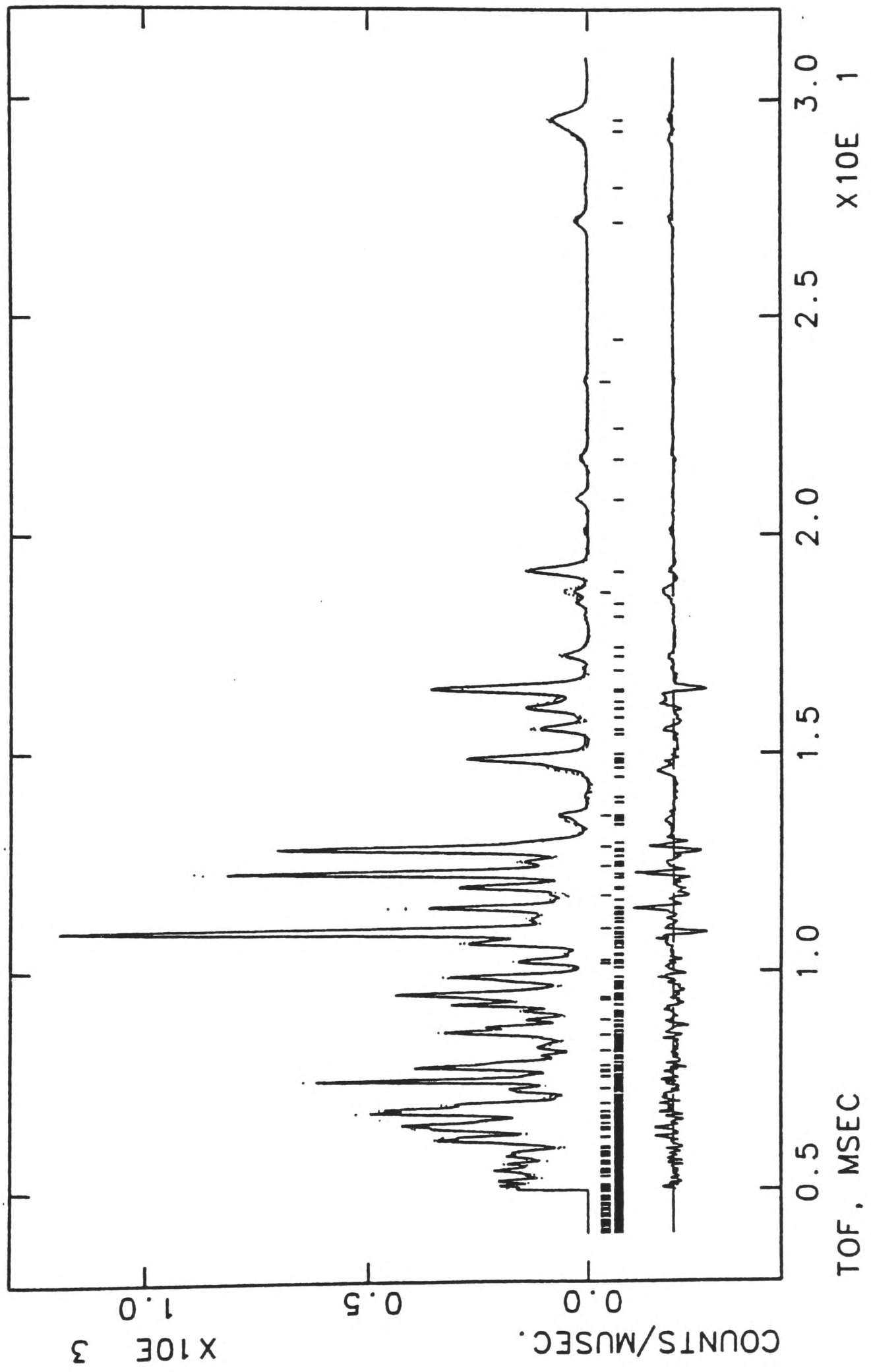
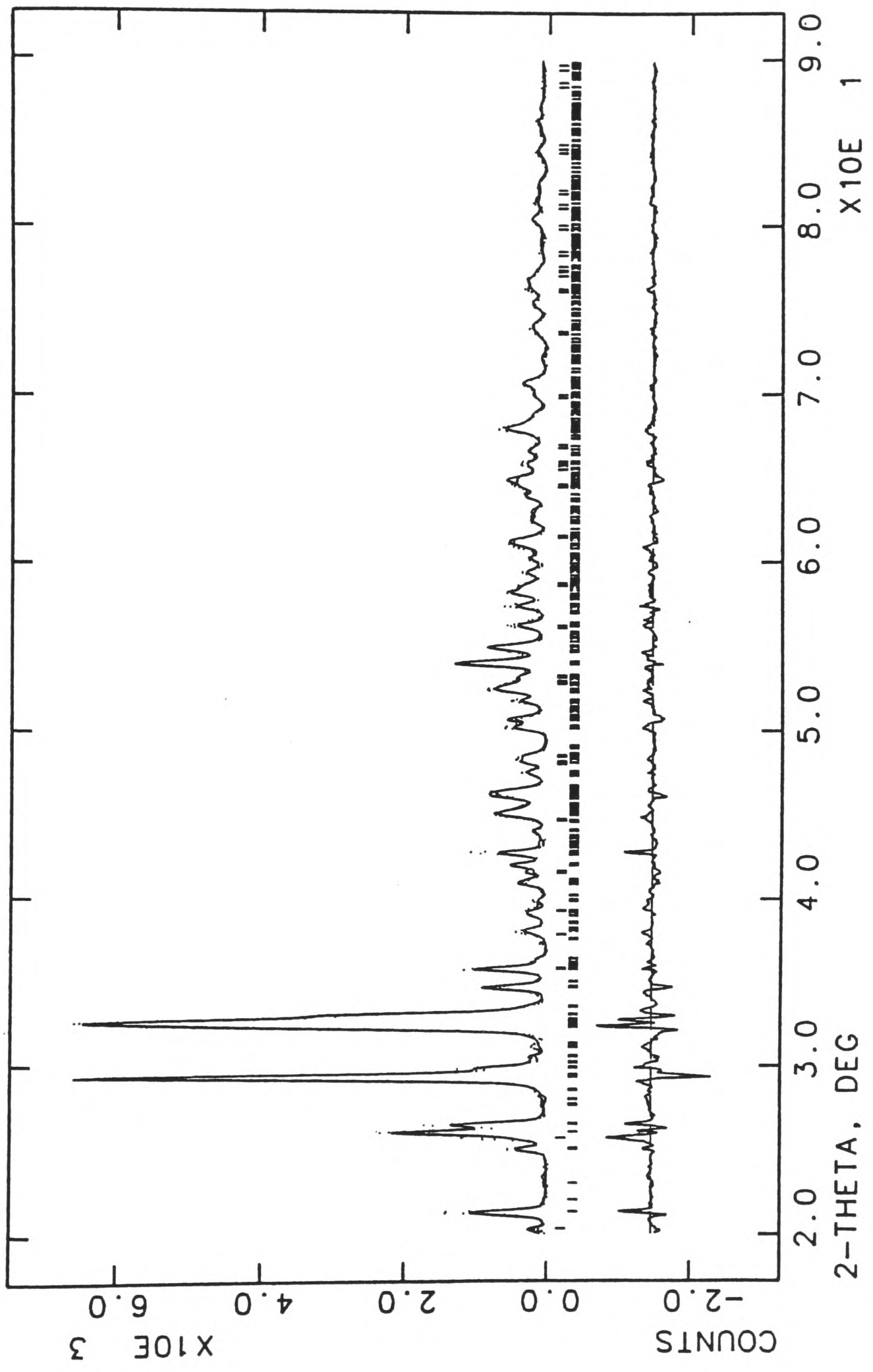


Figure 5.3.Id Observed (dots), calculated (continuous curve) and difference plots of X-ray diffraction data on KGTP.



ordering over the two Ti sites, Ge preferentially substituting into the Ti(2) sites. The ordering can also be seen from the Ti-O bond lengths, those around Ti(2) are shorter than those around Ti(1), as would be expected on majority substitution of the smaller Ge atom. The distortion in the $Ti(1)O_6$ octahedron as measured by Δ, is only marginally less than that in KTP, while that in $Ti(2)O_6$ is considerably lower, indicating that Ge adopts a more regular coordination.

To determine the sensitivity of the data to the Ti/Ge occupancy, the occupancies were fixed at the values shown below while the other parameters were refined. When the ordering was made complete the isotropic thermal parameters were larger than seen in other refinements while when the metal distribution was random they were negative. The residuals indicate that the refined composition gives the best fit to the data:

ordering		wR_p		χ^2
	148°	90°	60°	
refined occupancies	5.43	5.72	6.68	10.98
random occupancies	6.15	6.93	8.83	15.77
Ti(1),Ge(2) fully ordered	5.69	6.22	8.05	13.89

Bond valence calculations[1136] carried out for KGTP and KTP (Table 5.3.4) corroborate the refined occupancies, site 1 being more favourable for Ti and site 2 for Ge. The bond valence sum of Ti on the Ti(2) site is greater than that for KTP, indicating that the presence of the smaller Ge atom has reduced the size of the Ti(2) octahedron.

Table 5.3.4 Bond valence parameters calculated for KGTP, KSTP and KTP[743].

	site 1	site 2
$KTiOPO_4$	4.17(2)	4.17(2)
$K(Ti_{0.5}Ge_{0.5})OPO_4$		
Ti	4.30(9)	4.93(6)
Ge	3.59(7)	4.11(5)
$K(Ti_{0.5}Sn_{0.5})OPO_4$		
Ti	3.77(5)	3.58(5)
Sn	4.81(6)	4.57(6)

The Lorentzian component observed in the KGTP peak shape, but not in any other KTP isomorphs, is an indication of increased strain within the structure, perhaps due to the considerable difference in size between Ti and Ge. The difficulty of synthesis and relatively high $\chi^{(2)}$ may also reflect this strain.

The nonlinear optical properties of $K(Ti_{1-x}Ge_x)OPO_4$ would be expected to be similar to those of the KSTP solid solution series. In both cases, substitution takes place preferentially at the less distorted Ti(2) site. The SHG ability of a solid solution member will decrease rapidly as x increases, until all the Ti(2) sites contain the less distorted substituted atom. At this point the long range long-short bond alternation along the TiO_6 helices is broken as alternate octahedra in the helices are regular. This critical composition will be reached at a lower concentration of Ge than Sn due to the more complete ordering that occurs in the $K(Ti_{1-x}Ge_x)OPO_4$ solid solution. Any further decrease in SHG ability will be caused by the replacement of individual distorted octahedra, which are postulated to play a

smaller role in production of the large nonlinear optical coefficients.[57]

Refinement of the structure of $K(Ti_{1-x}Ge_x)OPO_4$ using combined X-ray and time-of-flight neutron diffraction data has shown that Ge substitutes preferentially into the Ti(2) sites in KTP, with a more regular octahedral coordination and provided evidence for some structural subtleties beyond the current capacity of Rietveld refinement.

5.4 As substitution into KTP isomorphs

Replacement of P by As is the only substitution that has been shown to improve the SHG properties of KTP.[150] This section reports the synthesis and structure of $KTiO(P_{0.5}As_{0.5})O_4$ (KTAP) and $RbTiO(P_{0.5}As_{0.5})O_4$ (RTAP), and SHG testing of the $KTiO(P_{1-x}As_x)O_4$ solid solution series.

5.5.1 Synthesis of $MTiO(P_{0.5}As_{0.5})O_4$ compounds (M=K,Rb)

Powder samples of these materials were made by high temperature solid state synthesis following the reactions:

$$K_2CO_3 + 2KH_2PO_4 + 4TiO_2 + 2NH_4H_2AsO_4 \rightarrow 4KTiO(P_{0.5}As_{0.5})O_4 + CO_2 + 2NH_3 + 5H_2O$$

$$Rb_2CO_3 + 2TiO_2 + NH_4H_2AsO_4 + NH_4H_2PO_4 \rightarrow 2RbTiO(P_{0.5}As_{0.5})O_4 + CO_2 + 2NH_3 + 5H_2O$$

The final synthesis temperature of 900°C was held for three days with daily grinding. The X-ray diffraction pattern of the KTAP sample indexed on the primitive orthorhombic cell:

a=12.9695(8) b=10.6898(7) c=6.4932(4)Å V=900.2(2)Å^3

which is close to the mean of the volumes of KTP and KTA (871 and 923Å^3 respectively) indicating that the $KTiO(P_{0.5}As_{0.5})O_4$ isomorph has been formed.

Single crystals were grown from a flux of general formula: $6KTiOAsO_4 + 4(4K_2WO_4 + As_2O_5 + K_2O)$ which had been found to be suitable for the growth of KTA crystals. A fraction of the As was replaced by P to synthesize $KTiO(P_{1-x}As_x)O_4$ materials where x = 0.25, 0.5 and 0.75, an approach which had not been successful in the preparation of Sn isomorphs. The starting materials were melted into a crucible, then held at 1000°C for 24 hours to equilibrate before being cooled slowly between 1000 and 700°C, (through the crystallisation temperature). After

prolonged boiling in deionised water, crystals were extracted from the flux whose diffraction pattern indexed on the following cells:

target	a	b	c	V	x
0.75	13.061(3)	10.738(3)	6.538(2)	917.0(4)	0.87
0.5	12.981(3)	10.669(3)	6.489(2)	898.7(4)	0.50
0.25	12.891(1)	10.635(2)	6.452(2)	885.0(3)	0.25

The composition (x) was deduced from a Vegard's Law plot of composition against unit cell volume.

5.4.2 Time-of-flight neutron powder diffraction study of $KTiO(P_{0.5}As_{0.5})O_4$ (KTAP)

Time of flight neutron powder diffraction data were collected on the powder KTAP sample at GPPD, Argonne National Lab., in run number 4741. The 148°, 90° and 60° banks were used in the structure refinement. The starting model was taken from a single crystal structure determination of KTP[159]. The thermal parameters were constrained to a single value for each atom type, with one parameter for both P and As. The Ti(1) y parameter was held to fix the floating origin along y and no P-O bond constraints were applied. Final data collection parameters are given in Table 5.4.2.1, atom coordinates and thermal parameters in Table 5.4.2.2 , selected bond distances and angles in Table 5.4.2.3 and final profile plots in Figure 5.4.2.I.

An X-ray data set was collected on a Scintag PADV diffractometer for use in a joint X-ray and neutron analysis of the KTAP structure. However the X-ray data were only poorly fitted by the model, (Figure 5.4.2.II), even when the neutron data were excluded from the refinement; the degree of ordering

Table 5.4.2.1 Data collection and refinement parameters of $KTiO(P_{0.5}As_{0.5})O_4$.

Diffractometer	GPPD, Argonne National Laboratory		
	148°	90°	60°
Data range (ms)	5.074-30.995	4.50-30.992	5.00-30.99
Total observations	11094		
Contributing reflections	4408	2520	396
Sample can	10mm vanadium can		
R_p %	2.60	2.98	3.96
wR_p %	4.10	4.05	5.34
R_I %	2.29	2.78	2.81
$R_{expected}$ %	1.61	1.51	2.57
x^2	6.241		
Model refinement			
Space group	$Pn2_1a$		
unit cell	a=12.9695(8) b=10.6896(7) c=6.4932(4)Å		
	$V=900.2(2)Å^3$		
scattering lengths ($\times10^{-14}$m)	K:0.367, Ti:-0.344, As:0.658, P:0.513, O:0.5805		
no. of parameters	96		
Diffractometer coefficients			
	148° bank	90° bank	60° bank
DIFC	unrefined	7697.3(8)	5443.2(8)
DIFA	-3.3(2)	-1.4(2)	-0.5(1)
Zero	-12.9(5)	-12.0(6)	-11.3(8)
Profile shape	Gaussian convoluted with double exponential		
	148° σ_1:91(2) σ_2:1.2(5)		
	90° σ_1:158(2) σ_2:4.1(5)		
	60° σ_1:218(3) σ_2:4.3(3)		
Background	8 term cosine Fourier series		

Table 5.4.2.2 Atom coordinates and isotropic thermal parameters of $KTiO(P_{0.5}As_{0.5})O_4$.

	x	y	z	$U_{iso}(Å^2)$	occupancy
Ti(1)	0.3719(2)	0	0.5004(12)	0.0081(6)	
Ti(2)	0.2513(5)	0.2471(11)	0.2749(7)	0.0081(6)	
P(1)	0.5003(4)	0.2557(8)	0.3305(3)	0.0049(2)	0.56(1)
As(1)	0.5003(4)	0.2557(8)	0.3305(3)	0.0049(2)	0.44(1)
P(2)	0.1799(1)	0.5074(9)	0.4992(8)	0.0049(2)	0.44(1)
As(2)	0.1799(1)	0.5074(9)	0.4992(8)	0.0049(2)	0.56(1)
K(1)	0.3797(4)	0.3117(9)	0.7877(8)	0.0172(6)	
K(2)	0.1113(4)	0.0625(9)	0.7003(8)	0.0172(6)	
O(1)	0.4852(3)	0.1423(7)	0.4925(5)	0.0092(1)	
O(2)	0.5076(3)	0.3836(7)	0.4628(4)	0.0092(1)	
O(3)	0.3998(3)	0.2717(9)	0.1951(5)	0.0092(1)	
O(4)	0.5971(3)	0.2343(8)	0.1776(5)	0.0092(1)	
O(5)	0.1052(4)	0.5376(8)	0.3044(7)	0.0092(1)	
O(6)	0.1110(3)	0.4780(8)	0.6929(6)	0.0092(1)	
O(7)	0.2600(3)	0.6254(8)	0.5407(6)	0.0092(1)	
O(8)	0.2529(3)	0.3893(8)	0.4622(6)	0.0092(1)	
O(9)	0.2224(3)	0.6346(8)	-.0362(6)	0.0092(1)	
O(10)	0.2204(3)	0.3810(8)	0.0506(6)	0.0092(1)	

Table 5.4.2.3 Selected bond distances (Å) and angles (°) in $KTiO(P_{0.5}As_{0.5})O_4$ compared with those in KTP[74] and KTA[175].

		KTAP	KTP	KTA
Ti(1)	-O(1)	2.116(6)	2.161(4)	2.13(1)
	-O(2)	2.011(6)	1.957(4)	1.95(1)
	-O(5)	2.036(10)	2.047(4)	2.00(2)
	-O(6)	2.023(10)	1.900(4)	2.00(2)
	-O(9)	1.904(8)	1.993(4)	1.96(2)
	-O(10)	1.777(7)	1.718(4)	1.73(1)
Ti(2)	-O(3)	2.012(7)	2.037(3)	2.02(1)
	-O(4)	2.028(7)	1.979(3)	1.99(2)
	-O(7)	2.006(7)	1.966(4)	1.94(2)
	-O(8)	1.947(8)	1.994(4)	1.98(2)
	-O(9)	1.751(6)	1.738(4)	1.77(2)
	-O(10)	2.081(6)	2.101(4)	2.10(2)
Ti(1)-O(9)-Ti(2)		137.0(4)	135.5	138.01
Ti(1)-O(10)-Ti(2)		138.7(4)	132.9	141.43
P(1)	-O(1)	1.617(6)	1.523(4)	1.63(2)
	-O(2)	1.618(6)	1.550(4)	1.66(1)
	-O(3)	1.582(6)	1.549(4)	1.72(2)
	-O(4)	1.617(6)	1.547(4)	1.71(1)
mean		1.609(12)	1.542(8)	1.68(3)
P(2)	-O(5)	1.626(6)	1.541(4)	1.69(1)
	-O(6)	1.574(6)	1.533(4)	1.63(2)
	-O(7)	1.656(6)	1.551(4)	1.68(2)
	-O(8)	1.596(6)	1.543(4)	1.70(1)
mean		1.613(12)	1.542(8)	1.68(3)

		KTAP
K(1)	-O(1)	2.971(6)
	-O(2)	2.792(7)
	-O(3)	2.692(6)
	-O(5)	2.939(6)
	-O(7)	3.154(6)
	-O(8)	2.804(6)
	-O(9)	3.125(6)
	-O(10)	2.781(7)

		KTAP
K(2)	-O(1)	2.716(6)
	-O(2)	2.989(6)
	-O(3)	3.111(7)
	-O(4)	3.071(6)
	-O(5)	2.818(6)
	-O(7)	2.851(6)
	-O(8)	3.070(7)
	-O(9)	2.758(7)
	-O(10)	3.078(7)

Figure 5.4.2.Ia Observed (dots), calculated (continuous curve) and difference plots of GPPD 148° data on $KTiO(P_{0.5}As_{0.5})O_4$.

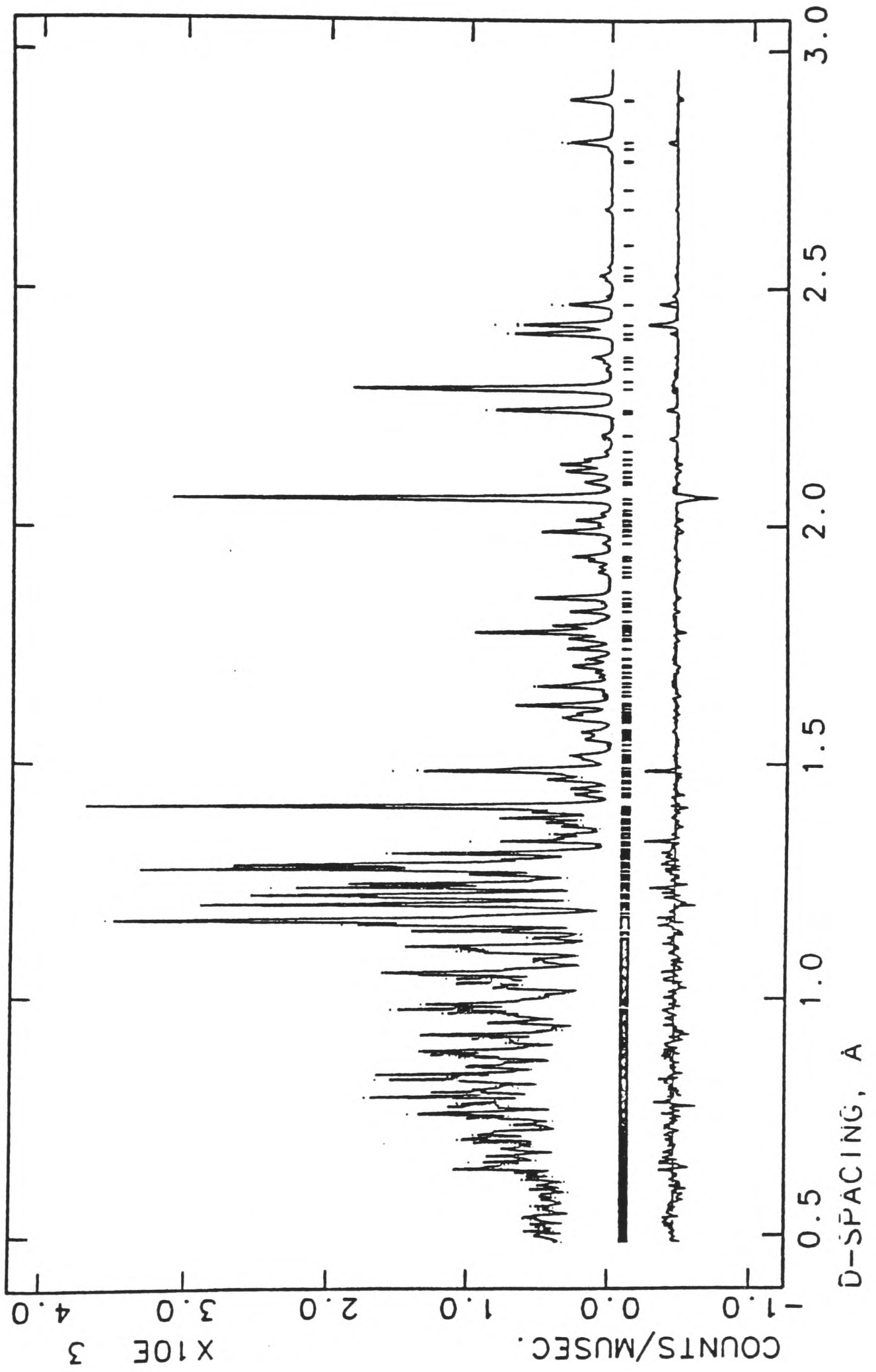


Figure 5.4.2.Ib Observed (dots), calculated (continuous curve) and difference plots of GPPD 90° data on $KTiO(P_{0.5}As_{0.5})O_4$.

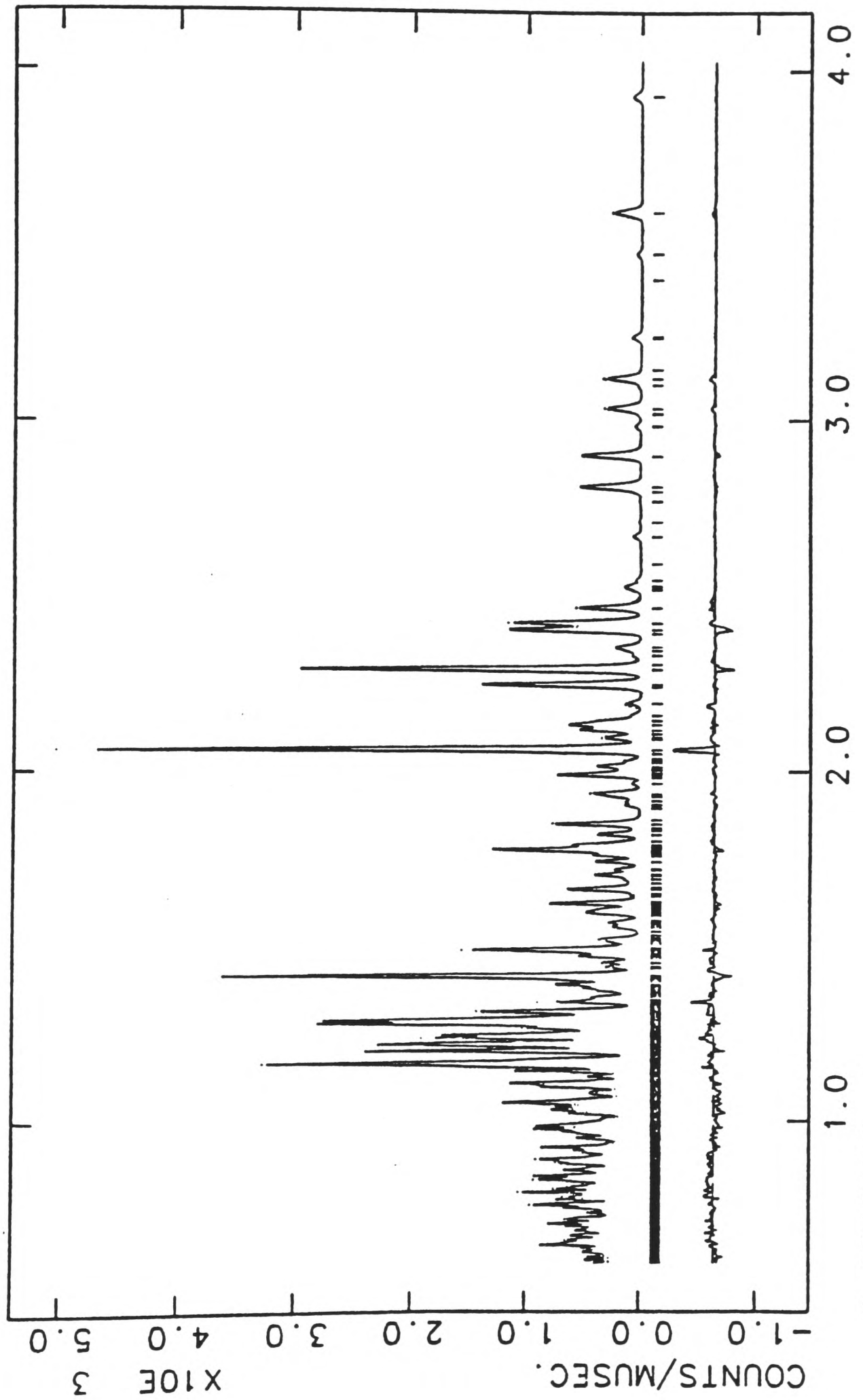
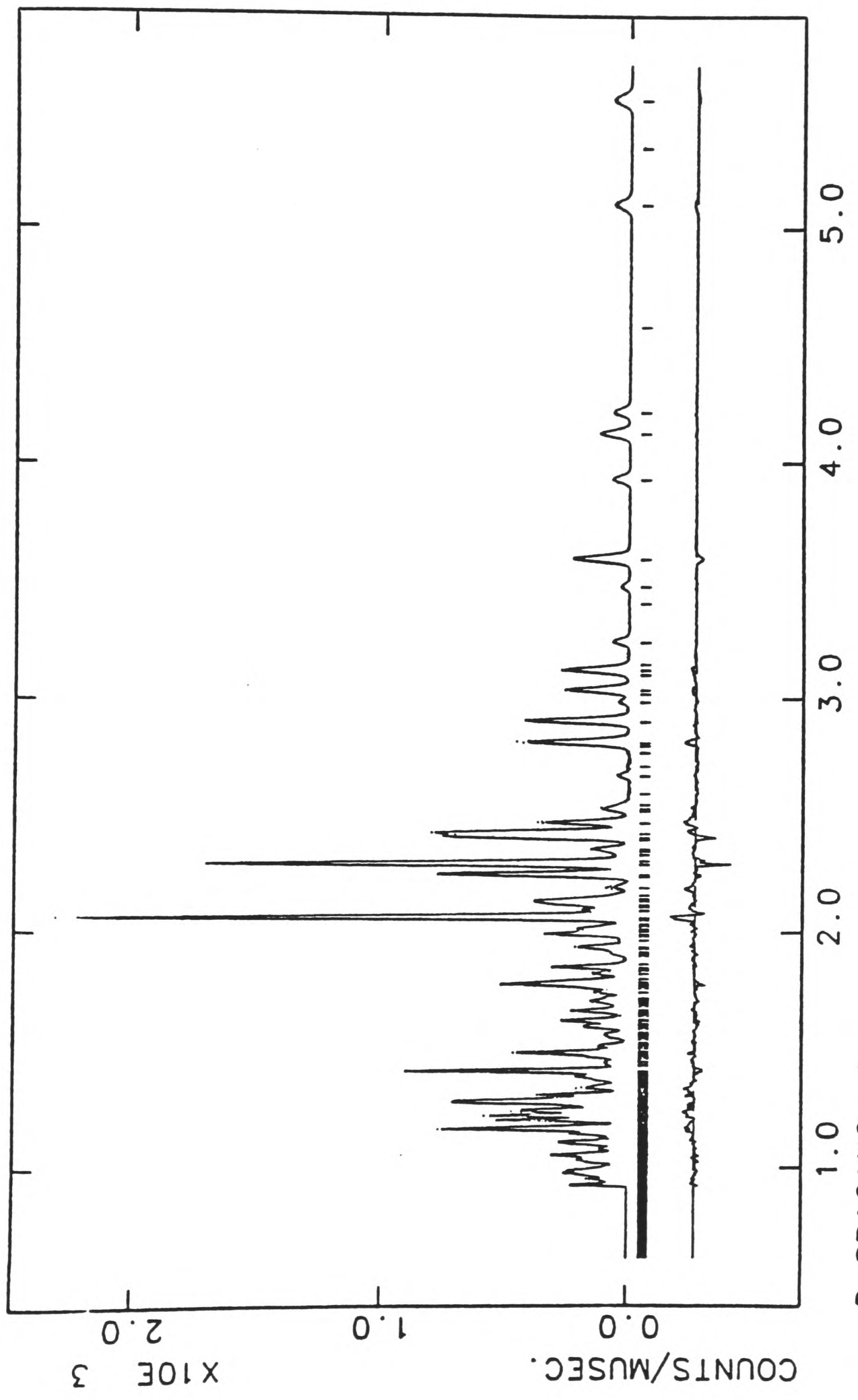


Figure 5.4.2.Ic Observed (dots), calculated (continuous curve) and difference plots of GPPD 60° data on $KTiO(P_{0.5}As_{0.5})O_4$.



of P and As was unchanged from that in the joint refinement. This result indicates that the difference in the neutron scattering lengths of P and As (.513 and .658x10^{-14}m respectively) is sufficient to distinguish them using neutron data alone.

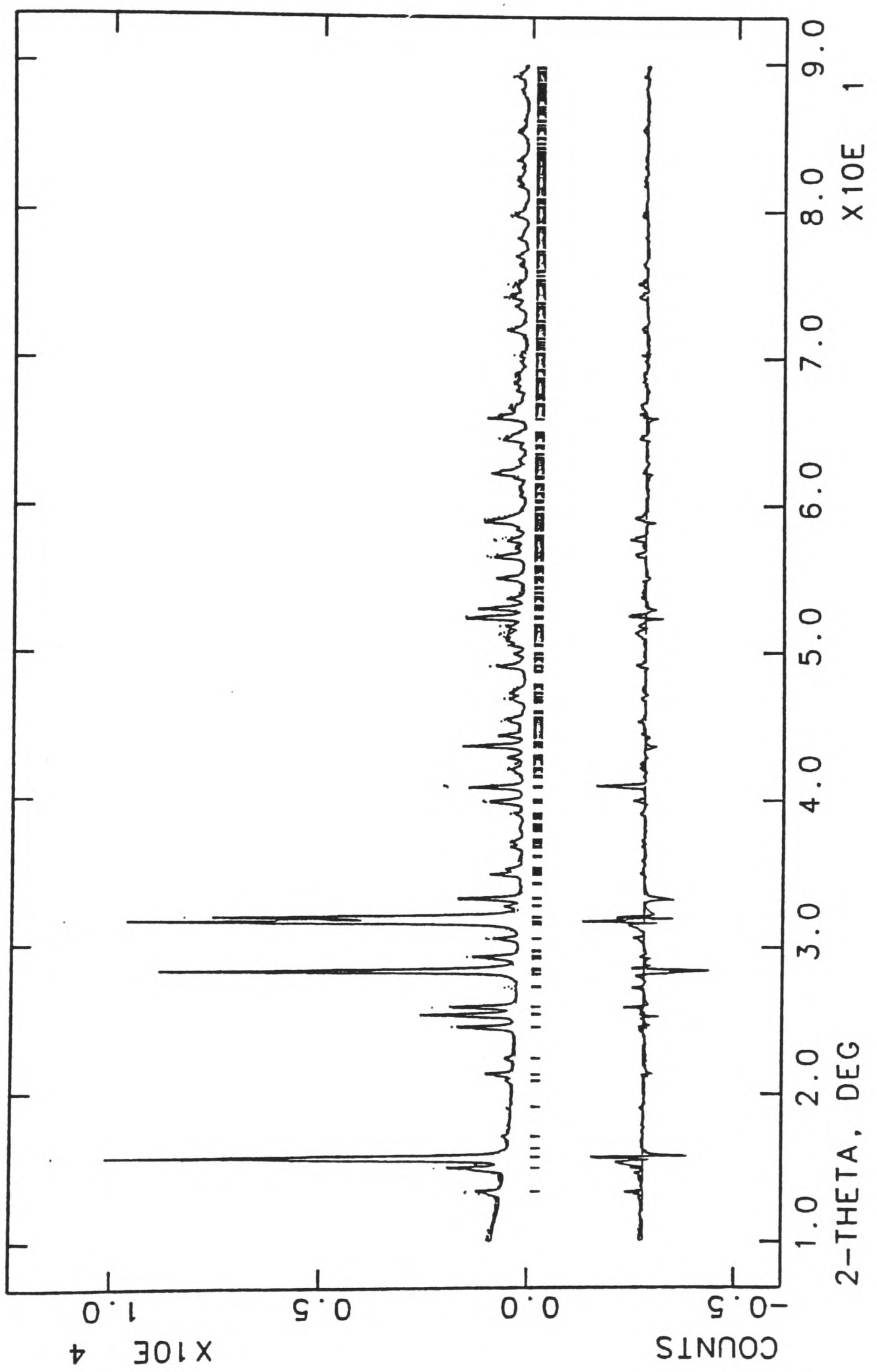
Discussion

The structure of KTAP has been determined by neutron powder diffraction. The distribution of As and P over the tetrahedral sites is essentially random unlike the clear ordering seen on substitution of Sn for Ti and Rb or Na for K. There is a very slight preference of As for the P(2) site. This partial ordering is also revealed in the P-O bond lengths, the mean X-O bond length around the P(2) site being marginally longer than that around P(1), while the average bond length of the two sites is equal in the two solid solution end-members. Bond valence calculations carried out on KTAP, KTP and KTA reflect the slight ordering, site 1 being marginally more favourable for P and less favourable for As than site 2. In a similar manner to the KSTP case, the valences appear too large for the smaller cation and too small for the larger, as the O positions around a site are determined as the weighted average of those around P and those around As. Individual sites will be of the correct size for the cation contained within them.

Bond valence parameters for KTAP and the solid solution end-members KTP and KTA[173].

	P(1)	P(2)
$KTiO(P_{0.5}As_{0.5})O_4$		
P	4.10(4)	4.05(5)
As	6.15(6)	6.07(7)
$KTiOPO_4$	4.90(3)	4.90(3)
$KTiOAsO_4$	5.05(11)	5.06(12)

Figure 5.4.2.II Observed (dots), calculated (continuous curve) and difference plots of Philips data on $KTiO(P_{0.5}As_{0.5})O_4$.



5.4.3 SHG measurements in the $KTiO(P_{1-x}As_x)O_4$ solid solution field

The second harmonic radiation generated from a KTA crystal has been shown[150] to be greater than that from KTP, KTA having a figure of merit (d^2/n^3) 2.3 times that of KTP. However el Brahimi and Durand[173] measured the relative SHG of a variety of cation-substituted KTP derivatives by the powder method and found that with an average particle size of 100μm the signal from KTA was a quarter that from KTP. This fraction increased with particle size, I(2ω) of KTA becoming greater than that of KTP when the particles were larger than about 220μm in size. The SHG apparatus used in the experiments below is described in Chapter 2.6.

a) Experiments on phase-matchable powders

In an initial experiment to test the apparatus, powder samples of quartz, KTP and $LiNbO_3$ were tested. The signal from the quartz sample was negligible compared to that from KTP, which in turn was only half the 532nm radiation recorded from $LiNbO_3$. These results indicate that materials known to be phase-matchable, (KTP, $LiNbO_3$) can be distinguished from non-phase-matchable ones and also that the signals from two materials with large nonlinear coefficients may be differentiated.

The SHG detected depended greatly on the sample used, initially even more than a change in composition. Three flux-grown samples of KTP, ground and sieved to preserve the fraction with particle size >100μm, were measured:

1. 10.7±0.6 2. 11.38±0.44 3. 10.59±0.59,

and gave values within two esd of one another. However KTA samples of similar size and origin, (although in general less transparent and more coloured than the KTP samples) had a greater spread of values:

1. 6.52±0.20 2. 7.44±0.18 3. 7.81±0.23.

Therefore although any of these KTP samples would be representative of the material, the second harmonic generated by a particular KTA sample might not be. When samples of KTP and KTA were measured in the same experiment, the KTP values were again mutually consistent while the intensities measured from KTA were both higher and lower than KTP:

KTP	KTA
7.9±0.17	6.7±0.09
7.74±0.10	8.0±0.14

The relative ability of KTP and KTA to generate second harmonic radiation could not be determined by this apparatus using samples of particle size greater than the coherence length. This may have been due to the poor packing statistics of a small number of relatively large particles, but the intensity measured also seemed to depend more strongly on the synthesis conditions, (affecting the degree of transparency and the presence of coloured impurities), than on the difference in target composition.

b)measurements on powders of particle size less than the coherence length in reflection

To determine whether the second harmonic radiation detected from powders of particle size less than the coherence length would be as dependent on the formation conditions as the results above, the samples were ground to a fine powder before being

funnelled into cuvettes. The apparatus was rearranged to detect reflected radiation from the sample cuvette, since the closely-packed cuvette scattered previously-transmitted radiation. The first experiments demonstrated that 5μm powders derived from ground crystals clumped together into agglomerates of ~100μm in diameter, even after being put through a 53μm mesh sieve. These did not pack into the cuvette as efficiently as the 5μm solid state synthesized powder. The powder made a better reflecting medium due to the larger number of particles per reflecting area, and had more particles correctly oriented to produce second harmonic radiation than in the flux-grown materials. The second harmonic intensity obtained from powders of particle size less than the coherence length (l_c~10μm for KTP), appears critically dependent on the method of preparation of the material and its effective particle size.

Three KTP, two KTAP and two KTA samples, all prepared by high temperature solid state methods, (with a visually estimated particle size of 8μm), were tested in rotation. Each sample was measured seven times and the mean results obtained were:

	KTP	KTAP	KTA
	6.1±0.2	6.0±0.3	7.0±0.2
	5.6±0.4	6.5±0.2	6.8±0.2
	4.4±0.6		
mean	5.5±0.7	6.2±0.4	6.7±0.2

The mean non-phase-matched SHG ability increases with As incorporation, consistent with the result from the single crystal SHG measurements on KTA[150], and in contrast to the effect seen by el Brahimi et al.[173]

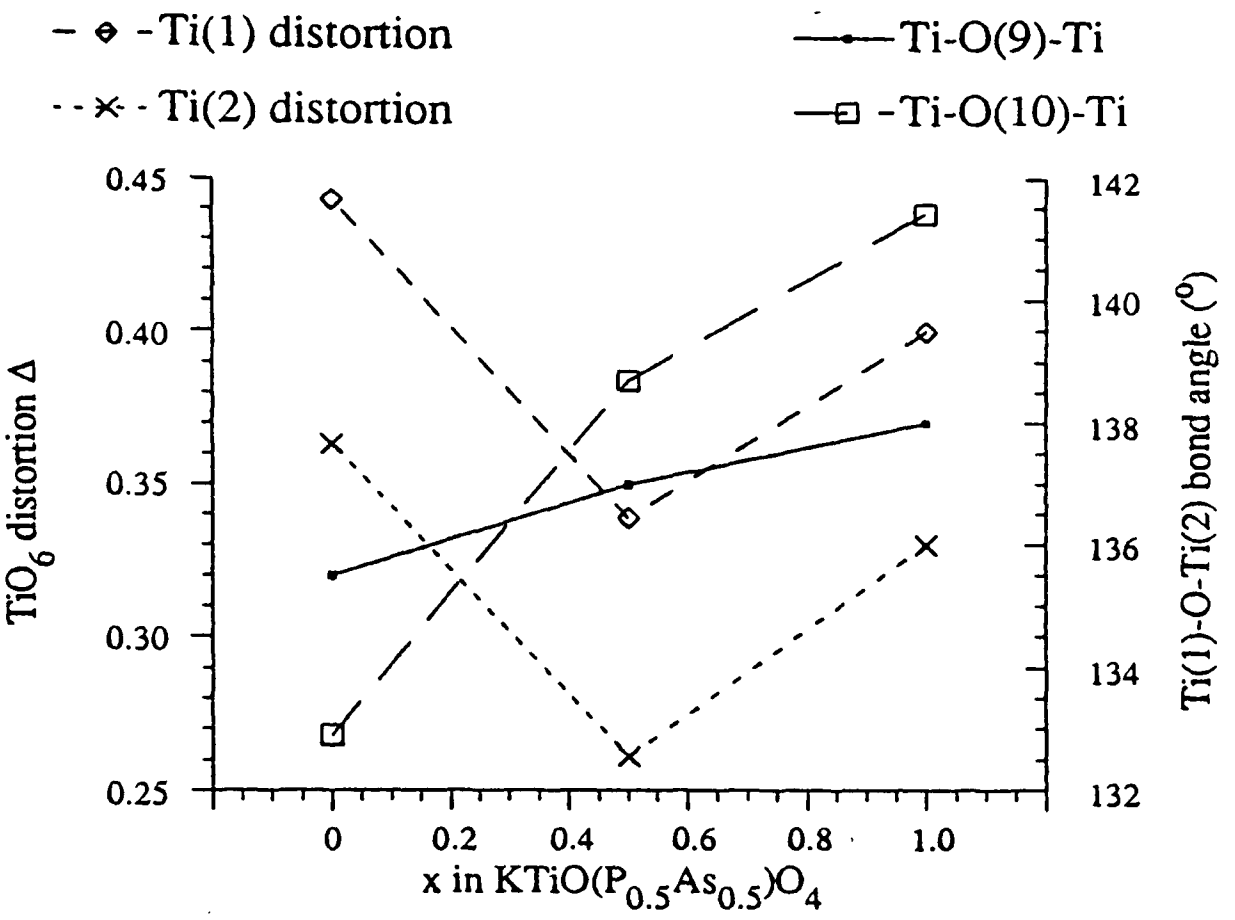
The measured SHG is compared to the structural features thought to be responsible for the large nonlinear coefficients

in Figure 5.4.3.I. The distortion of the TiO_6 octahedra (measured by Δ, the difference between the longest and shortest Ti-O bonds), is approximately the same in KTP and KTA. The angle between octahedra, (Ti-O-Ti), is a measure of the relative orientation of the individual octahedra, (see sections 3.6.2 and 4.5), and both these angles increase with increasing concentration of As, correlating with the nonlinear properties. This expansion is to be expected as the larger AsO_4 groups cause the framework to expand, which is accommodated by straightening out the coiled helical chains of TiO_6 octahedra, (the TiO_6 octahedra being unchanged in size), thus increasing the Ti-O-Ti angle. In the K-substituted KTP materials (Chapters 3 and 4), a decrease in this angle appeared detrimental to the SHG ability. These KTAP solid solution results indicate that an increased angle accompanies greater SHG ability, consistent with the earlier work. From these results it appears that the "phosphate" groups have an effect on the nonlinear coefficients not accounted for in the usual models which consider only the distorted TiO_6 octahedra.

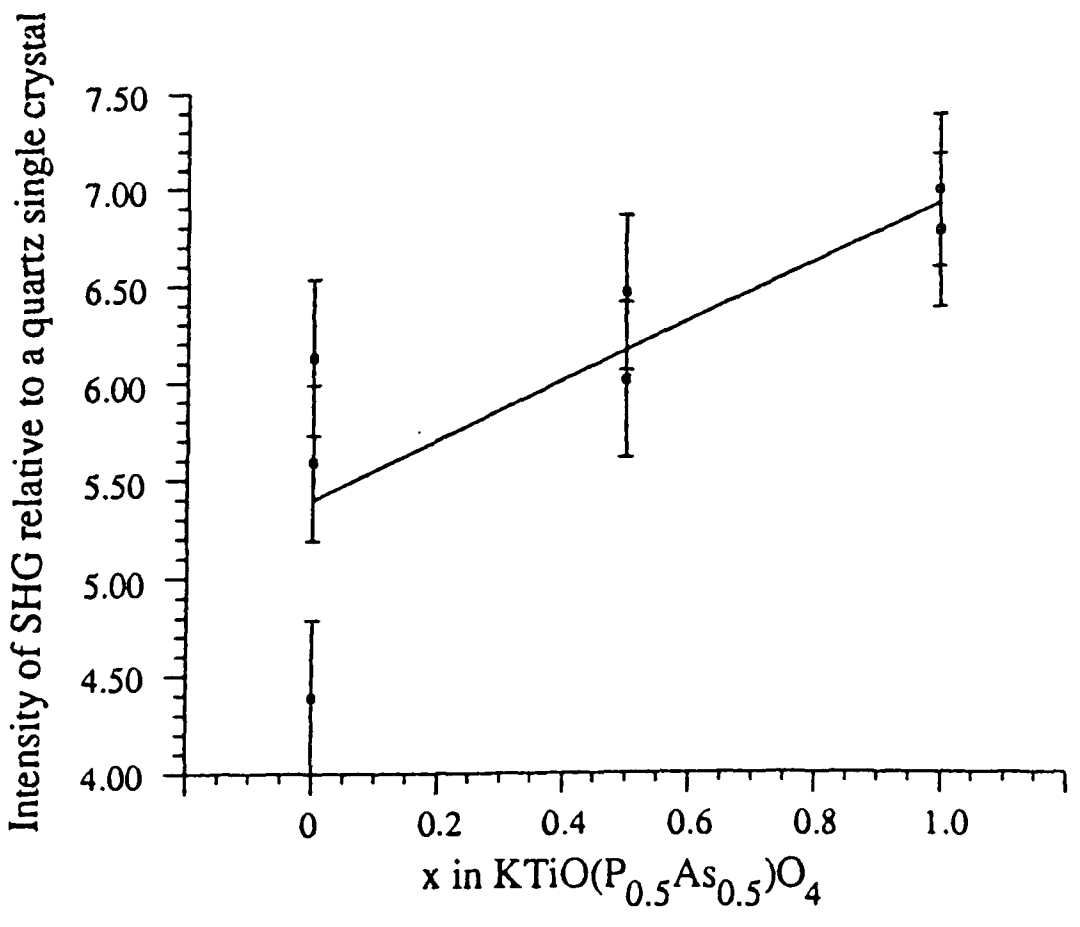
The SHG measurement from powders is critically dependent both on particle size and method of preparation of the material. To obtain reliable measurements of relative SHG ability, samples need to be prepared under identical conditions.

Figure 5.4.3.I Comparison of a) structural parameters thought responsible for the large nonlinear optical coefficients with b) SHG measured for members of the $KTiO(P_{1-x}As_x)O_4$ solid solution relative to a quartz crystal reference.

a)



b)



5.4.4 X-ray powder diffraction study of $RbTiO(P_{0.5}As_{0.5})O_4$ (RTAP)

Data on this material were collected on the STOE STADI-P diffractometer in the Clarendon laboratory. The published single crystal structure of KTP[743] was used as the starting model for the refinement, with Ti(1) y held to fix the origin along y. The thermal parameters were constrained to a single value for each atom type. Once the refinement had converged an impurity phase was observed in the pattern. A search of the Powder Diffraction File revealed that the diffraction pattern of Rb_2TiO_4 (30-1094) matched a number of these peaks, but the crystal structure of this material has not been reported, so could not be modelled. Data collection parameters are given in Table 5.4.4.1, atom coordinates and thermal parameters in Table 5.4.4.2, selected bond distances and angle in Table 5.4.4.3 and final profile plots in Figure 5.4.4.I.

Discussion

The structure of $RbTiO(P_{0.5}As_{0.5})O_4$ has been refined from X-ray powder diffraction data. The P and As are randomly distributed over the two P sites in the structure, with the preference of P for site 1 being less evident than in the KTAP structure. The absence of neutron diffraction data means that the O positions are not well defined and the bond lengths are unreliable. For instance, although the average "P"-O bond length in RTAP is longer than that in RTP, (as expected on substitution of the larger As), the bond lengths cover a much wider range and the tetrahedra appear irregular. Valence calculations[1362] also suffer from the unreliability of the bond lengths, site 2 appears unsuitable for both P and As (Table 5.4.4.4).

Table 5.4.4.1 Data collection and refinement parameters of $RbTiO(P_{0.5}As_{0.5})O_4$

Diffractometer	STOE STADI-P	
Data range (°2Θ)	3-57.656	55-109.656
Step size (°)	0.014	
Total observations	8376	
Contributing reflections	132	615
R_p (%)	8.01	6.59
wR_p (%)	12.84	8.57
R_I (%)	11.17	15.01
$R_{expected}$ (%)	7.61	10.94
x^2	1.490	
Space group	$Pn2_1a$	
unit cell	a=13.1060(3) b=10.6707(2) c=6.6023(1)Å	
	$V=923.34(4)Å^3$	
No. of parameters	76	
Profile shape	Pseudo-Voigt	
	Low angle bank W:13(4) X:9.7(7) asym -3.1(9)	
	High angle W:7.3(6) x:7.1(2) asym. 1.66(9)	
Background	3 term cosine Fourier series	

Table 5.4.4.2 Atom coordinates and isotropic thermal parameters of $RbTiO(P_{0.5}As_{0.5})O_4$

	x	y	z	$U_{iso}(Å^2)$	occupancy
Ti(1)	0.3715(6)	0	0.496(2)	0.040(2)	
Ti(2)	0.2524(9)	0.254(2)	0.271(1)	0.040(2)	
P(1)	0.4988(6)	0.257(1)	0.3256(9)	0.025(2)	0.513(9)
As(1)	0.4988(6)	0.257(1)	0.3256(9)	0.025(2)	0.487(9)
P(2)	0.1779(5)	0.506(1)	0.508(1)	0.025(2)	0.487(9)
As(2)	0.1779(5)	0.506(1)	0.508(1)	0.025(2)	0.513(9)
Rb(1)	0.3898(5)	0.329(1)	0.7822(7)	0.051(1)	
Rb(2)	0.1133(5)	0.077(1)	0.6859(7)	0.051(1)	
O(1)	0.481(3)	0.150(3)	0.470(4)	0.022(2)	
O(2)	0.508(2)	0.390(3)	0.489(4)	0.022(2)	
O(3)	0.364(2)	0.304(3)	0.182(4)	0.022(2)	
O(4)	0.587(2)	0.222(3)	0.178(4)	0.022(2)	
O(5)	0.090(2)	0.563(3)	0.289(3)	0.022(2)	
O(6)	0.119(2)	0.490(3)	0.707(4)	0.022(2)	
O(7)	0.261(2)	0.643(3)	0.487(5)	0.022(2)	
O(8)	0.271(2)	0.398(3)	0.431(4)	0.022(2)	
O(9)	0.238(2)	0.634(3)	0.999(5)	0.022(2)	
O(10)	0.212(2)	0.371(3)	0.075(4)	0.022(2)	

Figure 5.4.4.I Observed (dots), calculated (continuous curves) and Difference plots for $RbTiO(P_{0.5}As_{0.5})O_4$.

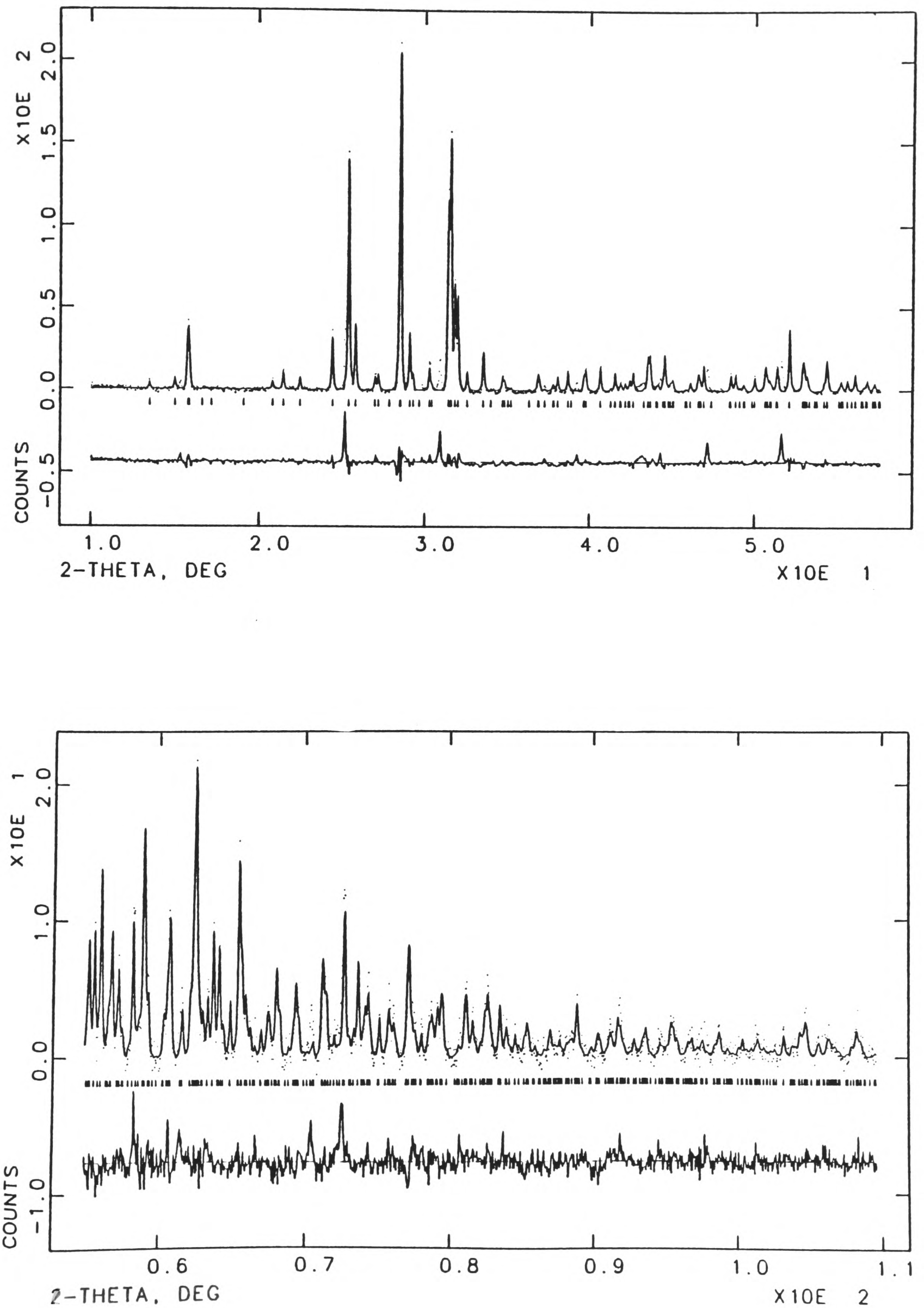


Table 5.4.4.3 Selected bond distances (Å) and angles (°) in $RbTiO(P_{0.5}As_{0.5})O_4$ compared with those in RTP[159].

		RTAP	RTP			RTAP	RTP
Ti(1)	-O(1)	2.16(3)	2.133(7)	Ti(2)	-O(3)	1.67(3)	2.058(5)
	-O(2)	1.97(3)	1.950(7)		-O(4)	2.23(3)	2.021(5)
	-O(5)	2.11(2)	2.081(8)		-O(7)	2.23(3)	1.976(8)
	-O(6)	1.91(3)	2.029(8)		-O(8)	1.88(3)	2.000(9)
	-O(9)	2.02(3)	1.971(7)		-O(9)	1.98(3)	1.736(8)
	-O(10)	1.84(3)	1.711(7)		-O(10)	1.87(3)	2.098(8)
P(1)	-O(1)	1.51(3)	1.526(8)	P(2)	-O(5)	1.95(3)	1.539(7)
	-O(2)	1.78(3)	1.546(9)		-O(6)	1.54(3)	1.526(7)
	-O(3)	2.06(3)	1.534(6)		-O(7)	1.82(3)	1.538(7)
	-O(4)	1.56(3)	1.538(6)		-O(8)	1.76(3)	1.526(8)
mean		1.73(11)	1.536(4)			1.77(7)	1.532(3)

Table 5.4.4.4 Bond valence parameters for RTP[159], KTAP and KTA.

		site 1	Site 2
RTP		4.98(5)	5.03(5)
RTAP	P	3.49(16)	2.92()
	As	5.2(2)	4.38()
KTA		5.05(11)	5.06(12)

Conclusions

Partial ordering takes place on substitution for the Ti in KTP or RTP, Sn or Ge substituting preferentially into the more regular Ti(2) site. When 50%As replaces P in KTP or RTP, it does so in a random fashion, there is very small preference for site 2. Therefore the sites within the framework are more similar than the two cavity sites where complete ordering of substituents can occur. Measurements on the second harmonic generating ability of finely ground $KTiOP_{1-x}As_xO_4$ powders indicated that the second harmonic intensity increases with increasing As content.

The KSTP structure has been published as:

Crennell S.J., Owen J.J., Cheetham A.K., Kaduk J.A. and Jarman R.H., *Eur. J. Solid State Inorg. Chem.*, 28, 397, (1991).

CHAPTER SIX

6.1 Synthesis and characterisation of cation and framework substituted KTP isomorphs

The synthesis of a series of KSP isomorphs analogous to the cation-exchanged KTP isomorphs of Chapter 3 was attempted by high temperature solid state synthesis. The $K_{0.5}Rb_{0.5}SnOPO_4$ (KRSP) material was successfully prepared in the reaction:

$$2KH_2PO_4 + Rb_2CO_3 + 4SnO_2 + 2NH_4H_2PO_4 \rightarrow 4K_{0.5}Rb_{0.5}SnOPO_4 + 2NH_3 + CO_2 + 5H_2O$$

but the only crystalline phase obtained in attempted preparations of $K_{0.5}Na_{0.5}SnOPO_4$, $Na_{0.5}Rb_{0.5}SnOPO_4$ and $K_{1-x}Cs_xSnOPO_4$ (where x = 0.1, 0.2, 0.3 and 0.5), was SnO_2. Analytical electron microscopy cannot be used to determine the K concentration in Sn-containing materials as the Sn(L_α) and K(K_α) emissions (3.444 and 3.313keV respectively), are not resolvable. However the Rb:P ratio obtained for KRSP, $c_{Rb} = 0.48(7)c_P$, was consistent with the synthesis target composition.

Substitution of the larger Sn atom into the KTP framework increases the size of the framework cavities, the mean K-O bond lengths in KSP (2.87(14) and 3.00(20)Å)[1683] being greater than those in KTP (2.84(12) and 2.93(15)Å). This increase in size appears to make KSP unsuitable for Na substitution, so in order to investigate the effect on cation ordering of Sn substitution into the framework, a series of 50%Sn substituted, mixed cation KTP isomorphs were prepared in the reactions:

$$2KH_2PO_4 + Na_2CO_3 + 2SnO_2 + 2TiO_2 + 2NH_4H_2PO_4 \rightarrow 4K_{0.5}Na_{0.5}Ti_{0.5}Sn_{0.5}OPO_4 \text{ (KNSTP)} + 2NH_3 + 5H_2O + CO_2$$

$$Rb_2CO_3 + Na_2CO_3 + 2SnO_2 + 2TiO_2 + 4NH_4H_2PO_4 \rightarrow 4Na_{0.5}Rb_{0.5}Ti_{0.5}Sn_{0.5}OPO_4 \text{ (NRSTP)} + 4NH_3 + 6\ H_2O + 2CO_2$$

$$2KH_2PO_4 + Rb_2CO_3 + 2SnO_2 + 2TiO_2 + 2NH_4H_2PO_4 \rightarrow 4K_{0.5}Rb_{0.5}Ti_{0.5}Sn_{0.5}OPO_4 \text{ (KRSTP)} + 2NH_3 + 5H_2O + CO_2$$

Analytical electron microscopy was carried out on all these materials and the results obtained were consistent with the synthetic target compositions:

	c_{Ti}/c_P	c_{Rb}/c_P
KNSTP	0.54(3)	
NRSTP	0.42(4)	0.57(12)
KRSTP	0.55(4)	0.51(7)

In KNSTP the cation composition could not be determined due to the Sn (L_α), K (K_α) emission overlap.

6.2 Combined X-ray and time-of-flight neutron powder diffraction study of $K_{0.5}Rb_{0.5}SnOPO_4$

Time-of-flight neutron powder diffraction data from KRSP were collected in run number 5875 on the POLARIS diffractometer, Rutherford Appleton Laboratory. X-ray data were collected on a Stoe STADI-P diffractometer.

The published KSP structure[168] was used as the starting model for refinement in GSAS, with Rb occupying 50% of each K site. Once the model had converged, a number of small unindexed peaks were observed, some of which were due to a cassiterite (SnO_2) impurity. These could be modelled using the literature structure of SnO_2[174], but the remainder of the peaks did not match any material in the Powder Diffraction File. Peaks of the unknown phase in isolated regions of the pattern were excluded from the analysis.

The Sn(1) y parameter was used to fix the origin along the y direction, and P-O bond lengths were restrained to the range 1.54(1)Å. The thermal parameters were constrained to a single

value for each atom type, and to a single value for both cations. The total occupancy on a site, and the occupancy of each cation over the two sites, were constrained to unity. Data collection and refinement parameters are given in Table 6.2.1, atom coordinates and thermal parameters in Table 6.2.2, selected bond distances in Table 6.2.3 and final profile plots in Figure 6.2.1.

Discussion

The structure of $K_{0.5}Rb_{0.5}SnOPO_4$ has been determined by combined analysis of time-of-flight neutron and X-ray powder diffraction data. There is partial cation ordering over the two cation sites in the KTP structure, Rb substituting preferentially into site 2. However the extent of the ordering (site 2: 36(2)%K, 64(2)%Rb), is less than that obtained in KRTP (chapter 3.5, site 2: 29(2)%K, 71(2)%Rb).

The cation-oxygen bond lengths in KRSP are compared to those in KSP and RTP[159] in Table 6.2.3. The cation ordering is reflected in the mean bond lengths of KRSP, the K(1)-O bonds being shorter than K(2)-O bonds; having values in between the K-O and Rb-O bonds of the end-members. The cation-oxygen bonds around the K(2) site do not change on substitution of the larger Rb ion, while those around the smaller K(1) increase in KRSP relative to KSP, making the two cation sites more similar and reducing the preference of the smaller K for site 1. Substitution of Rb has little effect on the SnO_6 octahedra, the mean Sn-O bond lengths in KRSP are unchanged from those in KSP.

The results of bond valence calculations[136] on KRSP, KSP, RTP and KRTP are presented in Table 6.2.4. The Sn substitution has increased the size of both cation sites relative to those in

Table 6.2.1 Data collection and refinement parameters for $K_{0.5}Rb_{0.5}SnOPO_4$.

Diffractometer	POLARIS, RAL, C bank	Stoe STADI-P
Data range	3.996-20ms	10-100°2θ
Contributing reflections	2013	1062
Total number of observations	7477	
Scattering lengths /10^{-14}m	K:0.367, Rb:0.708, Sn:0.623, P:0.513, O:0.5805	
No. parameters	112	
Sample can	12mm Vanadium can	flat plate
R_p (%)	6.28	11.58
wR_p (%)	3.56	15.56
R_f (%)	2.54	6.66
$R_{expected}$ (%)	1.96	20.42
χ^2	1.723	

Phase 1: $K_{0.5}Rb_{0.5}SnOPO_4$

space group $Pn2_1a$

unit cell a=13.2382(4)Å, b=10.7083(3)Å, c=6.5581(2)Å

V=929.66(6)Å^3

Phase 2: SnO_2 (Cassiterite)

space group $P4_22_12$

atom parameters and unit cell unrefined

Profile neutron Gaussian convoluted with double exponential

σ_1: 97(2) σ_2: 0.02(7)

X-ray Pseudo-Voigt GW:5.87(4), LX:-8.71(3),

LY:14.49(9), asym. -4.88(1)

Background 3 term cosine Fourier series, (X-ray fixed at low angles)

Table 6.2.2 Atom coordinates and isotropic thermal parameters of $K_{0.5}Rb_{0.5}SnOPO_4$

	x	y	z	$U_{iso}(Å^2)$	occupancy
Sn(1)	0.3725(2)	0	0.4929(8)	0.0005(4)	
Sn(2)	0.2508(5)	0.2561(9)	0.2563(9)	0.0005(4)	
P(1)	0.5038(4)	0.2525(7)	0.3383(4)	0.0015(4)	
P(2)	0.1769(2)	0.5048(7)	0.4962(9)	0.0015(4)	
K(1)	0.3741(6)	0.3150(8)	0.776(1)	0.0222(10)	0.64(2)
Rb(1)	0.3741(6)	0.3150(8)	0.776(1)	0.0222(10)	0.36(2)
K(2)	0.1057(5)	0.0650(7)	0.6758(10)	0.0222(10)	0.36(2)
Rb(2)	0.1057(5)	0.0650(7)	0.6758(10)	0.0222(10)	0.64(2)
O(1)	0.4896(4)	0.1375(6)	0.4768(10)	0.0034(2)	
O(2)	0.5209(4)	0.3657(7)	0.4797(10)	0.0034(2)	
O(3)	0.4106(4)	0.2846(7)	0.2075(10)	0.0034(2)	
O(4)	0.5973(3)	0.2397(7)	0.2012(9)	0.0034(2)	
O(5)	0.1064(4)	0.5263(8)	0.3135(9)	0.0034(2)	
O(6)	0.1105(5)	0.4763(8)	0.6828(10)	0.0034(2)	
O(7)	0.2399(3)	0.6242(6)	0.5286(9)	0.0034(2)	
O(8)	0.2554(4)	0.4006(7)	0.4595(9)	0.0034(2)	
O(9)	0.2261(4)	0.6449(7)	-.020(1)	0.0034(2)	
O(10)	0.2341(5)	0.3824(8)	0.0270(10)	0.0034(2)	

Table 6.2.3 Selected bond distances (Å) in $K_{0.5}Rb_{0.5}SnOPO_4$.

		KRSP	KSP			KRSP	KSP
Sn(1)	-O(1)	2.142(6)	2.091(7)	Sn(2)	-O(3)	2.162(8)	2.134(5)
	-O(2)	2.023(7)	2.093(7)		-O(4)	2.058(8)	2.102(5)
	-O(5)	2.140(8)	2.111(6)		-O(7)	2.058(8)	2.051(6)
	-O(6)	2.062(9)	2.064(5)		-O(8)	2.044(8)	2.076(7)
	-O(9)	2.029(7)	1.978(6)		-O(9)	1.914(11)	1.957(5)
	-O(10)	1.905(8)	1.975(7)		-O(10)	2.035(10)	1.961(5)
Δ		0.24	0.14			0.25	0.18
mean		2.05(8)	2.05(6)			2.05(7)	2.05(7)

P(1)	-O(1)	1.541(2)	P(2)	-O(5)	1.536(2)	
	-O(2)	1.543(2)		-O(6)	1.537(2)	
	-O(3)	1.541(2)		-O(7)	1.542(2)	
	-O(4)	1.536(2)		-O(8)	1.543(2)	

		KRSP	KSP	RTP
K(1)	-O(1)	3.131(9)	2.995(7)	3.040(8)
	-O(2)	2.801(10)	2.753(4)	2.738(8)
	-O(3)	2.889(8)	2.845(5)	2.784(7)
	-O(5)	3.111(10)	3.005(4)	2.997(8)
	-O(7)	3.033(9)	3.042(4)	3.211(7)
	-O(8)	2.760(9)	2.770(7)	2.831(7)
	-O(9)	2.975(9)	2.955(5)	3.159(7)
	-O(10)	2.582(11)	2.611(6)	2.997(8)
mean		2.91(18)	2.87(14)	2.97(16)
K(2)	-O(1)	2.856(8)	2.736(6)	2.743(7)
	-O(2)	3.367(9)	3.256(8)	3.106(8)
	-O(3)	3.018(9)	3.123(7)	3.102(8)
	-O(4)	3.102(8)	3.148(5)	3.038(8)
	-O(5)	2.839(9)	2.856(6)	2.858(6)
	-O(7)	3.151(9)	2.987(6)	2.989(7)
	-O(8)	3.153(8)	3.182(7)	3.127(8)
	-O(9)	2.709(8)	2.664(5)	2.784(6)
	-O(10)	3.045(8)	3.058(7)	3.103(7)
mean		3.03(19)	3.00(20)	2.98(14)

Figure 6.2.Ia Observed (dots), calculated (continuous curve) and difference plots of POLARIS C-bank data from $K_{0.5}Rb_{0.5}SnOPO_4$.

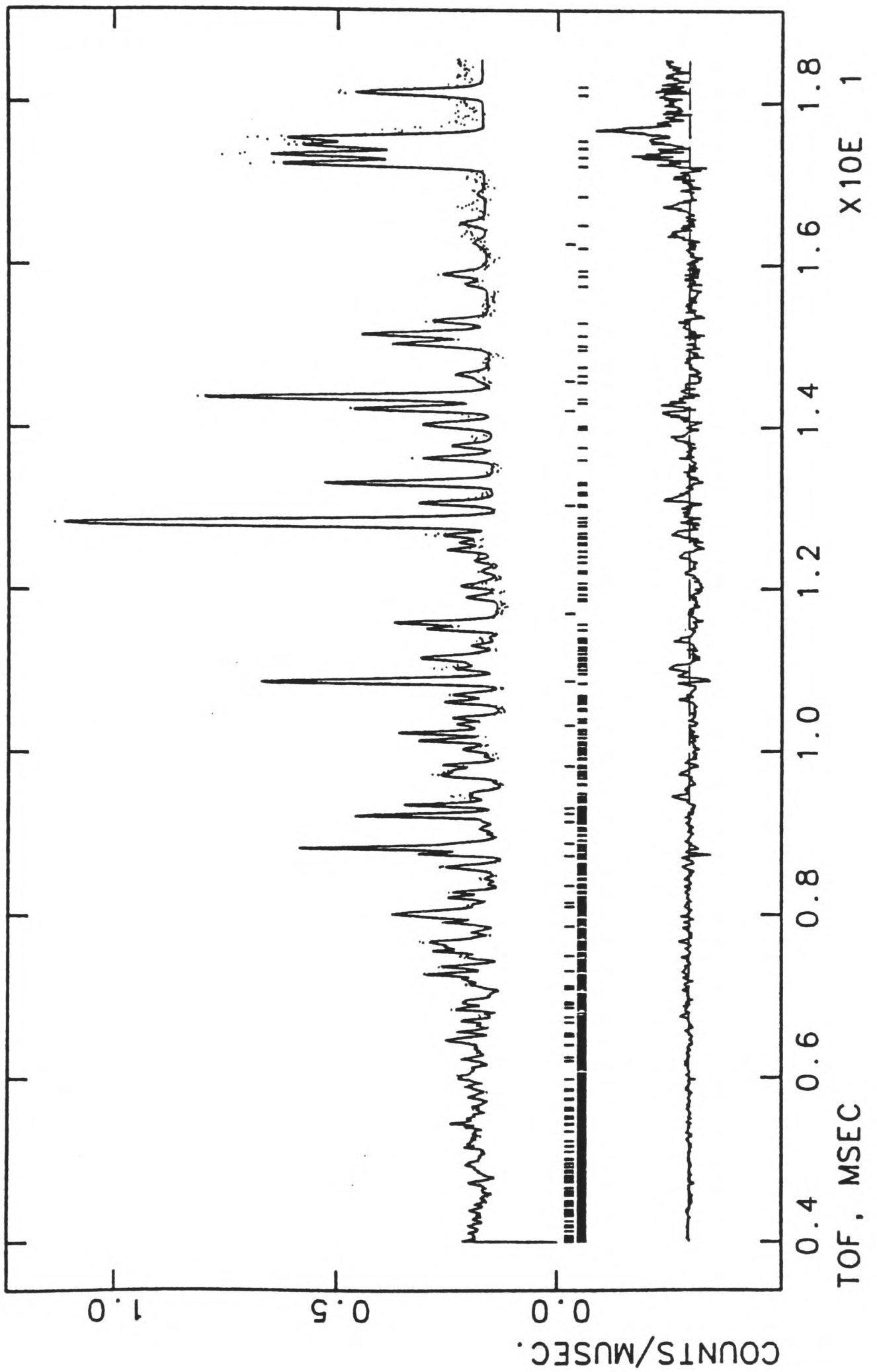
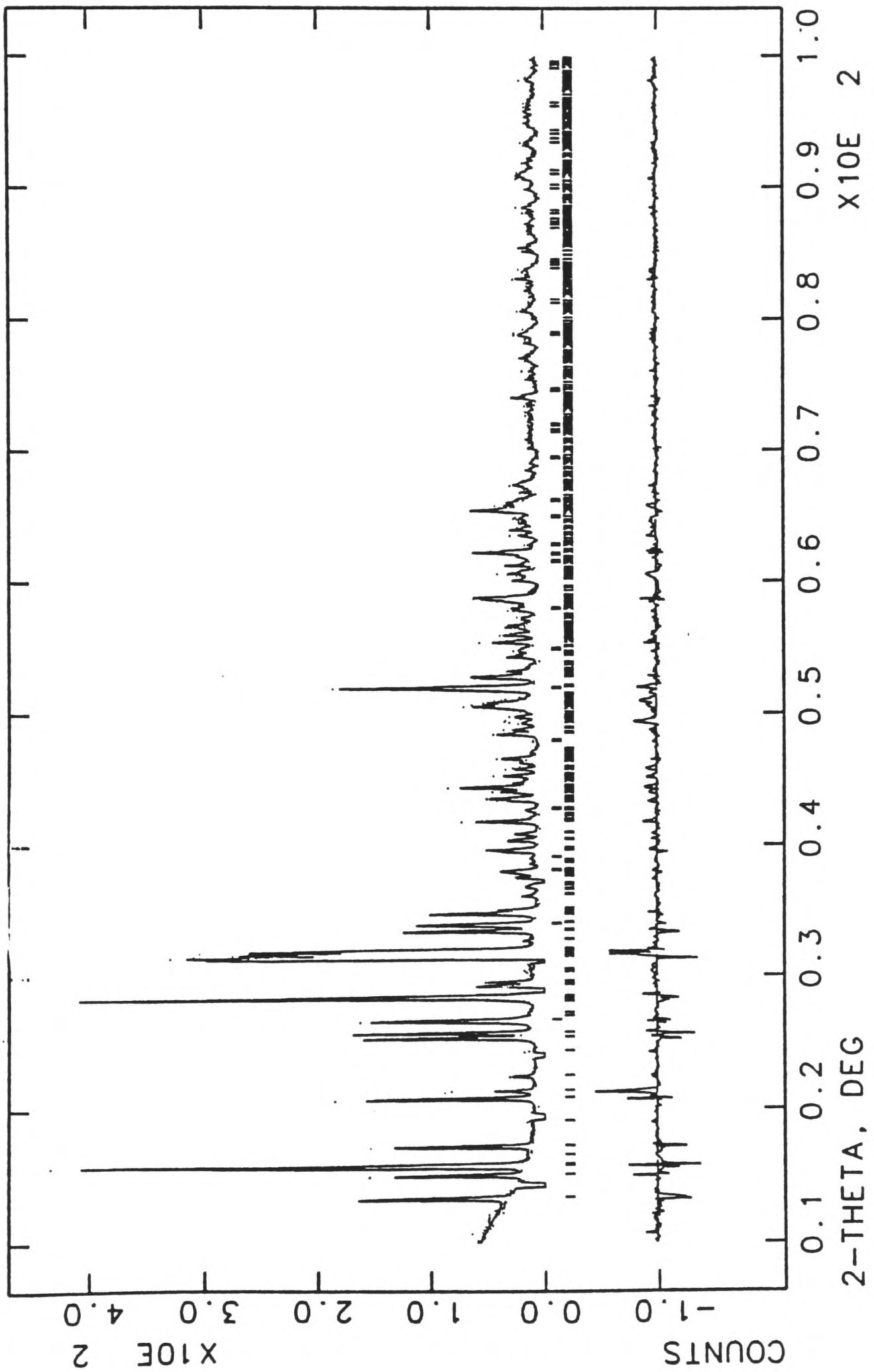


Figure 6.2.Ib Observed (dots), calculated (continuous curve) and difference plots of X-ray data from $K_{0.5}Rb_{0.5}SnOPO_4$.



KRTP, reducing the valence parameters. In KRTP site 1 was too small for Rb so that although both cations favour the K(2) site, 71%K was driven into K(1). In KRSP, both sites have increased in size, making the K(1) site less unfavourable for Rb, and the cation ordering over the two sites is reduced.

Table 6.2.4 Bond valence parameters calculated for KRSP, KRTP (chapter 3.5), KSP[c160] and RTP[c159].

	K(1)	Rb(1)	K(2)	Rb(2)
$KSnOPO_4$	1.16(1)		0.98(1)	
$K_{0.5}Rb_{0.5}SnOPO_4$	1.10(1)	1.57(2)	0.875(8)	1.30(1)
$K_{0.5}Rb_{0.5}TiOPO_4$	1.17(1)	1.66(1)	0.99(1)	1.41(1)
$RbTiOPO_4$		1.46(1)		1.39(1)

Sn substitution into KTP isomorphs increases the size of the K(1) framework cavity, and reduces cation ordering, which depends on the cavity size and difference in ionic radii of the cations.

6.3 Combined X-ray and time-of-flight neutron powder diffraction study of $K_{0.5}Na_{0.5}Sn_{0.5}Ti_{0.5}OPO_4$

Time-of-flight neutron powder diffraction data were collected on GPPD, Argonne National Laboratory, and all three data banks were used in the structure refinement. X-ray data were collected on a Philips diffractometer.

The starting model for the structure refinement was taken from the published KTP structure,[174] with 50%Sn placed on both Ti sites, and 50%Na on the K sites. The total occupancy on each substituted site, and of each atom over the two sites, was constrained to unity. The O(1) y coordinate was used to fix the origin in the y direction, and the P-O bond lengths were restrained to the range 1.54(1)Å. The presence of an SnO_2 impurity was indicated by a number of unindexed peaks. The cassiterite structure was taken from the literature[174] and used to model the impurity with its structural parameters unrefined. Initially the isotropic thermal parameters were constrained to a single value for each atom type. However, when the occupancies and thermal parameters were refined simultaneously, the thermal parameters of Ti and Sn became negative while that of Na increased to a value, (0.11(1)$Å^3$), much greater than that seen in the KNTP single crystal structures (chapter 4, 0.025(3)$Å^3$); in addition the K/Na ordering was considerably less than that seen in KNTP. The difference between K and Na, and the position of Ti(1) are determined solely by the X-ray data, and although the independent determination of each of these is possible, (Chapters 3.3 and 5.2), there does not appear to be enough information to refine them together.

To determine the effect of different thermal parameters on the

apparent degree of K and Na ordering over the two cation sites in KNSTP, the thermal parameters were fixed at values on either side of a reasonable range, and the site occupancies refined:

Na U_{iso} ($Å^3$)	K U_{iso} ($Å^3$)	Na(1), K(1) (=K(2), Na(2))
0.04	0.02	0.76(3), 0.24(3)
0.02	0.04	0.63(4), 0.37(4)

This result shows that the thermal parameters have an effect on the site occupancies, but while the thermal parameters remain within the range seen in other KTP isomorphs, the ordering remains in the same direction (i.e. a higher proportion of Na on site 1) and is only partial. The cation thermal parameters were constrained to a single value in subsequent refinement cycles.

In the KSTP refinement, the isotropic thermal parameters of Ti and Sn were within one e.s.d. of each other (0.0105(16) and 0.0101(9)$Å^3$ respectively), with the site 1 occupied by 63.9(4)% Ti and 36.1(4)%Sn. However in KNSTP the thermal parameters had diverged from one another and decreased to -0.021(1) and 0.003(1) respectively without a marked effect on the relative occupancy of site 1 (67.6(2)%Ti and 32.4(2)%Sn) so in subsequent refinement cycles the Ti and Sn isotropic thermal parameters were constrained to a single value.

Data collection and refinement parameters are given in Table 6.3.1, atom coordinates and isotropic thermal parameters in Table 6.3.2, selected bond distances and angles in Table 6.3.3 and final profile plots in Figure 6.3.I.

Table 6.3.1 Data collection and refinement parameters for $K_{0.5}Na_{0.5}Sn_{0.5}Ti_{0.5}OPO_4$.

Diffractometer	GPPD, Argonne National Lab.			Philips
	148°	90°	60°	Nicolet L11 automation
Data range	4.98–30.995	4.5–30.992	5.0–30.99ms	5–100°2θ
Contributing reflections	6025	3449	1397	507
Total number of observations	11109			
Sample can	10mm Vanadium can			flat plate
R_p (%)	3.18	3.66	4.68	6.10
wR_p (%)	4.44	5.14	6.98	8.28
R_f (%)	4.90	3.63	4.84	7.8
$R_{expected}$ (%)	1.97	1.88	3.19	2.24
x^2	7.114			

Phase 1: $K_{0.5}Na_{0.5}Sn_{0.5}Ti_{0.5}OPO_4$

space group $Pn2_1a$

unit cell a=12.8826(4)A, b=10.6384(4)A, c=6.3898(2)A

V=875.72(8)A^3

Phase 2: SnO_2

space group $P4_22_12$

atom positions and unit cell unrefined

Scattering lengths /10^{-14}m K:0.367, Na:0.363, Sn:0.623, Ti:-0.344, P:0.513, O:0.5805

No. parameters 112

Profile:neutron Gaussian convoluted with double exponential

	148°bank	90° bank	60°bank
σ_1	178(7)	204(6)	246(7)
σ_2	4(1)	10(1)	6.0(9)

X-ray Pseudo-Voigt
GW:10(1), LX:1.6(4), LY:32(1), asym.:9.02(9)

Background 6 term Fourier series

Table 6.3.2 Atom coordinates and isotropic thermal parameters of $K_{0.5}Na_{0.5}Sn_{0.5}Ti_{0.5}OPO_4$.

	x	y	z	$U_{iso}(A^2)$	occupancy
Ti(1)	0.3702(4)	0.019(2)	0.5010(24)	-.0008(9)	0.669(3)
Sn(1)	0.3702(4)	0.019(2)	0.5010(24)	-.0008(9)	0.331(3)
Ti(2)	0.2542(6)	0.2678(9)	0.2442(14)	-.0008(9)	0.331(3)
Sn(2)	0.2542(6)	0.2678(9)	0.2442(14)	-.0008(9)	0.669(3)
P(1)	0.4965(5)	0.2755(6)	0.3439(4)	0.0029(5)	
P(2)	0.1835(2)	0.5298(8)	0.4970(11)	0.0029(5)	
K(1)	0.3553(5)	0.3124(8)	0.7632(8)	0.030(2)	0.27(4)
Na(1)	0.3553(5)	0.3124(8)	0.7632(8)	0.030(2)	0.73(4)
K(2)	0.1029(6)	0.0930(9)	0.6770(13)	0.030(2)	0.73(4)
Na(2)	0.1029(6)	0.093(9)	0.6770(13)	0.030(2)	0.27(4)
O(1)	0.4876(6)	0.1563	0.481(1)	0.0073(3)	
O(2)	0.5173(5)	0.3900(5)	0.483(1)	0.0073(3)	
O(3)	0.4025(5)	0.3013(8)	0.1980(9)	0.0073(3)	
O(4)	0.5911(5)	0.2629(8)	0.1913(9)	0.0073(3)	
O(5)	0.1136(5)	0.5472(9)	0.3030(8)	0.0073(3)	
O(6)	0.1087(5)	0.5012(9)	0.6817(9)	0.0073(3)	
O(7)	0.2516(5)	0.6469(7)	0.5162(9)	0.0073(3)	
O(8)	0.2572(4)	0.4195(7)	0.4558(8)	0.0073(3)	
O(9)	0.2261(6)	0.6618(7)	-.021(1)	0.0073(3)	
O(10)	0.2294(6)	0.4044(8)	0.030(1)	0.0073(3)	

Table 6.3.3 Selected bond distances (Å) and angles (°) in $K_{0.5}Na_{0.5}Sn_{0.5}Ti_{0.5}OPO_4$.

		KNSTP	KSTP	KTP
Ti(1)	-O(1)	2.110(14)	2.040(11)	2.161(4)
	-O(2)	1.996(14)	2.019(11)	1.987(4)
	-O(5)	1.965(16)	2.059(12)	2.047(4)
	-O(6)	2.067(16)	2.039(12)	1.900(4)
	-O(9)	1.970(15)	1.939(10)	1.993(4)
	-O(10)	1.778(14)	1.865(10)	1.718(4)
Δ		0.33(3)	0.19(2)	0.443(6)
mean		1.98(10)	2.00(7)	1.97(14)
Ti(2)	-O(3)	1.965(9)	2.041(10)	2.037(3)
	-O(4)	2.145(9)	2.074(10)	1.979(3)
	-O(7)	1.945(10)	1.979(11)	1.966(4)
	-O(8)	2.105(10)	2.057(11)	1.994(4)
	-O(9)	1.894(10)	1.957(11)	1.738(4)
	-O(10)	2.019(11)	1.949(11)	2.101(4)
Δ		0.25(2)	0.12(2)	0.363(6)
mean		2.01(9)	2.01(5)	1.97(11)

	KNSTP		KNSTP
P(1)-O(1)	1.546(4)	P(2)-O(5)	1.543(4)
-O(2)	1.533(4)	-O(6)	1.553(4)
-O(3)	1.552(4)	-O(7)	1.529(4)
-O(4)	1.566(4)	-O(8)	1.532(4)

	KNSTP	KNTP		KNSTP	KNTP
K(1)-O(1)	2.985(10)	2.798(5)	K(2)-O(1)	2.727(10)	2.741(6)
-O(2)	2.869(11)	2.932(6)	-O(2)	3.301(10)	2.991(5)
-O(3)	2.846(10)	2.729(5)	-O(3)	3.107(10)	3.081(6)
-O(5)	2.861(11)	2.710(5)	-O(4)	2.971(9)	3.011(5)
-O(7)	2.758(10)	2.752(5)	-O(5)	2.834(11)	2.830(6)
-O(8)	2.600(10)	2.571(5)	-O(7)	2.922(11)	2.928(6)
-O(9)	2.640(11)	2.684(6)	-O(8)	3.135(10)	3.114(6)
-O(10)	2.550(11)	2.536(6)	-O(9)	2.643(11)	2.685(7)
			-O(10)	3.093(11)	3.083(6)
mean	2.76(14)	2.71(12)		2.97(20)	2.94(15)

	KNSTP	KNTP	KSTP
Ti(1)-O(9)-Ti(2)	127.0(6)	134.8(3)	126.1(5)
Ti(1)-O(10)-Ti(2)	132.7(7)	132.6(3)	137.1(5)

Figure 6.3.Ia Observed (dots), calculated (continuous curve) and difference plots of GPPD 148^{o} data on $K_{0.5}Na_{0.5}Sn_{0.5}Ti_{0.5}OPO_4$.

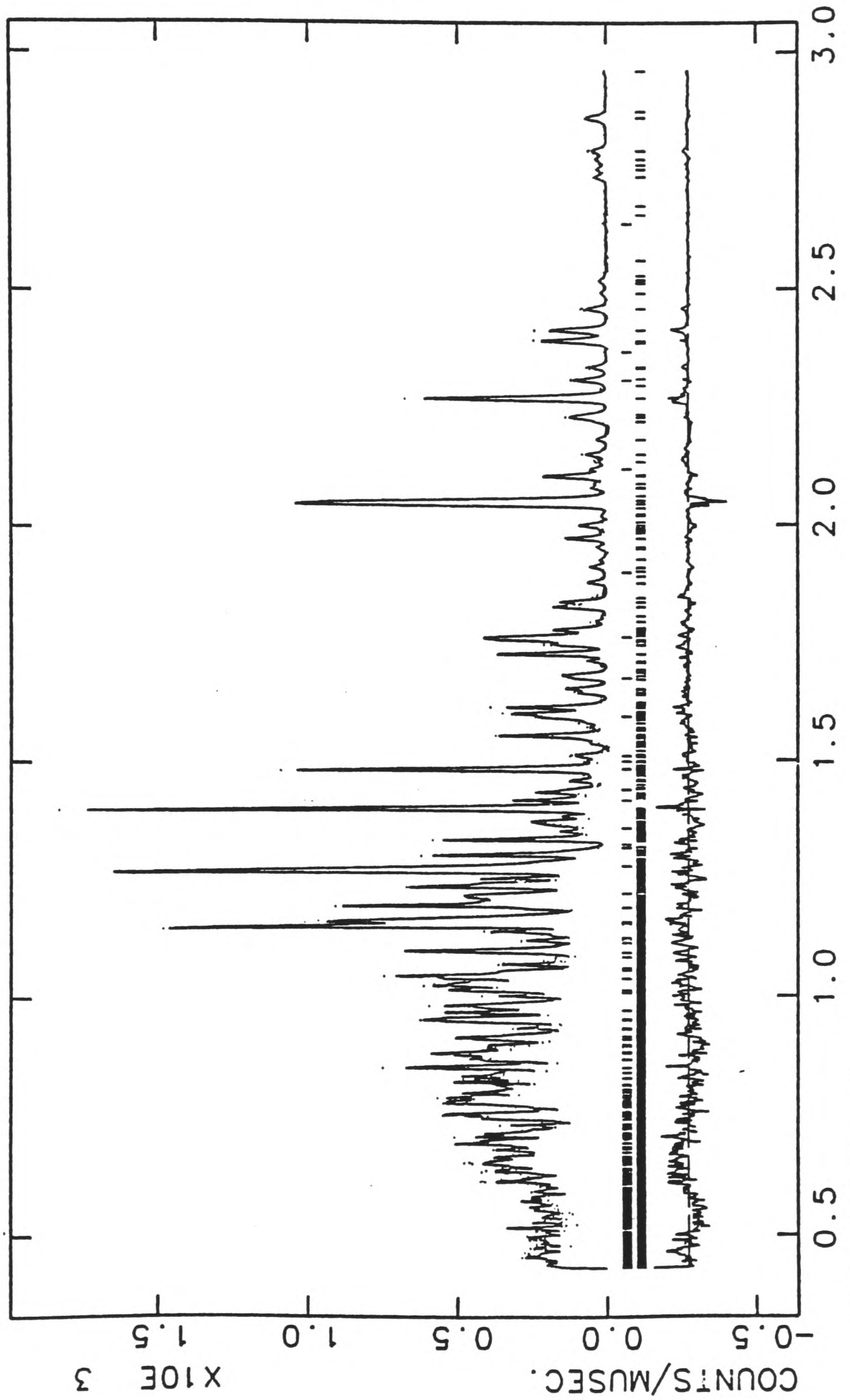


Figure 6.3.Ib Observed (dots), calculated (continuous curve) and difference plots of GPPD 90° data on $K_{0.5}Na_{0.5}Sn_{0.5}Ti_{0.5}OPO_4$.

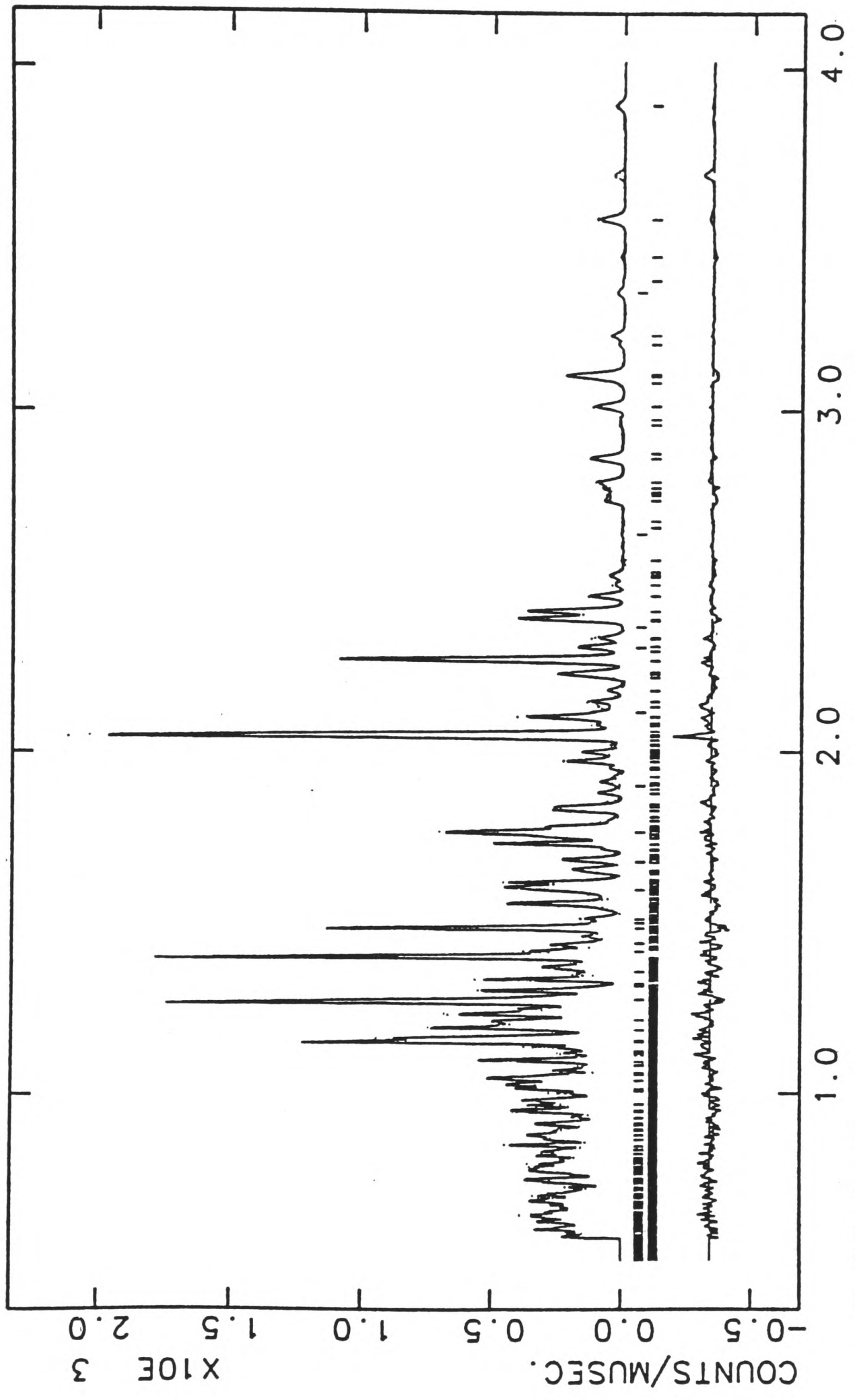


Figure 6.3.Ic Observed (dots), calculated (continuous curve) and difference plots of GPPD 60° data on $K_{0.5}Na_{0.5}Sn_{0.5}Ti_{0.5}OPO_4$.

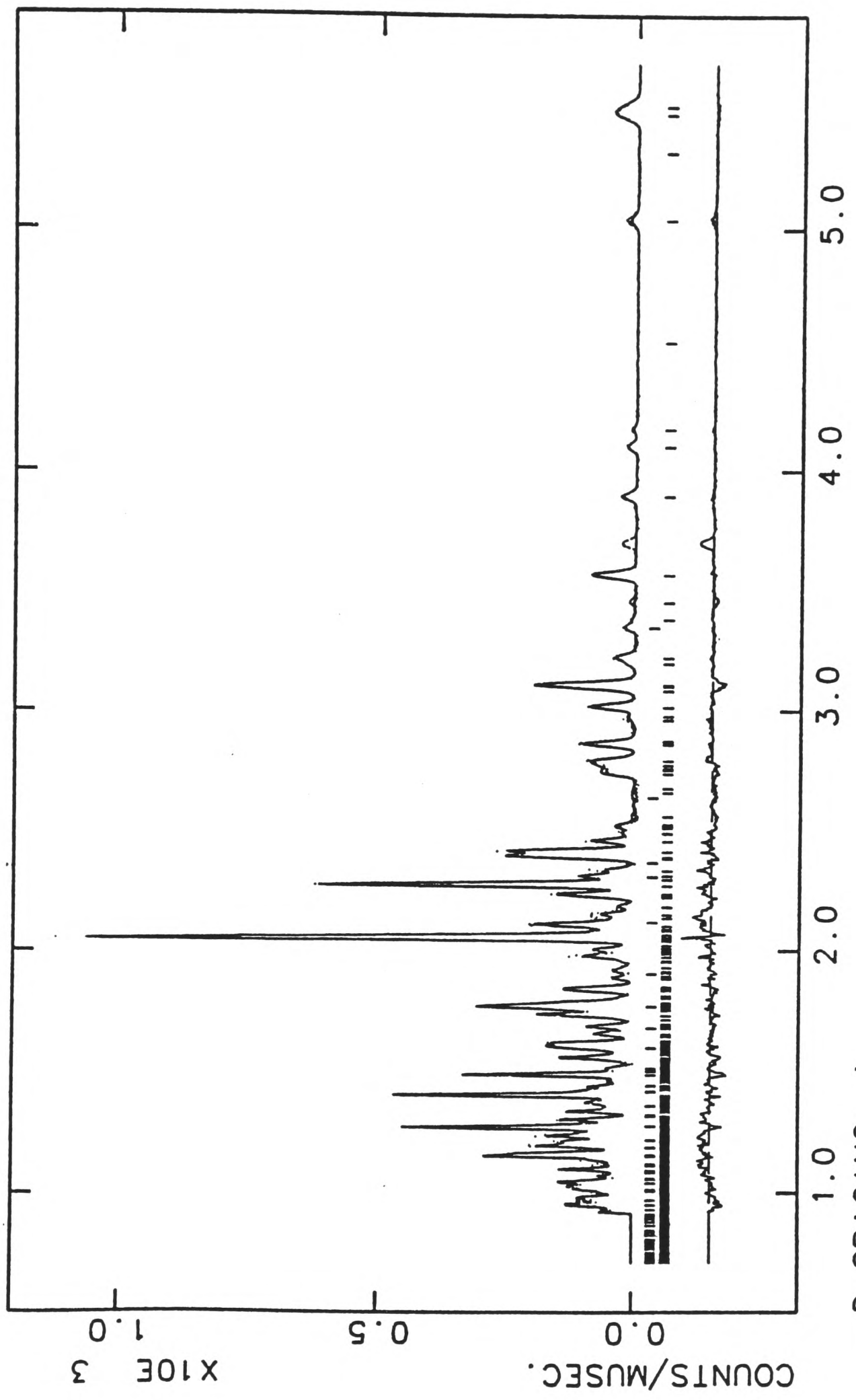
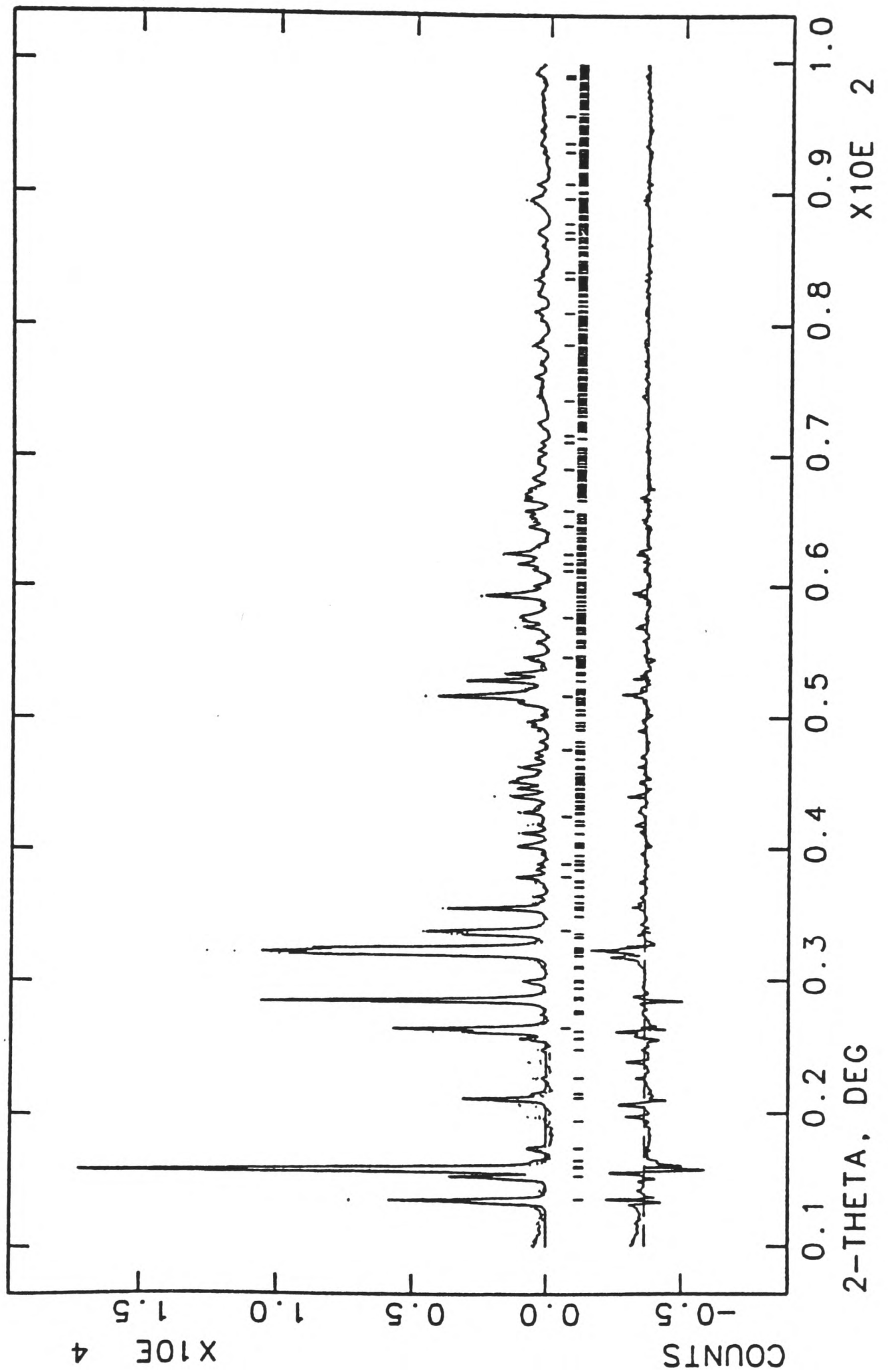


Figure 6.3.Id Observed (dots), calculated (continuous curve) and difference plots of X-ray data on $K_{0.5}Na_{0.5}Sn_{0.5}Ti_{0.5}OPO_4$.



Discussion

The structure of KNSTP has been determined by combined analysis of X-ray and neutron diffraction data. The X-ray data were required to differentiate between K and Na, the neutron scattering lengths of which are too similar to be distinguished (0.367 and 0.363×10^{-14}m respectively), and to define the Ti(1) site which has a weighted average neutron scattering length of almost zero: $0.669\times-0.344 + 0.331\times0.623 = -.036\times10^{-14}$m

The NLO properties of KNSTP can be predicted by analogy with other isomorphs. Substitution of 50%K in KTP by Na (to form KNTP) did not reduce the large nonlinear optical coefficients of KTP markedly[84], so any reduction in measured SHG from KNSTP due to the presence of Na is predicted to be small. However, substitution of Ti by Sn significantly reduces the SHG ability of KTP isomorphs[175] so the 50% Sn substitution in KNSTP should reduce the SHG signal to a value similar to that of KSTP.

Sn ordering

There is partial ordering of Sn over the two Ti sites (site 1: 0.669(3)Ti, 0.331(4)Sn; site 2: 0.331(3)Ti, 0.669(3)Sn). This degree of ordering is very similar to that seen in KSTP (chapter 5.2; site 1: 0.639(4)Ti, 0.361(4)Sn, site 2: 0.359(4)Ti, 0.646(4)Sn)). The average M-O (M=Ti/Sn) bond length in KNSTP is longer than that in KTP, as expected on substitution of the larger Sn atom, and the distortion measured by Δ (the difference between the longest and shortest M-O bond) decreases as Sn more commonly adopts a regular O coordination. The distortion of the Ti(2) octahedron is less than that of $Ti(1)O_6$, consistent with the greater proportion of Sn on this site.

Bond valence calculations[136] carried out on KNSTP, KSTP and

the solid solution end-members KTP and KSP indicate that the Ti(2) site in KNSTP has a very similar environment to that in KSTP, while the Ti(1) site has decreased in size. This decrease makes the Ti(1) site more favourable for Ti and increases the degree of Ti/Sn ordering over the two sites relative to that in KSTP.

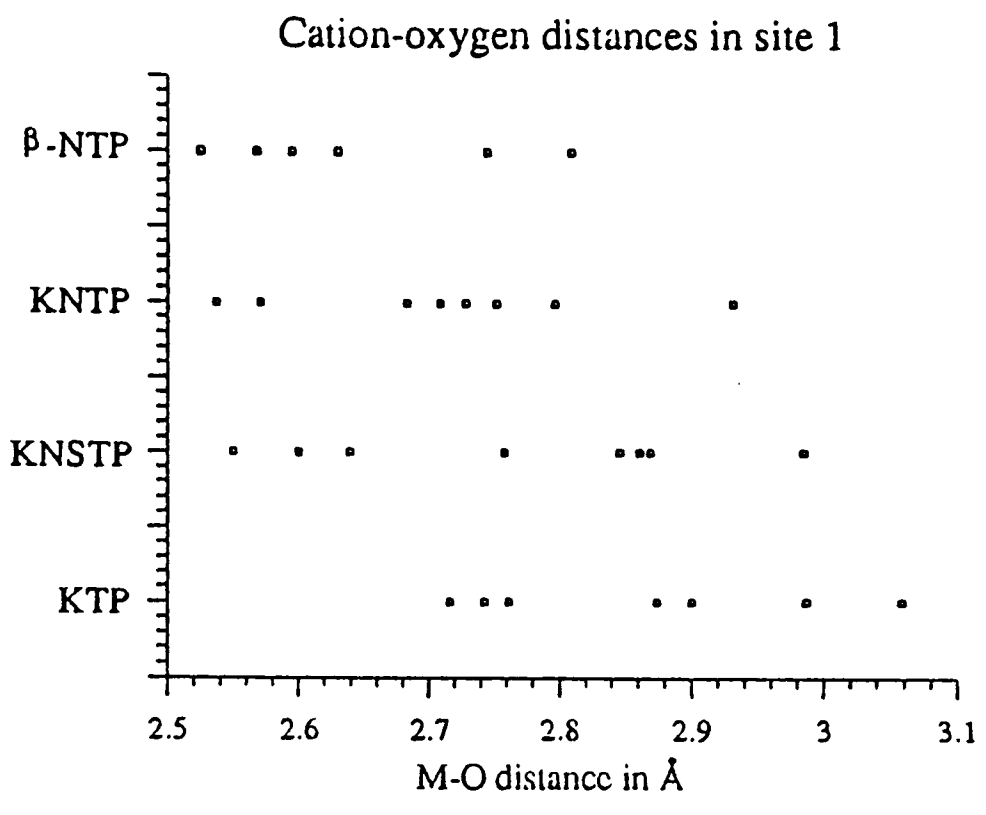
	Ti(1)	Sn(1)	Ti(2)	Sn(2)
KTP	4.17(2)		4.17(2)	
KSTP	3.77(5)	4.81(6)	3.58(5)	4.57(6)
KNSTP	4.01(7)	5.11(9)	3.62(5)	4.61(6)
KSP		4.10(5)		4.12(5)

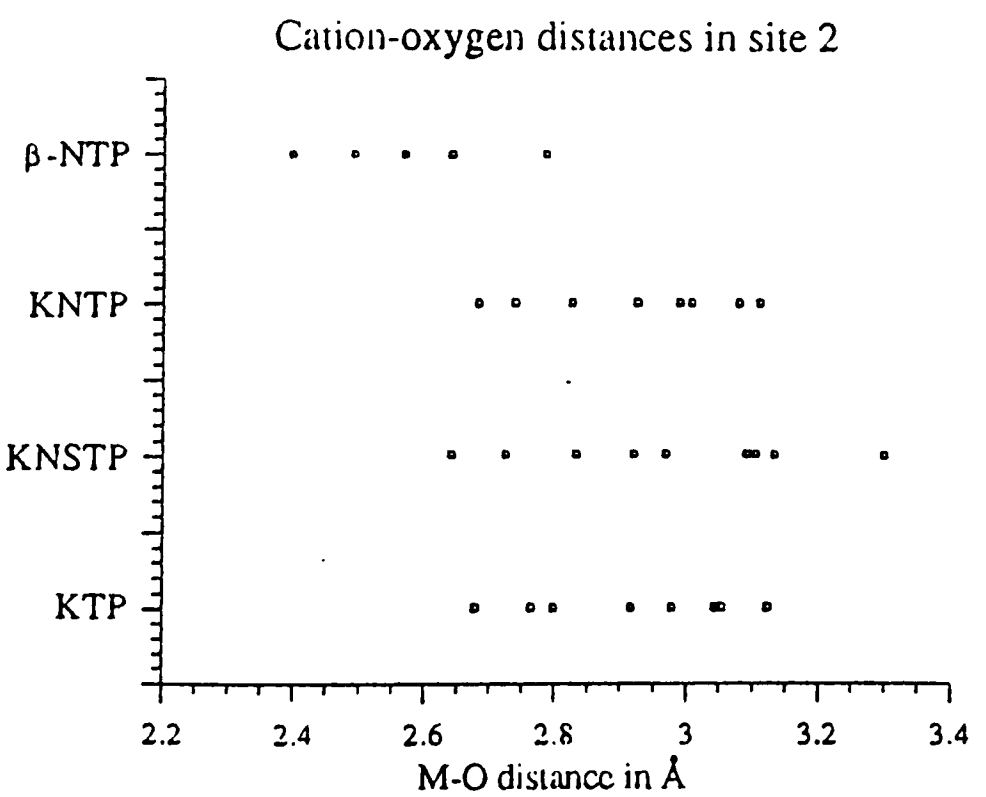
Cation ordering

In KNTP (Chapter 3.3), there is complete ordering over the two cation sites, Na occupying the K(1) site and K occupying K(2). However in KNSTP the extent of the ordering is reduced, only 73% of the K(1) site being occupied by Na, 27% occupied by K. The average bond length around the K(1) site has slightly increased due to the presence of the larger K ion (Figure 6.3.II).

The valence of Na has decreased in both cation sites on substitution of the larger Sn into the framework. In KNTP the Na(1) valence is comparable to that in β-NTP, while that of Na(2) is much lower, indicating that site 1 is the preferred site for Na occupation, and driving K onto site 2 in almost complete ordering (site 1: 0.96Na, 0.04(7)K; site 2: -0.05(8)Na, 1.05(8)K). In KNSTP site 1 is still more favourable for Na, but neither site has Na valences comparable to those in β-NTP, so the driving force is not as strong, and the cations are only partially ordered over the two sites.

Figure 6.3.II A comparison of cation-oxygen bond lengths in KNSTP with those in KNTP, β-NTP[84] and KTP[74].





	Na(1)	K(1)	Na(2)	K(2)
β-NTP	0.76(1)		0.65(1)	
KNTP	0.72(1)	1.74(1)	0.45(1)	1.05(1)
KNSTP	0.64(1)	1.57(2)	0.34(1)	1.08(1)
KTP		1.23(1)		1.12(1)

Sn substitution changes the degree of cation ordering in Na substituted KTP isomorphs by increasing the size of the framework cavity. Na substitution into KSTP has a much smaller effect, marginally increasing the Ti/Sn ordering by reducing the size of the Ti(1) octahedron.

6.4 Combined X-ray and time-of-flight neutron powder diffraction study of $Na_{0.5}Rb_{0.5}Sn_{0.5}Ti_{0.5}OPO_4$

Time-of-flight neutron diffraction data from $Na_{0.5}Rb_{0.5}Sn_{0.5}Ti_{0.5}OPO_4$ (NRSTP), were collected on GPPD, Argonne National Lab., in run number 4764. Three data banks were used in the structure refinement. X-ray diffraction data were collected on a Philips diffractometer, and combined analysis of the X-ray and neutron data was undertaken in GSAS.

The NRTP structure (Chapter 3.4) was used as the starting model for the refinement, with Na occupying 50% of the Rb sites, and Sn 50% of the Ti sites. During the refinement two impurity phases were identified, SnO_2 (Cassiterite) and $NaTi_2(PO_4)_3$. These structures were taken from the literature[174,177] and used to model the impurity peaks with structural parameters unrefined. The O(1) y coordinate was held to fix the origin along y and the P-O bond lengths were restricted to the range 1.54(1)A. The thermal parameters were constrained to a single value for each atom type, and the Ti/Sn and Na/Rb sites were each described by a single thermal parameter. The total occupancy of a site, and the total Na, Rb, Ti and Sn occupancies were constrained to unity. Data collection and refinement parameters are given in Table 6.4.1, atom coordinates and isotropic thermal parameters in Table 6.4.2, selected bond lengths in Table 6.4.3 and final profile plots in Figure 6.4.I.

Discussion

The structure of NRSTP has been determined through combined analysis of X-ray and time-of-flight neutron data. The ordering of Sn over the two Ti sites is indistinguishable from that in

Table 6.4.1 Data collection and refinement parameters for $Na_{0.5}Rb_{0.5}Sn_{0.5}Ti_{0.5}OPO_4$.

Diffractometer	GPPD, Argonne National Lab.			Philips, Nicolet L11 automation
	148°	90°	60°	
Data range	4.98-30.995	4.5-30.992	5.0-30.99(ms)	10-100°2θ
Contributing reflections	7239	2562	921	757
Total number of observations	13454			
Sample can	10mm vanadium can			flat plate
R_p (%)	3.10	3.14	4.26	6.21
wR_p (%)	4.44	4.33	5.71	8.57
R_f (%)	6.91	4.02	5.96	11.55
$R_{expected}$	1.73	1.66	2.81	2.24
χ^2	7.546			

Phase 1: $Na_{0.5}Rb_{0.5}Sn_{0.5}Ti_{0.5}OPO_4$

space group $Pn2_1a$

unit cell a=13.1435(5)Å, b=10.6433(3)Å, c=6.5478(3)Å

V=915.97(4)Å^3

Phase 2: SnO_2 atom positions and unit cell unrefined[c174]

Phase 3: $NaTi_2(PO_4)_3$ model unrefined[c177]

Scattering lengths/10^{-14}m: Na:0.363, Rb:0.708, Sn0.623, Ti-0.344, P:0.513, O:0.5805

No. parameters 104

Profile:neutron Gaussian convoluted with double exponential

	148°bank	90°bank	60°bank
σ_1	319(12)	270(12)	273(14)
σ_2	7(1)	13(2)	3(3)

X-ray Pseudo-Voigt
GW:2(2), LX:6.8(9), LY:28(2), asym.:9.5(2)

Background neutron 8 term cosine Fourier series
X-ray 5 term cosine Fourier series

Table 6.4.2 Atom coordinates and thermal parameters of $Na_{0.5}Rb_{0.5}Sn_{0.5}Ti_{0.5}OPO_4$.

	x	y	z	$U_{iso}(Å^2)$	occupancy
Ti(1)	0.3716(8)	-.012(2)	0.481(3)	-.003(1)	0.670(5)
Sn(1)	0.3716(8)	-.012(2)	0.481(3)	-.003(1)	0.330(5)
Ti(2)	0.249(1)	0.2451(13)	0.239(2)	-.003(1)	0.330(5)
Sn(2)	0.249(1)	0.2451(13)	0.239(2)	-.003(1)	0.670(5)
P(1)	0.4981(6)	0.2571(8)	0.3369(7)	0.0016(5)	
P(2)	0.1780(4)	0.5028(9)	0.5018(17)	0.0016(5)	
Na(1)	0.3817(7)	0.3246(10)	0.7793(14)	0.022(2)	0.46(2)
Rb(1)	0.3817(7)	0.3246(10)	0.7793(14)	0.022(2)	0.54(2)
Na(2)	0.0996(8)	0.0792(12)	0.896(16)	0.022(2)	0.54(2)
Rb(2)	0.0996(8)	0.0792(12)	0.6896(16)	0.022(2)	0.46(2)
O(1)	0.4856(6)	0.1490	0.4916(13)	0.0103(3)	
O(2)	0.5176(7)	0.3751(8)	0.4678(13)	0.0103(3)	
O(3)	0.4026(6)	0.2837(10)	0.2079(13)	0.0103(3)	
O(4)	0.5871(6)	0.2414(11)	0.1867(11)	0.0103(3)	
O(5)	0.1135(9)	0.5318(11)	0.3114(13)	0.0103(3)	
O(6)	0.1074(8)	0.4719(10)	0.6821(13)	0.0103(3)	
O(7)	0.2540(7)	0.6104(9)	0.5413(15)	0.0103(3)	
O(8)	0.2446(7)	0.3848(10)	0.4717(17)	0.0103(3)	
O(9)	0.2371(6)	0.6291(9)	-.0244(16)	0.0103(3)	
O(10)	0.2163(6)	0.3723(10)	0.0446(14)	0.0103(3)	

Table 6.4.3 Selected bond distances (A) in

$Na_{0.5}Rb_{0.5}Sn_{0.5}Ti_{0.5}OPO_4$

		NRSTP	KSTP	RTP
Ti(1)	-O(1)	2.280(18)	2.040(11)	2.133(7)
	-O(2)	1.914(18)	2.019(11)	1.950(7)
	-O(5)	2.221(21)	2.059(12)	2.081(8)
	-O(6)	1.986(21)	2.039(12)	2.029(8)
	-O(9)	2.077(19)	1.939(10)	1.971(7)
	-O(10)	1.736(18)	1.865(10)	1.711(7)
Δ		0.54(3)	0.19(2)	0.42(1)
mean		2.04(18)	2.00(3)	1.98(13)
Ti(2)	-O(3)	2.073(15)	2.041(10)	2.058(5)
	-O(4)	2.181(15)	2.074(10)	2.021(5)
	-O(7)	1.934(15)	1.979(11)	1.976(8)
	-O(8)	2.130(16)	2.057(11)	2.000(9)
	-O(9)	1.989(15)	1.957(11)	1.736(8)
	-O(10)	1.907(14)	1.949(11)	2.098(8)
Δ		0.27(3)	0.12(1)	0.36(1)
mean		2.04(10)	2.01(5)	1.98(12)

P(1)	-O(1)	1.542(2)	P(2)	-O(5)	1.539(2)
	-O(2)	1.543(2)		-O(6)	1.538(2)
	-O(3)	1.539(2)		-O(7)	1.539(2)
	-O(4)	1.537(2)		-O(8)	1.543(2)

		NRSTP	NRTP			NRSTP	NRTP
K(1)	-O(1)	2.985(13)	2.89(1)	K(2)	-O(1)	2.675(14)	2.826(9)
	-O(2)	2.764(14)	2.79(1)		-O(2)	3.226(14)	3.205(9)
	-O(3)	2.853(11)	2.88(1)		-O(3)	3.148(15)	3.024(9)
	-O(5)	3.124(13)	2.71(1)		-O(4)	3.013(11)	2.993(8)
	-O(7)	3.366(13)	2.75(1)		-O(5)	2.847(16)	2.854(8)
	-O(8)	2.777(13)	2.53(1)		-O(7)	3.019(15)	3.042(9)
	-O(9)	3.275(14)	2.57(1)		-O(8)	3.447(13)	3.098(9)
	-O(10)	2.829(12)	2.55(1)		-O(9)	2.617(13)	2.818(8)
					-O(10)	3.407(12)	3.069(9)
mean		3.00(22)	2.71(14)			3.05(28)	3.00(13)

	NRSTP	NRTP	KSTP
Ti(1)-O(9)-Ti(2)	121.9(8)	134.5(6)	126.1(5)
Ti(1)-O(10)-Ti(2)	144.2(9)	131.3(6)	137.1(5)

Figure 6.4.Ia Observed (dots), Calculated (continuous curve) and difference plots of GPPD 148° data from $Na_{0.5}Rb_{0.5}Sn_{0.5}Ti_{0.5}OPO_4$.

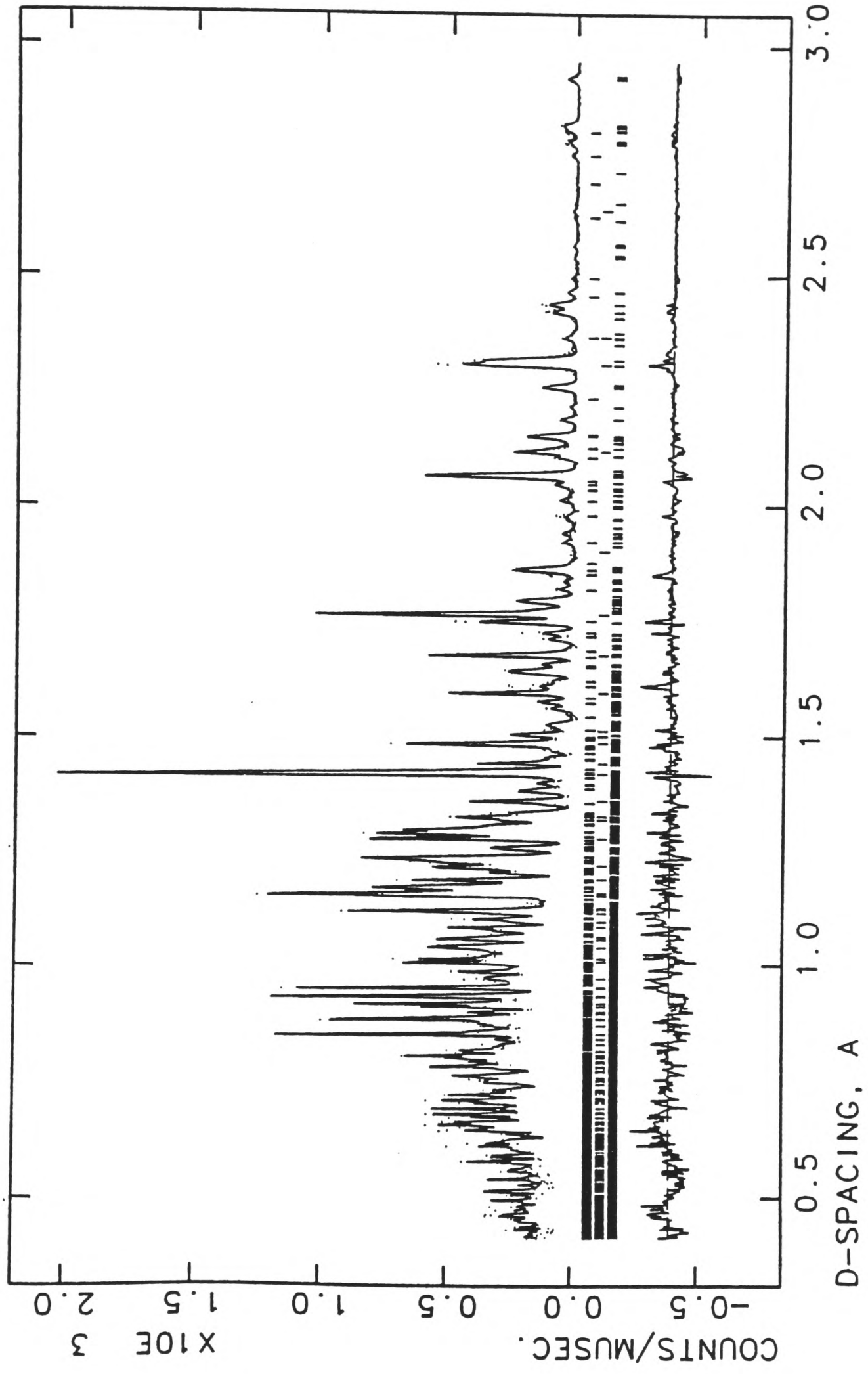


Figure 6.4.Ib Observed (dots), Calculated (continuous curve) and difference plots of GPPD 90° data from $Na_{0.5}Rb_{0.5}Sn_{0.5}Ti_{0.5}OPO_4$.

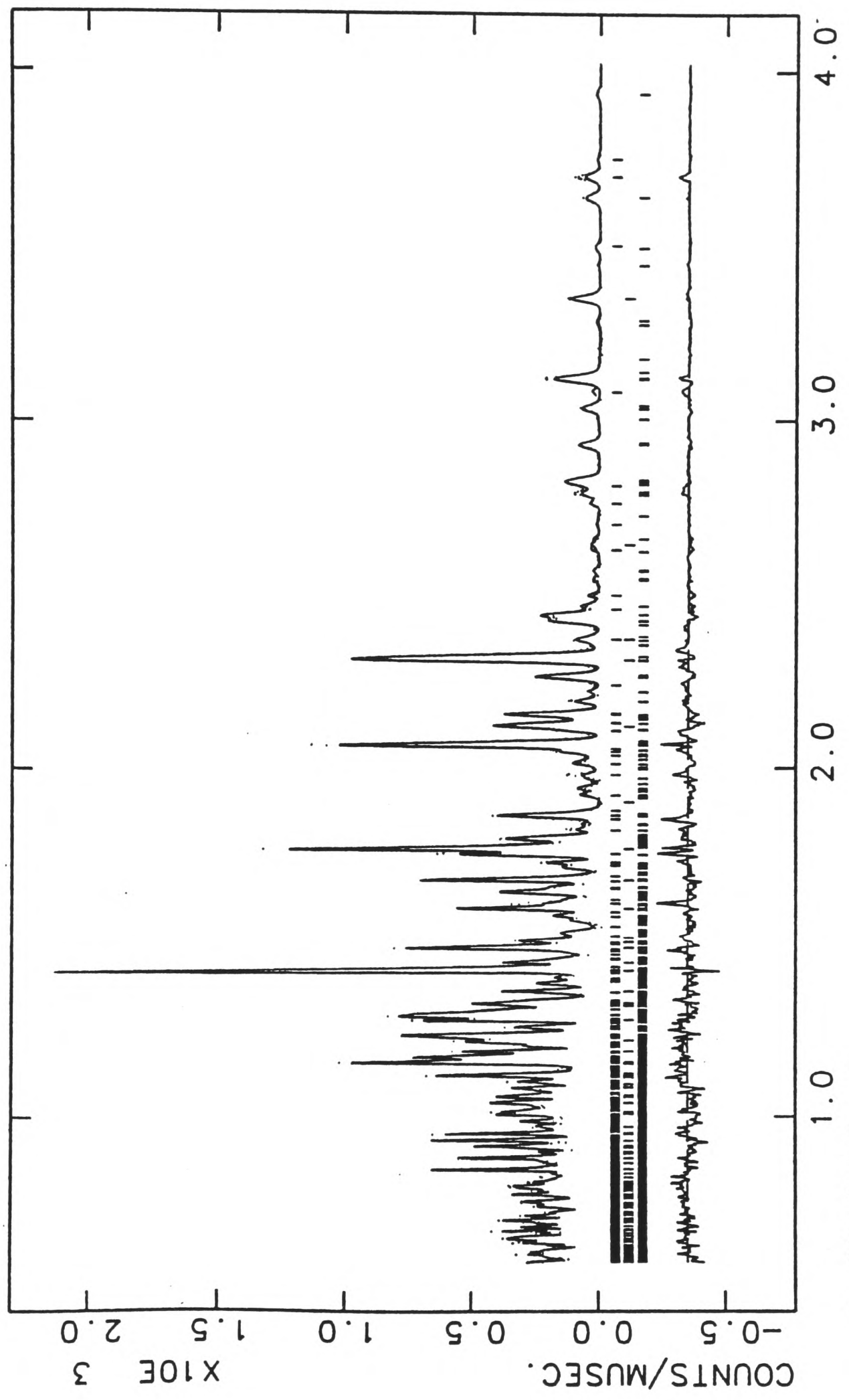


Figure 6.4.Ic Observed (dots), Calculated (continuous curve) and difference plots of GPPD 60° data from $Na_{0.5}Rb_{0.5}Sn_{0.5}Ti_{0.5}OPO_4$.

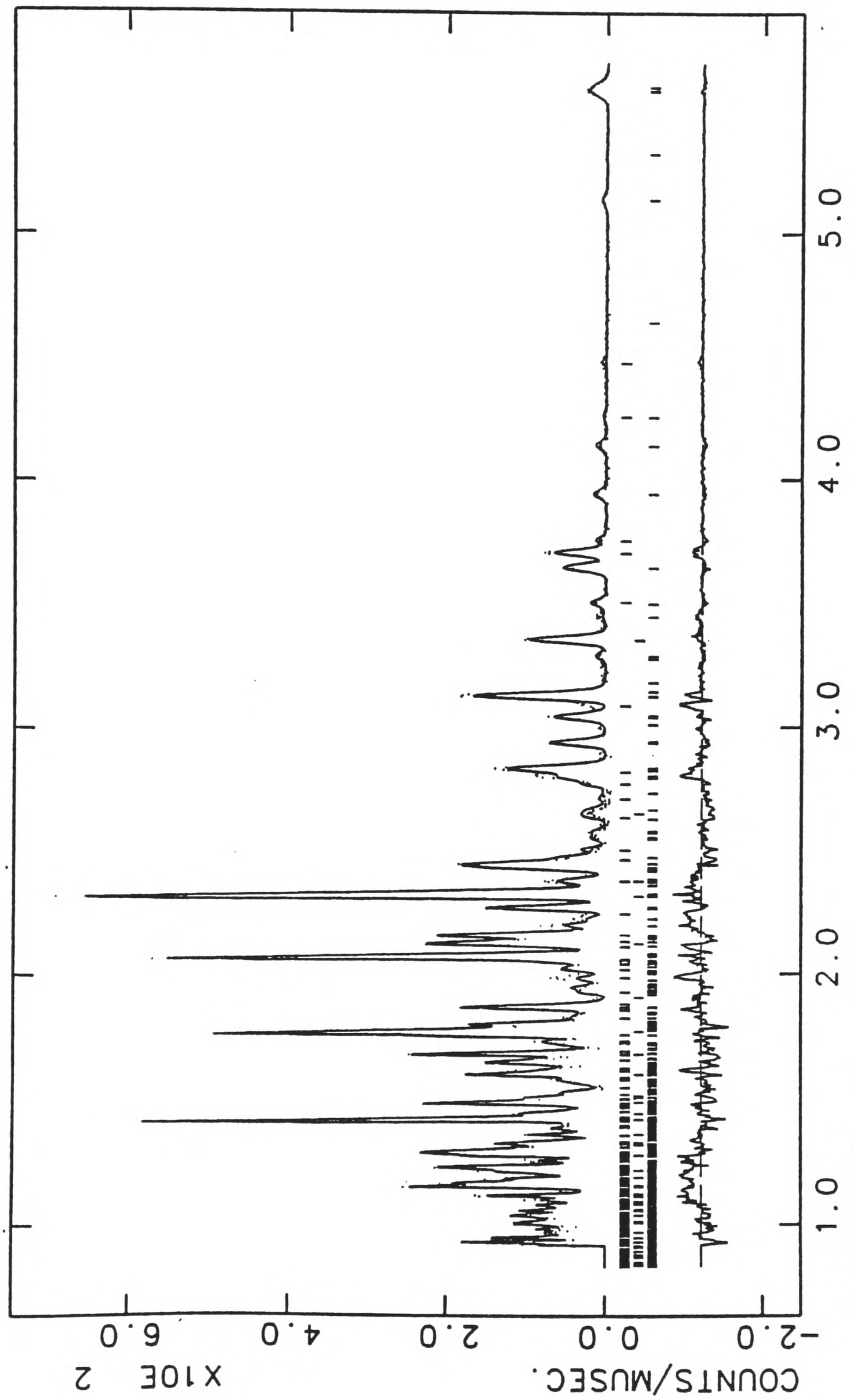
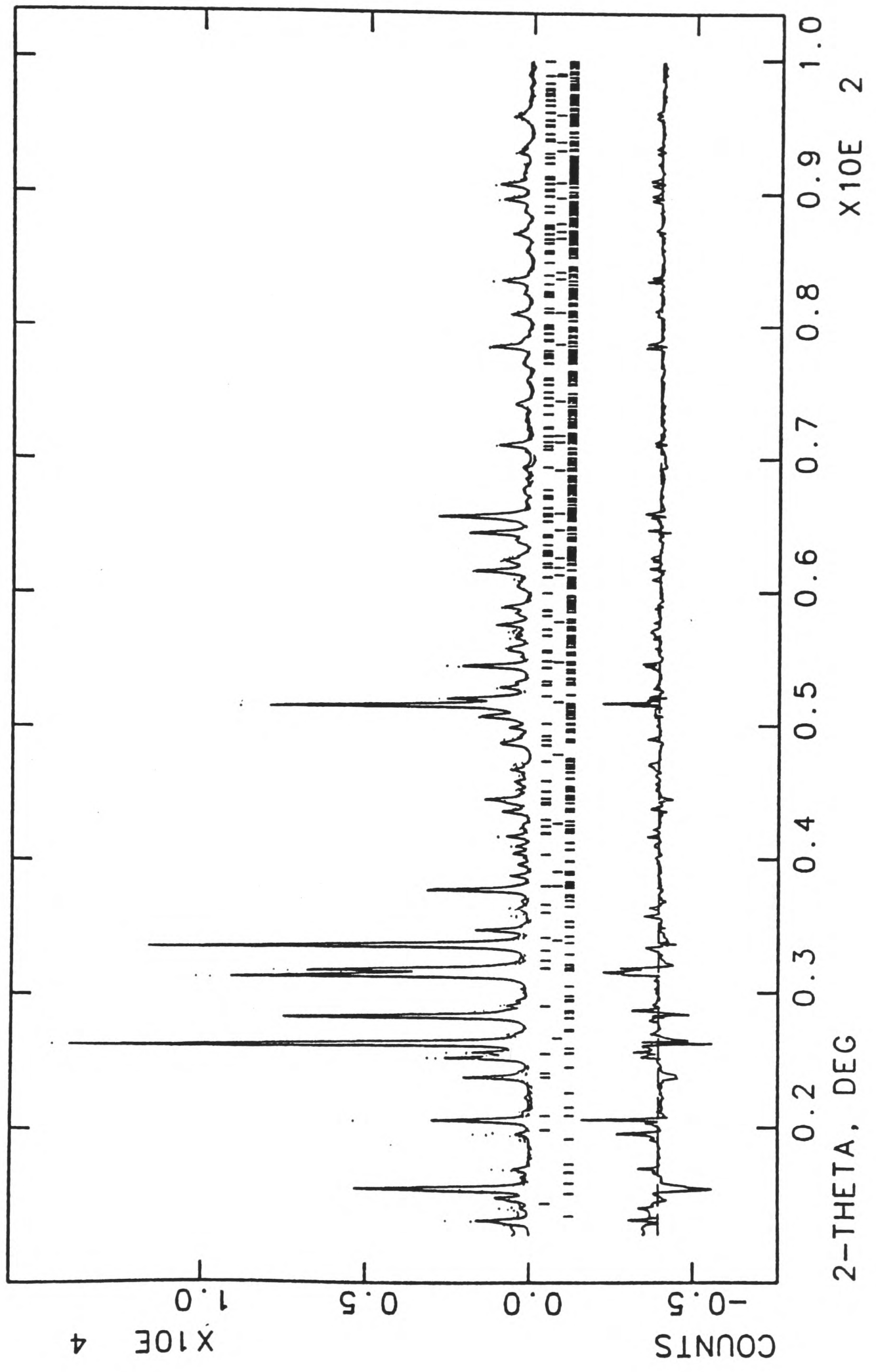


Figure 6.4.Id Observed (dots), Calculated (continuous curve) and difference plots of X-ray data from $Na_{0.5}Rb_{0.5}Sn_{0.5}Ti_{0.5}OPO_4$.



KNSTP, while Na and Rb enter the K sites in an almost random fashion, in contrast to the complete ordering seen in $Na_{0.5}Rb_{0.5}TiOPO_4$.

Sn ordering

The mean Ti-O bond length increases slightly around both Ti sites in NRSTP relative to RTP, as expected on substitution of the larger Sn atom. The distortion Δ is greater in the $Ti(1)O_6$ octahedron than in $Ti(2)O_6$ which correlates with the greater proportion of Ti found on that site, as Sn tends to form more regular coordination. The Ti and Sn valences have been calculated for NRSTP, and compared with those in RTP, KSP and KSTP.

	Ti(1)	Sn(1)	Ti(2)	Sn(2)
RTP	4.15(3)		4.05(4)	
KSTP	3.77(5)	4.81(6)	3.58(5)	4.57(6)
NRSTP	3.74(9)	4.8(2)	3.43(6)	4.38(8)
KSP		4.10(5)		4.12(5)

The Ti(1) and Sn(1) parameters are very similar to those in KSTP, indicating that there is no change to the Ti(1) site on cation substitution. However the valences of both Ti(2) and Sn(2) are smaller than in KSTP, an indication that the Ti(2) site has increased in size. This makes the site more favourable for Sn although the degree of Ti/Sn ordering observed has not significantly increased relative to that in KSTP.

Cation ordering

In NRTP there is complete cation ordering (site 1:0.97(3)Na, 0.03(3)Rb, site 2: 0.04(3)Na, 0.96(3)Rb), in contrast to NRSTP in

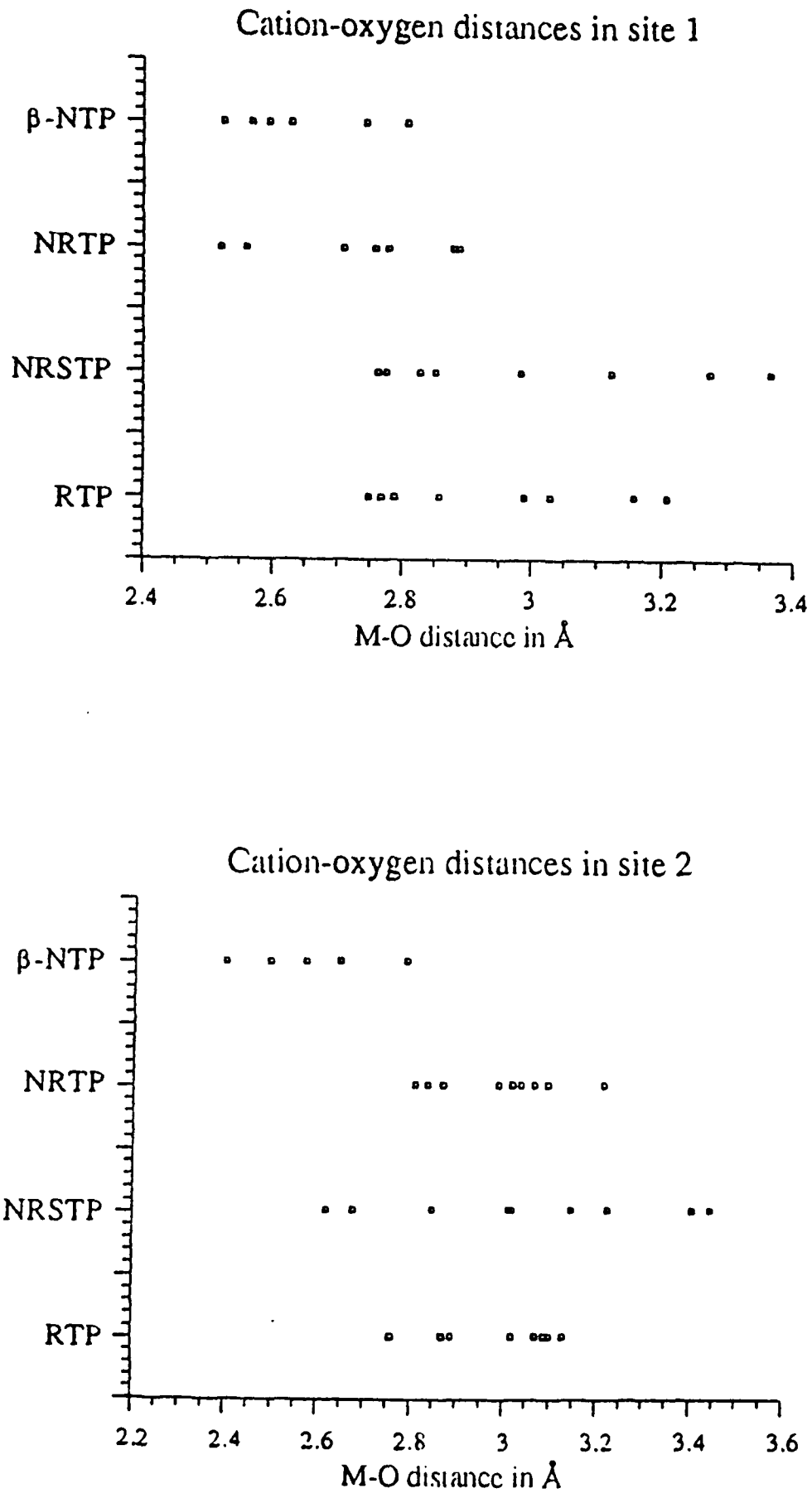
which the cation distribution is essentially random (site 1: 0.46(2)Na, 0.54(2)Rb, site 2: 0.54(2)Na, 0.46(2)Rb). The cation distributions are reflected in the cation-oxygen bond lengths, those in NRTP are shorter around site 1 than site 2, correlating with the 96% occupancy of site 1 by Na, while in NRSTP the bond lengths of the two sites are similar indicating a random cation distribution (Figure 6.4.II).

Bond valence parameters have been calculated for NRSTP, NRTP, RTP and β-NTP. The observed position of the cation site within a framework cavity is determined by the position of the dominant scatterer. In NRTP the dominant scatter in K(1) is Na and in K(2) is Rb, so the Na(1) and Rb(2) valences are very similar to those of the corresponding sites in β-NTP and RTP.

	Na(1)	Rb(1)	Na(2)	Rb(2)
β-NTP	0.76(1)		0.65(1)	
NRTP	0.74(1)	2.57(4)	0.38(1)	1.33(1)
NRSTP	0.31(1)	1.33(2)	0.34(1)	1.43(2)
RTP		1.46(1)		1.39(1)

However the Rb(1) valence in NRTP is too large, being calculated for an Rb atom on a Na site, and similarly the valence of Na(2) is too small. In NRSTP the valences for a cation are similar on the two sites, consistent with the essentially random cation distribution observed. Since the X-ray and neutron scattering power of Na is considerably less than that of Rb, Rb is the dominant scatter on both cation sites in NRSTP, so the calculated Rb valences are similar to those in RTP; the Na valences are too small, being calculated for Na at the Rb site. In reality the Na will be at positions in the cavities with shorter cation-oxygen

Figure 6.4.II Comparison of cation-oxygen bond lengths in NRSTP with those in NRTP, β-NTP[843] and RTP[1693].



bonds, but the scattering from these sites is swamped by that from the observed Rb sites.

Substitution of Na and Rb for K has marginally increased the size of the Ti(2) site but noticeably increased the degree of Ti/Sn ordering relative to that in KSTP. Substitution of 50%Ti by Sn in NRTP increased the size of the K(1) site to the point where there is no preferential cation substitution onto either site and Na and Rb are randomly distributed.

6.5 A combined X-ray and time-of-flight neutron powder study of $K_{0.5}Rb_{0.5}Sn_{0.5}Ti_{0.5}OPO_4$

An X-ray powder diffraction data set was collected on a Stoe STADI-P diffractometer and used to refine the KTP starting model.[159] Time-of-flight neutron diffraction data were collected on GPPD at Argonne National Lab., in run number 4765. Three data banks were used in a combined refinement of the KNSTP structure with the X-ray data. Initially the occupancies of K, Rb, Ti and Sn were set to 50% on each site. The O(1) y parameter was fixed to define the origin along y, and the P-O bonds were restrained to 1.54(1)Å to restrict movement in the framework. The occupancies of each site, and the total occupancy of K, Rb, Sn and Ti were constrained to be unity. SnO_2 was modelled as an impurity phase in the refinement; other unindexed lines matched the $RbTi_2(PO_4)_3$ pattern in the Powder Diffraction File, whose structure has not been reported.

Initially the thermal parameters were constrained to a single value for each atom type. The converged refinement of this model contained the cation thermal parameters: K:0.097(8)Å^3 and Rb:0.012(1)Å^3 (with site 1 containing 0.66(1)K, 0.34(1)Rb and site 2, 0.34(1)K, 0.66(1)Rb). K and Rb are of reasonably similar size (ionic radii 1.33 and 1.47Å respectively), so would be predicted to occupy similar sites within the TiO_6-PO_4 framework cavities, with similar thermal motion. To obtain more reasonable thermal parameters, the thermal parameters of K and Rb, and those of Ti and Sn, were constrained to a single value in subsequent refinement cycles. Final data collection and refinement parameters are given in Table 6.5.1, atomic coordinates and thermal parameters in Table 6.5.2, selected bond distances in

Table 6.5.3 and final profile plots in Figure 6.5.I.

Table 6.5.1 Data collection and refinement parameters for $K_{0.5}Rb_{0.5}Sn_{0.5}Ti_{0.5}OPO_4$

Diffractometer	GPPD, Argonne National Lab			STOE STADIP
	148°bank	90°bank	60°bank	θ-2θ
Data range	4.0-30.995	4.5-30.992	5.0-30.99ms	10-85°2θ
Contributing reflections	6642 from KRSTP phase	3551	1387	383
Total no. of observations	11109			
Sample can	10mm diameter vanadium can			flat plate
R_p (%)	3.31	3.39	3.86	8.14
wR_p (%)	4.91	4.92	5.87	10.90
R_f (%)	4.77	2.69	2.92	7.47
$R_{expected}$	1.78	1.71	2.91	12.27
χ^2	7.448 for 129 parameters			
Phase 1: $K_{0.5}Rb_{0.5}Sn_{0.5}Ti_{0.5}OPO_4$				
space group	$Pn2_1a$			
unit cell	a=13.0440(5)Å, b=10.6304(4)Å, c=6.4961(3)Å			
	V=900.8(1)Å^3			
Phase 2: SnO_2 (Cassiterite structural parameters unrefined)				
Scattering lengths/10^{-14}m	K:0.367, Rb:0.708, Sn:0.623, Ti:-0.344, P:0.513 O:0.5805			
Profile:neutron	Gaussian convoluted with double exponential			
		148°	90°	60°
	σ_1	297(7)	302(6)	297(6)
	σ_2	14(2)	10(1)	6.5(7)
X-ray	Pseudo-Voigt			
	GW:17(2), LX:-3.1(9), LY:31(3), asym.-1.7(4)			
Background	6 term cosine Fourier series			

Table 6.5.2 Atom coordinates and isotropic thermal parameters of $K_{0.5}Rb_{0.5}Sn_{0.5}Ti_{0.5}OPO_4$

	x	y	z	$U_{iso}(A^2)$	occupancy
Ti(1)	0.3732(4)	0.0048(11)	0.4953(15)	0.00018(7)	0.661(3)
Sn(1)	0.3732(4)	0.0048(11)	0.4953(15)	0.00018(7)	0.339(3)
Ti(2)	0.2499(6)	0.2573(9)	0.2495(11)	0.00018(7)	0.339(3)
Sn(2)	0.2499(6)	0.2573(9)	0.2495(11)	0.00018(7)	0.661(3)
P(1)	0.4970(4)	0.2636(6)	0.3387(4)	0.00476(4)	
P(2)	0.1804(2)	0.5104(9)	0.4980(10)	0.00476(4)	
K(1)	0.3812(5)	0.3150(7)	0.7813(9)	0.0264(8)	0.77(1)
Rb(1)	0.3812(5)	0.3150(7)	0.7813(9)	0.0264(8)	0.23(1)
K(2)	0.1078(3)	0.0774(6)	0.6919(7)	0.0264(8)	0.23(1)
Rb(2)	0.1078(3)	0.0774(6)	0.6919(7)	0.0264(8)	0.77(1)
O(1)	0.4803(3)	0.1479	0.477(1)	0.0090(2)	
O(2)	0.5081(5)	0.3828(4)	0.4725(9)	0.0090(2)	
O(3)	0.4008(3)	0.2766(7)	0.2014(8)	0.0090(2)	
O(4)	0.5893(3)	0.2363(7)	0.1936(8)	0.0090(2)	
O(5)	0.1089(6)	0.5368(7)	0.3132(10)	0.0090(2)	
O(6)	0.1123(5)	0.4838(7)	0.6887(10)	0.0090(2)	
O(7)	0.2478(4)	0.6260(8)	0.5362(10)	0.0090(2)	
O(8)	0.2522(4)	0.3981(7)	0.4649(10)	0.0090(2)	
O(9)	0.2292(4)	0.6367(7)	-.0240(9)	0.0090(2)	
O(10)	0.2194(4)	0.3796(7)	0.0394(9)	0.0090(2)	

Table 6.5.3 Selected bond distances (Å) in $K_{0.5}Rb_{0.5}Sn_{0.5}Ti_{0.5}OPO_4$.

		KRSTP	KSTP			KRSTP	KSTP
Ti(1)	-O(1)	2.069(10)	2.040(11)	Ti(2)	-O(3)	2.003(8)	2.041(10)
	-O(2)	2.031(10)	2.019(11)		-O(4)	2.139(9)	2.074(10)
	-O(5)	2.106(11)	2.059(12)		-O(7)	1.967(10)	1.979(11)
	-O(6)	2.013(11)	2.039(12)		-O(8)	2.049(11)	2.057(11)
	-O(9)	1.941(10)	1.939(10)		-O(9)	1.971(10)	1.957(11)
	-O(10)	1.819(9)	1.865(10)		-O(10)	1.926(10)	1.949(11)
Δ		0.28(2)	0.19(2)			0.21(1)	0.12(1)
mean		2.00(9)	2.00(3)			2.01(7)	2.01(5)

P(1)	-O(1)	1.540(4)	P(2)	-O(5)	1.547(4)
	-O(2)	1.543(4)		-O(6)	1.551(4)
	-O(3)	1.545(4)		-O(7)	1.532(4)
	-O(4)	1.557(4)		-O(8)	1.532(4)

		KRSTP	KRTP	KRSP
K(1)	-O(1)	2.954(9)	2.864(7)	3.131(9)
	-O(2)	2.699(9)	2.704(8)	2.801(10)
	-O(3)	2.771(7)	2.716(7)	2.889(8)
	-O(5)	2.967(8)	2.945(8)	3.111(10)
	-O(7)	3.100(9)	3.107(7)	3.033(9)
	-O(8)	2.799(9)	2.806(8)	2.760(9)
	-O(9)	3.099(8)	3.063(7)	2.975(9)
	-O(10)	2.782(8)	2.758(9)	2.582(11)
mean		2.90(14)	2.87(14)	2.91(18)
K(2)	-O(1)	2.819(8)	2.760(7)	2.856(8)
	-O(2)	3.145(7)	3.088(6)	3.367(9)
	-O(3)	3.200(8)	3.097(6)	3.018(9)
	-O(4)	3.030(6)	3.041(6)	3.102(8)
	-O(5)	2.859(8)	2.792(7)	2.839(9)
	-O(7)	2.969(8)	2.988(8)	3.151(9)
	-O(8)	3.180(7)	3.153(7)	3.153(8)
	-O(9)	2.623(7)	2.753(8)	2.709(8)
	-O(10)	3.238(6)	3.198(7)	3.045(8)
mean		3.01(20)	2.99(16)	3.03(19)

	KRSTP	KRTP	KSTP	KRSP
Ti(1)-O(9)-Ti(2)	127.8(5)	136.4(5)	126.1(5)	127.6(4)
Ti(1)-O(10)-Ti(2)	137.9(5)	134.8(5)	137.1(5)	137.4(4)

Figure 6.5.Ia Observed (dots), calculated (continuous curve) and difference plots of GPPD 148° data from $K_{0.5}Rb_{0.5}Sn_{0.5}Ti_{0.5}OPO_4$.

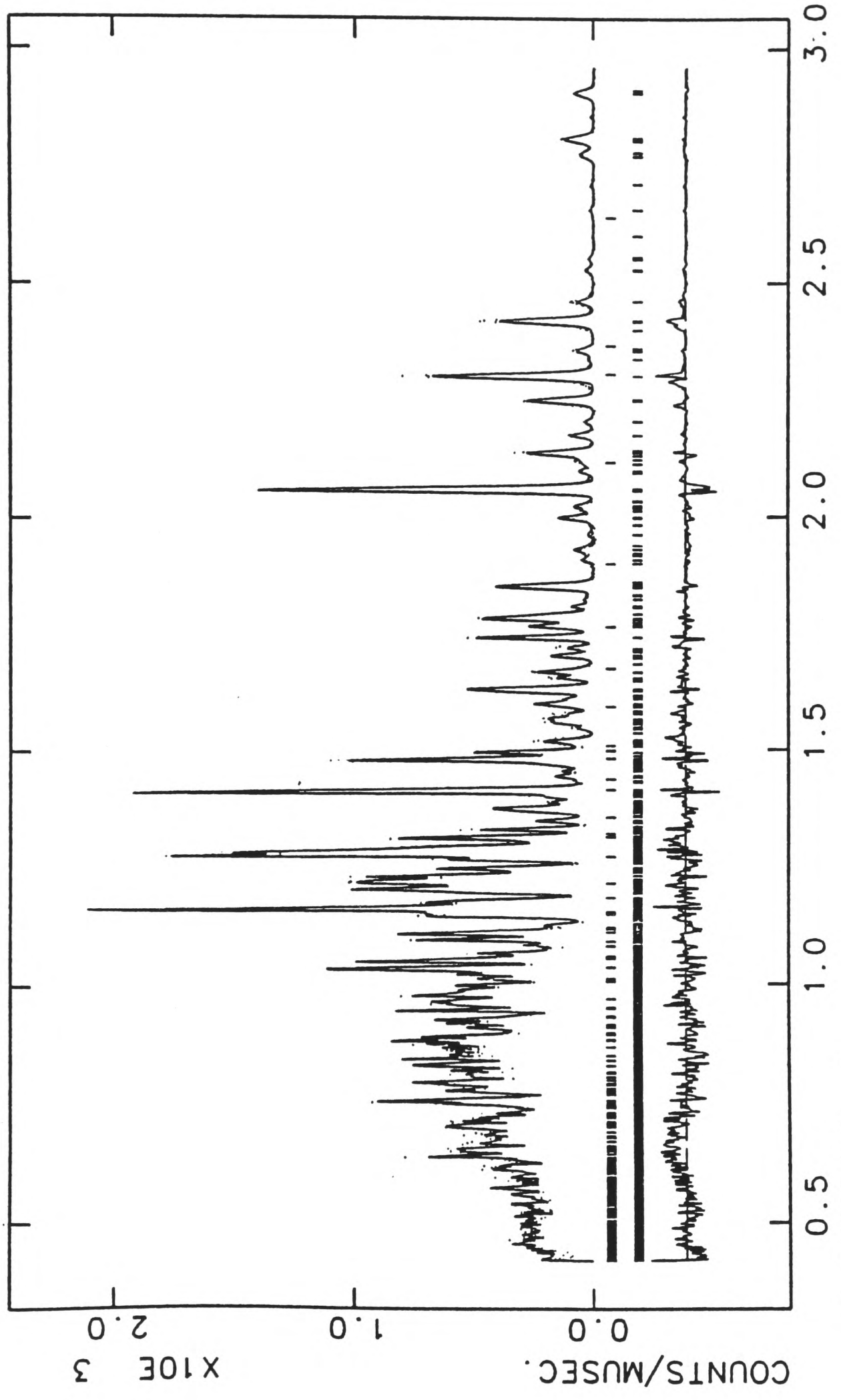


Figure 6.5.Ib Observed (dots), calculated (continuous curve) and difference plots of GPPD 90° data from $K_{0.5}Rb_{0.5}Sn_{0.5}Ti_{0.5}OPO_4$.

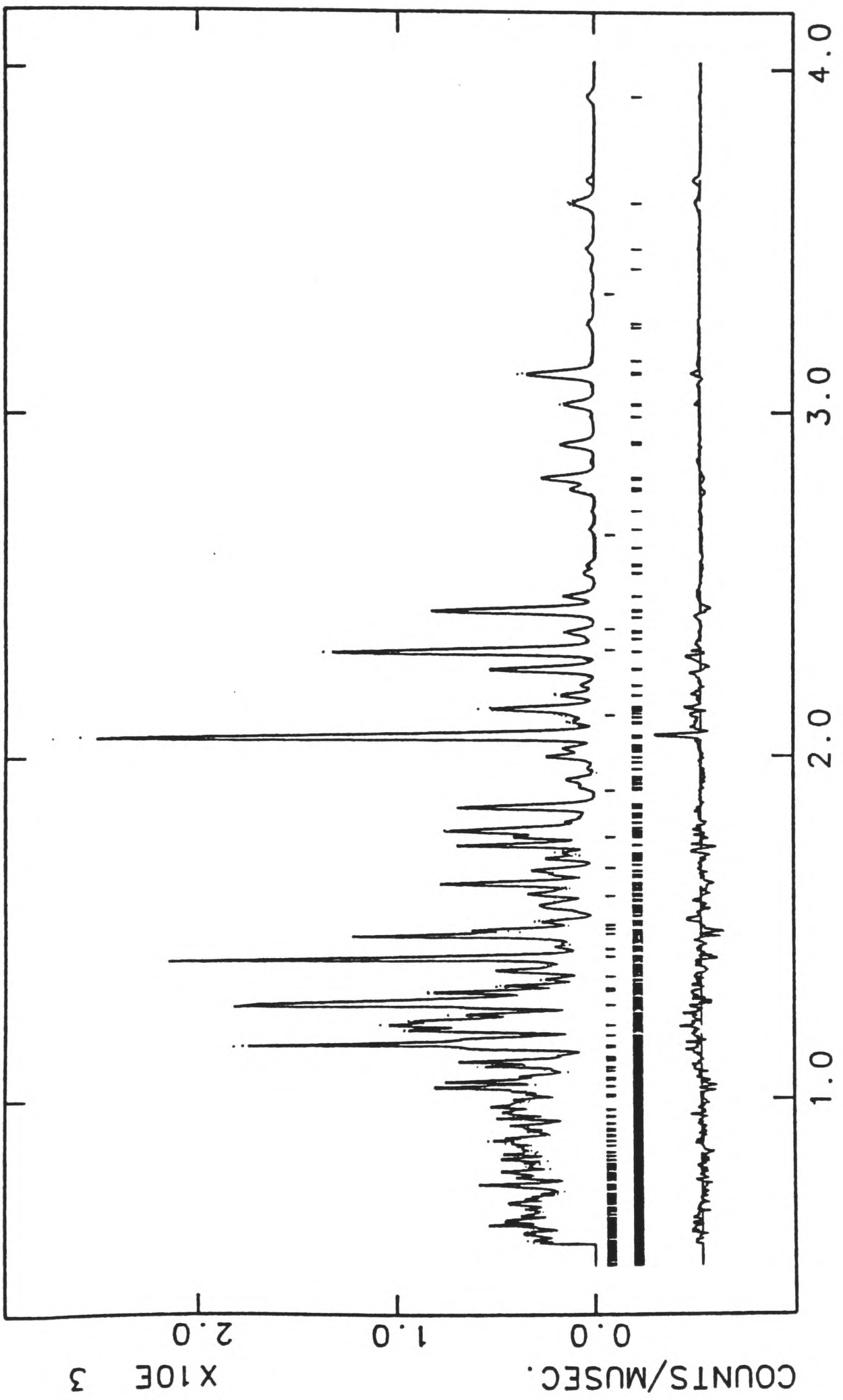


Figure 6.5.Ic Observed (dots), calculated (continuous curve) and difference plots of GPPD 60° data from $K_{0.5}Rb_{0.5}Sn_{0.5}Ti_{0.5}OPO_4$.

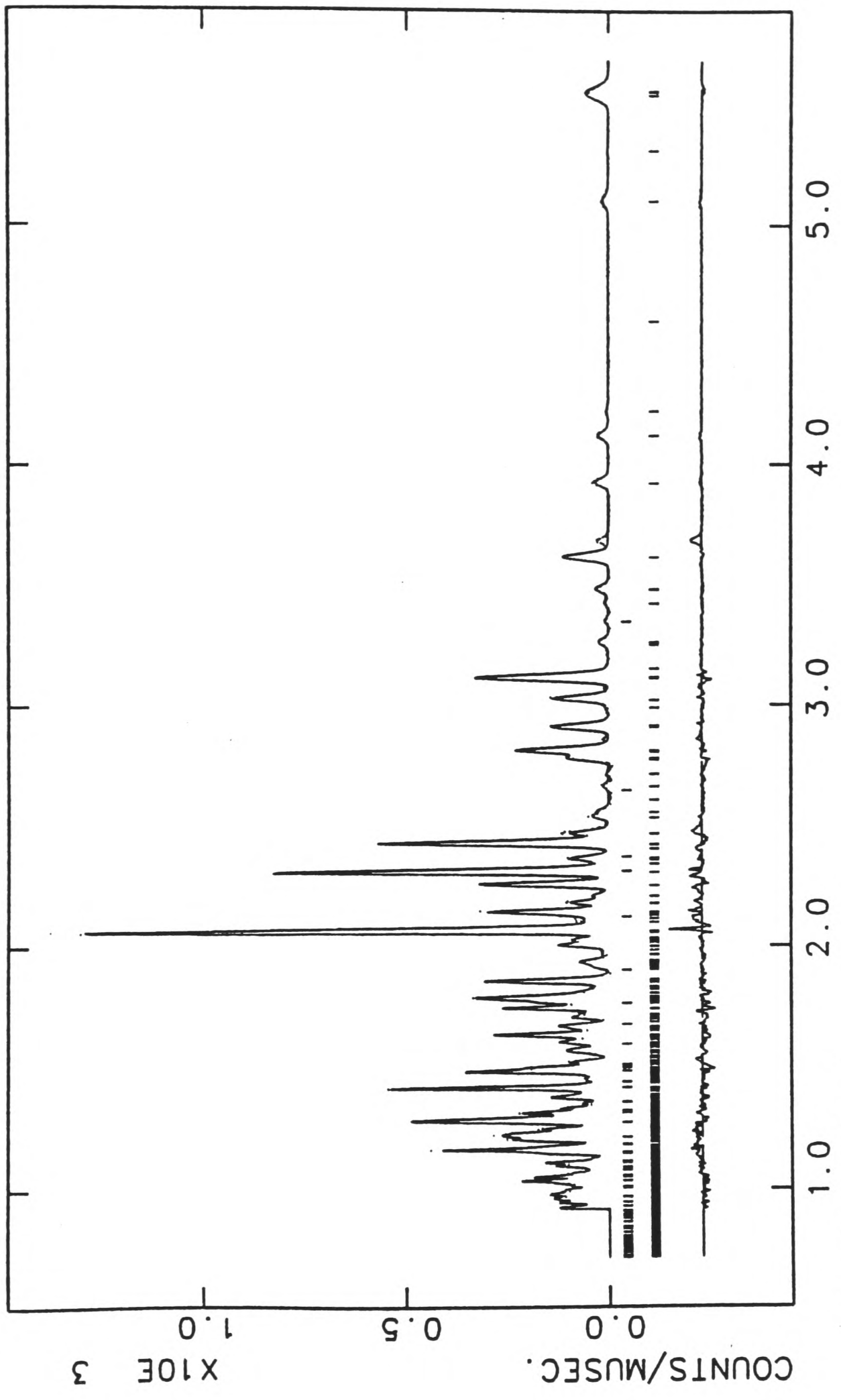
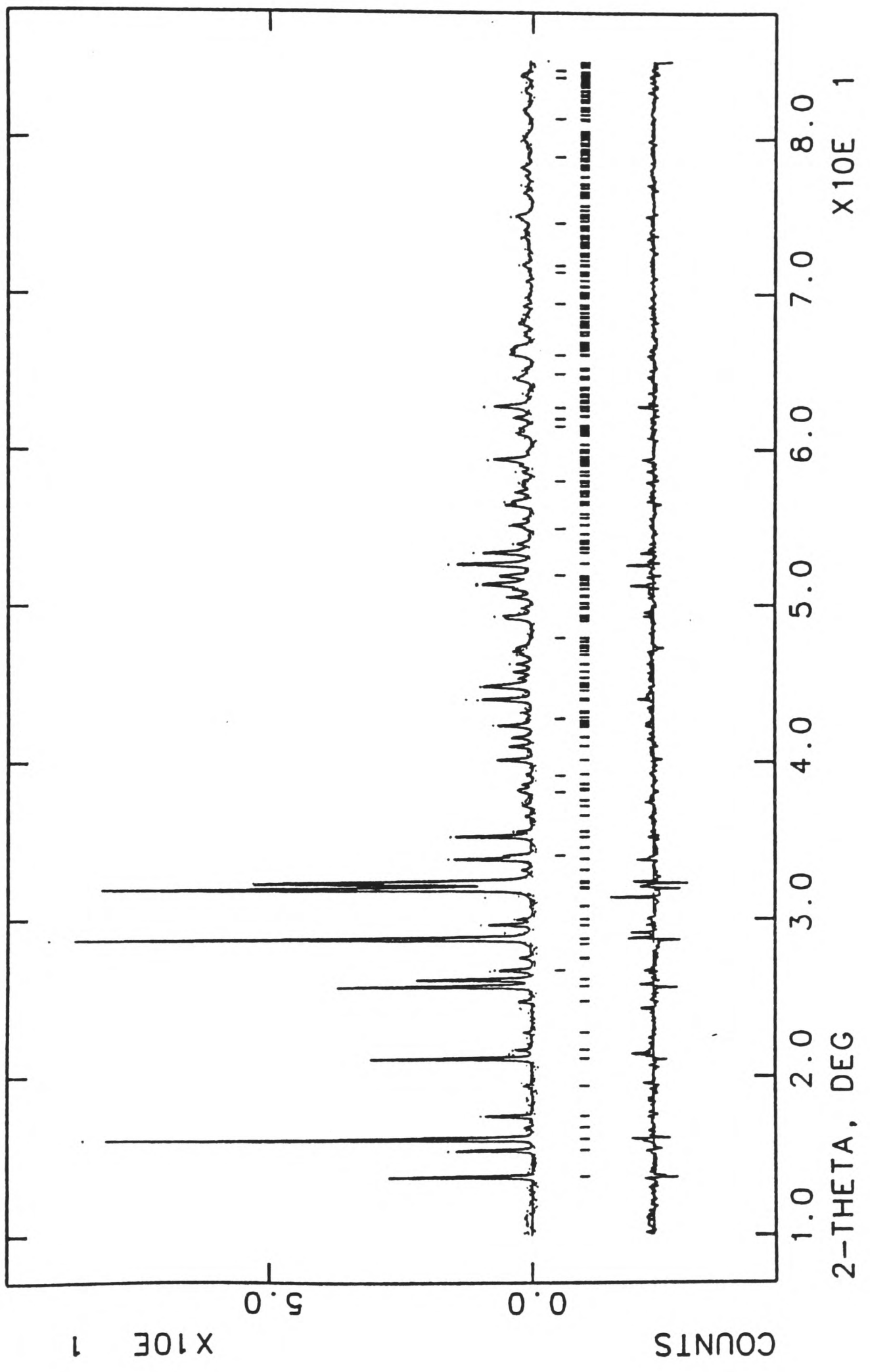


Figure 6.5.Id Observed (dots), calculated (continuous curve) and difference plots of X-ray data from $K_{0.5}Rb_{0.5}Sn_{0.5}Ti_{0.5}OPO_4$.



Discussion

The structure of KRSTP has been determined through combined analysis of X-ray and time-of-flight neutron powder diffraction data. The distribution of Ti and Sn over the two Ti sites is very similar to that in KNSTP and NRSTP, while the degree of ordering over the K sites is greater than in either of the other MM'STP materials.

Sn and Ti ordering

A comparison with the bond lengths of KSTP (Table 6.5.3) shows that the mean bond lengths do not change on substitution of Rb into the framework cavities. Bond valence calculations for KRSTP and other solid solution members give the following parameters:

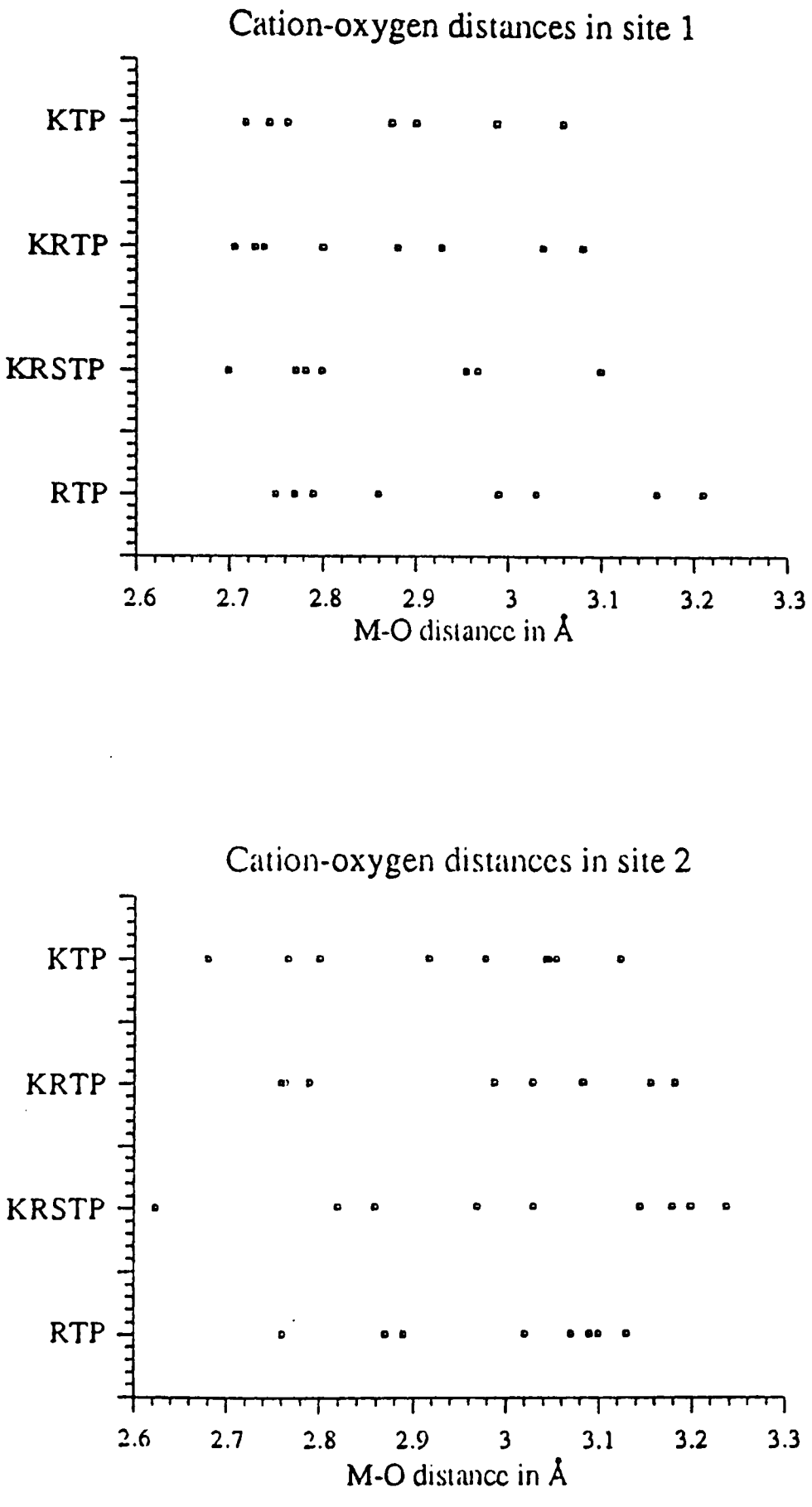
	Ti(1)	Sn(1)	Ti(2)	Sn(2)
KTP	4.17(2)		4.17(2)	
RTP	4.15(3)		4.05(3)	
KSTP	3.77(5)	4.81(6)	3.58(5)	4.57(6)
KRSTP	3.80(5)	4.85(7)	3.61(4)	4.60(5)
KSP		4.10(5)		4.12(5)

The Ti and Sn valences change little when Rb is substituted for K in KSTP, being only marginally larger in KRSTP. This slight decrease in the size of the Ti/Sn site makes Ti(1) more favourable for Ti and thereby increases the ordering of Ti and Sn over the two sites in the KRSTP structure.

Cation ordering

The cation-O distances in KRSTP are compared with those in KRTP and KRSP in Table 6.5.3 and Figure 6.5.II. The average bond length of both sites increases on Sn substitution, the cavities

Figure 5.6.II Comparison of cation-oxygen bond lengths in KRSTP, KRTP, KTP[274], KSP[1683] and RTP[1893].



increasing in size as the larger Sn enters the TiO_6-PO_4 framework. Bond valence parameters for K and Rb in the two sites have been calculated for KRSTP and the solid solution end-members:

	K(1)	Rb(1)	K(2)	Rb(2)
KTP	1.23(1)		1.12(1)	
RTP		1.46(1)		1.39(1)
KRTP	1.17(1)	1.66(1)	0.99(1)	1.41(1)
KRSTP	1.09(1)	1.55(1)	0.982(5)	1.40(1)
KRSP	1.10(1)	1.57(2)	0.875(8)	1.30(1)
KSP	1.16(1)		0.98(1)	

Generally the substitution of Sn into the framework causes the valences of the K and Rb sites to decrease, reflecting the increase in cavity size. As the dimensions of the sites increase, site 1 becomes slightly more favourable for Rb and the degree of cation ordering decreases over the solid solution as a whole, as the cations can be more equally distributed.

However the cavity size does not increase linearly with the Sn content. In KRSTP the valences of K(1) and Rb(1) are equal to those in KRSP while those of K(2) and Rb(2) have not decreased relative to those in KRTP; i.e. there is no change in the size of K(2) on 50% Sn substitution.

Chapter 3.6 discussed the partial ordering in KRTP; site 2 of KRTP is preferred by both cations but site 1 also has a K valence less than that in KTP so Rb substitutes into site 2 to a greater extent. In KRSTP site 1 is larger and the K(1) valence is closer to the ideal value of unity. The preference of K for site 2, in competition with Rb, is less intense in KRSTP and the ordering over the two cation sites is greater than in KRTP. In

KRSP all the sites with the exception of Rb(1) have valences less than those in the solid solution end-members, making the preference for site 2 less marked and reducing the cation ordering:

KRTP	KRSTP	KRSP
71(2):29(2)	77(1):23(1)	64(2):36(2)

Rb substitution into KSTP has only a small effect on the framework, marginally reducing the size of both Ti sites and marginally increasing the degree of Ti/Sn ordering. Complete Sn substitution into KRTP increases the cavity size and decreases the site ordering in KRSP relative to KRTP. In the 50% substituted KRSTP, the K(1) site increases in size while K(2) remains unchanged and the ordering increases as K(1) becomes more favourable for K occupancy.

6.6 Mechanisms of substituent ordering in the framework and cation cavities of $KTiOPO_4$

6.6.1 Effect on the framework of cation substitution

Sn preferentially substitutes into the Ti(2) site in KTP, the site occupancies in KSTP being:

site 1 0.639(4)Ti, 0.361(4)Sn,

site 2 0.354(5)Ti, 0.646(5)Sn.

The substitution of any other cation into KSTP marginally increases the Sn:Ti ordering by a similar degree:

KNSTP	NRSTP	KRSTP
0.669(3);0.331(3)	0.670(5);0.330(5)	0.661(3);0.339(3)

The extent of the ordering is the same in the three MM'STP

compounds within three e.s.d.s. However the marginal increase appears to be caused by different mechanisms. In KNSTP, substitution of Na into the cavities decreases the size of the Ti(1) site more than that of Ti(2), and increases the amount of ordering by making this site less suitable for Sn occupation. Substitution of Rb into KSTP decreases the dimensions of both sites, again making the Ti(1) site less favourable for Sn. Substitution of both Na and Rb into KSTP enlarges Ti(2) to a greater extent than Ti(1), making Ti(2) less suitable for Ti substitution.

Therefore cation substitution affects ordering within the KTP framework, but the extent of disruption to the ordering seems to be limited.

6.6.2 Effect on cation ordering of Sn substitution

Substitution of Sn into KTP isomorphs containing Na decreases the ordering markedly, from 100% in KNTP to 73% in KNSTP and from 100% in NRTP to 50% in NRSTP. This is achieved by an increase in the size of the K(1) cavity, making it less favourable for Na than in the pure Ti KTP isomorphs. In KRSTP the ordering is marginally greater than that in KRTP, Sn substitution increases the size of the K(1) cavity in a similar fashion to that in the other isomorphs. The ordering in KRTP is only partial unlike that in KNTP and NRTP and is achieved through competition between Rb and K for the K(2) site, resulting in the majority of K remaining on K(1) while Rb substitutes mainly on K(2). Increasing the size of K(1) makes it more favourable for K and reduces the competition of K with Rb for the K(2) site.

In all three cases, alteration of the ordering takes place

through an increase in the size of the K(1) site. The KRTP-KRSTP-KRSP solid solution series demonstrates that when all the Ti has been exchanged by Sn, both cation cavities have increased in size but the increase in K(1) is achieved between zero and 50%Sn and the K(2) between 50 and 100%Sn. This sequential increase can be explained by an examination of the cation-Ti distances given in Table 6.6.1. The shortest interaction is that of Ti(2) to K(1), followed by that of Ti(1) to K(2). Sn preferentially substitutes into the Ti(2) site, increasing the dimensions of the framework close to K(1) first, with K(2) only being significantly affected when more than 50%Sn is present. The proximity of Ti(1) to K(2) and Ti(2) to K(1) is shown in Figure 6.6.I.

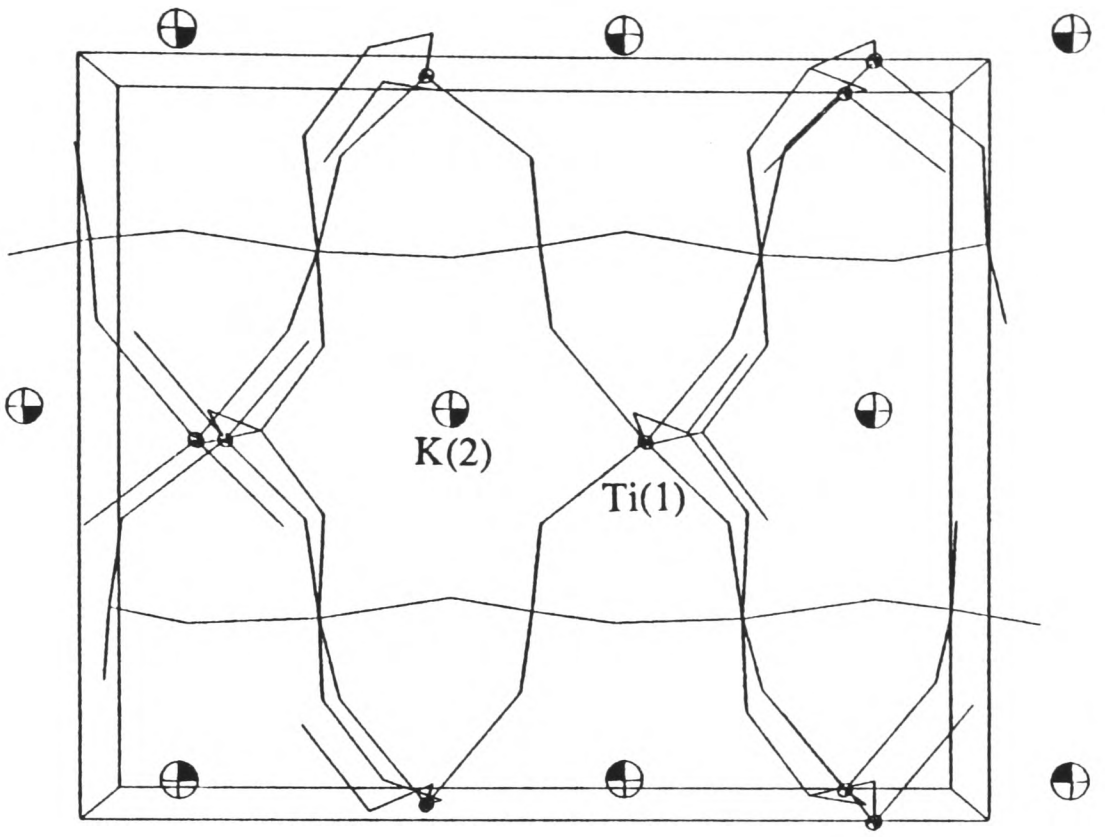
Table 6.6.1 Cation-Ti distances in MM'STP materials

	Ti(1)-K(1)	Ti(1)-K(2)	Ti(2)-K(1)	Ti(2)-K(2)
KNSTP	3.566(17)	3.716(11)	3.370(12)	3.860(12)
	3.939(13)	3.718(13)	3.600(12)	3.950(11)
mean	3.78(19)	3.72(1)	3.49(12)	3.91(5)
NRSTP	3.98(2)	3.95(2)	3.58(2)	3.96(2)
	4.05(2)	3.82(2)	4.04(1)	4.09(2)
	4.09(2)			
mean	4.04(5)	3.89(7)	3.81(23)	4.03(7)
KRSTP	4.125(10)	3.769(8)	3.544(10)	3.918(9)
	4.191(10)	3.754(8)	3.904(9)	3.893(8)
	3.787(12)			
mean	4.04(18)	3.762(8)	3.72(18)	3.91(1)

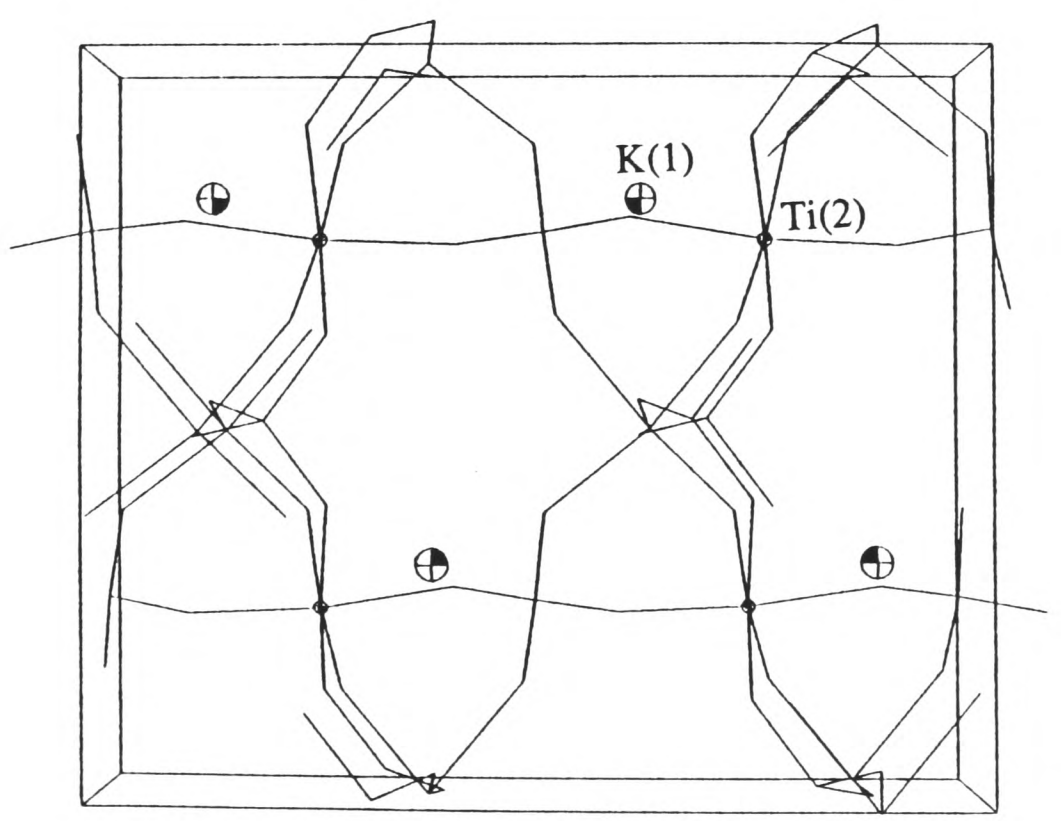
Therefore framework substitution has a marked effect on cation ordering due to the preferential increase of the K(1) framework cavity on 50% Sn substitution.

Figure 6.6.I The unit cell of $KTiOPO_4$, viewed down the c axis showing a) the Ti(1) and K(2) sites and b) the Ti(2) and K(1) sites

a)



b)



CHAPTER SEVEN

7.1 Introduction

Some batches of KTP crystals grown from a flux in the Amoco Research Center were pale green in colour. Analysis of the material indicated that the colouration was due to accidental Cr incorporation.

The substitution of other transition metals for Ti in KTP has been reported. For instance V(IV) forms a complete $KTi_{1-x}V_xOPO_4$ solid solution. The structure of KVP is very similar to that of KTP[170], with chains of distorted V-O-V- bonds which include the shortest known metal-O bond in a KTP isomorph (V(1)-O(10) = 1.673Å). Metals in other oxidation states have been partially substituted for KTP, crystals containing 8%Nb have been characterised with the Nb(V) being charge balanced by K deficiency.[178] However in order to synthesise a complete solid solution with a transition metal in another oxidation state, the substitution for Ti must be accompanied by the exchange of another atom in the structure to maintain charge neutrality. In $KFeFPO_4$ the substitution of Fe(III) was accompanied by exchange of F for O. The F substitutes into the Ti-O-Ti chains exclusively, removing the long and short bond alternation, to form regular FeO_6 octahedra.[179]

KTP doped with 100ppm Cr has been investigated for possible use as a combined laser host and SHG device.[180] The green crystals showed Cr(III) absorption peaks, Cr(III) being charge balanced by O vacancies. Type I phase-matching is possible for the spectral region of greatest fluorescence. Cr-doping has also been used to reduce the ionic conductivity of KTP crystals.[181] Crystals synthesised at high temperature contain O vacancies

compensated for by K deficiency. The latter facilitates K migration, increasing the conductivity. Substitution of 700ppm Cr(III) for Ti(IV) reduces the need for K deficiency, thereby decreasing the conductivity by three orders of magnitude. To investigate the substitution of larger quantities of Cr for Ti in KTP in a controlled fashion, Cr-doped materials were prepared by high temperature flux growth and solid state synthesis.

7.2 Inclusion of Cr in KTP isomorphs

7.2.1 Synthesis

a) Flux growth. The composition of the flux used was: $0.47K_2O + 0.38P_2O_5 + 0.15TiO_2$, with 10% and 20% of the Ti replaced by Cr in two flux growths. The correct molar ratio of starting materials (K_2CO_3, $NH_4H_2PO_4$, TiO_2 and Cr_2O_3) were melted into a platinum crucible and left to equilibrate for 24 hours at 1100°C before slow cooling through the crystallization temperature. When cool, the crystals were extracted by prolonged boiling in distilled water. The 10% Cr-doped flux yielded a small quantity of brown crystals. Analytical electron microscopy indicated that less than 5%Cr had been incorporated into the KTP crystals ($c_{Cr} = 0.03(1)c_P$, $c_{Ti} = 1.02(5)c_P$). The 20%Cr-doped flux had a much larger yield of green crystals, accompanied by some brown crystals and white powder. The results of analytical electron microscopy carried out on 25 crystallites of the green material ($c_{Cr} = 0.23(1)c_P$, $c_{Ti} = 0.41(2)c_P$) gave a composition of $KCr_{0.30}Ti_{0.53}P_{1.3}$. Electron diffraction photographs taken by Nicola Stedman were consistent with cubic symmetry indicating that the sample was not isomorphous with KTP.

b) Solid state synthesis. The synthesis of a series of compounds across the $KTi_{1-x}Cr_xOPO_4$ solid solution was attempted, with x = 0.05, 0.1, 0.15 and 0.2. The powders were heated to 950°C for three days with daily grinding. The end-products were brown, the colour becoming more intense as the concentration of Cr increased. Analytical electron microscopy was carried out on these materials:

x=0.05	$c_{Ti} = 0.99(5)c_P$	$c_{Cr} = 0.04(3)$
x=0.1	$c_{Ti} = 0.97(5)c_P$	$c_{Cr} = 0.06(1)$
x=0.15	$c_{Ti} = 0.95(5)c_P$	$c_{Cr} = 0.07(2)$
x=0.2	$c_{Ti} = 0.98(5)c_P$	$c_{Cr} = 0.10(2)$.

The c_{Cr} gradually increases, but is considerably less than the target compositions, implying that there is a limit to the amount of Cr that can be accommodated within the KTP framework.

A powder synthesised with the target composition $KCr_{0.4}Ti_{0.6}P_{1.5}$, (the composition of the green flux-grown crystals), was bright green. Analytical electron microscopy carried out on 25 crystallites of this sample gave the composition: $KCr_{0.35(1)}Ti_{0.61(3)}P_{1.5}$. In addition, three of the 25 crystallites appeared to be almost pure KTP, having a K:Ti:P ratio of ~ 1:1:1.

7.2.2 Rietveld analysis of X-ray diffraction data from Cr-doped KTP isomorphs.

Analytical electron microscopy demonstrated that only a limited percentage of Cr could be accommodated in the KTP framework. X-ray diffraction data from "$KCr_xTi_{1-x}OPO_4$" powders (where x = 0.05 to 0.2), were collected on a STOE Stadi-P diffractometer and the published KTP structure[74] was used as

the starting model for Rietveld refinements. The small amount of observed X-ray data available meant that even with the inclusion of P-O bond length restraints, the Ti-O bond lengths obtained varied widely, as the O positions were not well defined. Refinement parameters and Ti-O bond lengths are presented in Table 7.2.1 and final profile plots in Figure 7.2.I.

The unit cell volume of the KTP phase did not change significantly as the amount of Cr in the starting materials increased. This, together with the analytical electron microscopy result that the percentage of Cr does not increase in proportion to the target composition, indicates that there is a limited capacity for Cr substitution, (~5%), in the KTP structure. As the percentage of Cr increases in the reagents, an impurity phase appears in the powder data. The visible peaks fitted the $K_2Ti_2(PO_4)_3$ cell (see part 7.4), so the published structure[182] was used to model the impurity. The 100% peak of the $K_2Ti_2(PO_4)_3$ phase is predicted at 28.8°2θ with Cu $K_{\alpha 1}$ radiation, where it is swamped by the (230)/(031) peak of the KTP phase. However the 80% peak, at 34.2°, is not so obscured and the increase in the amount of the $K_2Ti_2(PO_4)_3$ phase can be monitored using this peak (Figure 7.2.II). However the X-ray powder refinements provided no information on the distribution of Cr over the two Ti sites in the KTP phase. To obtain more reliable bond lengths and an idea of the Ti/Cr ordering, single crystal X-ray and time-of-flight neutron diffraction data were collected.

Table 7.2.1 X-ray powder diffraction analysis parameters for "$KCr_xTi_{1-x}OPO4$" samples where x=0.05, 0.1, 0.15 and 0.2.

%Cr in solid state	5	10	15	20
Residuals				
wR_p (%)	5.68	6.59	6.81	6.89
R_p (%)	4.37	4.79	5.33	5.42
R_I (%)	8.81	18.56	14.12	19.43
$R_{expected}$ (%)	7.45	7.92	8.20	7.88
x^2	0.489	0.543	0.522	0.573
Unit cell				
a	12.8196(4)	12.8100(5)	12.8194(4)	12.8107(4)
b	10.5763(2)	10.5700(2)	10.5694(2)	10.5691(2)
c	6.4066(2)	6.4033(5)	6.4067(2)	6.4007(2)
V	868.64(4)	867.01(5)	868.07(4)	866.63(2)
Bond lengths (A)				
Ti(1)-O(1)	2.16(2)	2.16(3)	2.12(2)	2.21(3)
-O(2)	1.94(2)	1.95(3)	1.94(3)	1.78(3)
-O(5)	2.05(2)	1.91(3)	2.08(2)	2.04(3)
-O(6)	2.04(2)	2.28(3)	2.01(3)	2.02(2)
-O(9)	2.02(2)	2.04(3)	1.96(3)	2.05(3)
-O(10)	1.67(2)	1.66(3)	1.76(3)	1.65(3)
Ti(2)-O(3)	1.96(2)	2.01(3)	2.02(3)	2.04(3)
-O(4)	2.08(2)	1.95(3)	2.03(3)	2.01(3)
-O(7)	1.90(2)	1.72(2)	1.87(3)	1.94(3)
-O(8)	2.10(3)	2.25(4)	2.03(3)	1.89(3)
-O(9)	1.87(3)	1.88(4)	1.84(4)	1.95(4)
-O(10)	2.02(2)	1.97(3)	2.08(3)	1.98(3)

Data collected on a STOE Stadi-P diffractometer using $CuK_{\alpha 1}$ radiation, 10 to 80°2θ with 0.014° step size.

Figure 7.2.I Observed (dots), calculated (continuous curve) and difference plots for "$KCr_xTi_{1-x}OPO_4$" samples.

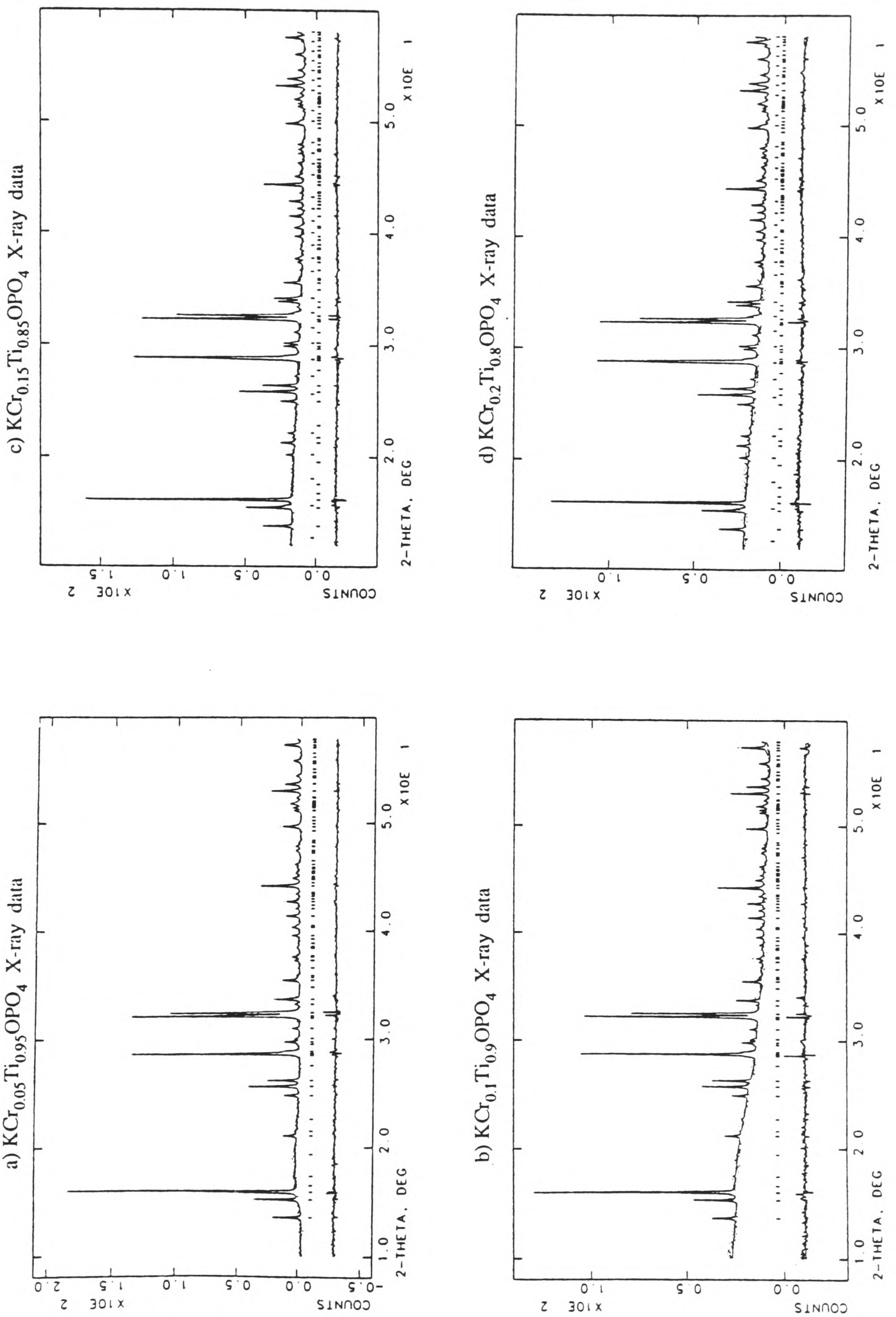
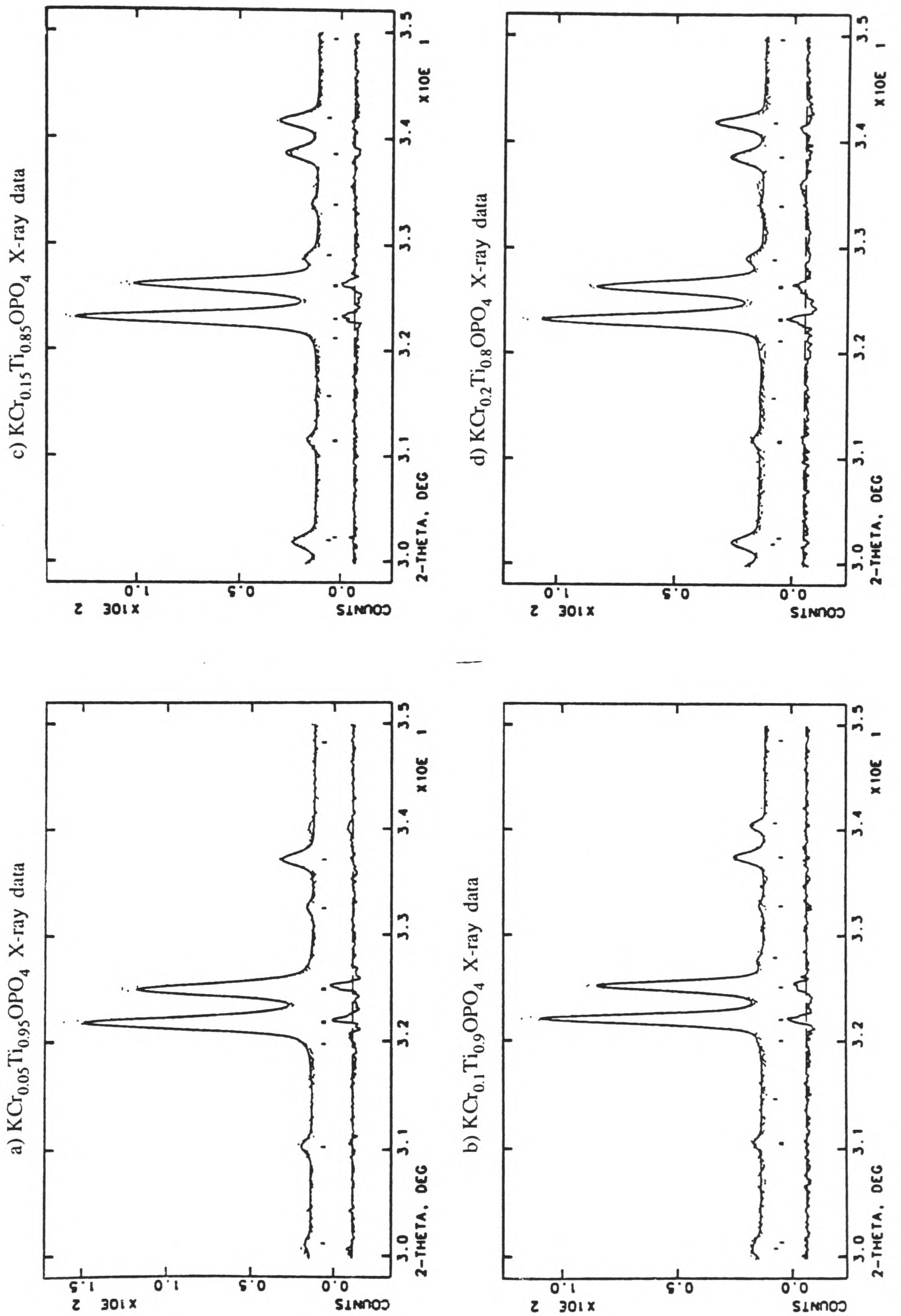


Figure 7.2.II. The 30 to 35°2θ region of the "$KCr_xTi_{1-x}OPO_4$" profile plots showing the growth in the 80% peak of the $K_2Ti_2(PO_4)_3$ at 34.2°



7.3 Structure determination of $KTi_{0.95}Cr_{0.05}OPO_4$.

7.3.1 Single crystal X-ray structure determination of flux-grown $KTi_{0.95}Cr_{0.05}OPO_4$.

A brown crystal of octahedral form was selected and mounted on a glass fibre. Preliminary Weissenberg photographs indicated that the crystal had orthorhombic symmetry consistent with a KTP isomorph.

The crystal was centred on an Enraf-Nonius CAD4 diffractometer, and 25 reflections were measured from a Polaroid rotation photograph, centred and indexed on the primitive orthorhombic cell:

a=12.8181(16) b=10.5871(17) c=6.4053(9)Å V=869.2(2)Å^3

High angle reflections (θ>20°) were measured and centred, then used to refine this orientation matrix, giving the final cell:

a=12.8140(13) b=10.5833(11) c=6.4021(10)Å V=868.2(3)Å^3.

Data, including all Friedel pairs, were collected from 0 to 58° in θ. An azimuthal scan was collected on the (1,0,-3) reflection, (for which χ was greater than 85°), for use in the semi-empirical absorption correction. Data reduction and all subsequent calculations were carried out using the Oxford CRYSTALS package.[107] Data collection parameters are given in Table 7.3.1.

Structure refinement

The published single crystal structure of KTP[74] was used as a starting model for the analysis of the $KTi_{0.95}Cr_{0.05}OPO_4$ data. The refinement proceeded smoothly to give an R-factor of 3.28%. However the largest peak in a difference Fourier map, ρ=2.36e/Å^{-3} was 0.54Å from Ti(2). This peak refined isotropically as a Cr atom with an occupancy of 0.015(1) to give

Table 7.3.1 Data collection and structure refinement parameters for $KTi_{0.95}Cr_{0.05}OPO_4$.

Molecular formula	$KTi_{0.98}Cr_{0.02}OPO_4$
Formula weight	198.57
Crystal size	0.15x0.15x0.25mm
Unit cell	a=12.8140(13) b=10.5833(11) c=6.4021(10)A
	$V=868.2(3)A^3$
Space group	$Pn2_1a$
Dc/gcm^{-3}	3.0354
F(000)	760
z	4
linear absorption coeff.	$32.490cm^{-1}$
X-radiation	Mo Kα graphite monochromator
2θ max °	116
scan type	ω-2θ
scan width	$0.79 + 0.35\tan\theta$
min/max scan °	1.3, 5.9
total data	12225
observed data	9610
$I>n\sigma(I)$, n=	3
absorption corr. min, max	1.37, 1.60
min,max h,k,l	(0,0,0), (30,25,15)
Weighting scheme coeff.	11.5, -3.43, 9.95
$\Delta\rho/eA^{-3}$	1.53
Final shift/error	0.17
R %	3.24
wR %	4.07

Table 7.3.2 Atom coordinates and isotropic thermal parameters of $KTi_{0.95}Cr_{0.05}OPO_4$.

	x	y	z	U_{iso}(Å²)	occupancy
Ti(1)	0.37300(1)	0.00172(7)	0.49997(3)	0.0055	
Ti(2)	0.24664(1)	0.25271(7)	0.26866(3)	0.0049	0.985(1)
Cr(2)	0.2416(8)	0.279(1)	0.216(2)	0.002(2)	0.015(1)
P(1)	0.49798(2)	0.26108(8)	0.33580(4)	0.0050	
P(2)	0.18063(2)	0.51330(7)	0.50208(5)	0.0052	
K(1)	0.37784(3)	0.31274(8)	0.78021(5)	0.0168	
K(2)	0.10544(3)	0.06721(8)	0.69960(7)	0.0181	
O(1)	0.48577(7)	0.1511(1)	0.4863(2)	0.0084	
O(2)	0.50966(7)	0.3839(1)	0.4655(2)	0.0080	
O(3)	0.40035(6)	0.2805(1)	0.1987(1)	0.0076	
O(4)	0.59349(6)	0.2415(1)	0.1933(1)	0.0077	
O(5)	0.11236(7)	0.5419(1)	0.3110(1)	0.0075	
O(6)	0.11125(8)	0.4879(1)	0.6916(1)	0.0088	
O(7)	0.25292(7)	0.6281(1)	0.5397(1)	0.0084	
O(8)	0.25270(8)	0.4000(1)	0.4610(2)	0.0081	
O(9)	0.22480(7)	0.6437(1)	-.0334(1)	0.0077	
O(10)	0.22364(7)	0.3904(1)	0.0411(2)	0.0085	

Anisotropic thermal parameters (x100) ($Å^2$)

	U(11)	U(22)	U(33)	U(23)	U(13)	U(12)
Ti(1)	0.585(4)	0.538(4)	0.537(4)	0.056(4)	-.022(4)	-.037(4)
Ti(2)	0.446(4)	0.446(4)	0.625(5)	-.047(5)	-.022(4)	0.055(4)
P(1)	0.403(6)	0.520(7)	0.607(7)	0.027(7)	0.006(6)	-.081(6)
P(2)	0.638(7)	0.459(7)	0.487(7)	-.085(6)	-.002(7)	0.034(5)
K(1)	2.28(1)	2.27(1)	1.073(9)	0.133(9)	0.43(1)	0.64(1)
K(2)	1.258(9)	2.56(1)	2.07(1)	-.13(1)	0.513(9)	-.01(1)
O(1)	0.85(2)	0.88(2)	1.01(3)	0.37(2)	-.18(2)	-.23(2)
O(2)	0.79(2)	0.82(2)	1.08(3)	-.34(2)	0.18(2)	-.30(2)
O(3)	0.48(2)	1.10(2)	0.84(2)	0.08(2)	-.09(2)	-.03(2)
O(4)	0.46(2)	1.13(3)	0.93(2)	-.12(2)	0.15(2)	0.05(2)
O(5)	0.96(2)	0.96(2)	0.49(2)	0.01(2)	-.08(2)	0.24(2)
O(6)	1.10(2)	1.16(3)	0.56(2)	0.04(2)	0.12(2)	-.18(2)
O(7)	0.97(2)	0.75(2)	1.03(2)	-.31(2)	0.13(2)	-.26(2)
O(8)	1.10(3)	0.68(2)	1.08(2)	-.33(2)	-.31(2)	0.38(2)
O(9)	0.81(2)	0.79(2)	0.90(2)	0.29(2)	-.07(2)	-.23(2)
O(10)	0.83(2)	0.87(2)	1.01(3)	0.23(2)	0.11(2)	0.28(2)

a final R-factor of 3.24%. The total occupancy on the Ti(2) site was constrained to unity. The position adopted by any Cr substituted on Ti(1) was not determined, since the largest remaining peak in a final difference Fourier map (ρ = 1.55e/A^{-3}) was situated 0.62A from K(2). Atom coordinates and thermal parameters are given in Table 7.3.2, and selected bond distances and angles in Table 7.3.3.

Discussion

The structure of Cr-doped KTP has been determined by single crystal X-ray diffraction. The X-ray scattering power of Ti is very similar to that of Cr, so the occupancies of the two metals could not be refined on the same site. However the position of Cr in the Ti(2) site was sufficiently different from that of Ti to appear as a peak in a difference Fourier map, and to subsequently refine isotropically. The coordination about site Ti(2) is shown in Figure 7.3.I. Ti and Cr have very different neutron scattering lengths, so to investigate the possibility of Cr ordering, time-of-flight neutron powder diffraction data were collected on the "$KTi_{0.95}Cr_{0.05}OPO_4$" sample made by solid state methods.

7.3.2 Time-of-Flight neutron powder diffraction study of "$K(Ti_{0.95}Cr_{0.05})OPO_4$".

Time-of-flight neutron diffraction data were collected from the 5%Cr-doped KTP powder on the POLARIS diffractometer, Rutherford Appleton Laboratory, in run number 5873. Only data from the C-bank of detectors were used in the refinement, together with the powder X-ray data, which proceeded readily using the X-ray $K(Ti_{0.95}Cr_{0.05})OPO_4$ atom coordinates as the starting model. The final refinement cycle without including Cr

Table 7.3.3 Selected bond distances (Å) and angles (°) in $KTi_{0.95}Cr_{0.05}OPO_4$ compared with those of KTP[74].

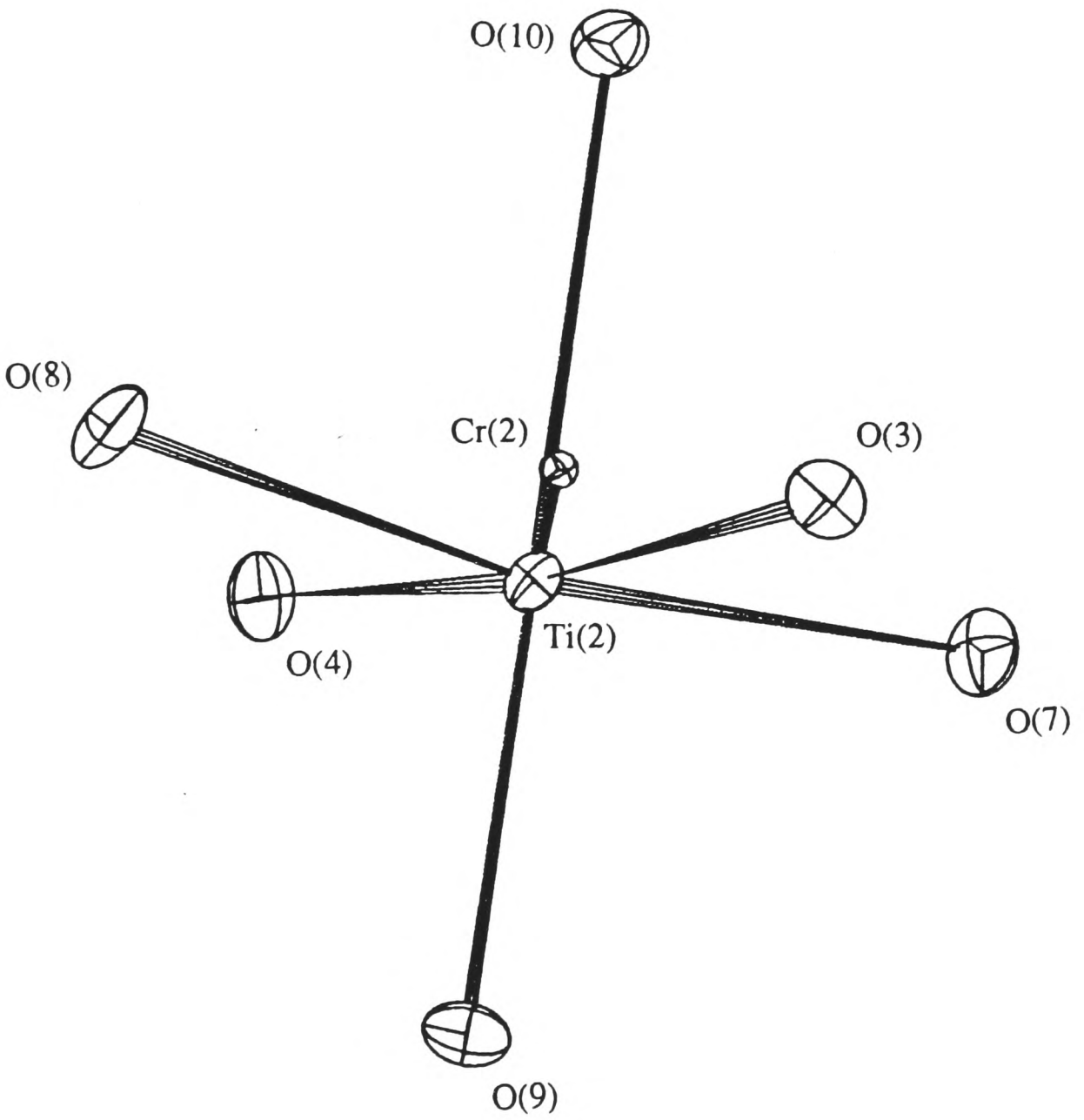
	Crystal	Powder	KTP
Ti(1)-O(1)	2.1437(8)	2.134(5)	2.161(4)
-O(2)	1.9656(8)	1.959(5)	1.957(4)
-O(5)	2.0448(8)	2.014(7)	2.047(4)
-O(6)	1.9901(9)	2.022(7)	1.900(4)
-O(9)	1.9680(8)	1.935(6)	1.993(4)
-O(10)	1.7293(9)	1.751(6)	1.751(6)

	Ti(2)	Cr(2)		
Ti(2)-O(3)	2.0412(8)	2.04(1)	2.023(7)	2.037(3)
-O(4)	1.9811(8)	2.02(1)	1.989(7)	1.979(3)
-O(7)	1.9713(9)	1.96(1)	1.976(6)	1.966(4)
-O(8)	1.9879(8)	2.03(1)	1.976(7)	1.994(4)
-O(9)	1.7526(8)	2.19(1)	1.773(6)	1.738(4)
-O(10)	2.0815(9)	1.64(1)	2.061(6)	2.101(4)
-Cr(2)	0.44(1)			

Ti(1)-O(9)-Ti(2)	135.57(5)	136.1(4)	135.5
Ti(1)-O(10)-Ti(2)	133.23(5)	132.6(3)	132.9

	Crystal	Powder		Crystal	Powder
P(1)-O(1)	1.5192(9)	1.5416(24)	P(2)-O(5)	1.5341(9)	1.5447(25)
-O(2)	1.5501(9)	1.5461(24)	-O(6)	1.5279(9)	1.5366(25)
-O(3)	1.5420(8)	1.5481(25)	-O(7)	1.5471(9)	1.5509(24)
-O(4)	1.5403(8)	1.5397(25)	-O(8)	1.5364(8)	1.5403(24)
K(1)-O(1)	2.895(1)	2.876(5)	K(2)-O(1)	2.680(1)	2.687(5)
-O(2)	2.735(1)	2.722(6)	-O(2)	2.972(1)	3.028(5)
-O(3)	2.716(1)	2.724(5)	-O(3)	3.035(1)	3.143(5)
-O(5)	2.876(1)	2.903(5)	-O(4)	3.123(1)	3.045(5)
-O(7)	3.064(1)	3.118(6)	-O(5)	2.805(1)	2.779(6)
-O(8)	2.757(1)	2.786(6)	-O(7)	2.907(1)	2.892(6)
-O(9)	2.994(1)	3.030(6)	-O(8)	3.039(1)	3.105(6)
-O(10)	2.715(1)	2.711(7)	-O(9)	2.759(1)	2.706(6)
			-O(10)	3.054(1)	3.117(6)

Figure 7.3.I Oxygen coordination around the Ti(2) site. Bonds to the minor Cr(2) are not drawn for clarity.



had residuals wR_p 6.01 and 2.37% (X-ray and neutron data respectively) and x^2 = 1.253. Cr were then placed on the Ti sites, constrained to have the same atom coordinates and thermal parameters as the Ti atoms. The total occupancy on each site was constrained to unity, and the P-O bond lengths were restrained to 1.54(1)Å. The neutron data were excluded below 4000ms as the peak-to-background ratio was low and the vast number of reflections calculated in that region were not well fitted. Final refinement parameters are given in Table 7.3.4, atom coordinates and thermal parameters in Table 7.3.5 and selected bond distances and angles in Table 7.3.3. Final profile plots are given in Figure 7.3.II.

Discussion

The structure of $KTi_{0.95}Cr_{0.05}OPO_4$ has been determined by joint analysis of neutron time-of-flight and X-ray diffraction data. The Cr appears to be randomly distributed over the two Ti sites, in contrast to the ordering seen on Sn or Ge substitution. This result implies that there was an equal amount of Cr on the Ti(1) site in the single crystal structure, but that the site occupied by Cr was too close to that of Ti to be detected.

The ^{31}P M.A.S.N.M.R. spectrum of this material, (run by Lucy Bull), shows one broad peak, at a chemical shift very close to that of KTP. This is further evidence that Cr can substitute into KTP; the doublet found in the ^{31}P MASNMR spectrum of KTP itself has been broadened by the substitution of paramagnetic Cr onto both Ti sites, but remains at a similar chemical shift position. (Figure 7.3.III)

The presence of 5%Cr does not greatly alter the KTP structure. However the difference between the longest and

Table 7.3.4 Powder diffraction data collection and refinement parameters for $KTi_{0.95}Cr_{0.05}OPO_4$.

Data collection	neutron	X-ray
Diffractometer	POLARIS, (R.A.L.)	STOE Stadi-P
Data range	3.996-20ms	10-60°2θ
Step size		0.014°
Contributing reflections	1885	129
Total number of observations	10524	
R_p (%)	4.70	4.65
wR_p (%)	2.53	6.02
$R_{expected}$ (%)	1.81	7.45
R_I (%)	1.19	9.67
χ^2	0.957	
Space group	$Pn2_1a$(33)	
unit cell (Å)	a=12.8188(3) b=10.5747(2) c=6.4067(2)Å V=868.45(6)Å^3	
Scattering lengths[11,73]/10^{-14}m	K:0.367 Ti:-0.344 Cr:0.3635 P:0.513 O:0.5805	
no. parameters	88	
Background	Cosine Fourier series, neutron 8 terms, X-ray 5 terms	
Peak shape	neutron: Gaussian convoluted with double exponential σ_1:125(1) σ_2:1.29(3) X-ray: Pseudo-Voigt W:17.6(5) X:17.0(7) shift:0.59(7)	

Table 7.3.5 Atomic coordinates and thermal parameters obtained by powder diffraction for $KTi_{0.95}Cr_{0.05}OPO_4$.

	x	y	z	U_{iso}(Å^2)	occupancy
Ti(1)	0.3722(2)	-.0033(5)	0.5044(10)	0.0067(7)	0.968(6)
Cr(1)	0.3722(2)	-.0033(5)	0.5044(10)	0.0067(7)	0.032(6)
Ti(2)	0.2477(4)	0.2470(7)	0.2689(7)	0.0067(7)	0.968(6)
Cr(2)	0.2477(4)	0.2470(7)	0.2689(7)	0.0067(7)	0.032(6)
P(1)	0.4983(3)	0.2574(3)	0.3360(2)	0.0046(3)	
P(2)	0.1802(1)	0.5097(5)	0.5001(7)	0.0046(3)	
K(1)	0.3796(4)	0.3094(5)	0.7789(7)	0.0191(6)	
K(2)	0.1058(4)	0.0690(5)	0.6948(7)	0.0191(6)	
O(1)	0.4841(2)	0.1457	0.4879(5)	0.0078(2)	
O(2)	0.5099(3)	0.3803(2)	0.4647(4)	0.0078(2)	
O(3)	0.4000(3)	0.2719(5)	0.1976(5)	0.0078(2)	
O(4)	0.5939(3)	0.2342(5)	0.1955(5)	0.0078(2)	
O(5)	0.1093(4)	0.5358(4)	0.3099(6)	0.0078(2)	
O(6)	0.1121(3)	0.4804(5)	0.6915(6)	0.0078(2)	
O(7)	0.2555(3)	0.6219(4)	0.5398(6)	0.0078(2)	
O(8)	0.2507(3)	0.3945(4)	0.4583(6)	0.0078(2)	
O(9)	0.2249(3)	0.6350(5)	-.0327(6)	0.0078(2)	
O(10)	0.2239(3)	0.3809(5)	0.0399(7)	0.0078(2)	

Figure 7.3.IIa Observed (dots), calculated (continuous curve) and difference plots of POLARIS c-bank data on $KTi_{0.95}Cr_{0.05}OPO_4$

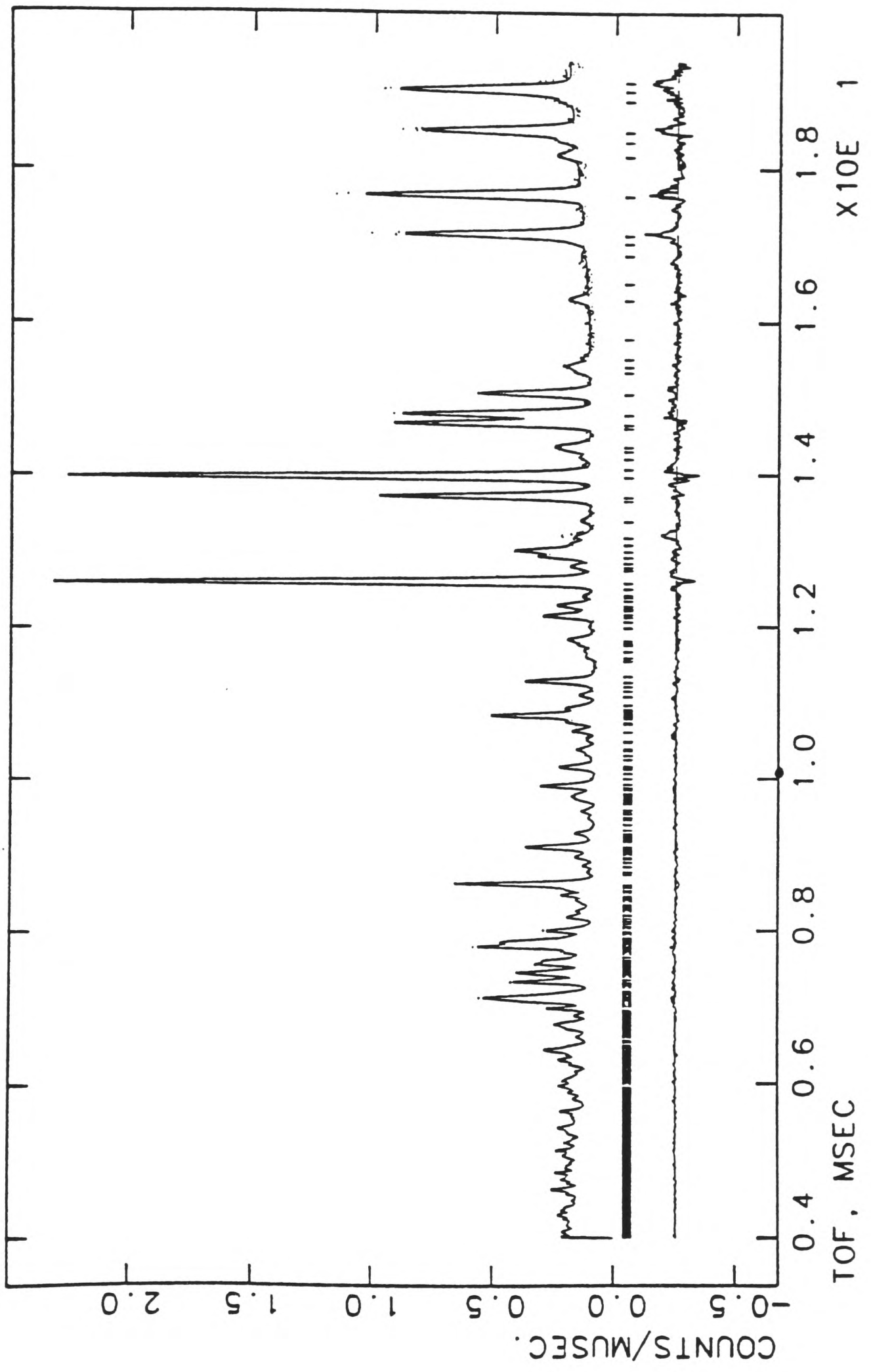
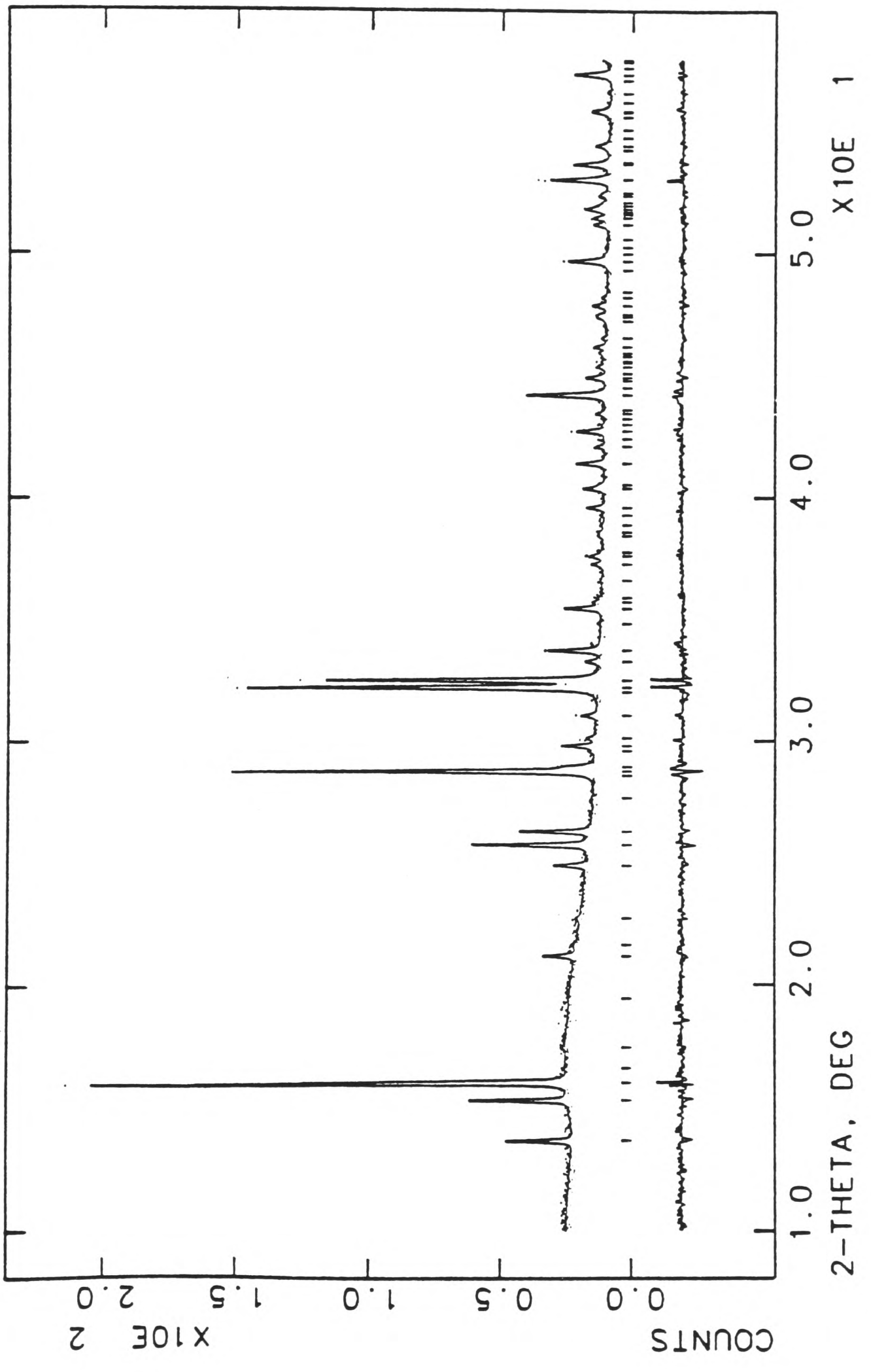


Figure 7.3.IIb Observed (dots), calculated (continuous curve) and difference plots of the X-ray data on $KTi_{0.95}Cr_{0.05}OPO_4$.



shortest Ti-O bonds in the TiO_6 octahedra (Δ) does marginally decrease when Cr is substituted. This would be expected, since Cr tends to have a more regular O coordination. The anisotropic thermal parameters of the oxygens surrounding the Ti(2) site in the single crystal structure cover a similar range to those obtained in the KNTP single crystal structures (Chapter 4), so if 2% of these oxygens are shifted to a more regular geometry to accommodate Cr, this cannot be detected.

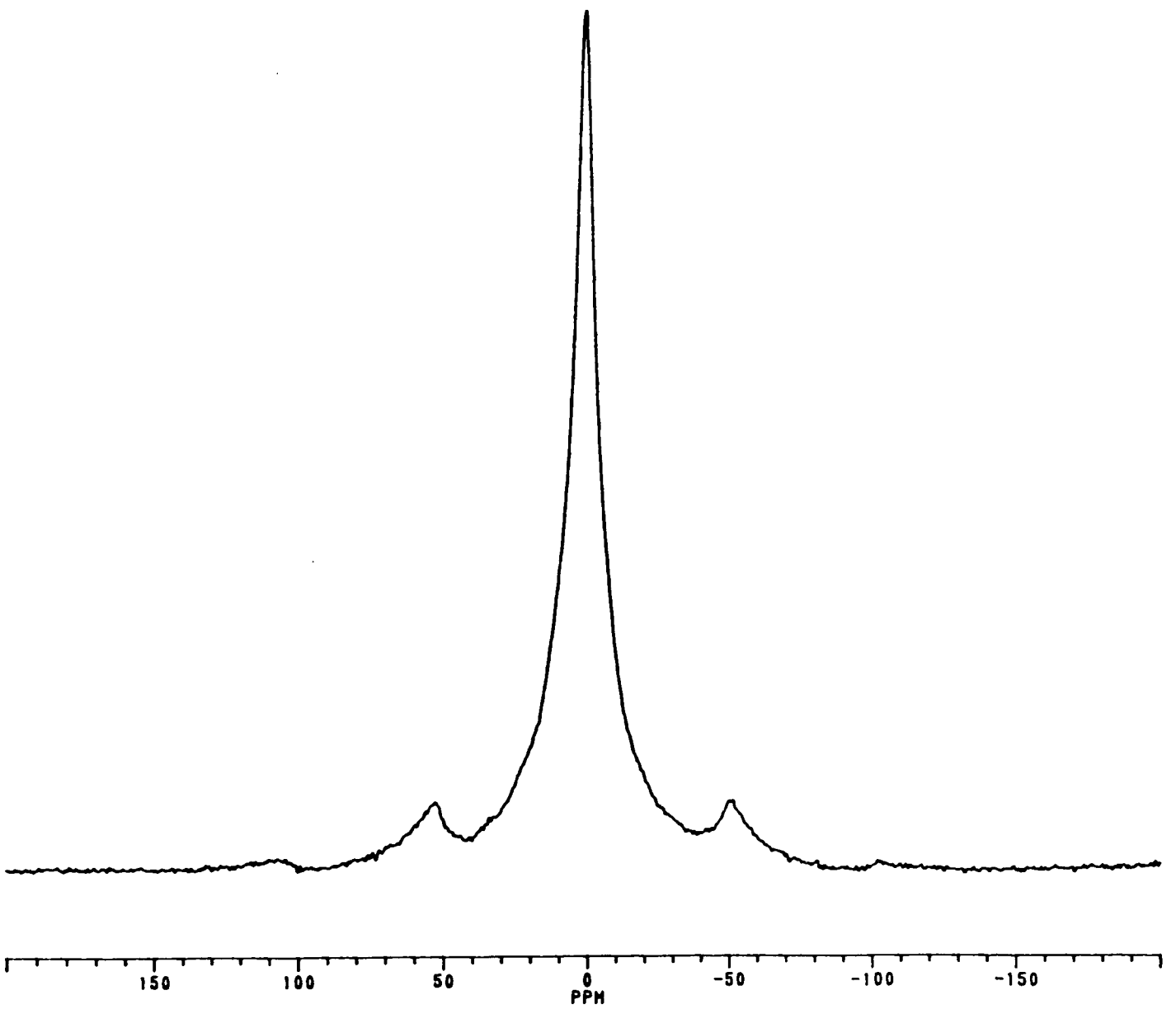


Figure 7.3.III ^{31}P M.A.S.N.M.R. spectrum of $KTi_{0.98}Cr_{0.02}OPO_4$, (spinning speed 4110Hz, recycle delay 5s).

In the green Cr_2O_3 starting material, Cr is in the trivalent state. However bond valence sums calculated[1363] for the Cr(2) site in the brown $KTi_{0.98}Cr_{0.02}OPO_4$ crystal:

Cr(III): 3.40 Cr(IV): 4.18

indicate that the Cr has been oxidised upon entering the Ti(2) site. The oxygens used in this calculation are those corresponding to the Ti octahedron, within which the Cr is displaced, but there is no evidence that the oxygens undergo a major reorganisation on Cr substitution (except one very short Cr-O bond). The change in colour from green to brown also tends to support the hypothesis of a change in oxidation state.

7.4 Structure determination of $K_2Ti_{1.2}Cr_{0.8}(PO_4)_3$.

The crystals grown from a flux containing 20%Cr were not isomorphous with KTP. The composition of the material was found by analytical electron microscopy to be $KTi_{.62}Cr_{.38}P_{1.8}$, and the structure was found to be cubic from electron diffraction photographs. The structure determination was undertaken using both single crystal X-ray and neutron powder techniques since the former cannot reliably distinguish Cr from Ti.

7.4.1 Single crystal structure determination of flux-grown $K_2Ti_{2-x}Cr_x(PO_4)_3$.

A green crystal grown from a flux containing 20%Cr was mounted and centred on an Enraf-Nonius CAD4 diffractometer. Reflection positions at high x and θ were measured from a Polaroid rotation photograph and when centred and indexed, gave the unit cell:

a=9.798(4) b=9.802(4) c=9.802(3)Å V=941.4(6)Å^3.

Reflections with $\theta > 20^o$ were used to refine the cell and gave the final values:

a=9.793(2) b=9.795(3) c=9.801(2)Å V=940.1(4)Å^3.

Data were collected from 0 to 50° in θ. Azimuthal scans were collected on the (513) reflection (x > 85°) for use in the empirical absorption correction. 7463 reflections were detected, of which, after data reduction, 2317 were classed as observed. Final data collection parameters are given in Table 7.4.1.

Structure refinement

A search of the Inorganic Chemical Structures database revealed the mixed valence material $K_2Ti_2(PO_4)_3$ with a similar

Table 7.4.1 Data collection and structure refinement parameters for $K_2Ti_{2-x}Cr_x(PO_4)_3$.

Molecular formula	$K_2Ti_{2-x}Cr_x(PO_4)_3$
Formula weight	463.01
Crystal size	0.09x0.14x0.29mm
Crystal system	cubic
a/Å	9.796(2)
Space group	$P2_13$ (198)
D_c/gcm^{-3}	3.272
F(000)	900
z	4
linear absorption coeff.	$34.300cm^{-1}$
X-radiation	Mo Kα graphite monochromator
2θ max°	100
scan type	ω-2θ
scan width	$0.67+ 0.35\tan\theta$
min/max scan°	1.3, 5.9
total data	7463
observed data	2317
$I>n\sigma(I)$,n=	3
absorption corr. min,max	1.33, 1.47
min,max h,k,l	(-11,-1,-1), (20,20,15)
no. of parameters	76
weighting scheme coeff.	3.19(2), -2.01(1), 1.88(2)
$\Delta\rho/eÅ^{-3}$	1.13
Final shift/error	0.24
Final R (%)	2.77
Final wR (%)	3.09

cubic cell (a=9.8688(6)Å) to that found for the $K_2Ti_{2-x}Cr_x(PO_4)_3$ compound.[1823] $K_2Ti_2(PO_4)_3$ is isomorphous with the mineral langbeinite and its atom coordinates were used as a starting model in the analysis of the data. Refinement of atom coordinates and isotropic thermal parameters gave an R-factor of 4.48% with chemically reasonable bond distances and angles.

Cr atoms were placed at the Ti positions and the total site occupancy constrained to that of the special position, but refinement of independent atom coordinates for the two species was unstable. The proximity of Ti and Cr in the Periodic Table means that the sites occupied by the ions, and their thermal parameters, may be too similar to be distinguished using X-ray data. In subsequent cycles of refinement the atom coordinates and anisotropic thermal parameters were constrained to be the same for both Ti and Cr within a site. The refinement of the occupancies was constrained so that the shifts on a site were equal and opposite. K occupancies were also refined as K deficiency had been noted by Leclaire et al[1823]. The atomic coordinates and thermal parameters are given in Table 7.4.2 and selected bond lengths and angles in Table 7.4.3.

Discussion

The structure of the green crystals obtained from a K-Ti-P flux containing 20%Cr has been shown to be isomorphous with $K_2Ti_2(PO_4)_3$. The Langbeinite structure consists of isolated TiO_6 octahedra sharing all vertices with PO_4 tetrahedra (Figure 7.4.I), in contrast to KTP where two octahedral vertices are linked to other TiO_6 to form helices. The octahedra are more regular than those found in KTP and this, together with the removal of any possibility of delocalisation along TiO_6 chains,

Table 7.4.2 Atom coordinates and thermal parameters of $K_{1.8}Ti_{1.2}Cr_{0.8}(PO_4)_3$.

	x	y	z	U_{equiv}(Å^2)	occupancy
Ti(1)	0.66346(2)	0.66346(2)	0.66346(2)	0.0046	0.66(2)
Cr(1)	0.66346(2)	0.66346(2)	0.66347(2)	0.0046	0.34(2)
Ti(2)	0.39198(2)	0.39198(2)	0.39198(2)	0.0050	0.55(2)
Cr(2)	0.39198(2)	0.39198(2)	0.39198(2)	0.0050	0.45(2)
K(1)	0.95956(6)	0.95956(6)	0.95956(6)	0.0220	0.958(6)
K(2)	0.18144(5)	0.18144(5)	0.18144(5)	0.0178	0.838(6)
P(1)	0.47722(4)	0.70635(4)	0.37622(4)	0.0043	
O(1)	0.6020(1)	0.8288(1)	0.7513(1)	0.0089	
O(2)	0.4524(1)	0.2973(1)	0.2295(1)	0.0099	
O(3)	0.4856(1)	0.5576(1)	0.3294(1)	0.0087	
O(4)	0.5539(2)	0.7289(2)	0.5108(1)	0.0100	

Anisotropic thermal parameters (x100)

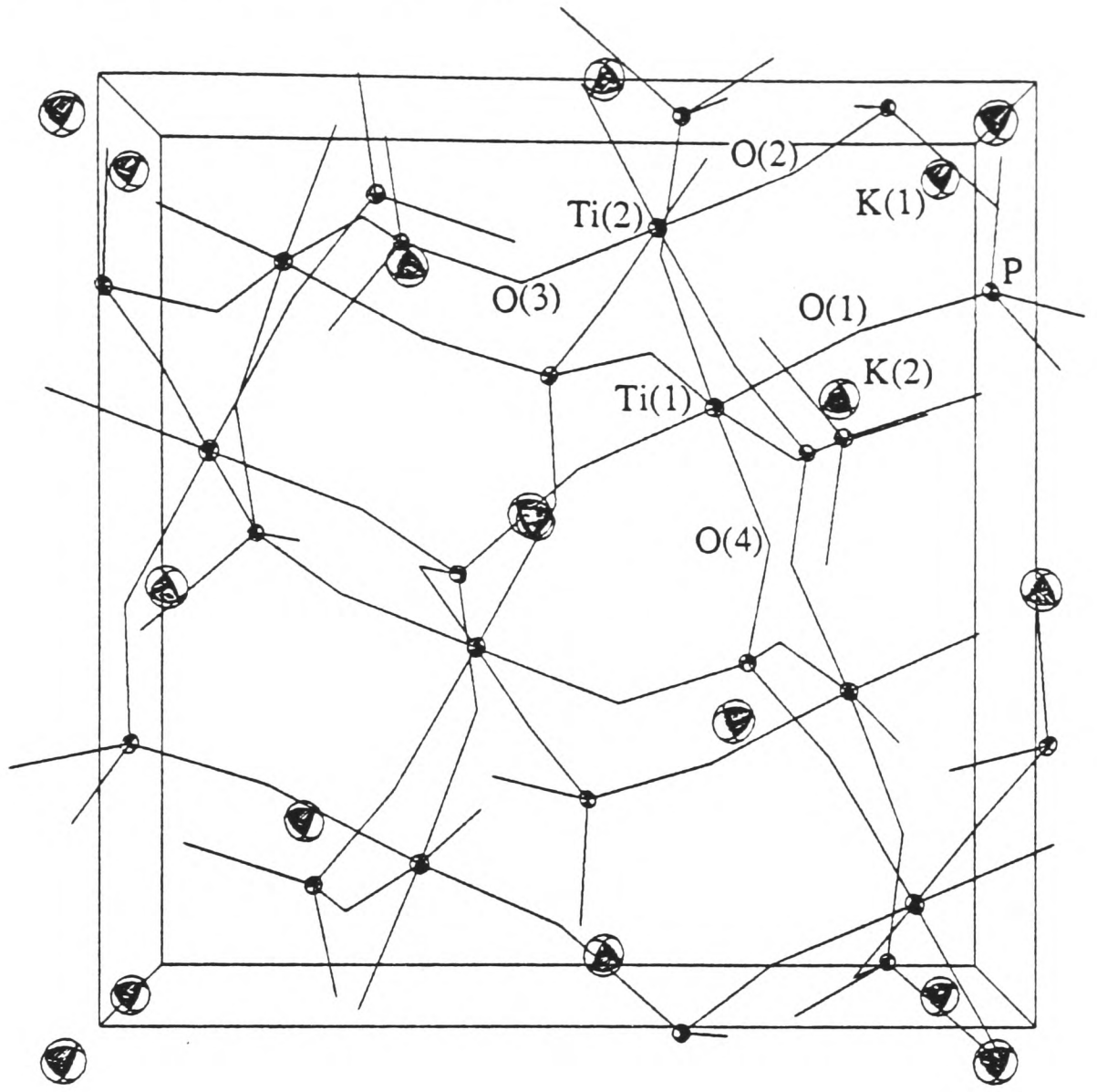
	U(11)	U(22)	U(33)	U(23)	U(13)	U(12)
Ti(1)	0.465(5)	0.465(5)	0.465(5)	-.020(5)	-.020(5)	-.020(5)
Ti(2)	0.503(5)	0.503(5)	0.503(5)	0.045(5)	0.045(5)	0.045(5)
K(1)	2.21(2)	2.21(2)	2.21(2)	0.13(2)	0.13(2)	0.13(2)
K(2)	1.80(2)	1.80(2)	1.80(2)	-.15(2)	-.15(2)	-.15(2)
P(1)	0.42(1)	0.45(1)	0.43(1)	0.065(8)	-.019(8)	0.00(8)
O(1)	1.47(4)	0.49(3)	1.21(4)	-.35(3)	0.08(3)	-.07(3)
O(2)	1.50(5)	0.97(4)	1.09(4)	-.47(3)	0.46(4)	0.13(3)
O(3)	1.18(4)	0.51(3)	1.26(4)	-.12(3)	0.36(3)	-.10(3)
O(4)	1.32(4)	1.52(5)	0.87(4)	0.19(3)	-.69(3)	-.09(3)

Table 7.4.3 Selected bond distances (A) in $K_{1.6}Ti_{1.2}Cr_{0.8}(PO_4)_3$

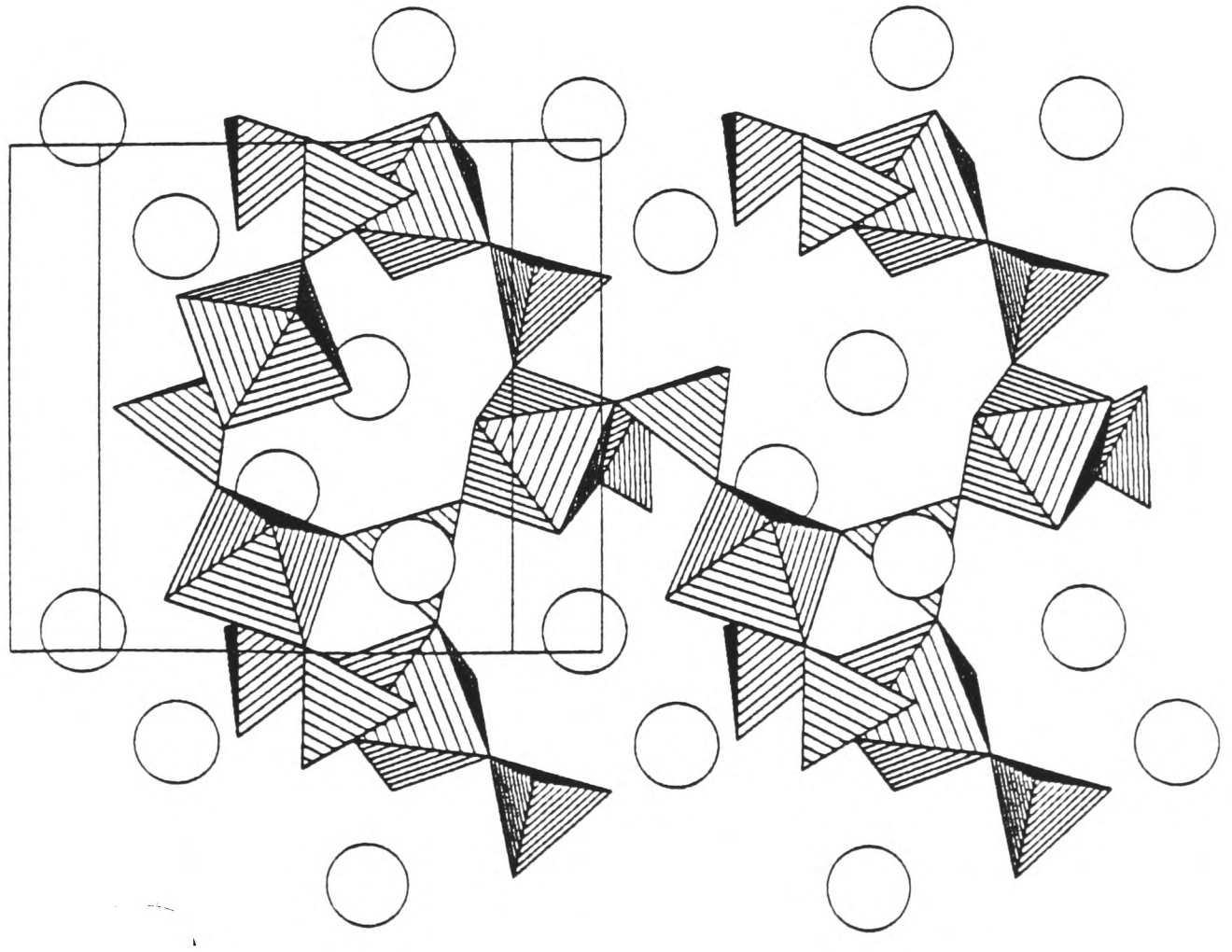
		crystal	powder	$K_2Ti_2(PO_4)_3$
Ti(1)	-O(1)x3	1.930(1)	1.915(3)	1.933(4)
	-O(4)x3	1.949(1)	1.949(3)	1.955(4)
mean		1.940	1.930	1.944
Ti(2)	-O(2)x3	1.935(1)	1.947(3)	2.027(4)
	-O(3)x3	1.962(1)	1.939(3)	2.027(4)
mean		1.948	1.943	2.027
P(1)	-O(1)	1.527(1)	1.531(1)	1.532(4)
	-O(2)	1.530(1)	1.532(1)	1.522(4)
	-O(3)	1.530(1)	1.530(1)	1.521(4)
	-O(4)	1.533(1)	1.530(1)	1.539(4)
K(1)	-O(2)x3	3.018(1)	3.001(3)	2.932(4)
	-O(3)x3	2.846(1)	2.853(4)	2.932(4)
	-O(4)x3	3.095(2)	3.103(4)	3.188(4)
K(2)	-O(1)x3	2.862(1)	2.875(4)	2.902(4)
	-O(2)x3	2.925(2)	2.912(6)	2.924(4)
	-O(4)x3	2.979(2)	2.986(4)	2.939(4)

Figure 7.4.I a) A diagram of the unit cell of $K_2Ti_{2-x}Cr_x(PO_4)_3$, b) a partial view of the structure showing the isolated PO_4 tetrahedra and TiO_6 octahedra.

a)



b)



will severely reduce the nonlinear properties of $K_2Ti_2(PO_4)_3$ relative to KTP.

Refinement of the K occupancies revealed that the material is K deficient, with K being lost selectively from the K(2) site, as seen in $K_{1.75}Ti_2(PO_4)_3$,[1e2] to give an overall formula of $K_{1.6}Ti_{1.21}Cr_{0.79}(PO_4)_3$. In $K_2Ti_2(PO_4)_3$ the Ti occurs in the IV and III oxidation states to an equal extent, but in $K_{1.6}Ti_{1.2}Cr_{0.8}(PO_4)_3$ there is an increase in the IV to III ratio, which is charge balanced by the reduction in K content. The IV/III ratio balanced by a loss of 0.2K is 1.2(IV):0.8(III), which suggests that Ti and Cr are both in their more favourable oxidation states of IV and III respectively. The magnetic moment of ground $K_{1.6}Ti_{1.2}Cr_{0.8}(PO_4)_3$ crystals (measured by Joanne Warner on a SQUID susceptometer) was 4.13BM, a value comparable to the theoretical spin-only moment for Cr(III) (μ_s = 3.87) and greater than would be expected for Cr(IV) (μ_s = 2.87). This is further evidence that Cr is in the (III) oxidation state.

7.4.2 Time-of-flight neutron and X-ray powder diffraction study of $K_2Ti_{2-x}Cr_x(PO_4)_3$.

Time-of-flight neutron diffraction data were collected on POLARIS, Rutherford Appleton Laboratory, (run number 5874), from the 40%Cr langbeinite powder sample, and combined with the X-ray powder diffraction data in the analysis of the $K_2Ti_{2-x}Cr_x(PO_4)_3$ structure. The single crystal structure was used as the starting model for refinement in GSAS. Once the majority phase had converged, peaks due to impurities of a KTP isomorph and Cr_2O_3[1e3] were observed and added to the refinement with their model parameters fixed. A soft constraint was applied to the P-O

bond lengths in the Langbeinite phase, restricting them to the range 1.53(1)Å seen in the single crystal structure determination. Due to the difference in neutron scattering by Ti and Cr, the occupancies could be readily refined. K occupancies were also refined as K deficiency had been noted by Leclaire et al[1823]. The total occupancy on each octahedral site was constrained to unity. Final refinement parameters are given in Table 7.4.4, Atomic coordinates in Table 7.4.5, bond lengths in Table 7.4.3 and the final profile plots in Figure 7.4.II.

Discussion

There is partial ordering over the two Ti sites, Cr preferentially occupying Ti(2) as seen in the X-ray single crystal structure, and the ability of neutron diffraction to differentiate between Ti and Cr meant that the total composition of the structure did not have to be constrained in the powder diffraction study. The refined composition of $K_{1.9}Ti_{1.21}Cr_{0.79}(PO_4)_3$ is very similar to the synthesis target composition of $K_2Ti_{1.2}Cr_{0.8}(PO_4)_3$, with the K(2) site again being K deficient. A metal (Ti/Cr) oxidation state ratio of 1.1(IV):0.9(III) would be charge balanced by the refined occupancy of 1.9(K). Thus in $K_{1.9}Ti_{1.2}Cr_{0.8}(PO_4)_3$, more Ti could be in the favourable Ti(IV) oxidation state and only 0.1Ti is required to be in the Ti(III) oxidation state, (assuming all the Cr is present as Cr(III)). This is in agreement with the refined composition in the single crystal structure.

The bond lengths and angles are compared with those of $K_2Ti_2(PO_4)_3$ in Table 7.4.3. In both materials the bonds around the Ti(2) site are longer than those around Ti(1), which suggests that the Ti(2) site is occupied by metals in the (III)

Table 7.4.4 Powder diffraction data collection and refinement parameters of $K_2Ti_{1.2}Cr_{0.8}(PO_4)_3$.

Data collection	neutron	X-ray
Diffractometer	POLARIS	STOE Stadi-P
Data range	4-19.5ms	10-60°2θ
Step size		0.014°
Contributing reflections	741	58
Total no. observations	10378	
R_p (%)	4.07	5.53
wR_p (%)	3.69	4.38
R_I (%)	2.24	18.09
$R_{expected}$ (%)	5.62	6.88
χ^2	0.483	

Space group		$P2_13$
Unit cell		a=9.7902(1)Å, V=938.38(4)Å^3
scattering lengths/10^{-14}m		K:0.367, Ti:-0.344, Cr:0.3635, P:0.513, O:0.5805
Number of parameters		64
Background	neutron	6 term cosine Fourier series
	X-ray	4 term cosine Fourier series
Peak shape	neutron:	Gaussian convoluted with double exponential σ_1:100(1) σ_2: 1.5(3)
	X-ray:	Pseudo Voigt W:14.8(2), Y:10.5(3), shift:-20.6(3)

Figure 7.4.IIa Observed (dots), calculated (continuous curve) and difference plots of POLARIS C-bank data for $K_2Ti_{1.2}Cr_{0.8}(PO_4)_3$.

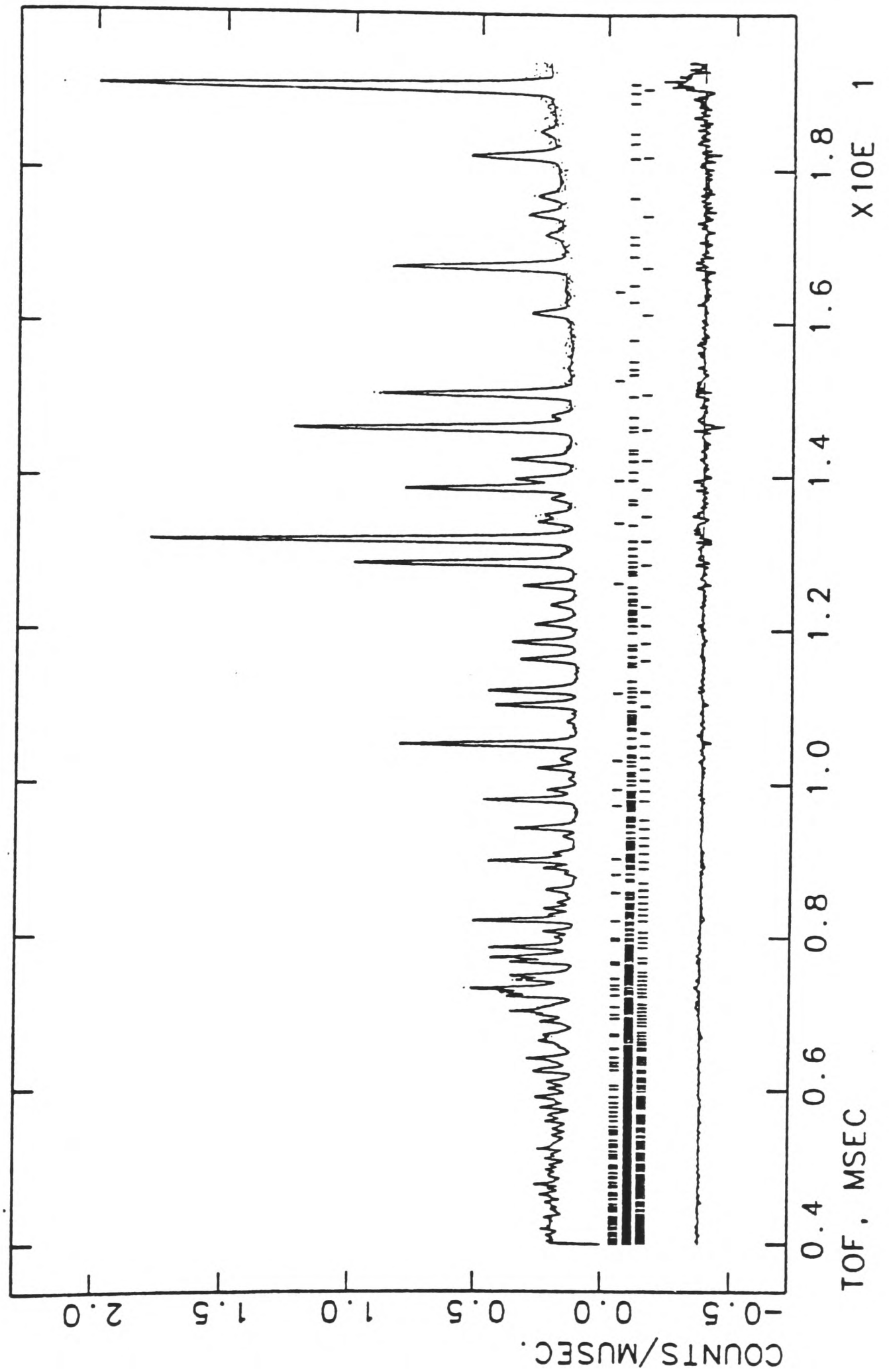


Figure 7.4.IIb Observed (dots), calculated (continuous curve) and difference plots of X-ray data for $K_2Ti_{1.2}Cr_{0.8}(PO_4)_3$.

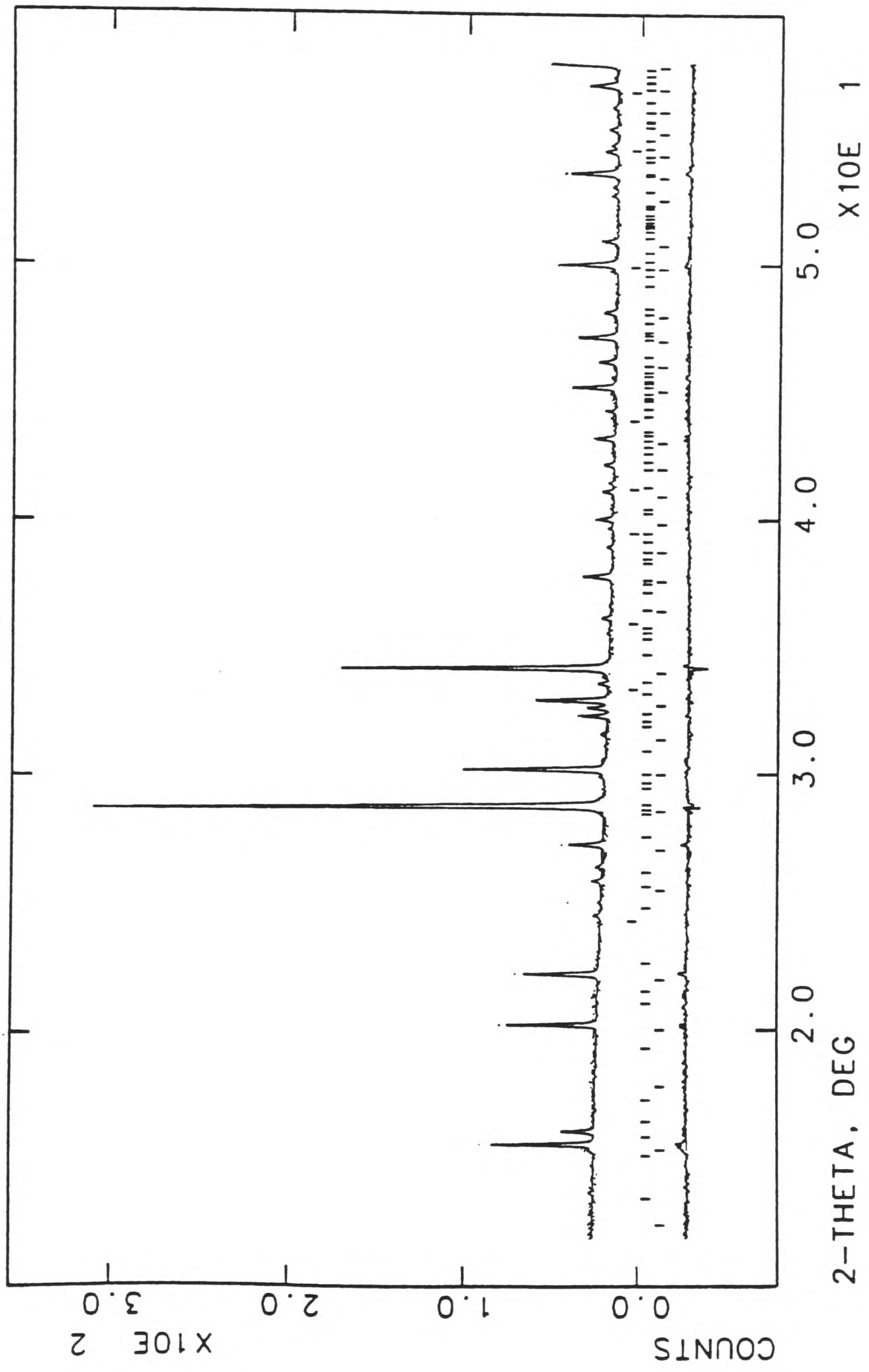


Table 7.4.5 Atom coordinates and thermal parameters of $K_2Ti_{1.2}Cr_{0.8}(PO_4)_3$.

	x	y	z	U_{iso}(Å^2)	occupancy
Ti(1)	0.6633(3)	0.6633(3)	0.6633(3)	-0.003(1)	0.694(6)
Cr(1)	0.6633(3)	0.6633(3)	0.6633(3)	-0.003(1)	0.306(6)
Ti(2)	0.3931(2)	0.3931(2)	0.3931(2)	0.001(2)	0.549(6)
Cr(2)	0.3931(2)	0.3931(2)	0.3931(2)	0.001(2)	0.451(6)
P(1)	0.4764(2)	0.7064(1)	0.3761(2)	0.0007(4)	
K(1)	0.9595(3)	0.9595(3)	0.9595(3)	0.021(1)	0.992(8)
K(2)	0.1826(3)	0.1826(3)	0.1826(3)	0.021(1)	0.870(8)
O(1)	0.6028(2)	0.8275(2)	0.7507(2)	0.0084(3)	
O(2)	0.4526(2)	0.2985(2)	0.2286(2)	0.0084(3)	
O(3)	0.4847(2)	0.5572(2)	0.3304(2)	0.0084(3)	
O(4)	0.5530(2)	0.7279(2)	0.5106(2)	0.0084(3)	

oxidation state. The partial ordering is confirmed by the distribution of bond lengths; that around Ti(1) is not significantly changed from that in $K_2Ti_2(PO_4)_3$ where the sole occupant is Ti(IV), while the Ti(2)-O bonds are significantly shorter than the Ti(III)-O bonds in $K_2Ti_2(PO_4)_3$ which can be explained by substitution of the smaller Cr(III) ion for Ti(III).

A bond valence calculation carried out on $K_2Ti_{1.2}Cr_{0.8}(PO_4)_3$ indicates that while Cr(IV) and Cr(III) are equally well suited to either site, Ti(III) is unstable in both. Therefore Ti would be predicted to occur as Ti(IV) and occupy site 1 while Cr(III) occupied site 2. The neutron diffraction study indicates that the ordering is not complete but that the majority of Ti is on the Ti(1) site, with the majority of Cr being on the Ti(2) site.

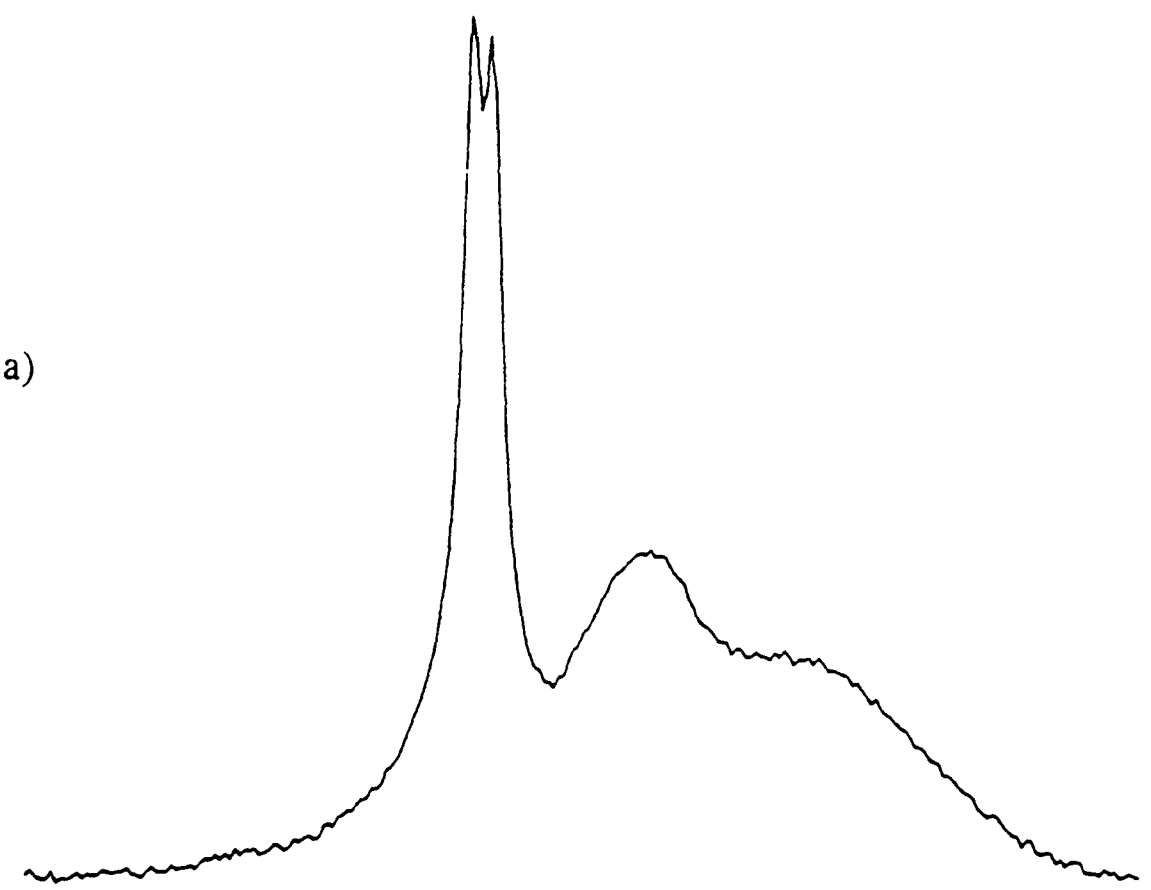
Table 7.4.6 Bond valence parameters for $K_2Ti_{1.2}Cr_{0.8}(PO_4)_3$

	site 1	site 2
Ti(IV)	4.288(6)	4.188(5)
Ti(III)	4.088(6)	3.988(5)
Cr(IV)	4.124(6)	4.022(5)
Cr(III)	3.353(5)	3.275(4)

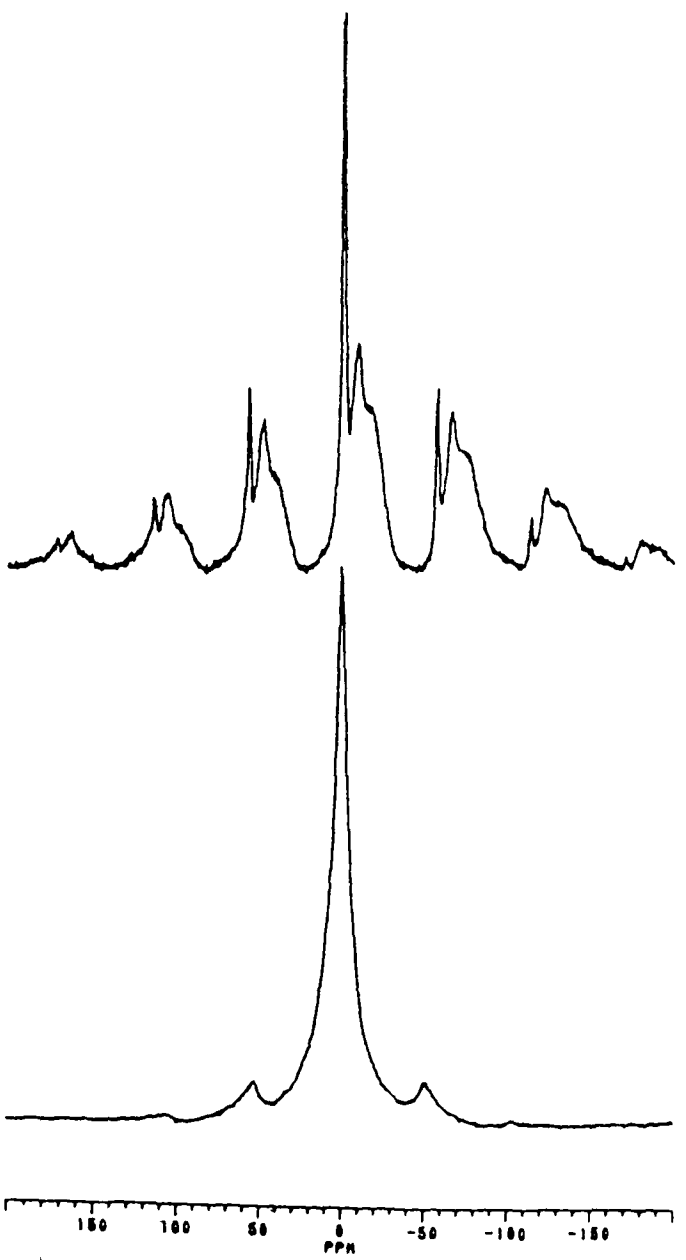
The ^{31}P M.A.S.N.M.R spectrum of the $K_{1.9}Ti_{1.2}Cr_{0.8}(PO_4)_3$ powder (collected by Lucy Bull) is shown in Figure 7.4.IIIa. It contains two distinct types of peaks, a doublet (1.63 and 0.63ppm) of narrow peak width, and a (barely resolved) pair of broad peaks at -7.7 and -16.7ppm. The former appears almost identical to the ^{31}P M.A.S.N.M.R. spectrum of KTP (Figure 3.5.IIIa, peaks at 1.9 and 0.6ppm), so can be attributed to the impurity "KTP isomorph" detected in the powder diffraction study. The narrow lineshape of this pair of peaks is in contrast to that seen in $KTi_{0.95}Cr_{0.05}OPO_4$ (Figure 7.3.III), where the addition of 5% of paramagnetic Cr broadened the peak of the KTP derivative; the material in this sample appears to be pure KTP with no Cr inclusion. In Figure 7.4.IIIb the ^{31}P M.A.S.N.M.R. spectrum of $K_{1.9}Ti_{1.2}Cr_{0.8}(PO_4)_3$ is compared to that of $KTi_{0.95}Cr_{0.05}OPO_4$ on the same scale. The two broad peaks in the spectrum of $K_2Ti_{1.2}Cr_{0.8}(PO_4)_3$ are attributed to the P of the Langbeinite phase in environments with combinations of Ti and Cr in the four neighbouring octahedra.

Figure 7.2.III a) ^{31}P M.A.S.N.M.R. spectrum of $K_{1.9}Ti_{1.2}Cr_{0.8}(PO_4)_3$. Spinning speed = 4622Hz, recyle delay of 60s, (no signal saturation). b) Comparison of ^{31}P M.A.S.N.M.R. spectra of $K_{1.9}Ti_{1.2}Cr_{0.8}(PO_4)_3$ and $KTi_{.98}Cr_{.02}OPO_4$.

a)



b)



7.5 Summary of Chapter 7

KTP phase

Electron microscopy indicated that a small amount of Cr had been incorporated into the KTP solid solution, but only up to a maximum of ~5%. The Cr(2) site was sufficiently different to the Ti(2) site to be distinguished in the single crystal study and their occupancies refined. The only evidence of O reorganisation to accommodate Cr was one short Cr(2)-O bond. The neutron powder diffraction study indicated that Cr was randomly distributed over the two sites so it seems likely that there was an equal quantity of Cr on Ti(2) in the single crystal but the positions occupied were too similar to be differentiated. ^{31}P M.A.S.N.M.R. spectrum of this material had one broad peak at the KTP chemical shift position, interpreted as the substitution of the paramagnetic Cr ion into an unchanged KTP structure.

Langbeinite phase

As the Ti sites are special positions in this space group, the Cr sites could not be resolved, and the occupancies of the two species were refined on the same site to give the overall composition $K_{1.8}Ti_{1.2}Cr_{0.8}(PO_4)_3$ with the majority of Cr on site 2. The measured magnetic moment of the material indicated that Cr was in the (III) oxidation state. The neutron powder refinement corroborated the metal distribution, but the ordering was not complete. The refined composition and magnetic moment were interpreted as indicating that the majority of Cr is in the Cr(III) state, on the Ti(2) site in this structure.

The ^{31}P M.A.S.N.M.R spectrum of the solid state powder sample contained a sharp doublet at the KTP chemical shift, and a broad

hump, assigned to pure KTP and the Cr-doped Langbeinite phase respectively. This indicates that it is more energetically favourable for the Cr to enter the Langbeinite phase than the KTP structure.

CHAPTER EIGHT

This thesis has described an investigation into the substitution chemistry of $KTiOPO_4$, (KTP). In earlier work, complete substitution for K, Ti and P had been demonstrated. However KTP has two formula units per asymmetric unit, so two distinct K, Ti and P sites exist, making substituent ordering possible over the two sites. In this work a series of partially substituted KTP solid solution members were synthesised to investigate whether preferential substitution into one of the two available sites would allow the selective modification of the nonlinear optical properties of KTP.

8.1 Cation substitution into KTP

The synthesis and structural characterisation of cation-substituted KTP isomorphs were described in Chapters three and four. $K_{0.5}Na_{0.5}TiOPO_4$ (KNTP) and $Na_{0.5}Rb_{0.5}TiOPO_4$ (NRTP) show almost complete cation ordering, Na substituting preferentially into the K(1) site, while in $K_{0.5}Rb_{0.5}TiOPO_4$ (KRTP) the ordering is only partial:

	K(1)	K(2)
KNTP	0.96(7)Na:0.04(7)K	-0.05(8)Na:1.05(8)K
NRTP	0.97(3)Na:0.03(3)Rb	0.04(3)Na:0.96(3)Rb
KRTP	0.71(2)K :0.29(2)Rb	0.29(2)K :0.71(2)Rb

The degree of ordering seems to be controlled by the difference in ionic radii of the cations, with the smaller K(1) site being occupied by the smaller cation. The ordering in KRTP is only partial, as K and Rb are closer in size (1.33 and 1.47Å respectively) than either K and Na (0.97Å) or Rb and Na.

X-ray diffraction from ion-exchanged KNTP crystals, (annealed at 700°C to remove any concentration gradients), confirmed the high degree of cation ordering found by powder diffraction.

However the single crystal data were of sufficiently high resolution to define the positions of a small amount of the minority cation within the cavity (i.e. K in K(1) and Na in K(2)). Bond valence calculations carried out on KNTP revealed that the cations move from the average position within the cavity, (found in the powder diffraction study), to separate sites with more suitable coordination for the individual cation (determined in the high resolution crystal structure). X-ray data were also collected from an unannealed ion-exchanged crystal which diffracted X-rays out to 50° in θ (MoK_α radiation) and produced a well-defined structure. This revealed that the material was free from concentration gradients and that cations substituted into a KTP substrate to produce an ion-exchanged waveguide at 350°C should form a phase with long range cation order. Annealing the crystal improved the precision of the refinement but did not markedly alter the degree of cation ordering.

Correlation with nonlinear optical properties

As Na substitutes into KTP, the second harmonic output remains at a high level until 65% of the K has been exchanged by Na, after which it decreases rapidly. To correlate with this, a structural parameter would have to remain constant between KTP and KNTP, only changing markedly between KNTP and β-NTP. Potentially significant factors in the large nonlinear susceptibility of KTP are the distortion within the TiO_6 octahedra and the angles between octahedra in the TiO_6 helical chains (Ti-O-Ti). The Ti-O bond lengths do not change appreciably along the KNTP solid solution series, but the Ti-O(9)-Ti angle does correlate with the nonlinear optical

properties (Table 3.3.3).

$RbTiOPO_4$ has similar nonlinear optical properties to KTP and the structural properties of the $Rb_{1-x}Na_xTiOPO_4$ solid solution series show similar trends to those in $K_{1-x}Na_xTiOPO_4$, so the second harmonic intensity would again be expected to decrease at compositions with x greater than about 65%. In $K_{0.5}Rb_{0.5}TiOPO_4$ the Ti–O(9)–Ti angle increases on Rb substitution by an amount only one third of the magnitude of the decrease seen in KNTP and without a detectable increase in the second harmonic output.

Previous work[57,64,158] on β–AgTP and $(NH_4H)TP$ shows similar trends to that seen in this work. The second harmonic intensity detected from β–AgTP is three orders of magnitude less than that of KTP, while the Ti(1)–O(9)–Ti(2) angle (129.5(6)°) is less than that of β–NTP (SHG one tenth of KTP). In $(NH_4H)TP$ the Ti(1)–O(9)–Ti(2) angle is 127.4° and the second harmonic generated is comparable to that of AgTP. A decrease in the Ti–O(9)–Ti angle correlates with decreased nonlinear optical properties in cation-substituted MTP materials.

8.2 Substitution into the KTP framework

Sn and Ge have been partially exchanged into the KTP framework to form $KTi_{0.5}Sn_{0.5}OPO_4$ (KSTP), $RbTi_{0.5}Sn_{0.5}OPO_4$ (RSTP) and $KTi_{0.5}Ge_{0.5}OPO_4$ (KGTP), in which Ti and Sn/Ge are partially ordered to essentially the same extent:

	Ti(1)	Ti(2)
KSTP	0.639(4)Ti:0.361(4)Sn	0.354(5)Ti:0.646(5)Sn
RSTP	0.623(15)Ti:0.377(15)Sn	0.308(16)Ti:0.692(16)Sn
KGTP	0.767(4)Ti:0.233(4)Ge	0.339(5)Ti:0.661(5)Sn

The Sn/Ge atoms preferentially occupy the *trans*-linking Ti(2) site. The SHG efficiency of these materials decreases with increasing Sn content until, in $KSnOPO_4$, all the distorted TiO_6 octahedra have been replaced by regular SnO_6 octahedra and no

second harmonic radiation can be detected.

The replacement of P by As in the tetrahedral sites of KTP takes place in a random fashion, the As occupies a similar proportion of each of the two P sites of $KTiOP_{0.5}As_{0.5}O_4$ (KTAP) and $RbTiOP_{0.5}As_{0.5}O_4$ (RTAP):

	P(1)	P(2)
KTAP	0.555(12)P:0.445(12)As	0.445(12)P:0.555(12)As
RTAP	0.513(9)P:0.487(9)As	0.487(9)P:0.513(9)As

SHG measurements carried out on KTAP samples prepared by solid state synthesis, (hence having a particle size less than the coherence length), show an approximately linear increase of second harmonic output with As content. The distortions of the TiO_6 octahedra do not change in a systematic fashion on As incorporation, but both the Ti-O-Ti angles within the helical chains increase due to the increased size of the AsO_4 tetrahedra compared to the PO_4 species. An increase in SHG with increasing Ti-O(9)-Ti angle is consistent with the results obtained from alkali-metal cation exchanged materials.

8.3 Cation and Framework substitution

Simultaneous partial substitution for Ti and K in KTP was investigated by combined analysis of X-ray and time-of-flight neutron powder diffraction data from $K_{0.5}Na_{0.5}Ti_{0.5}Sn_{0.5}OPO_4$ (KNSTP), $Na_{0.5}Rb_{0.5}Ti_{0.5}Sn_{0.5}OPO_4$ (NRSTP), and $K_{0.5}Rb_{0.5}Ti_{0.5}Sn_{0.5}OPO_4$ (KRSTP). In all three cases the Ti/Sn ordering was almost unaffected by cation substitution:

	Ti(1)	Ti(2)
KSTP	0.639(4)Ti:0.361(4)Sn	0.354(5)Ti:0.646(5)Sn
KNSTP	0.669(3)Ti:0.331(3)Sn	0.331(3)Ti:0.669(3)Sn
NRSTP	0.670(5)Ti:0.330(5)Sn	0.330(5)Ti:0.670(5)Sn
KRSTP	0.661(3)Ti:0.339(3)Sn	0.339(3)Ti:0.661(3)Sn

The increase in cavity size caused by substitution of the larger Sn into the framework makes the K(1) site less suitable

for Na occupancy. This effect reduces the complete cation ordering seen in KNTP and NRTP to partial ordering in KNSTP and random substitution in NRSTP. In NRSTP, the large Rb ion coupled with Sn in the framework increases the cavity size until neither site is very suitable for Na occupancy and there is no driving force for alkali-metal ordering.

In the KRTP-KRSTP-KRSP solid solution series, the degree of K/Rb ordering determined from time-of-flight neutron powder

	K(1)	K(2)
KNTP	0.96(7)Na:0.04(7)K	-0.05(8)Na:1.05(8)K
NRTP	0.97(3)Na:0.03(3)Rb	0.04(3)Na:0.96(3)Rb
KRTP	0.71(2)K :0.29(2)Rb	0.29(2)K :0.71(2)Rb
KNSTP	0.73(4)Na:0.27(4)K	0.27(4)Na:0.73(4)K
NRSTP	0.46(2)Na:0.54(2)Rb	0.54(2)Na:0.46(2)Rb
KRSTP	0.77(1)K :0.23(1)Rb	0.23(1)K :0.77(1)Rb
KRSP	0.64(2)K :0.36(2)Rb	0.36(2)K :0.64(2)Rb

diffraction decreases with increasing Sn content across the series as a whole, although to a lesser extent than is seen in Na containing materials. The K/Rb ordering is apparently controlled by the competition of K and Rb for the larger K(2) site. The degree of ordering increases in KRSTP relative to that in KRTP due to an increase in the K(1) cavity size, making that site less unfavourable for K. The K(1) site is closer to the Ti(2) site than the Ti(1) site (with K(2) being closer to Ti(1)), so the preferential substitution of Sn into Ti(2) increases the size of the K(1) cavity, while the K(2) site is only significantly affected when more than 50%Sn has been substituted.

8.4 Cr inclusion in the K_2O-P_2O_5-TiO_2 system

A small quantity of Cr enters the Ti(1,2) sites of KTP in a random fashion, up to a maximum of approximately 5% Cr, after which the KTP phase occurs in equilibrium with a langbeinite

phase of undetermined Ti/Cr distribution. A sample prepared at a $K_2Ti_{1.2}Cr_{0.8}(PO_4)_3$ composition contained impurities of pure KTP and Cr_2O_3. These phase mixtures are indicative of a complex phase diagram.

The Cr doped into KTP is not ordered over the two Ti sites, unlike Sn or Ge in the $KTi_{0.5}(Sn/Ge)_{0.5}OPO_4$ materials. The brown colour of $KTi_{0.95}Cr_{0.05}OPO_4$ suggests that Cr is in the (IV) oxidation state, which is less common than Cr(III). This instability of Cr(IV) could be the driving force for formation of the langbeinite phase (which contains primarily Cr(III)), at higher Cr concentration.

The extent of alkali-metal cation ordering in MM'TP materials is dependent on the difference in ionic radii of the substituents, being complete in KNTP and NRTP but only partial in KRTP. Substitution of Sn into the framework reduces the cation ordering by increasing the size of the framework cavities. In MSTP materials, Sn preferentially enters the less distorted *trans*-linking Ti(2) site, independent of the alkali-metal cation. Sn substitution reduces the nonlinear optical properties by substitution of regular SnO_6 octahedra for distorted TiO_6 species. As enters the tetrahedral PO_4 sites in a random fashion and the SHG output increases linearly with increasing As incorporation.

Substitution for K and P in KTP have been shown to modify the nonlinear optical properties. These results show that the NLO properties cannot be calculated by consideration of only isolated Ti-O bonds or TiO_6 octahedra. The contribution from the other components in the structure, and also from condensation of the TiO_6 octahedra into chains must be considered. The

Ti-O(9)-Ti angle seems to correlate with second harmonic output, however there is at least one exception: $CsTiAsO_4$ has distorted TiO_6 octahedra[154] and a very large Ti-O(9)-Ti angle (144.9°), but the SHG detected from this material is only 0.06 times that of KTA.[155] This material also contradicts the theories of Stucky et al (chapter 1), in that the reduced electronegativity and increased coordination of Cs should increase the nonlinear optical properties. Further theoretical and structural work is required before the nonlinear optical properties of KTP isomorphs can be predicted with any certainty.

References

1. *Research on nonlinear optical materials - an assessment* eds. Dagenais M., Kelley P.L., *Appl. Opt.*, 26(2), 211, (1987).

2. Yariv A., *Quantum electronics* 3rd Ed., Wiley, N.Y., (1989)

3. Yariv A., *Optical electronics* 3rd Ed., Holt, Rinehard and Winston, N.Y. (1985).

4. Chemla D.S., *Rep. Prog. Phys.*, 43, 1191, (1980).

5. Hulme K.P., *Rep. Prog. Phys.*, 36, 497, (1973).

6. Born M. and Wolf E., *Principles of Optics* 6th Ed., Pergamon, Oxford, (1980).

7. Hon D., *"High average Power, Efficient Second Harmonic Generation" in Laser Handbook II*, Ed. Stitch M.L., North-Holland, (1979), p421.

8. Hobden M.V., *J. Appl. Phys.*, 38(11), 4365, (1967).

9. Chen C.-T., Liu G.-Z., *Ann. Rev. Mater. Sci.*, 16, 203, (1986).

10. Hutchings M.G., Gordon P.F., Morley J.O., *Proc. Inter. Conf. Mater. nonlinear and electro-optics*, Cambridge, 4-7 July, I.O.P., (1989), p97.

11. Tweig R.J., Jain K., *ACS Symp. Ser.*, 233, *Nonlinear optical properties of organic and polymeric materials*, ed. Williams D.J., 57, (1983).

12. Williams D., *Advan. Chem. Ser.*, 218, eds. Bowden M.J., Turner S.R., 297, (1988).

13. Sherwood J.N., *Phil. trans. R. Soc. Lond. A*, 330, 127, (1990).

14. Bailey R.T., Cruickshank F.R., Pavlides P., Pugh D., Sherwood J.N., *J. Phys. D: Appl. Phys.*, 24, 135, (1991).

15. Etter M.C., Frankenbach G.M., Adsmond D.A., *Mol. Cryst. Liq. Cryst.*, 187, 25, (1990).

16. Zyss J., Chemla D.S., Nicoud J.F., *J. Chem. Phys.*, 74(9), 4800, (1981).

17. Eaton D.F., Anderson A.G., Tam W., Wang Y., *J. Am. Chem. Soc.*, 109, 1886, (1987).

18. Cox S.D., Gier T.E., Stucky G.D., Bierlein J., *J. Am. Chem. Soc.*, 110, 2986, (1988).

19. Feast W.J., *Phil. Trans. R. Soc. Lond. A*, 330, 117, (1990).

20. Ulrich P.R., *Mol. Cryst. Liq. Cryst.*, 189, 3, (1990).

21. Li D., Minami N., Ratner M.A., Ye C., Marks T.J., Yang J., Wong G.K., *Synth. Metals*, 28, D585, (1989).

22. Singer K.D., Holland W.R., Kuzuk M.G., Wolk G.L., Cahill P.A., *Mol. Cryst. Liq. Cryst.*, 189, 123, (1990).

23. Stamatoff J., DeMartino R., Haas D., Khanarian G., Man H.T., Norwood R., Yoon H.N., *Angew. Makromol. Chem.*, 183, 151, (1990).

24. Leslie T.M., DeMartino R.N., Choe E.W., Khanarian G., Haas D., Nelson G., Stamatoff J.B., Stuetz D.E., Teng C.-C., Yoon H.-N., *Mol. Cryst. Liq. Cryst.*, 153, 451, (1987).

25. Eich M., Reck B., Yoon D.Y., Wilson C.G., Bjorklund G.C., *J. Appl. Phys.*, 66(7), 3241, (1989).

26. Groh W., Lupo D., Sixl H., *Angew. Chem. I.E.E.*, 28(11), 1548, (1989).

27. Fan Y.X., Eckardt R.C., Byer R.L., Route R.K., Feigelson R.S., *Appl. Phys. Lett.*, 45(4), 313, (1984).

28. Elsaesser T., Seilmeier A., Kaiser W., Koidl P., Brandt G., *Appl. Phys. Lett.*, 44(4), 383, (1984).

29. Jantz W., Koidl P., *Appl. Phys. Lett.*, 31(2), 99, (1977).

30. Matthes H., Viehmann R., Marschall N., *Appl. Phys. Lett.*, 26(5), 237, (1975).

31. Hanna D.C., Rampal V.V., Smith R.C., *IEEE J. Quant. Electron.*, QE10, 461, (1974).

32. Boyd G.D., Kasper H., McFee J.H., *IEEE J. Quant. Electron.*, QE7, 563, (1971).

33. Chemla D.S., Kupecek P.J., Robertson D.S., Smith R.C., *Opt. Commun.*, 3(1), 29, (1971).

34. Eckardt R.C., Fan Y.X., Byer R.L., Route R.K., Feigelson R.S., van der Laan J., *Appl. Phys. Lett.*, 47(8), 786, (1985).

35. Eckardt R.C., Fan Y.X., Byer R.L., Marquardt C.L., Storm M.E., Esterowitz L., *Appl. Phys. Lett.*, 49(11), 608, (1986).

36. Byer R.L., Choy M.M., Herbst R.L., Chemla D.S., Feigelson R.S., *Appl. Phys. Lett.*, 24(2), 65, (1974).

37. Byer R.L. *Ann. Rev. Mater. Sci.*, 4, 147, (1974).

38. Halbout J.-M., Blit S., Donaldson W., Tang C.L., *IEEE J. Quant. Electron.*, QE15(10), 1176, (1979).

39. Cheng K., Rosker M.J., Tang C.L., *Topics in Appl. Phys.*, 59, 209, (1987).

40. Cassidy C., Halbout J.-M., Donaldson W., Tang C.L., *Opt. Commun.*, 29(2), 243, (1979).

41. Chen C.T., Wu B., Jiang A., You G., *Scien. Sin.*, B28(3), 235, (1985).

42. Chen C.T., Wu Y., Li R., *Int. Rev. Phys. Chem.*, 8(1), 65, (1989).

43. Kato K., *IEEE J. Quant. Electron.*, QE22(7), 1013, (1986).

44. Eckardt R.C., Masuda H., Fan Y.X., Byer R.L., *IEEE J. Quant. Electron.*, QE26(5), 922, (1990).

45. Boyd G.D., Miller R.C., Nassau K., Bond W.L., Savage A., *Appl. Phys. Lett.*, 5(11), 234, (1964).

46. Byer R.L., Young J.F., Feigelson R.S., *J. Appl. Phys.*, 41(6), 2320, (1970).

47. Bryan D.A., Gerson R., Tomaschke H.E., *Appl. Phys. Lett.*, 44(9), 847, (1984).

48. Fukuda T., Uematsu Y., *Jap. J. Appl. Phys.*, 11(2), 163, (1972).

49. Dezhong S. *Mater. Res. Bull.*, 21, 1375, (1986).

50. Uematsu Y., *Jap. J. Appl. Phys.*, 13(9), 1362, (1974).

51. Gunter P., *Appl. Phys. Lett.*, 34(10), 650, (1979).

52. Baumert J.-C., Hoffnagle J., Gunter P., *Proc. SPIE, Int. Soc. Opt. Eng.*, 492, 374, (1984).

53. Nath G., Haussuhl S., *Appl. Phys. Lett.*, 14(5), 154, (1969).

54. Bogdanov S.F., Konvisar P.G., Rustamov S.R., *Sov. J. Quant. Electron.*, 15(10), 1409, (1985).

55. Nash F.R., Bergman J.G., Boyd G.D., Turner E.H., *J. Appl. Phys.*, 40(13), 5201, (1969).

56. Nath G., Mehmanesch H., Gsanger M., *Appl. Phys. Lett.*, 17(7), 286, (1970).

57. Stucky G.D., Phillips M.L.F., Gier T.E., *Chem. Mater.*, 1, 492, (1989).

58. Zumsteg F.C., Bierlein J.D., Gier T.E., *J. Appl. Phys.*, 47(11), 4980, (1976).

59. Stolzenberger R.A., *Appl. Opt.*, 27(18), 3883, (1988).

60. Fan T.Y., Huang C.E., Hu B.Q., Eckardt R.C., Fan Y.X., Byer R.L., Feigelson R.S., *Appl. Opt.*, 26(12), 2390, (1987).

61. Liu Y.S., Dentz D., Belt R., *Opt. Lett.*, 9(3), 76, (1984).

62. Anthon D.W., Crowder C.D., *Appl. Opt.*, 27(13), 2650, (1988).

63. Nishikawa T., Uesugi N., Ito H., *Appl. Phys. Lett.*, 55(19), 1943, (1989).

64. Ahmed F., *Appl. Opt.*, 28(1), 119, (1989).

65. Moody S.E., Eggleston J.M., Seamans J.F., *IEEE J. Quant. Electron.*, QE23(3), 335, (1987).

66. Gettemy D.J., Harker W.C., Lindholm G., Barnes N.P., *IEEE J. Quant. Electron.*, 24(11), 2231, (1988).

67. Bierlein J.D., Vanherzeele H., *J. Opt. Soc. Am. B*, 6, 622, (1989).

68. Eimerl D., *Proc. SPIE, Int. Soc. Opt. Eng.*, 681, 2, (1986).

69. Aleksandroskii A.L., Akhmanov S.A., D'yakov Y.A., Zheludev N.I., Pryalkin V.T., *Sov. J. Quant. Electron.*, 15(7), 885, (1985).

70. Kato K., *IEEE J. Quant. Electron.*, 24(1), 3, (1988).

71. Cheng L.K., Bosenberg W.R., Tang C.L., *Prog. Cryst. Gr. Charac.*, 20, 9, (1990).

72. Ouvrard L. *Comptes Rendus*, 111, 177, (1890).

73. Masse R., Grenier J.-C., *Bull. Soc. Fr. Miner. Cristallog.*, 94, 437, (1971).

74. Tordjman I., Masse R., Guitel J.C., *Z. Krist.*, 139, 103, (1974).

75. Voloshina I.V., Gerr R.G., Antipin M.Y., Tsirel'son V.G., Pavlova N.I., Struchkov Y.T., Ozerov R.P., Rez I.S., *Kristallog.*, 30, 668, (1985).

76. Levine B.F., *Phys. Rev.*, B7(6), 2600, (1973).

77. Levine B.F., *Phys. Rev.*, B7(6), 2591, (1973).

78. Levine B.F., *Phys. Rev.*, B10(4), 1655, (1974).

79. Zumsteg F.C., Bierlein J.D., Gier T.E., *J. Appl. Phys.*, 47(11), 4980, (1976).

80. Hansen N.K., Protas J., Marnier G., *C. R. Acad. Sci. Paris Ser. II*, 307, 475, (1988).

81. Phillips M.L.F., Harrison W.T.A., Gier T.E., Stucky G.D., Kulkarni G.V., Burdett J.K., *Inorg. Chem.*, 29, 2158, (1990).

82. Jarman R.H., Munowitz M., Harrison J.F., *J. Cryst. Growth*, 109, 353, (1991).

83. Phillips M.L.F., Harrison W.T.A., Stucky G.D., *Inorg. Chem.*, 29, 3245, (1990).

84. Phillips M.L.F., Harrison W.T.A., Stucky G.D., McCarran E.M., Calabrese J., in preparation.

85. Laurent Y., *Rev. Chim. Miner.*, 6, 1145, (1969).

86. Jacco J.C., Loiacono G.M., Jaso M., Mizell G., Greenberg B., *J. Cryst. Growth*, 70, 484, (1984).

87. Dezhong S., Chaoen H., *Prog. Cryst. Growth Charac.*, 11, 269, (1985).

88. Ballman A.A., Brown H., Olsen D.H., Rice C.E., *J. Cryst. Growth*, 75, 390, (1986).

89. Iliev K., Peshev P., Nikolov V., Koseva I., *J. Cryst. Growth*, 100, 219, (1990).

90. Iliev K., Peshev P., Nikolov V., Koseva I., *J. Cryst. Growth*, 100, 225, (1990).

91. Jarman R.H., *Solid State Ionics*, 32/33, 45, (1989).

92. *JCPDS*, International Centre for Diffraction Data, 1601 Park Lane, Swarthmore, Pennsylvania 19081, U.S.A.

93. Rae-Smith A.R., Chemical Crystallography Lab., Oxford.

94. Yvon K., Jeitschko W., Parthe E. *J. Appl. Cryst.*, 10, 73, (1977).

95. Pye M.F., Part II thesis, Oxford University, (1978), unpublished.

96. *JEOL documentation for the JEM2000FX EM*, JEOL Ltd, 1418 Kakagami Akishima, Tokyo 196, Japan.

97. *Tracor Northern documentation for the TN5500*, Tracor Northern Ltd, 2551 West Beltine Highway, Middleton, Wisconsin 53562.

98. Cliff G., Lorimer G.W., *J. Microsc.*, 103(2), 203, (1975).

99. Cheetham A.K., Skarnulis A.J., *Anal. Chem.*, 53, 1060, (1981).

100. Heinrich K.F.J., *The Electron Microprobe*, eds. Mc Kinley T.D., Heinrich K.F.J., Wittry D.B., Wiley, New York, (1966).

101. Stout G.H., Jensen L.H., *X-ray structure determination*, second edition, Wiley-interscience, New York, (1989).

102. *Enraf-Nonius CAD4 User Guide*, Delft, Holland (1984).

103. Buerger M.J., *Crystal Structure Analysis*, Wiley, New York, (1960).

104. Klug H.P., Alexander L.E., *X-ray Diffraction Procedures for polycrystalline and amorphous materials*, 2nd Ed., Wiley, New York, (1974).

105. *International Tables for Crystallography*, eds. Kasper J.S., Lonsdale K., Kynoch Press, Birmingham, 2, (1959).

106. North A.C.T., Phillips D.C., Matthews F.S., *Acta Cryst.*, A24, 351, (1968).

107. Watkin D.J., Carruthers J.R., Betteridge P.W., *CRYSTALS user guide*, Chemical Crystallography Laboratory, University of Oxford, (1989).

108. Larson A.C., in *Crystallographic Computing* ed. Ahmed F.R., Munksgaard, Copenhagen, p 291, (1970).

109. Flack H.D., Schwarzenbach D., *Acta Cryst.*, A44, 499, (1988).

110. Flack H.D., *Acta Cryst.*, A39, 876, (1983).

111. Prince E., *Mathematical techniques in Crystallography*, Springer-Verlag, (1982).

112. Rollett J.S., *Computing Methods in Crystallography*, Pergamon press, Oxford, (1965).

113. *International Tables for Crystallography Vol IV*, eds. Ibers J.A., Hamilton W.C., Kynoch Press, Birmingham, (1974).

114. Bacon G.E., *Neutron Diffraction*, Clarendon Press, Oxford (1975).

115. Hewat A.W., *Chemica Scripta*, 26A, 119, (1986).

116. Jackson P.F., Johnson B.F.G., Lewis J., Raithby P.R., McPartlin M., Nelson W.J.H., Rose K.D., Allibon J., Mason S.A., *J. Chem. Soc., Chem. Commun.*, 295, (1980).

117. Koester L., Yelon W.B., *Summary of low energy Neutron Scattering lengths and Cross-sections*, Netherlands Energy Research Foundation, Department of Physics, Petten, The Netherlands, (1982).

118. Blume M., *J. Appl. Phys.*, 57, 3615, (1985).

119. Gibbs D., Moncton D.E., D'Amico K.L., *J. Appl. Phys.*, 57, 3619, (1985) and Gibbs D., Moncton D.E., D'Amico K.L., Bohr J., Grier B.H., *Phys. Rev. Lett.*, 55, 234, (1985).

120. Albinati A., Willis B.T.M., *J. Appl. Cryst.*, 15, 361, (1982).

121. Fischer P., Zolliker P., Meier B.H., Ernst R.R., Hewat A.W., Jorgensen J.D., Rotella F.J., *J. Solid State Chem.*, 61, 109, (1986).

122. Cheetham A.K., in *Chemical Crystallography with Pulsed Neutrons and Synchrotron X-rays* , eds. Carrondo M.A., Jeffrey G.A., 137, (1988)

123. *ISIS User Guide*, RAL-88-030, February 1988.

124. Hewat A.W., *High Res. Powder Diff.*, 9, 69, (1986).

125. *Neutron Research Facilities at the ILL High Flux Reactor*, Institut Laue Langevin, Grenoble, France (July 1986).

126. Clearfield A., Rudolf P.R., *American Crystallographic Association Transactions*, 23, 35, (1987), ed. Craven B.M.

127. Crawford K., *Neutron News*, 1(3), 9, (1990).

128. Hull S., Mayers J., *User guide for the POLARIS powder diffractometer at ISIS*, RAL-89-118, (1989).

129. *STOE Stadi-P User manual revision 5.0*, STOE & CIE GmbH, D-1600, Darmstadt, Hilperstrasse 10, Postfach 4110, W. Germany.

130. Rietveld H.M., *Acta Cryst.*, 22, 151, (1967).

131. Rietveld H.M., *J. Appl. Cryst.*, 2, 65, (1969).

132. Larson A.C., Von Dreele R.B., *Los Alamos report LAUR 86-748*, (1987), unpublished.

133. Von Dreele R.B., Jorgensen J.D., Windsor C.G., *J. Appl. Cryst.*, 15, 581, (1982).

134. Abramowitz M., *Handbook of Mathematical functions: with formulas, graphs and mathematical tables*, ed. Stegun I., Dover, New York, (1964).

135. Caglioti G., Paoletti A., Ricci F.P., *Nucl. Instrum.*, 3, 223, (1958).

136. Brown I.D., in *Structure and Bonding in Crystals Vol II*, eds. O'Keefe M., Navrotsky A., Acad. Press., New York, (1980), p1.

137. Pauling L., *J. Amer. Chem. Soc.*, 51, 1010, (1929).

138. Brown I.D., Shannon R.D., *Acta Cryst.*, 29A, 266, (1973).

139. Brown I.D., Wu K.K., *Acta Cryst.*, 32B, 1957, (1976).

140. Brown I.D., Altermatt D., *Acta Cryst.*, 41B, 244, (1985).

141. Bjorkholm J.E., *IEEE J. Quantum Elec.*, 4, 970, (1968) and Bjorkholm J.E., *IEEE J. Quantum Elec.*, 5, 260, (1969).

142. Boyd G.D., Ashkin A., Dziedzic J.M., Klienman D.A., *Phys. Rev.*, 137A, 1305, (1965).

143. Maker P.D., Terhune R.W., Nisenoff M., Savage C.M., *Phys. Rev. Lett.* , 8(1), 21, (1962).

144. Jerphagnon J., Kurtz S.K., *Phys. Rev.*, B1, 1739,(1970).

145. Jerphagnon J., Kurtz S.K., *J. Appl. Phys.*, 41(4), 1667, (1970).

146. Wynne J.J., Bloembergen N., *Phys. Rev.*, 188(3), 1211, (1969).

147. Byer R.L., Harris S.E., *Phys. Rev.*, 168, 1064, (1968).

148. Kurtz S.K., Perry T.T., *J. Appl. Phys.*, 39(8), 3798, (1968).

149. Dougherty J.P., Kurtz S.K., *J. Appl. Cryst.*, 9, 145, (1976).

150. Bierlein J.D., Vanherzeele H., Ballman A.A., *Appl. Phys. Lett.*, 54(9), 783, (1989).

151. Bailey R.T., Blaney S., Cruickshank F.R., Guthrie S.M.G., Pugh D., Sherwood J.N., *Appl. Phys.*, B47, 83, (1988).

152. Bierlein J.D., Ferreti A., Brixner L.H., Hsu W.Y., *Appl. Phys. Lett.*, 50(18), 1216, (1987).

153. Wang J.Y., Liu Y.G., Wei J.Q., Shi L.P., Wang M., *Z. Krist.*, 191, 231, (1990).

154. Protas J., Marnier G., Boulanger B., Menaert B., *Acta Cryst.*, C45, 1123, (1989).

155. el Haidouri A., Durand J., Cot L., *Mat. Res. Bull.*, 25, 1193, (1990).

156. Bamberger C.E., Begun G.M., Cavin O.B., *J. Solid State Chem.*, 73, 317, (1988).

157. Nagornyi P.G., Kapshuk A.A., Stus N.V., Slobodyanik N.S., *Z. Neorg. Khimii*, 34, 3030, (1989).

158. Eddy M.M., Gier T.E., Keder N.L., Stucky G.D., Cox D.E., Bierlein J.D., Jones G. *Inorg. Chem.* , 27(11), 1856, (1988).

159. Jarman R.H., Kaduk J.A., unpublished single crystal studies of $KTiOPO_4$ and $RbTiOPO_4$.

160. *Users manual for Rietveld refinement at IPNS*. Also Von Dreele R.B., Jorgensen J.D., Windsor C.G., *J. Appl. Cryst.*, 15, 581,(1982).

161. Abrahams S.C., Bernstein J.L., *J. Chem. Phys.*, 55, 3206, (1971).

162. Owen J.J., *Part II Thesis*, Oxford University, (1990), unpublished. Also Crennell S.J., Owen J.J., Grey C.P., Cheetham A.K., Kaduk J.A., Jarman R.H., *J. Mater. Chem.*, 1, 113, (1991).

163. Alferness R.C., *IEEE J. Quantum Elec.*, QE-17(6), 946, (1981).

164. Bierlein J.D., Arweiler C.B., *Appl. Phys. Lett.*, 49(15), 917, (1986).

165. Roelofs M.G., *J. Appl. Phys.*, 65(12), 4976, (1989).

166. Laubacher D.B., Guerra V., Chouinard M.P., Liou J.Y., Wyant P.H., *Proc. SPIE-Int. Soc. Opt. Eng.*, 993, 80, (1988).

167. Bierlein J.D., Laubacher D.B., Brown J.B., van der Poel C.J., *Appl. Phys. Lett.*, 56(18), 1725, (1990).

168. Thomas P.A., Glazer A.M., Watts G.E., *Acta Cryst.*, B46, 333, (1990).

169. Avduevskaya K.A., Tananaev I.V., Mironova V.S., *Izv. Akad. Nauk. SSSR, Neorg. Mater.*, 1(6), 894, (1965).

170. Phillips M.L.F., Harrison W.T.A., Gier T.E., Stucky G.D., Kulkarni G.V., Burdett J.K., *Inorg. Chem.*, 29, 2158, (1990).

171. Crosnier M.-P., Guyomard D., Verbaere A., Piffard Y., *Eur. J. Solid State Inorg. Chem.*, 27(6), 845, (1990).

172. Pagnoux C., Guyomard D., Verbaere A., Piffard Y., Tournoux M., *C.R. Acad. Sci. Paris Ser.II*, 312, 611, (1991).

173. el Brahimi M., Durand J., *Rev. Chim. Miner.*, 23, 146, (1986).

174. Baur W.H., Khan A.A., *Acta Cryst.*, B27, 2133, (1971).

175. Jarman R.H., Grubb S.G., *Proc SPIE- Int. Soc. Opt. Eng.*, 968, 108, (1988).

176. Smith G.S., Isaacs P.B., *Acta Cryst.*, 17, 842, (1964).

177. Hagman L.-O., Kierkegaard P. *Acta Chem. Scand.*, 22, 1822, (1968).

178. Thomas P.A., Watts B.E. *Sol. St. Commun.*, 73(2), 97, (1990).

179. Belokoneva E.L., Yakubovich O.V, Tsirelson V.G., Urusov V.S., *Neorg. Mater.*, 26(3), 595, (1990).

180. Chou N.Y., Koker E.B., Barnes N.P., Loiacono G.M., *Advan. Sol. State Lasers, Tech. Dig.*, Mar 5-7 (1990), Salt Lake City, pMA4-1

181. McGee T.F., Blom G.M., Kostecky G., *J. Cryst. Growth*, 109, 361, (1991).

182. Leclaire A., Benmoussa A., Borel M.M., Grandin A., Raveau B., *J. Solid State Chem.*, 78, 227, (1989).

183. Battle P.D., Gibb T.C., Nixon S., Harrison W.T.A., *J. Solid State Chem.*, 75, 21, (1988).

184. Coda A., Pandarese F., *J. Appl. Cryst.*, 9, 193, (1976).

185. Yanovskii V.K., Voronkova V.I., *Sov. Phys. Solid State*, 27(7), 1308, (1985).

186. Phillips M.L.F., Gier T.E., Keder N.L., Stucky G.D., Bierlein J.D., *Solid State Ionics*, 32/33, 147, (1989).

APPENDICES

Appendix 1 Observed and calculated structure factors for the annealed and ion-exchanged $K_{0.5}Na_{0.5}TiOPO_4$ crystal.

Accompanying material
stored separately.
Search OLIS for shelfmark.

APPENDICES

Appendix 2 Observed and calculated structure factors for the ion-exchanged $K_{0.5}Na_{0.5}TiOPO_4$ crystal.

APPENDICES

Appendix 3 Observed and calculated structure factors for the $KTi_{0.95}Cr_{0.05}OPO_4$ crystal.

APPENDICES

Appendix 4 Observed and calculated structure factors for the $K_2Ti_{1.2}Cr_{0.8}(PO_4)_3$ crystal.